GPS Carrier Phase Tracking in Difficult Environments Using Vector Tracking For Precise Positioning and Vehicle Attitude Estimation

by

Scott M. Martin

A dissertation submitted to the Graduate Faculty of
Auburn University
in partial fulfillment of the
requirements for the Degree of
Doctor of Philosophy

Auburn, Alabama
May 6, 2017

Keywords: Vector Tracking, RTK GPS, GPS Attitude

Approved by

David M. Bevly, Chair, Professor of Mechanical Engineering
Song-yul Choe, Professor of Mechanical Engineering
John Hung, Professor of Electrical and Computer Engineering
David A. Cicci, Professor of Aerospace Engineering

Abstract

In this dissertation, two approaches are developed to improve the carrier phase tracking performance of a software-defined GPS receiver. The first approach combines a non-coherent vector tracking architecture with a local phase locked loop to improve carrier phase tracking performance of a stand-alone (i.e. not base station) GPS receiver. The Vector Frequency Locked Loop (VFLL) aided Phase Locked Loop (PLL) receiver is shown to provide a more robust carrier phase tracking performance at low carrier-to-noise density (C/N_0) ratios. The VFLL aided PLL is able to maintain phase lock of signal with 2 to 3 dB lower C/N_0 ratio. The more significant improvement is that, while the scalar tracking receiver quickly lost phase lock completely at low C/N_0 ratios, the VFLL aided PLL only slipped cycles.

The second approach is designed to include measurements from a local base station. The Real-Time Kinematic (RTK) vector phase locked loop receiver is derived. The RTK VPLL receiver is a true carrier phase tracking receiver in that the navigation filter is updated using correlator outputs, and there is no local loop filter for each tracking channel. The tracking loop is closed by predicting the received carrier phase using the navigation solution. Base station measurements are combined with relative position vector estimates from the navigation filter and fixed carrier ambiguities to close the tracking loops. In simulation, the RTK VPLL maintains phase lock at C/N_0 ratios 4 to 8 dB lower than a traditional scalar tracking receiver. During experimental testing, the RTK VPLL receiver maintains the navigation solution and carrier phase tracking throughout tests in moderate and heavy foliage. There are times during the experimental test that the RTK VPLL receiver slipped cycles of the carrier, and the navigation solution degrades as a result. The environment prevents the standard receiver from reporting a high precision solution for even longer periods.

Finally, the benefits of the RTK VPLL receiver design are investigated in a multi-antenna configuration. Data from multiple GPS antennas mounted on a rigid body may be used to estimate the attitude of the platform. The solution for finding the three Euler angles (i.e. roll, pitch, and yaw) of the platform given two relative position vectors is provided. Two studies are performed to identify possible improvements to the software receiver design developed in this dissertation. A modified two antenna RTK VPLL algorithm was developed and tested in simulation. It is shown that the two antenna algorithm does not significantly improve the carrier phase tracking performance at low C/N_0 ratios. An RTK carrier ambiguity estimation procedure is developed using the multiple antenna configuration and the known antenna separation distance. The new baseline constrained ambiguity estimation algorithm significantly reduces time to fix and provide a method for rejecting incorrect fixes.

Acknowledgments

I would first like to thank my wife Jill for her patience and support throughout the process of writing this dissertation. I would also like to thank my parents for supporting and nurturing me through the tough times in my life. My sister Stephanie has always been the smartest person I know. I would not be where I am today without all the knowledge she has shared with me.

I want to also acknowledge the team of researchers in the GPS and Vehicle Dynamics Laboratory. My adviser Dr. David Bevly has provided steady counsel throughout my time here at Auburn. I owe a great debt to the other members of the lab for all their help over the years. I would especially like to thank Lowell Brown for his friendship and insights during this journey.

Table of Contents

List of Figures

List of Tables

Chapter 1

Introduction and Background

The Global Positioning System (GPS) has become a workhorse in the position, navigation, and timing industry. It is used in diverse markets, providing value and integrity to military or civilian localization, navigation for commercial and personal transportation, and for precise timing in trading and power management.

1.1 Motivation

Civilian users have reaped the benefits of GPS localization accuracy for years using handheld devices capable of reporting the receiver position to within several meters of the true global position [46]. These devices work well with a clear line of sight to the satellites that are transmitting the GPS signal. However, the signal strength received by the user is weak, approximately 10^{-16} watts [46], and therefore susceptible to interference. Signal disruptions are caused by a variety of environmental factors including natural obstructions (e.g. trees, canyons), man made physical obstructions (e.g. building, bridges), and electromagnetic (e.g. signal jammers) interference. Currently, these factors, along with accuracy limitations, are the primary concerns that limit the adoption of GPS in markets like the booming commercial autonomous vehicle industry.

To address these two concerns, accuracy and reliability, this dissertation focuses on the development and testing of improved signal tracking capabilities for reliable differential GPS (DGPS) positioning in degraded environments. DGPS is a technique that uses data from a static GPS receiver mounted at a known location to improve the localization accuracy of a mobile rover receiver. The technique relies on mitigating correlated errors experienced by both receivers, such as atmospheric interference and satellite clock errors. The receiver

architecture that is developed in this dissertation combines DGPS positioning with a signal tracking approach called vector tracking. Vector tracking replaces traditional GPS signal tracking loops with a single filter responsible for maintaining the position, velocity, and time estimates of the receiver and for generating the local replica of the received signal used to generate error measurements.

1.2 Prior Art

In a traditional GPS receiver, a single, or scalar, tracking channel is assigned the responsibility of maintaining a synchronous copy of the binary pseudo random noise (PRN) code and the sinusoidal carrier wave for the signal received from each visible satellite. A block diagram of the process is shown in Figure 1.1. The signal received at the antenna passes through a radio frequency (RF) front end where it is filtered and mixed down to a lower intermediate frequency (IF) and sampled. The samples are then processed by several independent channels to produce measurements of code phase error and carrier frequency or carrier phase error. These measurements are filtered in a scalar tracking loop filter, and corrections are made to the local replicas of the PRN code and sinusoidal carrier. The numerically controlled oscillator (NCO) is adjusted to provide the correct code and carrier frequencies. Measurements of the range (or pseudorange) and range rate (pseudorange rate) are extrapolated from the local replicas of the PRN code and carrier. The navigation filter uses the pseudorange and pseudorange rate measurements to estimate position, velocity, and time. Note that the tracking and localization tasks are separate and distinct, and that there is no aiding across the individual tracking channels.

Vector tracking receivers replace the individual tracking loop filters with feedback from the navigation filter. A block diagram of a typical vector tracking architecture is shown in Figure 1.2. As seen in the figure, the loop filters have been removed, and the outputs of the navigation filter are used to steer each NCO to control the code and carrier frequencies of the local replicas. The design takes advantage of the fact that as the number of visible

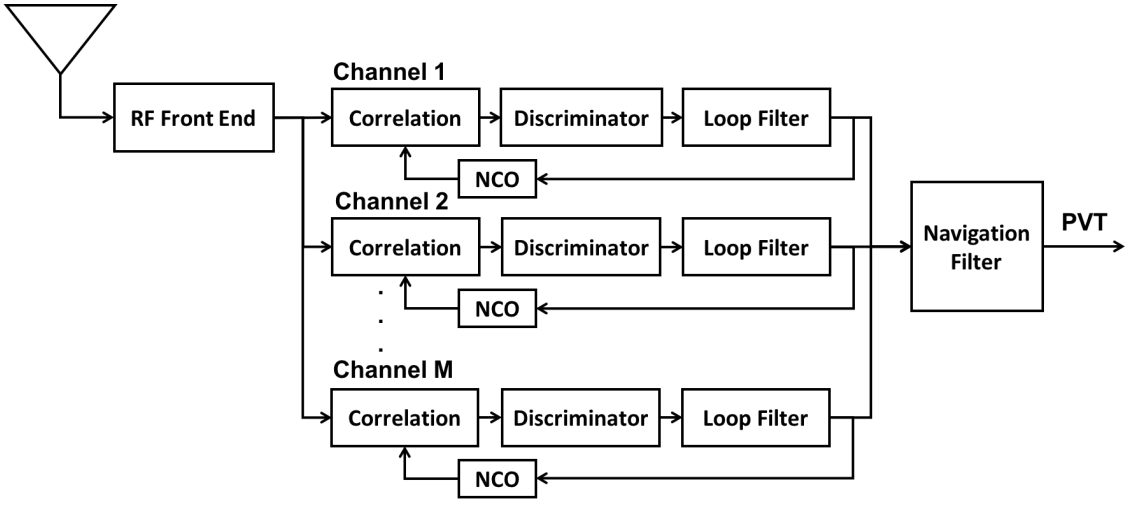

Figure 1.1: Block diagram of traditional scalar tracking receiver architecture.

satellites increase beyond four, the navigation solution becomes overconstrained. Four satellite signals are required to estimate the position, velocity, and clock states of the navigation filter. Additional measurements add redundency that improve the quality of the navigation solution. This means that accurate local replicas can be maintained for received satellite signals that are severely attenuated or temporarily blocked by environmental factors using the navigation information available from other satellites. Also, the sharing of information from channel to channel allows for improved tracking sensitivity and improved tracking in high dynamic situations [40].

1.2.1 Aided Tracking Architectures and Vector Tracking

A variety of architectures and algorithms have been developed over the last 25 years that exploit the spatial correlation of the signals received by the GPS receiver. In 1991, Sennott and Senffner published a paper at the Institute of Navigation GPS Conference describing methods for preventing carrier phase cycle slips by leveraging the satellite geometry [59]. One year later, the authors also filed a patent with the US Patent Office describing a receiver architecture with coupled signal tracking channels [60]. The vector delay locked loop (VDLL) for tracking the phase of the PRN code was another early form of vector tracking suggested by

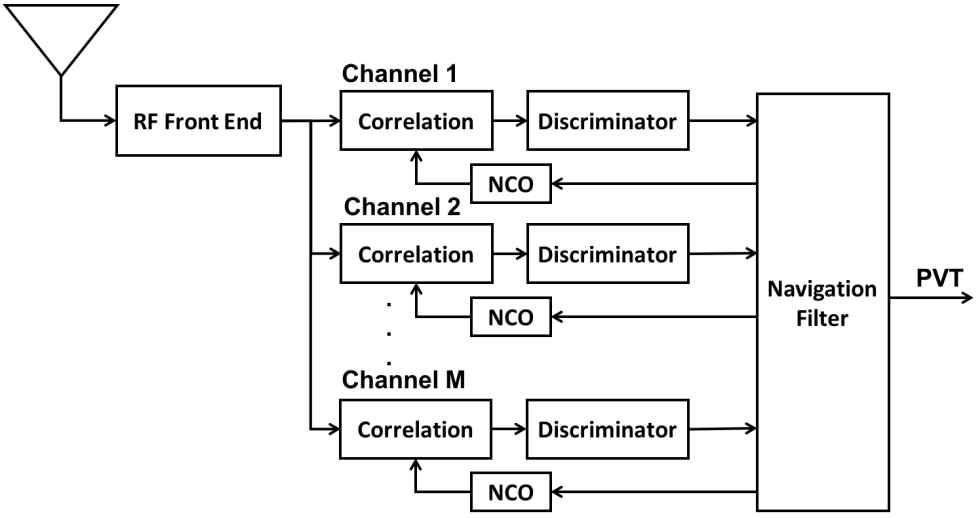

Figure 1.2: Block diagram of vector tracking receiver architecture.

Spilker in *Global Positioning System: Theory and Applications, Volume 1* [52]. All of these approaches, and the methods that followed, rely in some way on the relative position and/or velocity of the receiver and the satellites to predict the received signal structure. Many of the algorithms use an external sensor, typically an Inertial Measurement Unit (IMU), to track the motion of the receiver platform between GPS measurement updates. In the early 2000s, Gebre-Egziabher *et al.* analyzed the performance of carrier tracking loops aided with external Doppler information [2, 16, 17] and concluded that a 4 dB-Hz improvement in the carrier phase tracking threshold was possible with a tactical grade IMU. Other Ultra-Tight (UT), or Deeply Integrated (DI), approaches have been developed for improved tracking of the PRN code and/or carrier. They include both carrier frequency lock and carrier phase lock approaches that can be designated as non-coherent and coherent tracking respectively.

Non-Coherent Tracking Approaches

In a non-coherent tracking scheme, a measurement of the phase of the received sinusoidal carrier is not maintained. Rather, the carrier frequency of the local replica is updated to maintain frequency lock with the received signal. The reason for this approach is that the carrier phase lock is more difficult to maintain than carrier frequency lock. A traditional

scalar tracking receiver can maintain frequency lock as low as 21 dB-Hz carrier-to-noise density (C/N_0) ratio, but is only effective down to approximately 28 dB-Hz for phase tracking [16, 62]. Accordingly, there are a number of vector tracking approaches that focus on the combined tracking of the PRN code phase and the sinusoidal carrier frequency. These tracking algorithms are called vector delay and frequency locked loops (VDFLL). The non-coherent VDFLL can be characterized as either a pure vector tracking receiver or a DI system that includes an IMU to predict motion between receiver measurements.

There has been extensive work on developing, analyzing, and implementing VDFLL receiver algorithms. Lashley *et al.* analyzed the tracking performance of VDFLL in high dynamics and in low C/N_0 environments and compared the VDFLL performance to the performance of traditional scalar tracking receivers [37–39]. Clark investigated the integrity aspects of the VDFLL with a focus on fault detection and exclusion [9]. Later, Edwards and Keyser worked to implement the VDFLL architecture in a combined hardware/software real-time solution [14,33]. In other research, Pany *et al.* described and analyzed a "deep integration" of navigation and signal tracking and later evaluated its use in estimating received signal power [50, 51]. There are additional implementations and analysis showing improved tracking of weaker signals when stronger signals are available [27,28], describing an extended Kalman filter (EKF) approach to code phase tracking [71], and describing an open source VDFLL implementation [70].

In addition to references above, there are several sources that derive and analyze non-coherent vector tracking methods using IMU aiding. Researchers at Draper Laboratory investigated a VDLL implementation with IMU aiding focused on mitigating broad band jamming. The Draper work was published at multiple conferences and a patent was obtained [23–25]. An improvement of approximately 15 dB in code tracking sensitivity was asserted. Abbott and Lillo also patented an IMU aided VDFLL tracking strategy [1]. The primary difference in the Abbott scheme was the use of Kalman filters on each channel to estimate tracking errors between 1 Hz master filter updates. Paul Grove *et al.*, of QinetiQ,

presented findings on a non-coherent INS/GPS system which they optimized for signal to noise performance [21]. As part of the analysis, the authors address the impact of C/N_0 measurement accuracy on deep integration. More recently in 2011, Wang *et al.* studied the use of deep integration for autonomous train navigation [68].

Coherent Tracking Approaches

As stated previously, non-coherent tracking indicates that the receiver is designed without requiring accurate carrier phase tracking. This does not affect the traditional positioning capabilities of the GPS receiver as long as the satellite ephemerides are known. However, the receiver would be limited to the accuracy of the pseudorange measurement. With accurate carrier phase measurements, positioning accuracy can be improved by two orders of magnitude over the pseudorange based position solution. Several methods have been introduced to improve carrier phase tracking using IMU aiding, navigation solution feedback, or a combination of both. Phillip Ward developed and analyzed a scalar tracking method wherein the phase locked loop (PLL) was aided by a frequency discriminator and loop filter (i.e. frequency locked loop (FLL)), and showed carrier phase tracking at lower C/N_0 ratios in high and low dynamic scenario simulations [69]. This architecture was modified by Kiesel *et al.* and Deambrogio *et al.* by replacing the frequency discriminator with a frequency error estimate derived by the navigation processor creating a vector frequency lock loop (VFLL). Kiesel *et al.* analyzed the architecture in simulation, and showed improved carrier phase tracking during decreasing signal power ranging from 47 dB-Hz down to 23 dB-Hz C/N_0 [34]. Deambrogio *et al.* focused on carrier phase tracking during ionospheric scintillation, and provided carrier cycle slip and re-acquisition results using simulated scintillation data [12]. Researchers have published several works investigating deeply integrated GPS/INS integration methods for improved carrier tracking. Petovello *et al.* provided comparisons of a different cascaded implementations for DI where local loop filters are used to estimate specific signal parameters. The local loop filters are then periodically updated with

feedback from the navigation processor which is corrected with traditional pseudorange and Doppler measurements [53]. The authors were able to show 7 dB improvement of traditional constant gain scalar loops filters and 3 dB improvement over variable gain (e.g. estimator based) scalar loop filters [54–56].

One of the earlier vector based carrier phase tracking approaches was derived by Zhodzishsky *et al.* in 1998 called Co-OP tracking [72]. The approach used a combination of low bandwidth scalar tracking loops and feedback from the navigation processor. The Co-Op tracking algorithm differs from the VFLL technique described in that the carrier phase discriminator is used to correct the navigation solution, rather than the carrier frequency discriminator. More recently, researchers at the Technical University of Munich have developed a vector phase locked loop (VPLL) implementation which maintains phase lock by estimating position, clock, and atmospheric delay changes from epoch to epoch [26]. The algorithm requires estimation of ionospheric delay changes for each satellite being tracked and does not rely directly on the global navigation solution. Later, the authors added vector code tracking to the VPLL in an implementation they called "position domain joint tracking" and investigated performance in multipath environments [18, 19]. Soloviev et al. developed a deeply integrated GPS/INS vector phase tracking implementation [61–63]. The use of the IMU allows for extending the integration period well beyond the typical 20 ms up to 1s. The authors incorporated an energy based data bit estimator to allow for integration over bit transitions. The system was tested in-flight, in dense urban areas, and indoors, and presented results showing carrier phase tracking at 12 - 15 dB-Hz C/N_0. Finally in a recent study, Brewer derived a differential carrier phase tracking architecture that used base station measurements to aid in carrier phase tracking [6]. Brewer's implementation did not include the creation of the traditional accumulated Doppler measurements. Two static receivers were used in the study. Unlike the work by Brewer, the RTK VPLL developed in this dissertation uses the common accumulated Doppler measurements from the base station receiver and does not require a static rover receiver.

1.3 Contributions

All of the above references address improvement to the tracking of the GPS carrier phase. The underlying need for accurate carrier phase measurements is often not addressed or receives a brief mention. Accurate carrier phase measurement allows for estimating receiver position to within a few centimeters of the true position with data from a local base receiver using a process called real time kinematic (RTK) positioning. In this dissertation, the tracking of the carrier phase and the calculation of the RTK carrier phase based position solution are combined into one algorithm. Several contributions to the field of vector based carrier phase tracking are made in this dissertation:

- Development of an improved carrier phase tracking approach for a base station receiver experiencing degraded signals
- Simulation analysis of improved base station tracking in the presence of ionospheric scintillation
- Development and analysis of a software GPS receiver based RTK positioning algorithm
- Development of RTK VPLL carrier phase tracking architecture in a software GPS receiver
- Simulation analysis of the RTK VPLL receiver in presence of ionospheric scintillation and low C/N_0 signals
- Analysis of the RTK VPLL receiver using samples collected in clear sky and heavy foliage environments with comparison to survey grade GPS receiver
- Development and analysis of a multi-antenna RTK VPLL carrier phase based attitude estimation algorithm

1.4 Dissertation Outline

The remainder of this dissertation describes the development and/or performance analysis of a number of GPS receiver operations that provide either typical receiver measurements, like pseudorange and carrier phase, or typical receiver outputs, like position, velocity, and time. This dissertation focuses on the receiver operations that happen after the received signal is mixed down to an intermediate frequency and digitized. All the algorithms described and developed in this dissertation are designed to be implemented in a software GPS receiver. The software receiver allows for easy design change due to the inherent flexibility of software. However, the algorithms may also be implemented in hardware should the need arise. An outline of each chapter is provided in this section. Chapter 2 addresses the basic operations that all GPS receivers must accomplish to provide a user with estimates of position, velocity, and time. Traditional scalar receiver operations are described as a foundation for the advance signal tracking algorithms in the following chapters.

Next, in Chapter 3, factors that affect the tracking of the received GPS signal and the resulting impact of those factors of localization are addressed. The GPS receiver is affected by a number of environmental and hardware issues that must be considered in receiver design. More recently, malicious agents have become a more significant concern with the availability of software radios and low powered signal jammers. Chapter 3 focuses on more traditional environmental factors and their particular impact on carrier phase tracking loop designs.

RTK positioning requires accurate carrier phase measurements from a base receiver that is located at a known location. The stationary nature of the base receiver allows for a more specialized receiver design. A base station receiver architecture leveraging the nearly perfectly known Doppler frequency is described in Chapter 4. The impact the knowledge of the Doppler frequency on carrier phase tracking loop design is discussed. Simulation and live sky data are used to analyze the performance of the specialized carrier phase tracking receiver.

Chapter 5 focuses on computing RTK positions using carrier phase measurements from two software GPS receivers. RTK positioning requires precise carrier phase measurement, and care must be taken in the generation of carrier phase measurements in a software receiver. The measurements from the base receiver and the rover receiver must also be precisely synchronized. Once the measurements are available, the RTK positioning solution is calculated by estimating what is known as the carrier phase integer ambiguity. In Chapter 5, the generation of the carrier phase measurements at specific GPS times is addressed. Then, an algorithm for estimating the carrier ambiguity is described, and the RTK positioning results are compared to a survey grade GPS RTK solution.

The RTK solution described in Chapter 5 is the initialization procedure for the RTK VPLL architecture derived in Chapter 6. The RTK VPLL receiver uses the carrier phase measurement from the base station receiver and the relative position vector between receivers to track the carrier phase on the rover receiver. In Chapter 6, the algorithm is derived, and the performance of the RTK VPLL is analyzed using simulated and live sky data. The live sky data is compared to the RTK solution of a survey grade GPS receiver where available, and compared qualitatively to satellite imagery.

The precision of the carrier phase measurement allows for accurate attitude determination where multiple antennas are attached to a rigid body. In Chapter 7, a multi-antenna carrier phase based attitude determination algorithm is described. The accuracy of the attitude estimates are analyzed by comparison to a commercial off the shelf (COTS) multi-antenna GPS attitude system. Static and dynamic data are used to validate the performance of the attitude system. The final chapter, Chapter 8, provides concluding remarks and discusses directions for future work.

Chapter 2

GPS Receiver Operations

There are three main components of the Global Positioning System: the space segment, control segment, and user segment. The space and control segments are responsible for maintaining and transmitting the GPS signal that is then used by the user segment (i.e. GPS receiver) to compute position, velocity, and/or time. The space segment consists of a minimum of 24 satellites orbiting the Earth in six orbital planes. Each satellite broadcasts ranging codes and data messages modulated on a sinusoidal carrier centered at one of the GPS frequencies in the L-Band. The control segment is a series of ground based monitoring stations responsible for maintaining GPS time, maintaining the satellite orbits, and predicting parameters used to calculate satellite positions (i.e. ephemerides), among other tasks. The Master Control Station is located in Colorado Springs, Colorado [46].

GPS satellites currently transmit ranging codes and data messages at two primary frequencies, L1 = 1575.42 MHz and L2 = 1227.60 MHz, and new satellites launched in 2010 transmit a civilian signal at L5 = 1176.45 MHz [46]. Since that only an encrypted military signal is available on L2, and not all satellites are currently broadcasting L5, this dissertation only considers the L1 frequency signal. There are two binary ranging codes, the coarse acquisition (C/A) code and the precise encrypted (P(Y)) code, and one binary data message modulated on the GPS L1 carrier. The P(Y) is a military code that is only available to Department of Defense users. It is modulated on a 90 degrees phase shifted component of the GPS L1 carrier relative to the carrier on which the C/A code is modulated. This allows the GPS receiver to differentiate the binary code since the carriers are orthogonal [46]. Since encryption of the precise code is unknown to civilian users, the GPS receiver designs in this dissertation only address the C/A encoded GPS L1 signal. The C/A code, which is 1023

chips long and repeats every 1 ms (for a chipping rate of 1.023 MHz), is modulated onto the L1 carrier using binary phase shift key. A complete description of the signal structure is available in the interface specification for GPS [49].

Each satellite broadcasts a unique C/A code which is nearly orthogonal to all other C/A codes. This allows GPS receivers to distinguish signals from each satellite operating on the principle of code division multiple access (CDMA). The combined signal transmitted by satellite i, including the military signal for completeness, is shown in Equation (2.1).

$$s^i_{L1}(t) = \sqrt{2P_{C_i}}C_i(t)D_i(t)\cos(2\pi f_{L1}t) + \sqrt{2P_{P_i}}P_i(t)D_i(t)\sin(2\pi f_{L1}t) \tag{2.1}$$

In Equation (2.1), P_{C_i} and P_{P_i} represent the power levels of the C/A and P(Y) signals respectively. The GPS L1 frequency f_{L1} is 1575.42 MHz. The variables $C_i(t)$ and $P_i(t)$ represent the C/A chip and P(Y) chip at time t, and $D_i(t)$ is the data message bit at time t. The term chip is used for the ranging code values to distinguish them from the data message bits that contain important satellite data and time information. The data message is a 50 Hz binary code containing the time of the transmitted signal, the satellite ephemerides, almanac ephemerides for other satellites, and ionospheric delay correction values. The satellite ephemerides are a set of parameters used by the receiver to calculate satellite position, velocity, and clock error for a given point in time. The ephemerides are updated periodically, and provide accurate satellite orbit parameters for 2 hours after broadcast. The rising edge of a data bit transition is synchronized to the rising edge of the beginning of a C/A code sequence. The synchronized data and C/A codes and the transmission time decoded from the data message allows the receiver to use the chips of the C/A code to determine the transmission time of a given received sample of the GPS signal. The GPS antenna and front-end are responsible for generating these samples.

2.1 Antenna and Front-End

The algorithms derived in this dissertation use downconverted digitized samples of the received GPS signal that are outputs of the GPS front-end. The antenna and front-end combine to amplify, filter, downconvert, and sample the GPS band. A block diagram of the process is shown in Figure 2.1. A typical GPS antenna is right hand circular polarized to match the polarization of the received signal. The two most commonly used antenna designs for GPS are patch and helical. Depending on the implementation, the user may choose an active or passive antenna. The passive antenna applies no gain to the received signal before it is transmitted to the front-end. This type of antenna is commonly used in hand-held devices were the cable from antenna to front-end is short. Longer cable runs, with increased signal losses, require some amplification at the antenna. In this scenario, an active antenna is used, and the receiver or an external source (e.g. bias-tee) must supply power to the antenna for the amplifier [5].

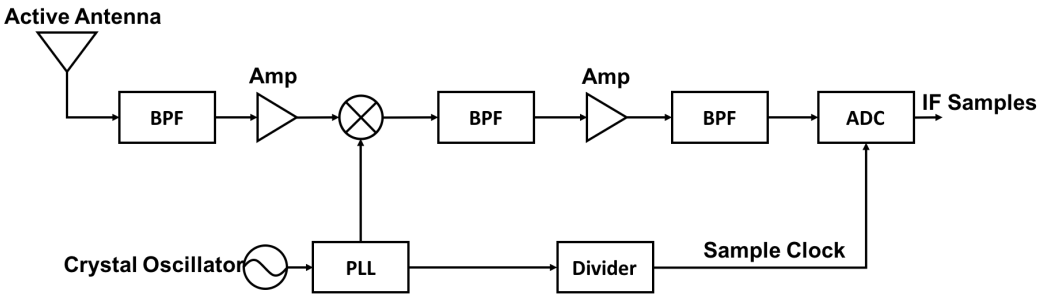

Figure 2.1: Block diagram of typical GPS antenna and front-end components.

The front-end is made up of a series of filters and amplifiers followed by an analog to digital converter (ADC) that samples the conditioned signal. As seen in the figure above, the signal from the antenna is first band pass filtered, then amplified. Next, the signal is mixed with a local oscillator that is normally a combination of a low cost temperature compensated crystal oscillator (TCXO) and a phase lock loop. The local oscillator is also used as the sample clock after additional band pass filtering and amplification of the incoming

signal. The final amplifier may be a variable gain amplifier used to ensure that all bits of the ADC are excited. The amplifier gain is controlled with feedback from the ADC, a process called automatic gain control (AGC).

Other than the ADC, the primary function of the front-end components is to down-convert the received signal from the GPS L1 frequency (f_{L1}) to a lower, more manageable intermediate frequency while maintaining the modulation and Doppler frequency. The mixing process results in the sum of two sinusoidal components with frequencies equal to the sum and difference of the receiver carrier frequency and the local oscillator frequency (f_X) terms as seen in Equation (2.2).

$$\begin{aligned} C_i(t)D_i(t)\cos(2\pi f_{L1}t + 2\pi f_D t)\cos(2\pi f_X t) \\ = \frac{1}{2}C_i(t)D_i(t)\cos(2\pi f_{L1}t + 2\pi f_D t - 2\pi f_X t) + \\ \frac{1}{2}C_i(t)D_i(t)\cos(2\pi f_{L1}t + 2\pi f_D t + 2\pi f_X t) \end{aligned} \quad (2.2)$$

Note that the received carrier frequency is the sum of GPS L1 and the Doppler frequency, which is due to the relative velocities of the satellite and receiver. In the equation, it is clear that the time varying modulation information is maintained, and the Doppler frequency (f_D) is unchanged. The high frequency component is mitigated by either a low pass or band pass filter. The new carrier frequency is now the sum of the Doppler frequency and the intermediate frequency (f_{IF})

$$C_i(t)D_i(t)\cos(2\pi f_{L1}t + 2\pi f_D t)cos(2\pi f_X t) \approx \frac{1}{2}C_i(t)D_i(t)\cos(2\pi(f_{IF} + f_D)t) \quad (2.3)$$

where the intermediate frequency is the difference between GPS L1 and the frequency of the local oscillator.

$$f_{IF} = f_{L1} - f_X \quad (2.4)$$

After the signal is conditioned and sampled by the front-end, coarse code phase and carrier frequency are determined for all satellite signals contained in the sampled data in the acquisition phase, which is discussed in the next section.

2.2 Acquisition

The GPS receiver must generate a perfectly aligned replica of the received satellite signal to decode the navigation message and calculate a measurement of the range to the satellite. This goal is accomplished by first generating a coarse estimate of the phase of the C/A code and of the carrier frequency in the acquisition phase. Then, the coarse estimates are refined in tracking loops which are discussed in Section 2.3. In the acquisition phase, the receiver leverages the cross-correlation properties of the C/A code and sinusoidal carrier to identify the satellite signals that are in view. Three acquisition procedures are discussed in this dissertation: serial search, parallel frequency search, and parallel code search. The descriptions that follow are based on the software receiver design presented in [5].

2.2.1 Serial Search Acquisition

The serial search method of acquisition is possibly the most intuitive of these approaches. There are a deterministic number of possible code phases for a given set of samples. Also, there is a limited range of Doppler frequency for a receiver that is static or moving at a moderate velocity. For a static receiver, the satellite orbits dictate that the Doppler frequencies, which are normally bound by ± 5 kHz. A dynamic receiver may experience Doppler frequencies on the order of ± 10 kHz. To ensure frequency lock in the tracking loop, the estimated Doppler provided by the acquisition search should be accurate to within approximately 500 Hz. For the dynamic receiver scenario, the receiver is required to search 41 possible frequencies to ensure that the error is less than 500 Hz. In the serial search method, each of these frequency bins is tested with every possible code phase (0 - 1022

chips). A block diagram of the algorithm used to generate the test statistic for each of these frequency and code phase combinations is shown in Figure 2.2.

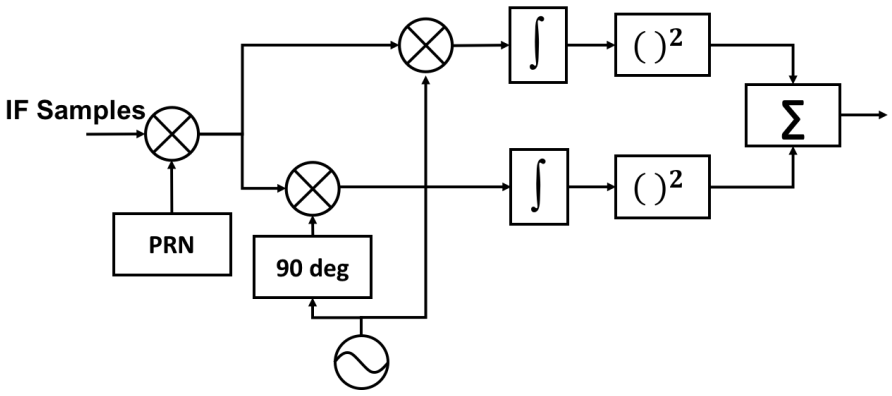

Figure 2.2: Block diagram of serial search acquisition algorithm.

In the figure, PRN stands for pseudorandom noise, another name for the C/A code. For each of the frequency and code phase possibilities, the IF samples from the GPS front-end are first multiplied by the C/A code. Then, the resulting values are multiplied by in-phase and quadrature copies of the sinusoidal carrier that was generated using a specific carrier frequency. The samples are then accumulated, squared, and the in-phase and quadrature branches are summed. The output of the algorithm is a test statistic that is normally compared to the test statistics for all other code phase and carrier frequency combinations. If the ratio of the highest output to the second highest output exceeds a predefined threshold, the satellite signal is considered acquired and the code phase and carrier frequency of the highest output value is used to initialize a tracking channel for that satellite signal.

2.2.2 Parallel Frequency Search Acquisition

To improve the efficiency of the acquisition routine over the serial search method, a parallel search routine can be employed. There are two critical parameters to be determined, code phase and carrier frequency, and the search for either can be performed in parallel while

the other parameter is varied as in the serial method. First, there is the parallel frequency search approach for which a block diagram is provided in Figure 2.3.

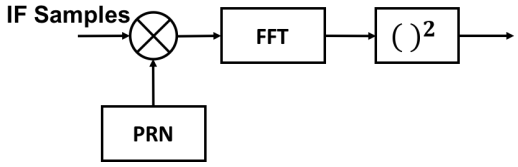

Figure 2.3: Block diagram of parallel frequency search acquisition algorithm.

In this acquisition routine, the IF samples from the GPS front-end are multiplied by the C/A code for every possible code phase as in the serial search method. However, the resulting values are not multiplied by every possible carrier frequency. Alternatively, the samples for each code phase possibility are converted into the frequency domain using the fast Fourier transform (FFT). In the frequency domain, if the code phase is correctly aligned with the code phase of a received satellite signal, there will be a visible peak value. This peak can be tested by comparison to other values in the same way as described for the serial search approach. This method significantly reduces the search space from 1023*41 in the serial search approach to 1023 in the parallel frequency search.

2.2.3 Parallel Code Search Acquisition

As with the parallel frequency search method, the acquisition procedure can also be parallelized in terms of the code phase. The parallel frequency search reduced the search space from 1023*41 to 1023; a parallel code phase search reduces the search space to 41 possible carrier frequencies. The reduction in the search space in the parallel frequency search is achieved at the expense of adding an FFT to the procedure. In the parallel code search method, there are two FFTs and an inverse FFT (IFFT) that must be performed. A block diagram of the method is shown in Figure 2.4.

To perform a parallel code phase search, the IF samples are initially multiplied by in-phase and quadrature sinusoids for each carrier frequency to be tested. The resulting values

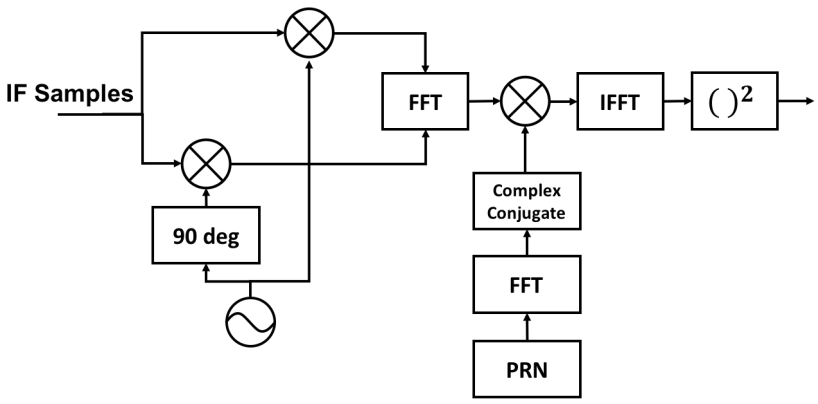

Figure 2.4: Block diagram of parallel code search acquisition algorithm.

are combined into complex values with the in-phase branch supplying the real values and the quadrature branch providing the imaginary values. The samples are then transformed into the frequency domain using the FFT. The C/A is also transformed into the frequency domain, and the complex conjugate is computed. The two sets of frequency domain samples are then multiplied, and the result is converted back into the time domain using the IFFT. Performing multiplication in the frequency domain is equivalent to performing convolution in the time domain. This means that the new time domain samples represent all possible code phase values for the C/A code. At this point, peaks in the time domain values are identified using the same ratio test described above. The parallel code search acquisition method was used in all software receiver implementations discussed in this dissertation.

2.3 Tracking

To calculate estimates of position, a local replica of all received satellite signals must be maintained by the GPS receiver. This local replica is used to decode the 50 Hz data message, track the transit time of the signal from satellites to receiver, and track the Doppler frequency shift of the carrier due to the relative velocities of the satellite and receiver. Initial coarse estimates of the transit time, in the form of a code phase estimate, and Doppler frequency are determined by the acquisition search. These estimates are refined and maintained by

the tracking loops. The following sections address the signal structure after mixing and sampling in the front-end, the delay locked loop (DLL) used to track the code phase, and the frequency or phase locked loop (FLL or PLL) used to track the carrier.

2.3.1 Received Signal Models

An equation representing the transmitted GPS L1 signal was shown previously in Equation (2.1). The signal received at the antenna contains a time delay and frequency shift due to the relative position and velocity of the satellite and receiver. A mathematical model of the received GPS L1 signal for a single satellite, i, is given by

$$s^i_{L1}(t) = \sqrt{2P_{C_i}}C_i(t-\tau_i)D_i(t-\tau_i)\cos(2\pi(f_{L1}+f_D)t+\phi_i)+ \\ \sqrt{2P_{P_i}}P_i(t-\tau_i)D_i(t-\tau_i)\sin(2\pi(f_{L1}+f_D)t+\phi_i) \quad (2.5)$$

Note that the phase of the C/A code and navigation data message are shifted by τ_i seconds , and the carrier frequency is the sum of the transmitted frequency and the Doppler frequency. The signal at the antenna is then passed through the front-end where it is mixed with the intermediate frequency signal and sampled. The digitized IF samples are modeled by Equation (2.6).

$$s^i_{L1}(n) = \sqrt{2P_{C_i}}C_i(n)D_i(n)\cos(2\pi(f_{IF}+f_D)n+\phi_i)+\eta_i \quad (2.6)$$

Due to the bandpass filtering in the front-end around the GPS C/A code frequency, the encrypted P(Y) code has been removed and added to the thermal noise to form the noise term η_i . To isolate the data bit from the C/A code and carrier, the sampled signal is multiplied by a local replica signal with synchronized C/A code and carrier. Result of this multiplication for a perfectly aligned C/A code and carrier is shown in Equation (2.7)

$$\sqrt{2P_{C_i}}C_i(n)D_i(n)\cos(2\pi(f_{IF}+f_D)n+\phi_i)C^*_i(n)\cos(2\pi(f_{IF}+f^*_D)n+\phi^*_i)$$

$$= \frac{1}{2}\sqrt{2P_{C_i}}D_i(n) + \frac{1}{2}\sqrt{2P_{C_i}}D_i(n)\cos(4 * \pi(f_{IF} + f_D)n + 2\phi) \quad (2.7)$$

In this case, C_i^* is the replica C/A code, f_D^* is the replica Doppler frequency, and ϕ_i^* is the replica carrier phase. The high frequency term can then be mitigated with a low pass filter leaving only the data bit multiplied by the half the signal power.

In a traditional GPS receiver, the local replica of the C/A code, carrier frequency, and carrier phase are maintained in a tracking loop, using one channel per satellite signal. The tracking loop contains several components to complete this task, including the correlator, discriminator, loop filter, and numerically controlled oscillator (NCO). The process is outlined in the block diagram in Figure 2.5.

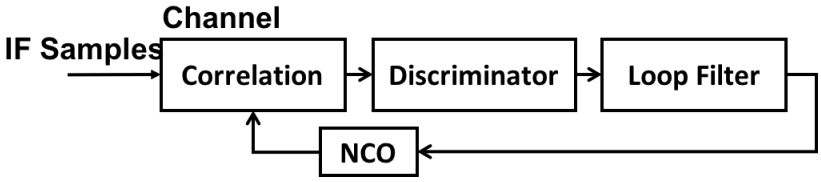

Figure 2.5: Block diagram of tracking loop components used to maintain local replica signal.

The correlation step in Figure 2.5 is common to both code and carrier tracking. In all, the incoming IF samples are mixed with six different replica signals that allow the receiver to generate measurements of the code phase error, carrier frequency error, and carrier phase error. The mixing is normally performed on samples containing a complete cycle of the C/A code (1 ms) with the outputs of the correlators accumulated over that interval. This process, called integrate and dump, low pass filters the signal and increases the signal to noise ratio. The six replica signals are formed from a combination of early, prompt, and late replica C/A codes and two in-phase and quadrature carriers. A block diagram showing the process of generating these six correlators is shown in Figure 2.6.

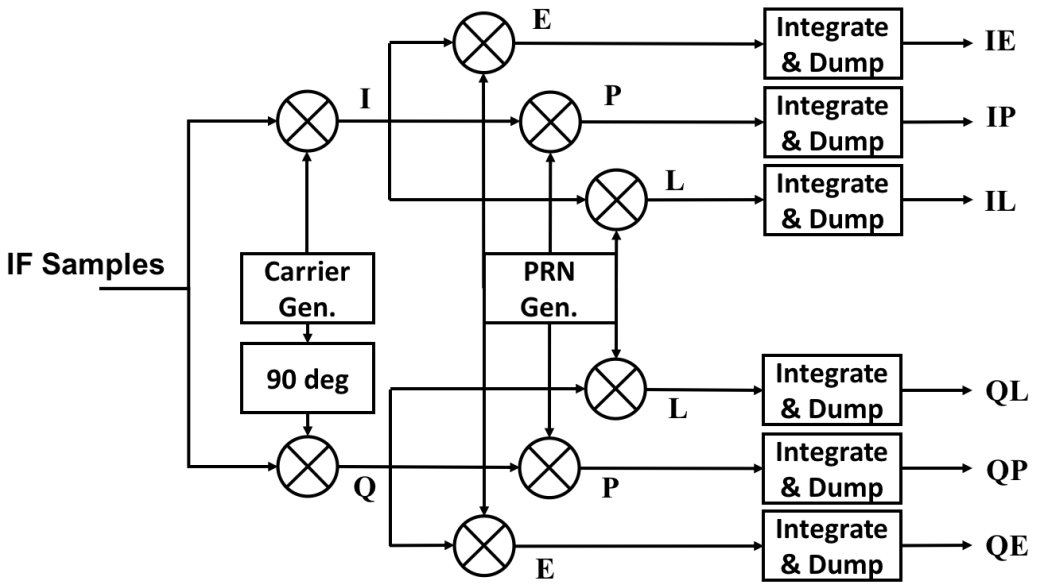

Figure 2.6: Block diagram of generation of six correlator outputs.

The outputs of the correlators are a function of the three errors of interest. A mathematical model of the in-phase and quadrature outputs is given in Equation (2.8).

$$I(k,\gamma) = AR(\epsilon+\gamma)D(k)\cos(\pi f_e T + \delta\phi) + \eta_I(k) \tag{2.8a}$$

$$Q(k,\gamma) = AR(\epsilon+\gamma)D(k)\sin(\pi f_e T + \delta\phi) + \eta_Q(k) \tag{2.8b}$$

This model can be used to represent the early, prompt, or late correlator outputs by selecting γ, the correlator offset. The correlator offset typically takes on values $-\frac{1}{2}$, 0, and $\frac{1}{2}$ chip for the early, prompt, and late correlator respectively. The code phase, carrier frequency, and carrier phase errors are represented by ϵ, f_e, and $\delta\phi$ respectively. The code phase error is seen in the equation as the argument of the C/A code autocorrelation function. The autocorrelation function is shown in Figure 2.7 for phase errors ranging from -1 to 1 chip. Again, $\eta(k)$ is used to represent zero mean Gaussian additive noise. The correlation amplitude, A, is a function of the integration time T, the C/N_0 ratio, and the frequency

error as seen in the Equation (2.9).

$$A = \sqrt{2\frac{C}{N_0}T}\frac{sin(\pi f_e T)}{\pi f_e T} \tag{2.9}$$

In the next two sections, the algorithms used to maintain accurate code and carrier replicas are discussed, including generating observations of the errors and updating the replica signal to regulate those errors.

2.3.2 Code Tracking

In Section 2.3.1, the correlation step of the tracking loop was described in detail. The remaining three steps as seen in Figure 2.5 are the discriminator, loop filter, and NCO. The discriminator functions are responsible for generating usable error values from the correlator outputs. C/A code phase lock is maintained using a delay lock loop (DLL) which uses the intentionally advanced and delayed code replicas to estimate code phase error. The reason for using these values rather than the prompt error signal is clear when examining the autocorrelation of the C/A code. The ideal autocorrelation function of the GPS C/A code is shown in Figure 2.7. As seen in the figure, the autocorrelation function is reflective about zero chip error, and therefore the correlator output would return the same value for $\pm\epsilon$ phase error. For this reason, the code phase error discriminator is calculated using the early and late signals. The simplest and most intuitive code discriminator is $IE - IL$; however, this discriminator requires accurate carrier phase tracking and knowledge of the data bit to be useful. It is common to use both the in-phase and quadrature signal to remove the dependency on carrier phase lock. The code phase discriminator used in the software receiver implementations described in this dissertation is the normalized early minus late power discriminator, which is represented mathematically in Equation (2.10).

$$\tilde{\epsilon} = \frac{\sqrt{IE^2 + QE^2} - \sqrt{IL^2 + QL^2}}{\sqrt{IE^2 + QE^2} + \sqrt{IL^2 + QL^2}} \tag{2.10}$$

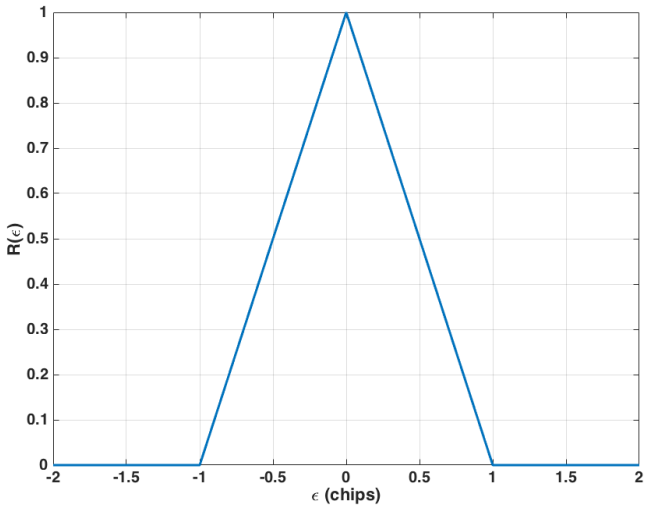

Figure 2.7: Ideal autocorrelation function of GPS C/A code.

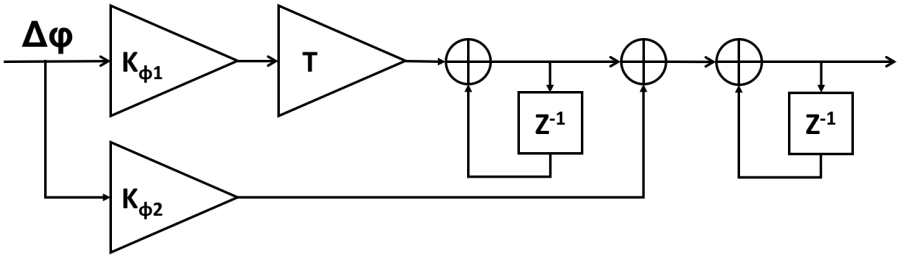

Figure 2.8: Loop filter and NCO integrator of a second order digital DLL.

The normalized early minus late power discriminator has a linear relationship with code phase error up to $\pm\frac{1}{2}$ chip, and provides meaningful error measurements up to $\pm\frac{3}{2}$ chips. For perspective, an error of $\frac{1}{2}$ chip equates to approximately 150 meters of range error.

Discriminator measurements are noisy observations of code phase error that are filtered in the DLL to maintain an accurate replica of the received C/A code signal. The DLL includes both the loop filter and the NCO which each add integrators to the loop. The total loop order is determined by the number of integrators in the loop filter plus one integrator from the NCO, and it is the total loop order that is considered when designing the loop filter. A block diagram representing the loop filter and NCO integrator of a digital second order DLL is shown in Figure 2.8 [32]. Experience with classical analog control theory is

often used in the design of the loop constants $K_{\phi 1}$ and $K_{\phi 2}$. The constants are normally selected for a specified noise equivalent bandwidth, B_N, and damping ratio. In [32], typical values for the filter bandwidth as a function of B_N are provided for first, second, and third order loops. For a second order DLL, a typical B_N is 2 Hz, and the natural frequency of the loop can be calculated by Equation (2.11).

$$w_n = 1.89 B_N \tag{2.11}$$

Equation (2.11) assumes a damping ratio of 0.707. Care must be taken when the product $B_N T$ approaches 0.1 HzS as the assumptions used to generate Equation (2.11) begin to break down [32].

As seen in Figure 2.5, the last process in the DLL is the NCO. The NCO is used to advance the phase of the C/A code at a rate set by the loop filter. This results in the final integrator seen in Figure 2.8. The NCO maintains a replica signal with continuous phase (i.e. without instantaneous jumps in phase), and achieves and maintains phase lock by increasing or decreasing the rate of advance of the local replica C/A code.

2.3.3 Carrier Tracking

The traditional carrier tracking loop is designed in the same manner as the DLL discussed in Section 2.3.2; however the process of achieving phase lock can be more daunting. The acquisition process returns a carrier frequency estimate that must be refined before carrier phase lock is possible. It is common for the carrier tracking loop to be implemented in several stages of increasing precision to arrive at phase lock. The first stage of the process uses a high bandwidth frequency lock loop (FLL) to achieve frequency lock. A high bandwidth is chosen so that the carrier frequency of the local replica responds quickly to the large errors associated with the frequency estimates derived in the acquisition module. Once the FLL is in frequency lock, the carrier tracking loop may transition into a PLL or a

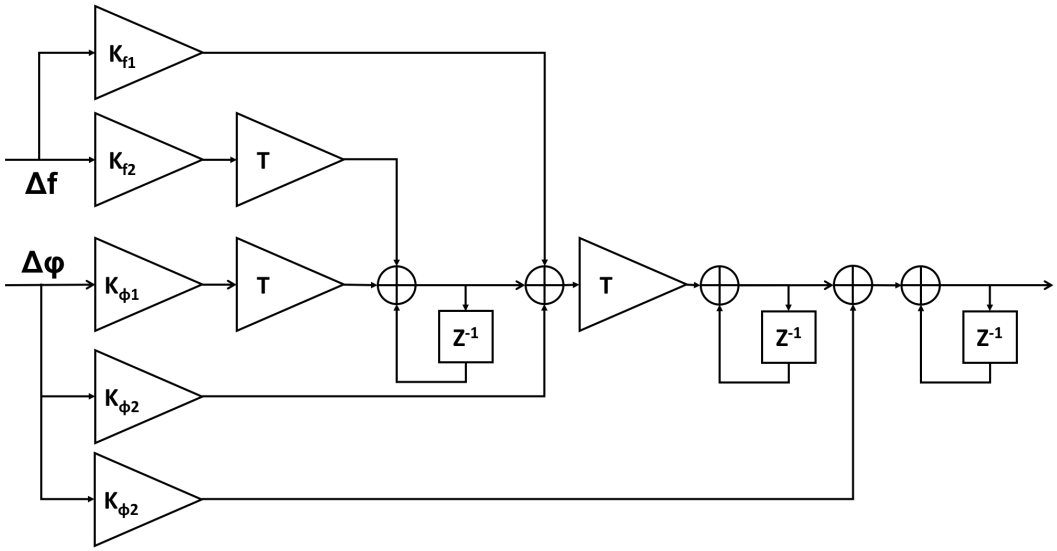

Figure 2.9: Loop filter and NCO integrator of a third order PLL aided by a second order FLL.

FLL aided PLL. In high noise or high dynamic environments, the FLL aided PLL provides improved performance over the traditional PLL. As stated in the introduction, [69] provided a detailed comparison of a FLL aided PLL and a traditional PLL is high noise/dynamic conditions. A block diagram of the loop filter and NCO integrator of a digital second order FLL aided third order PLL is shown in Figure 2.9. This filter implementation provides significant flexibility. Either error signal (i.e. phase error or frequency error) may be zeroed to remove the contribution of that particular filter to the total loop. That means that zeroing the frequency error, Δf, results in a traditional third order PLL. The filter coefficients are selected using the same criteria described for the DLL. The damping ratio and noise equivalent bandwidth are selected, and the constants are calculated from the damping ratio and loop natural frequency. Typically, the noise equivalent bandwidth of a FLL is set lower than for a PLL. Note that the precision of the carrier measurements (i.e. Doppler and phase) is significantly reduced when using a FLL in place of a PLL.

It is important to note that the primary difference between the FLL and PLL is the selection of the discriminator function. The FLL discriminator is selected to provide a measurement of carrier frequency error. The maximum likelihood carrier frequency error

estimator is the four-quadrant arctangent discriminator given by Equation (2.12).

$$\Delta f = \frac{\text{atan2}(IP_1IP_2 + QP_1QP_2, IP_1QP_2 - IP_2QP_1)}{t_2 - t_1} \tag{2.12}$$

In the above equation, in-phase prompt and quadrature prompt samples are taken at consecutive epochs, t_1 and t_2. The frequency discriminator uses the dot and cross product of the IP and QP samples to estimate frequency error. In a FLL, the errors are then processed by the loop filter to generate a new NCO carrier frequency. The FLL aided PLL uses both frequency and phase discriminators to drive the NCO.

Costas discriminators are normally used to estimate carrier phase error because the estimates are immune to the sign of the data bit. This robustness to a data bit change comes at the cost of reduced range. The four-quadrant arctangent discriminator can be used if the navigation data bits are known, and provide error estimates that are linear with respect to true error between ± 180 degrees of phase error. In general, the navigation data bit is unknown, causing the receiver designer to use the two-quadrant arctangent discriminator, given in Equation (2.13), which has an effective range of ± 90 degrees.

$$\Delta\phi = \text{atan}(\frac{QP}{IP}) \tag{2.13}$$

In harsh environments, like high dynamic or low signal strength, the carrier phase discriminators approach the saturation point as the PLL struggles to maintain phase. Eventually, the local replica contains a half or full cycle of error that is undetected by the phase discriminator, and the receiver slips to the next cycle of the carrier. This cycle slip can cause a phase change on the decoded navigation data bits, and adds one cycle of error to carrier phase measurements that will be discussed later in this chapter.

2.4 Data Message Decoding

Once the tracking loops are in code and carrier phase lock, the in-phase prompt correlator output produces an ambiguous copy of the transmitted navigation data bits as seen in Figure 2.10. Recall from Equation (2.8) that the correlator output is a function of the

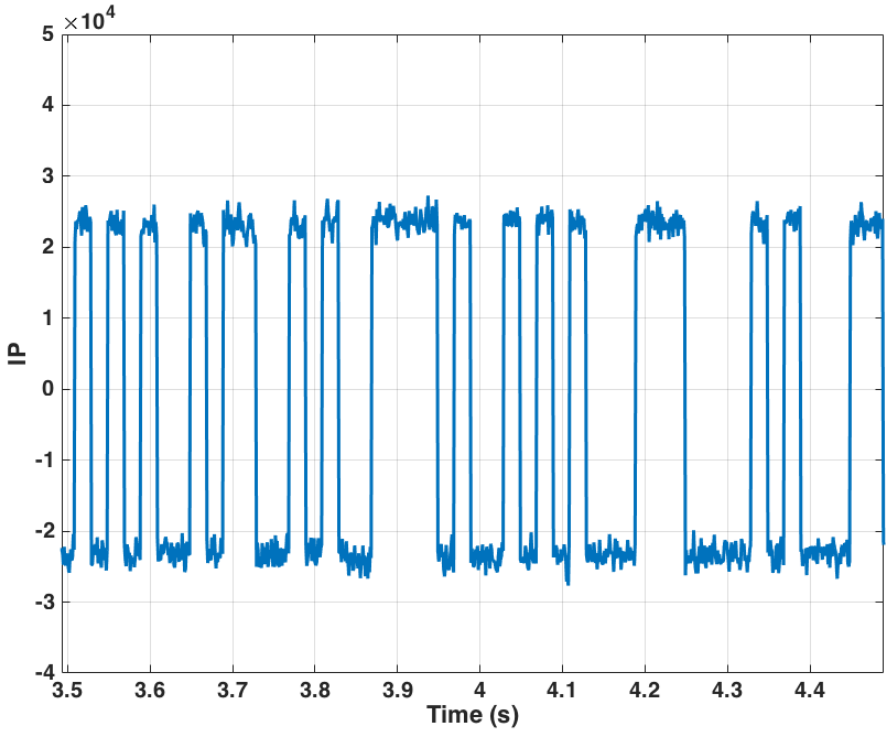

Figure 2.10: In-phase prompt correlator outputs showing navigation data message.

received signal power and the length of the integration period. The ambiguity (i.e. 180 degrees carrier phase ambiguity) is resolved by searching the received and decoded data bits for the GPS preamble. This known sequence of bits is transmitted by all satellites every six seconds, and by searching for both the positive and negative versions of the preamble, the receiver can resolve the half cycle carrier ambiguity.

The navigation data message is composed of words, subframes, and frames where a data word is made up of 30 bits, a subframe contains ten words, and a frame contains five subframes. The total message is made up of twenty-five frames, and is 12.5 minutes

long. The first three subframes contain information directly related to the satellite that is transmitting the message. The first subframe contains clock information that the receiver uses to calculate the time of transmission of the signal. Subframes two and three contain the satellite ephemerides for calculating satellite position. The remaining subframes contain ionospheric model parameters and almanac satellite ephemerides for the remaining satellites in the constellation. The receiver first finds the preamble in two consecutive words to ensure that it did not occur randomly in the navigation message, and then decodes the ephemerides for the transmitting satellite. Once the receiver has decoded the ephemerides, a position solution can be calculated.

2.5 Position, Velocity, and Time (PVT) Estimation

By maintaining an accurate local replica of the transmitted GPS signal, the receiver is able to determine the time of transmission of the output samples from the GPS front-end. Together with an approximate current GPS time (i.e. received time) of the signal, the receiver is able to observe the transit time of the signal from receiver to satellite. It is the accuracy of the atomic clock aboard the GPS satellites and the synchronization of the transmission of the GPS signal that allows the receiver to compute a position solution when four or more satellite signals are being tracked. The principle of trilateration shows that a user with observations of the range to three surveyed locations can uniquely identify its position. The principle is illustrated in Figure 2.5. The figure illustrates a two dimensional representation; however three dimensional positioning is possible with the same number of ranges as long as at least one of the transmitters is not coplanar with the other two transmitters. As previously stated, four GPS satellite observations are needed to compute a position solution. This is due to the limited accuracy of the clock in the receiver. With some exceptions, the GPS receiver has no notion of GPS time when it is first powered. Some COTS GPS receivers maintain the last observation of GPS time in non-volatile memory, and many receivers are able to "hot start" if given an initial GPS time. When tracking four GPS

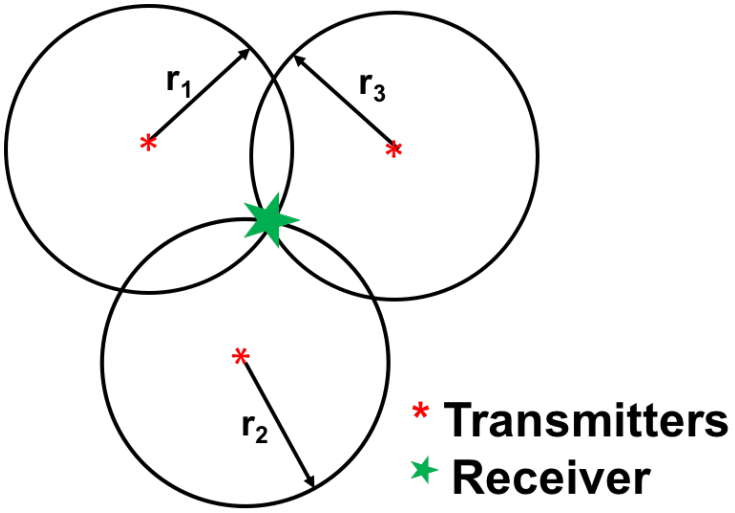

Figure 2.11: Trilateration allows a user to calculate position from three ranges to surveyed locations.

satellites, the receiver is able to estimate both position and the offset between the receiver clock and GPS time. Due to the geometric diversity of the satellite orbits, an earthbound receiver will typically be able to track five or more satellites in a clear sky environment.

2.5.1 Measurements

The true measurements of the GPS receiver are the correlator outputs and/or discriminator outputs described earlier in this chapter. These measurements allow the receiver to maintain accurate local replicas of the transmitted GPS signal that are shifted in time due to transit time of the signal as it propagates from satellite to receiver. To estimate position, velocity, and time, the receiver analyzes the local replica and determines the time shift and frequency shift of the signal induced by the relative position and velocity of the satellite and receiver. From the tracking channels, the receiver derives three primary observations: pseudorange, Doppler, and carrier phase. Some or all of these observations are used to estimate position, velocity, and time (PVT) at the receiver.

2.5.2 Pseudorange

The pseudorange measurement is derived from the local replica of the C/A code. With the decoded navigation message and the known chipping rating of the C/A code, the receiver accurately calculates the transmit time of the samples that are output from the front-end. If the receiver contained a perfect clock, the range from satellite to receiver could be calculated using Equation (2.14)

$$r_u^1 = (t_r - t_t)c \tag{2.14}$$

where t_r is the received time of the signal, t_t is the transmit time, and c is the speed of light in a vacuum. Since the receiver clock is driven by an imperfect oscillator and must be initialized on start-up, the received time is not known precisely. Therefore, the initial position and time solution is computed using time difference of arrival measurements. Figure 2.5.2 shows a graphical representation of the procedure for calculating the measurements. At a given point in time (i.e. a specific sample represented by the dotted red line in the figure), the transmit time for each tracking channel is calculated. In the figure, the boxes next to each channel represent the navigation message data bits. Using data messages and the number of whole and partial chips of the C/A code from the last data bit transition up to the current sample, the transmit time of the sample is calculated. The transit time for the earliest arriving signal is selected and the time of reception, t_r, of the sample is calculated using a nominal pseudorange value (typically $\rho_{nom} = 70$ ms) as seen in Equation (2.15).

$$t_r = t_0 + dt_1 + \rho_{nom} \tag{2.15}$$

The pseudorange for each remaining tracking channel is computed using this approximated received time using Equation (2.16).

$$\tilde{\rho}_2 = t_r - (t_0 + dt_2) \tag{2.16a}$$

$$\tilde{\rho}_3 = t_r - (t_0 + dt_3) \tag{2.16b}$$

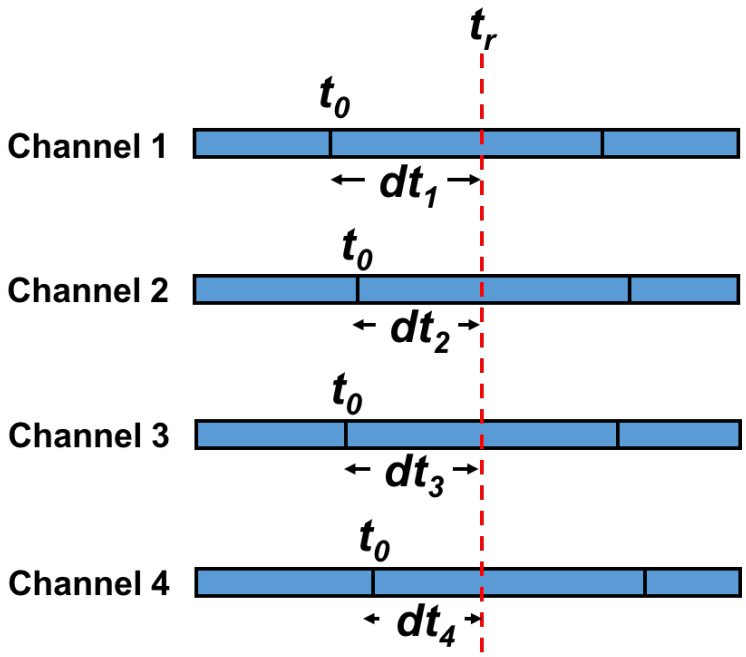

Figure 2.12: The time difference of arrival of the signals is used to calculate the first position and time estimates.

$$\tilde{\rho}_4 = t_r - (t_0 + dt_4) \tag{2.16c}$$

The measurements are called pseudoranges to highlight the deviation from the true range; most notably due to the difference between the nominal pseudorange and the true range on channel 1 which results in a large initial receiver time error. As previously stated, the time error can be estimated when more than three satellites are being tracked.

2.5.3 Pseudorange Rate

In addition to estimating position, the GPS receiver also provides an accurate estimate of the antenna velocity. The velocity estimate is calculated using observations of the Doppler frequency of the received signal. In Section 2.3.3, the process of tracking the carrier wave of the receiver signal was described. When phase or frequency lock is maintained, the tracking loop contains an accurate measurement of the Doppler frequency of the signal; where the

local carrier replica was shown in Equation (2.7). Recall that the Doppler frequency is the frequency difference between the transmitted and received signals, and that the received carrier frequency is a function of the transmitted frequency and the line of sight relative velocity of receiver and transmitter as seen in Equation (2.17).

$$f_r = f_t(1 - \frac{\dot{r}}{c}) \tag{2.17}$$

Rearranging Equation (2.7), and noting that $f_D^* \approx f_r - f_t$ when the tracking loop is locked, a measurement of the line of sight relative velocity, or range rate is calculated by Equation (2.18).

$$\tilde{\dot{\rho}} = -f_D^* \frac{c}{f_{L1}} \tag{2.18}$$

Note that the oscillator in the GPS front-end is not capable of generating a perfect intermediate frequency signal resulting in a change in the clock bias, or clock drift, which manifests in the estimated Doppler frequency. Accordingly, the range rate measurement is biased relative to the true range rate, and is referred to as the pseudorange rate measurement.

2.5.4 Carrier Phase Delta Range

When the tracking channels are implemented as PLLs, the receiver may also generate a carrier phase measurement using the phase of the NCO in the loop. The NCO increments the phase of the replica carrier, and when the PLL is locked, the phase of the NCO at any given sample is an accurate representation of fractional phase (portion of a cycle) of the received signal. This fractional phase represents a very precise but ambiguous measurement of the range to the satellite. The local phase estimate is typically accurate to within two percent of the wavelength of the transmitted carrier (i.e. $0.02\lambda = 0.02(0.1903m) \approx 4mm$). Unlike the binary code, the individual cycles of the carrier are indistinguishable from one another. The fractional carrier phase measurement is comparable to measuring a plank of wood with a tape measure with no labels. The plank could be measured to within 1/16th of

an inch, but the total length is unknown. The total number of whole cycles of the carrier is referred to as the carrier phase ambiguity. If the receiver only recorded the fractional carrier phase at each measurement epoch, the carrier phase ambiguity would change on each epoch due to the relative motion of the receiver and satellites. However, if the receiver keeps track of the change in the number of whole cycles of the carrier from epoch to epoch, the carrier phase ambiguity for each channel can be held constant. With estimation techniques that are described later in this dissertation, the constant carrier phase ambiguity can be resolved, and the carrier phase measurement can be used as a range measurement. Care must be taken when generating the carrier phase measurements to ensure that the fractional phase and change in whole cycles are maintained accurately, and to ensure that the constant carrier phase ambiguity in each channel is referenced to the same point in time. For more details on generating the carrier phase measurement, refer to [57]. In the software receiver designed for this dissertation, the carrier phase measurement was generated using Equation (2.19).

$$\tilde{\phi} = \phi_{NCO} + N_{t,t_s} - f_{IF}(t - t_s) - f_{IF}(t_s - t_0) + \phi_{halfcycle} \tag{2.19}$$

In the equation, ϕ_{NCO} is the current fractional cycle phase of the NCO in the PLL, $N_{t,ts}$ is the whole number of cycles of the NCO from the time that tracking started (t_s) to the current sample time. The remaining three terms are used to account for the portion of cycle advance due to the frequency of the front-end mixer, and a one half cycle ambiguity that is resolved by investigating the decoded preamble. The fourth term contains an initial time reference common to all channels.

Since the carrier phase ambiguity is constant from measurement to measurement, the most straightforward way to use the carrier phase measurement is to compute the change in range from satellite to receiver over a measurement epoch. The delta range measurement is computed by simply subtracting the carrier phase measurements for consecutive

measurement epochs as seen in Equation (2.20).

$$\Delta\tilde{\rho}^1_{t_1,t_2} = \tilde{\phi}^1_{t_2} - \tilde{\phi}^1_{t_1} \tag{2.20}$$

In the equation, the superscript represents the channel or satellite number. The delta range measurement may then be used to compute an estimate of the change in the position of the receiver over the measurement epoch.

2.5.5 Least Square Solutions

The three measurement types that are described in the previous sections are used to compute estimates of the position, velocity, and change in position of the GPS antenna. In Equations (2.16), (2.18), and (2.20), the calculations used to compute the measurements from the local replica signal were given. A model of the relationship of these measurements to the states of interest is needed to derive a solution to the estimation problem. Starting with the GPS pseudorange, a model of the measurement is given in Equation (2.21)

$$\rho_i = r^i_u + I^i_u + T^1_u + M^i_u + ct_u + ct^i + \eta_{\rho_i} \tag{2.21}$$

where r^1_u is the range from user (u) to satellite (i), I is the signal delay caused by the ionosphere, T is the troposphere delay, M is the delay caused by multipath signals, $c\delta t_u$ is the receiver clock bias, $c\delta t^i$ is the satellite clock bias, and η^i_u represents additive Gaussian noise. The true range from satellite to receiver has a nonlinear relationship to the position of the receiver as shown below.

$$r^i_u = \sqrt{(x^i - x_u)^2 + (y^i - y_u)^2 + (z^i - z_u)} \tag{2.22}$$

In this equation, x^i, y^i, and z^i are the positions of satellite 1 expressed in Earth Centered Earth Fixed (ECEF) coordinates. Likewise, x_u, y_u, and z_u are the receiver coordinates of the user in the ECEF frame.

Using Equation (2.22) and an initial estimate of the position and clock bias of the receiver, an estimated pseudorange is calculated.

$$\hat{\rho}_i = \sqrt{(x^i - \hat{x}_u)^2 + (y^i - \hat{y}_u)^2 + (z^i - \hat{z}_u)} + c\hat{t}_u \tag{2.23}$$

In Equation (2.23), the atmospheric delay and satellite clock error term have been ignored. These terms can be mitigated or removed using well known models and/or information contained in the transmitted navigation data message. Note also that the hat notation ($\hat{}$) is used to represent an estimated parameter. The satellite position is calculated using the broadcast ephemerides in the navigation data message. Care must be taken to account for the rotation of the ECEF coordinate frame during the transit of the signal from satellite to user. For more information on that calculation refer to [46].

Least squares is used to estimate a correction to the initial estimate of the receiver position and clock bias. Residuals are calculated using four or more pseudorange measurements and predictions.

$$\begin{bmatrix} \delta\rho_1 \\ \vdots \\ \delta\rho_m \end{bmatrix} = \begin{bmatrix} \tilde{\rho}_1 - \hat{\rho}_1 \\ \vdots \\ \tilde{\rho}_m - \hat{\rho}_m \end{bmatrix} \tag{2.24}$$

A linear measurement vector and measurement model, as seen in Equation (2.25), is derived by Taylor series expansion.

$$\begin{bmatrix} \delta\rho_1 \\ \vdots \\ \delta\rho_m \end{bmatrix} = \begin{bmatrix} a_x^1 & a_y^1 & a_z^1 & -1 \\ & & \vdots & \\ a_x^m & a_y^m & a_z^m & -1 \end{bmatrix} \begin{bmatrix} \delta x_u \\ \delta y_u \\ \delta z_u \\ c\delta t_u \end{bmatrix} \tag{2.25}$$

The model now has the form $z = Hx$, and the estimated correction vector is computed by $\delta X = (H^{\mathrm{T}}H)^{-1}H^{\mathrm{T}}z$. Note that a_x, a_y, and a_z are the line of sight unit vectors from receiver to satellite in the Earth Center Earth Fixed (ECEF) coordinate frame. The initial estimated position and clock bias are corrected, and the estimate can be refined by performing the operation iteratively until δX is sufficiently small using Equation (**??**).

$$\hat{X}_u(k) = \hat{X}_u(k-1) + \delta X_u \tag{2.26}$$

The formulation of the velocity estimation algorithm is similar to the position estimation solution. First, a model of the pseudorange rate measurement defined in Equation (2.18) is needed. The pseudorange range measurement can be modeled as the relative velocity of satellite and receiver projected onto the line of sight unit vector. Since the measurement is derived from the local replica carrier Doppler, the measurement is corrupted by the deviation from the nominal frequency of the frequency of the local oscillator. This error manifests as a changing bias in the pseudorange rate and is referred to as the clock drift. The atmospheric effects that were introduced in the pseudorange measurement are typically near constant over normal GPS measurement intervals, and therefore are not included in the pseudorange rate model shown below.

$$\dot{\rho}_i = \dot{r}_u^i + c\dot{t}_u + \eta_{\dot{\rho}_i} \tag{2.27}$$

Notice also that the satellite clock drift has been neglected due to the quality of the atomic clocks on board the satellites. To set up the least square solution, as in the case of the position estimation, an initial estimate of the velocity and clock drift are used to compute a prediction of the pseudorange rate measurement as seen in Equation (2.28)

$$\hat{\dot{\rho}}_i = \begin{bmatrix} \dot{x}^i - \hat{\dot{x}}_u & \dot{y}^i - \hat{\dot{y}}_u & \dot{z}^i - \hat{\dot{z}}_u \end{bmatrix} \begin{bmatrix} a_x^1 \\ a_y^1 \\ a_z^1 \end{bmatrix} + \hat{c\dot{t}}_u \tag{2.28}$$

The measurement vector is then constructed using measurements and predictions from at least four satellites

$$\begin{bmatrix} \delta\dot{\rho}_1 \\ \vdots \\ \delta\dot{\rho}_m \end{bmatrix} = \begin{bmatrix} \tilde{\dot{\rho}}_1 - \hat{\dot{\rho}}_1 \\ \vdots \\ \tilde{\dot{\rho}}_m - \hat{\dot{\rho}}_m \end{bmatrix} \tag{2.29}$$

and the measurement equation is given by:

$$\begin{bmatrix} \delta\dot{\rho}_1 \\ \vdots \\ \delta\dot{\rho}_m \end{bmatrix} = \begin{bmatrix} a_x^1 & a_y^1 & a_z^1 & -1 \\ & & \vdots & \\ a_x^m & a_y^m & a_z^m & -1 \end{bmatrix} \begin{bmatrix} \delta\dot{x}_u \\ \delta\dot{y}_u \\ \delta\dot{z}_u \\ c\delta\dot{t}_u \end{bmatrix} \tag{2.30}$$

After the initial position and velocity estimates have been determined, these values can be used as initialization values for successive least squares solutions as new measurements become available, or the initial position, velocity, bias, and drift can be used to initialize a Kalman filter estimator.

In addition to estimating position and velocity, the carrier phase delta range measurement is useful in estimating the change in the receiver position over the measurement interval. It is shown in [67] and [43], that the relative position of a lead and following vehicle could be estimated to within centimeters by combining the carrier phase based odometry with a differential GPS (DGPS) relative positioning algorithm. The relative position solutions were used by the robotic following vehicle to duplicate the path of the lead vehicle. DGPS will be addressed later in this dissertation. The time differenced carrier phase (TDCP) delta range measurement was introduced in Equation (2.20). To begin the derivation of the model for the delta range measurement, the carrier phase measurement model is provided below.

$$\phi^i = \frac{1}{\lambda}(r_u^i - I_u^i + T_u^i + M_u^i + ct_u + ct^i) + N_u^i + \eta_{\phi_i} \tag{2.31}$$

The carrier phase measurement is represented in cycles in Equation (2.31) with λ being the GPS L1 frequency wavelength ($\approx$ 19cm). The carrier ambiguity is represented by N_u^i. The delta range measurement is computed using Equation (2.20), and combined with Equation (2.31) results in the following model for the delta range measurements.

$$\Delta\rho^i_{t_1,t_2} = r^i_{u_{t_2}} - r^i_{u_{t_1}} + c(t_{u_{t_2}} - t_{u_{t_1}}) + \eta_{\Delta\rho} \tag{2.32}$$

The delta carrier phase has been multiplied by λ to convert the delta range measurement to units of meters. Notice that the ionosphere and troposphere induced delays are not included due to their strong temporal correlation, which means that they are essentially removed by subtracting consecutive measurements. The change in the satellite clock bias is also ignored. Any residual multipath is lumped in with the noise term, and the carrier ambiguity is constant and therefore is also removed through subtraction.

The states that are estimated using the delta range measurement are the change in the position and the change in the clock bias of the receiver from one measurement to the next. Linearizing and rearranging Equation (2.32) provides a relationship between the measurement and the estimated states Δx, Δy, Δz, and $c\Delta t$, as seen in Equation (2.33).

$$\begin{aligned}\Delta\rho^i_{t_1,t_2} = &\begin{bmatrix} a^i_{x_{t_2}} & a^i_{y_{t_2}} & a^i_{z_{t_2}} \end{bmatrix} \begin{bmatrix} x^i_{t_2} \\ y^i_{t_2} \\ z^i_{t_2} \end{bmatrix} - \begin{bmatrix} a^i_{x_{t_1}} & a^i_{y_{t_1}} & a^i_{z_{t_1}} \end{bmatrix} \begin{bmatrix} x^i_{t_1} \\ y^i_{t_1} \\ z^i_{t_1} \end{bmatrix} \\ &- \left(\begin{bmatrix} a^i_{x_{t_2}} & a^i_{y_{t_2}} & a^i_{z_{t_2}} \end{bmatrix} - \begin{bmatrix} a^i_{x_{t_1}} & a^i_{y_{t_1}} & a^i_{z_{t_1}} \end{bmatrix} \right) \begin{bmatrix} x_{u_{t_1}} \\ y_{u_{t_1}} \\ z_{u_{t_1}} \end{bmatrix} - \begin{bmatrix} a^i_{x_{t_2}} & a^i_{y_{t_2}} & a^i_{z_{t_2}} & 1 \end{bmatrix} \begin{bmatrix} \Delta x \\ \Delta y \\ \Delta z \\ c\Delta t \end{bmatrix}\end{aligned} \tag{2.33}$$

Using the approximate user position calculated with the GPS pseudorange measurement and the satellite positions for times t_1 and t_2, the four states are estimated using the iterative

least squares algorithm as described above. The measurement matrix is made up of the line of sight unit vectors from receiver to satellite and a column of ones as seen in the last term of Equation (2.33).

2.6 Conclusion

In this chapter, the operations of a GPS receiver have been described. Starting with the received RF signal at the antenna, the receiver converts the signal down to a lower intermediate frequency and samples the signal. The signal is then processed by the acquisition module to detect GPS satellite signals, and determine an approximate code phase and carrier frequency for each detectable signal. The tracking loops are then responsible for refining the coarse estimates from the acquisition module, and maintaining an accurate local replica of the received satellite signal. The in-phase prompt local replica is used to decode the navigation data message, and the local replicas are used to generate pseudorange, pseudorange rate, and carrier phase measurements. These measurements and the decoded satellite ephemerides are used to estimate the receiver position, velocity, and clock offset. Receiver designs vary, but these general operations are present in some form in all receivers. This background provides a foundation for the advanced tracking schemes that are derived in the following chapters of this dissertation. To facilitate rapid design implementation and testing, the algorithms described throughout this dissertation are implemented in software. The sampled signal output by the GPS front-end is the input to the software architecture. This dissertation focuses on signal tracking in particular, and therefore the acquisition procedure is not discussed in more detail. A parallel code search acquisition approach is used to initialize code phase and carrier frequency for the receiver designs described throughout the remainder of this dissertation.

Chapter 3

Factors Affecting Carrier Tracking and Receiver Localization

Designing tracking and positioning algorithms for the GPS receiver requires knowledge of a variety of factors that limit flexibility in the design. The factors affecting the receiver design are the local environment, the atmosphere, the receiver dynamics, and man-made interference. In this chapter, several of these factors are discussed and the impact on tracking loop design and/or measurement accuracy are addressed. The chapter begins with a review of two man-made interference types that are not the focus of this dissertation but warrant discussion because they threaten the accuracy and reliability of the GPS navigation solution. Then the naturally occurring interference sources are discussed. Finally, the error sources internal to the receiver are described.

3.1 Jamming

The primary man-made threat to civilian GPS users are low powered jammers. While it is not surprising that military receivers face the threat of electronic warfare, the availability of commercial GPS jamming devices is threatening personal navigation and could threaten autonomous navigation systems on future commercial vehicles. In a well publized event near Newark Liberty International Airport [20,44], a driver on a nearby highway disrupted ground based GPS aiding stations at the airport using a low-power personal privacy device (PPD). Devices like the one shown in Figure 3.1 are designed to create broadband interference near the GPS L1 frequency. In [47], the authors evaluate several devices, that while illegal, are available to users that are willing to bypass the law. The authors found that the majority of the devices used a linear chirp signal centered at or near the GPS L1 frequency with frequency sweeps ranging from approximately $\pm$ 5 MHz to $\pm$ 30 MHz. The sweep period

Figure 3.1: Commercial civilian personal privacy device. [4]

was normally around 10 microseconds, and the total power in the GPS band ranged widely from approximately 2 mW to 1W. Those power levels translate to an effective range of 150 to 800 meters. The effective range was tested by combining the jammer and a simulated GPS signal and transmitting the total signal to a GPS receiver in an RF shielded enclosure. The jammer signal was increasingly attenuated until the GPS receiver was able to track the simulated signal. The attenuation measured in decibels (dB) was converted to meters assuming unity gain at each antenna and accounting for expected path loss. Although the advanced tracking algorithms described later in this dissertation are not designed specifically to mitigate jamming, the increased tracking sensitivity should reduce the effective range of this type jammer.

3.2 Spoofing

Another form of man-made interference, called spoofing, is a structured interference signal designed to change the receiver measurements of range and frequency to cause inaccurate estimates of position, velocity, and time. The spoofing signal has the same structure as the GPS signal. Accordingly, the tracking components of the receiver will operate with

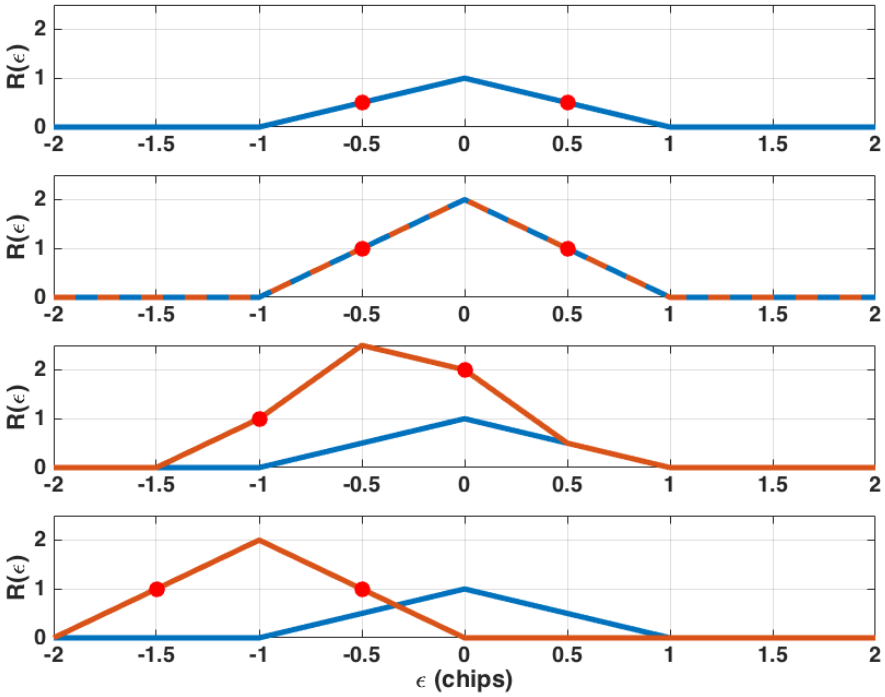

Figure 3.2: Advance spoofing attack with DLL drag off.

the spoofing signal in the same way as with the true signal. A typical GPS receiver will continue to track visible satellites and not re-enter the acquisition phase as long as four or more channels are operational. Therefore, the spoofing attack must be sophisticated enough to capture the GPS receiver during the tracking phase. In [29], the authors described an advanced spoofing attack in which the target receiver correlators are "tricked" by the attacker that transmits a near perfect copy of the received signal. The signal power of the attacker is higher than the low powered signal received directly from the satellite. The attacker may then start to shift the spoofing signal away from the true signal thereby capturing the tracking loops of the receiver. This is called "drag off" The process is shown in Figure 3.2. The figure represents a time lapse of the DLL correlator outputs increasing over time with each plot moving downward. In the top plot, only the true signal is present. The second plot shows the introduction of the spoofing signal, and the total received signal power increasing.

Next, the spoofing signal is shifted to start the drag off procedure. In the final plot, the receiver DLL is tracking the spoofing signal as indicated by the red dots representing the early and late correlator outputs.

A vector tracking receiver has some inherent protection against GPS spoofing in that the receiver navigation states are used to predict the signal tracking parameters. A well designed vector tracker contains some level of fault detection in the navigation processor that could detect and remove the erroneous discriminators that the spoofing signal produces. However, the fault detection methods are based on the statistical probability of a particular measurement occurring and the uncertainty in the navigation solutions leaves room for the well designed spoofing attack to corrupt the receiver. The limiting factor for the spoofer is the time taken to drag off the receiver correlators. If the spoofer attempts to capture the local replicas too quickly, the vector receiver will flag the resulting discriminator errors as faults and disregard the measurement. The sensitivity of the receiver to the treat is dependent on the uncertainty in receiver dynamics. Additionally, a high quality IMU can be integrated into the solution to reduce or potentially eliminate the drag off spoofing threat.

3.3 Multipath

Reflected signals are additional error sources introduced by the local environment near the GPS receiver. In addition to the direct line of sight signal from the GPS satellite, the antenna is also exposed to reflections of the GPS signal, particularly in urban areas with tall buildings as seen in Figure 3.3. The signal reflections are called mulitpath signals and can cause relatively large pseudorange biases. The multipath signals enter the receiver range and range rate measurements through the correlators. The multipath in-phase and quadrature correlator outputs, seen in Equation (3.1), are distorted by the non-line of sight signals causing the tracking loop to settle to a code phase that is shifted relative to the true line of

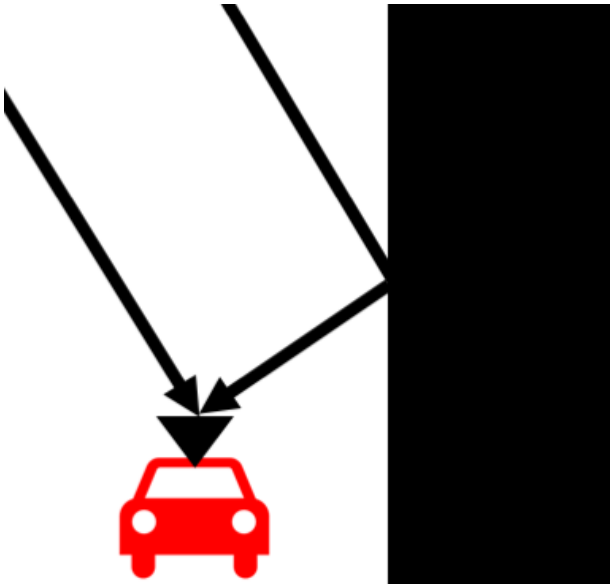

Figure 3.3: Direct line of sight signal plus the reflected multipath signal.

sight signal phase.

$$\begin{aligned} I(k,\tau) &= AR(\epsilon+\gamma)D(k)\cos(\pi f_e T + \delta\phi) \\ &\quad + A_m R_m(\epsilon_m+\gamma)D(k)\cos(\pi f_m T + \delta\phi_m) + \eta_I(k) \end{aligned} \tag{3.1a}$$

$$\begin{aligned} Q(k,\tau) &= AR(\epsilon+\gamma)D(k)\sin(\pi f_e T + \delta\phi) \\ &\quad + A_m R_m(\epsilon_m+\gamma)D(k)\sin(\pi f_m T + \delta\phi_m) + \eta_Q(k) \end{aligned} \tag{3.1b}$$

In the equation, A_m, ϵ_m, f_m, and $\delta\phi_m$ represent respectively the amplitude, code phase error, carrier frequency error, and carrier phase error of the local replica signal relative to the reflected signal. When the code discriminator function is applied to these correlator outputs it produces an erroneous measurement of the code phase (or range) error in the local replica signal. Using an early minus late power discriminator and assuming the code phase error relative to the reflected signal is less than $\frac{3}{2}$ chip [9], the discriminator bias

introduced by the multipath signal can be modeled by

$$Y_m = \begin{cases} A_m^2 2\epsilon_m + AA_m 2\epsilon_m \cos(\pi f_m T + \delta\phi_m) & \text{if } 0 \leq \epsilon_m \leq \frac{1}{2} \\ A_m^2(\frac{3}{2} - \epsilon_m)^2 + AA_m(\frac{3}{2} - \epsilon_m)\cos(\pi f_m T + \delta\phi_m) & \text{if } \frac{1}{2} \leq \epsilon_m \leq \frac{3}{2} \end{cases} \tag{3.2}$$

This discriminator bias is a function of the multipath to direct amplitude ratio (MDR) which is typically less than one (i.e. $AA_m > A_m^2$), and therefore, the second term in Equation (3.2) is typically the dominant term. This term has maximum magnitude when the argument of the cosine term is 0 or 180 degrees. The resulting maximum range error in the pseudorange measurement varies with MDR. In [9], error bounds for a MDR of 0.1 are provided, and show a maximum range of error of approximately $\pm$ 16 meters in steady state. It was shown in [9] that the vector tracking receiver provides improved range estimation in multipath environments over traditional scalar tracking architectures. This is particularly true when a subset of the total number of channels experience multipath signals. The range biases from the multipath subset are filtered by the navigation processor, and the vector tracking predicted signal parameters are a more accurate representation of the true signal than a scalar receiver would be capable of predicting.

In [64], the carrier phase bias introduced by multipath was investigated. For the case where the DLL tracking error is less than one chip and the MDR is less than one, the carrier phase bias must be less than 90 degress. By comparison to the potential 16 meter code bias, the carrier phase bias due to multipath is rather small. At the GPS L1 frequency, a maximum carrier phase bias of 90 degress translates to a range bias of approximately 4.8 cm. This level of bias is difficult to detect or mitigate using only GPS observations. The carrier phase bias also changes quickly for a receiver on a moving platform. For these reasons, the impact of multipath on carrier phase positioning is not addressed directly in the receiver designs derived in this dissertation.

3.4 Atmosphere

While jamming, spoofing, and multipath are locally generated effects that impact the tracking of the true GPS signal, the upper and lower atmosphere disrupt the GPS signal as it radiates from satellites to ground users. The atmosphere can be divided into several layers characterized by specific traits, but there are two main areas that affect the GPS signal: troposphere and ionosphere. The troposphere is the portion of the atmosphere nearest the ground, and the region where the vast majority of the water vapor in the Earth's atmosphere is located. The ionosphere resides at much higher altitude, and while not a distinct layer of the atmosphere, is characterized by a large number of free electron and charged ions that are energized by the sun. The impact of the troposphere and the ionosphere on GPS tracking and positioning are discussed in the subsections below.

3.4.1 Troposphere

The primary measurement used by the GPS receiver to compute an estimate of position is the transit time of the signal from satellite to receiver. This measurement is transformed into a range measurement by assuming that the propagation rate of the signal is constant over that range at the speed of light. This assumption is accurate for the majority of the distance from satellite to receiver as the signal propagates through free space, but once the signal enters the atmosphere the transmission rate is affected by the ionized and neutral gases and water vapor. The signal delays caused by neutral gases and water vapor will be referred to as the tropospheric delay despite the fact that some of the dry gas delay is introduced above the troposphere [64]. The propagation speed of a radio wave through a medium is defined by the refractive index of the medium. For the troposphere region of the atmosphere, the refractive index is slightly greater than one, meaning that the signal propagates at a rate slightly less than the speed of light [46]. This appears as an erroneous lengthening of the true range from satellite to receiver. The troposphere is a non-dispersive medium meaning that the refractive index is not dependent of the frequency of the signal.

There are three parameters needed to model the range error introduced by the troposphere: the wet delay, the dry delay, and the mapping function. As prefaced by the names, wet delay and dry delay represent the signal delays introduced by water vapor and dry gases, respectively. There are a number of models in the literature for approximating these delays as a function of satellite location, atmospheric pressure, temperature, and humidity. In this dissertation, the Saastamoinen model described in [46] was used to simulate the troposphere delay or to mitigate the resulting range error when applying pseudorange measurements in the receiver navigation processor. The wet and dry delay ($T_{z,w}$ and $T_{z,d}$ in units of meters) are shown in Equation (3.3).

$$T_{z,w} = 0.002277\left(\frac{1255}{T_0} + 0.05\right)e_0 \tag{3.3a}$$

$$T_{z,d} = 0.002277(1 + 0.0026\cos 2\phi + 0.00028H)P_0 \tag{3.3b}$$

where T_0 is the temperature in Kelvin, P_0 is the total pressure, e_0 is the partial pressure due to water vapor, ϕ is the latitude of the receiver, and H is the height of the receiver in kilometers.

The equations above are used to predict the total tropospheric delay in the zenith direction. Mapping functions are used to project that delay onto the correct elevation angle for each satellite being tracked. Given the elevation angle of the satellite, E, the mapping function, or more generically the obliquity factor, is calculated by Equation (3.4).

$$m_w = \frac{1}{\sin E + \frac{0.00035}{\tan E + 0.0117}} \tag{3.4a}$$

$$m_d = \frac{1}{\sin E + \frac{0.00143}{\tan E + 0.0445}} \tag{3.4b}$$

The troposphere induced range error in the pseudorange measurement is then calculated by Equation (3.5).

$$\tilde{T}_u^1 = T_{z,w}^1 m_w^1 + T_{z,d}^1 m_d^1 \tag{3.5}$$

Equation (3.5) can be applied in Equation (2.24) to correct the pseudorange measurement prior to computing the least squares position solution.

Typically, the values for the range errors introduced by tropospheric delays are on the order of 2 to 20 meters. Using the models above, the error can be reduced to a few centimeters depending on the elevation angle of the satellite and the accuracy of the meteorological data used in the model. Later in this dissertation, differential GPS techniques are discussed that reduce this error even further. The tropospheric affect on the GPS signal is normally slow changing, and therefore does not require special attention when designing the carrier phase tracking loop. Signal scintillation (i.e. fluctuations in amplitude or phase) due to the troposphere is possible, particularly for elevation angles below 10 degrees, but are small relative to other tracking concerns discussed later in this chapter.

3.4.2 Ionosphere

Like dry gases and water vapor in the troposphere, free electrons dictate the refractive index for the ionosphere. Gases in the ionosphere are ionized by ultraviolet radiation from the sun stripping off electrons during daylight hours, with the number of free electrons peaking around 2:00 PM local time [46, 64]. As the electron density increases, the magnitude of the refractive index increases. Unlike the troposphere, the ionosphere is a dispersive medium wherein the refractive index is a function of the transmitting frequency resulting in different delays on the GPS L1 and L2 frequencies. Due to this difference in delay, the dual frequency GPS user may use measurements from the two frequencies to mitigate any range error due to the ionosphere. Since only the L1 frequency is considered here, the ionosphere free range combination is not discussed in this dissertation. For information on dual frequency ionosphere free combination measurements see [32].

Ionosphere Delay

From [64], it is shown that the refractive index for the GPS carrier propagating through the ionosphere can be approximated to first order with Equation (3.6)

$$n_c = 1 - \frac{40.3 n_e}{f_{L1}^2} \tag{3.6}$$

where n_e is the electron density. By integrating the refractive index along the line of sight from satellite to receiver the total delay of the carrier (in units of meters) due to the ionosphere is represented by

$$I_\phi = -\frac{40.3 TEC}{f_{L1}^2} \tag{3.7}$$

where TEC represents the total electron content in a 1 meter squared cross-section extending from a satellite to receiver. Notice that the value is negative, meaning that the carrier is advanced by the ionosphere. This was seen previously in this dissertation in Equation (2.31). Comparing Equation (2.31) to Equation (2.21), the models show that the ionosphere affects the PRN code in the opposite direction to the advance of the sinusoidal carrier. This is supported by the relationship between the refractive indexes of the PRN code and the carrier.

$$n_{prn} = n_c + f_{L1} \frac{dn_c}{df} \tag{3.8}$$

From Equation (3.7) and Equation (3.8), it is clear that the delay on the PRN code (also in meters) is given by

$$I_\rho = \frac{40.3 TEC}{f_{L1}^2} \tag{3.9}$$

and that the ionosphere delay has the same magnitude for both the code and carrier of the GPS signal. As in the case of the tropospheric delay, the model above describes the ionospheric delay in the zenith direction. The obliquity factor must be applied to determine the delay along the line of sight from satellite to receiver.

The total electron content in the ionosphere is an unknown quantity. This value may be estimated by a base station and transmitted to local mobile users via a radio link, or the stand-alone GPS user can use broadcast parameters contained in the GPS ephemerides to compute an approximate delay using the Klobuchar model described in [35]. The Klobuchar model is based on eight total parameters that are updated approximately every six days (to reflect the current season and solar activity) and transmitted in subframe 4 of the navigation data message. The complete model contains several equations for computing the geomagnetic latitude of the projection of the ionosphere intersection point onto the Earth. A simplified version of the model, as given in [46], is shown in Equation (3.10).

$$\tilde{I}_u^1 = \begin{cases} cM_I\left(A_1 + A_2\cos\left(\frac{2\pi(t-A_3)}{A_4}\right)\right) & \text{if } |t-A_3| < \frac{A_4}{4} \\ cM_I A_1 & \text{otherwise} \end{cases} \tag{3.10}$$

In the above equation, the eight broadcast parameters have been combined to form the parameters A_2 and A_4. Parameters A_1 and A_3 are constant values 5×10^{-9} seconds and 50,400 seconds, respectively, and the obliquity factor is calculated by the following equation.

$$M_I = 1.0 + 16.0 \times (0.53 - E)^2 \tag{3.11}$$

For more detail on using the Klobuchar model see [35]. The Klobuchar model is used throughout this dissertation for simulating ionospheric induced range errors, and for correcting the ionospheric range error in pseudorange and carrier phase measurements.

In addition to introducing a range bias in the pseudorange and carrier phase measurements, the ionosphere also impacts the carrier phase tracking loop design. Changes in the ionospheric delay caused by fluctuations in TEC create signal dynamics that the carrier phase tracking loop must be able to track. Conditions in the ionosphere are seasonal and periodic with the rising and setting sun. Therefore, it is difficult to model the complete tracking loop response to changes in the TEC. It is useful to model the typical worst case

frequency shift in the received GPS signal due to ionosphere variability. According to [35], the maximum likely TEC rate of change (1×10^{15}) results in a frequency shift of 0.085 Hz. To a GPS receiver, this frequency shift equates to a rapid change in the line of sight relative velocity of the satellite and receiver. When designing the PLL, it is important to consider this rapid frequency change, or dynamic stress. The peak error in a third order PLL due to dynamic frequency stress can be approximated by the steady state error of a first order PLL having the same noise equivalent bandwidth, B_N [64]. The peak error is calculated as a function of the frequency shift (Δf) and the noise equivalent bandwidth using Equation (3.12).

$$\sigma_{\phi_{d,i}} = \frac{\Delta f}{4B_N}\frac{360}{3} \tag{3.12}$$

The phase error is multiplied by 360 to convert to degrees and divided by three because 0.085 Hz represents a three standard deviation error.

Using Equation (3.12), the dynamic stress caused by the maximum expected TEC variability can be calculated for various third order PLL bandwidth, as seen in Figure 3.4. The trend seen in Figure 3.4 is important in designing the bandwidth of the receiver PLL. Based on a 15 degree phase error tracking threshold (shown by the black line in the figure), a tracking loop with a noise bandwidth less than 0.2 Hz would struggle to track signal changes due to the ionosphere. Several additional errors are discussed in the remainder of this chapter that increase the minimum viable noise bandwidth significantly.

Ionosphere Scintillation

Before moving on to additional error sources affecting the GPS receiver, the phenomenon of ionospheric scintillation is discussed. Scintillation typically affects GPS users at low or high latitudes with the more severe effects occurring in the equatorial region. In that region, the free electrons and ions in the ionosphere begin to recombine forming plasma bubbles that disturb the GPS signal propagating towards Earth. These irregularities in the ionosphere cause fluctuations, or scintillation, of the amplitude and phase of the GPS signal. The

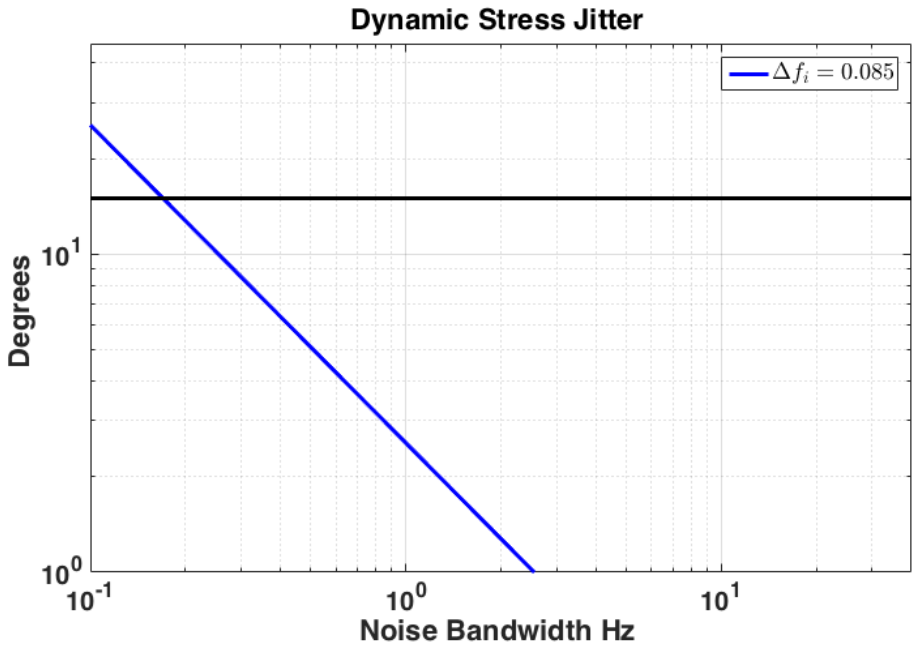

Figure 3.4: Maximum dynamic stress induced by TEC variability in ionosphere.

severity of the event is dependent on location, season, magnetic activity, and an eleven year cycle of high solar activity. Ionospheric scintillation is characterized by three parameters: the S_4 index which quantifies the magnitude of the amplitude fade, the intensity decorrelation time which quantifies the rate of the amplitude fade, and σ_s which quantifies the magnitude of the phase variations (σ_ϕ is normally used to represent the ionosphere scintillation induced phase variation, but in this dissertation σ_s is used to reduce confusion). The S_4 index has a theoretical range of zero to one where a value greater than 0.6 is considered strong scintillation. As the severity of the scintillation increases the decorrelation time decreases meaning that phase changes happen rapidly. This also corresponds to an increase in the phase scintillation index. The deep amplitude fades and rapid phase changes associated with strong scintillation can cause loss of lock and force the receiver into re-acquisition. In Figures 3.5 and 3.6, a time series of simulated amplitude ratios, and phase fluctuations are shown for two scenarios: moderate and strong scintillation.

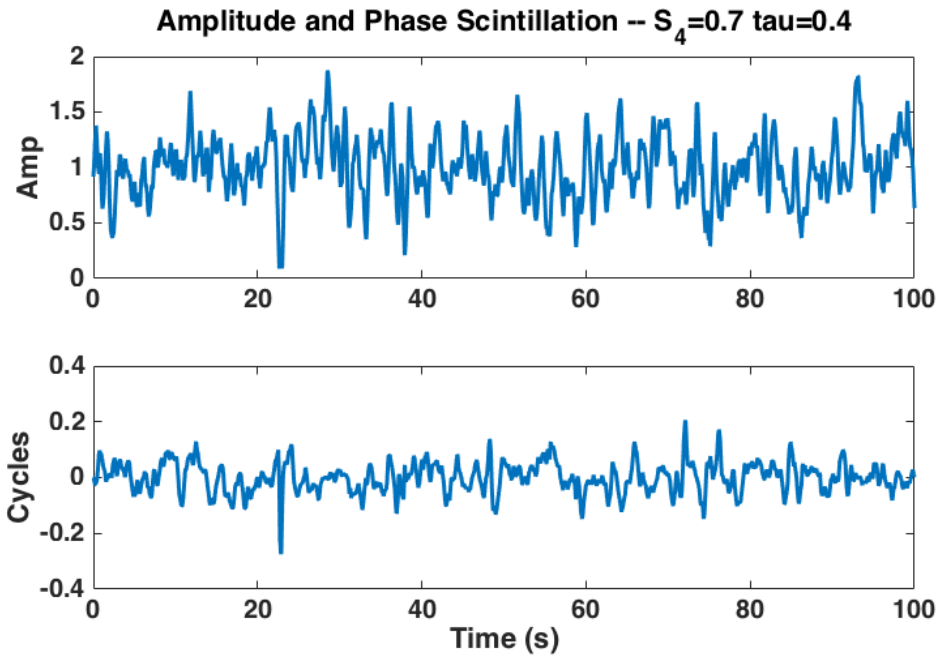

Figure 3.5: Simulated amplitude and phase scintillation for moderate scintillation scenario.

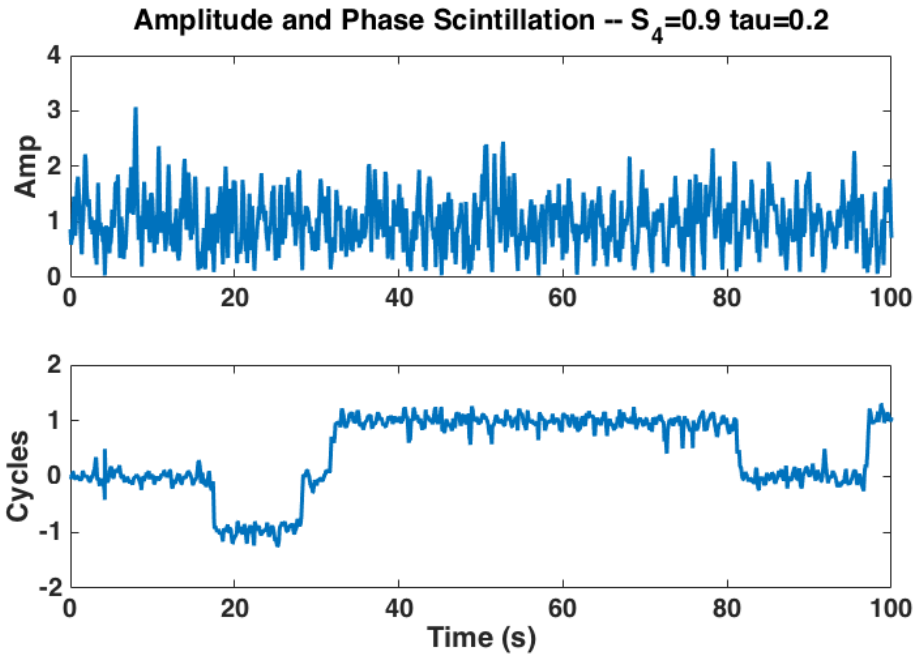

Figure 3.6: Simulated amplitude and phase scintillation for strong scintillation scenario.

The simulated data in Figures 3.5 and 3.6 was generated using a procedure outlined in [30]. In that reference, amplitude and phase scintillation data is generated such that the amplitude fading follows a Nakagami distribution and the rapid phase changes occur during periods of deep fading as is seen in empirical data. The S_4 index in each plot would indicate strong scintillation, meaning that the tracking ability of the receiver would likely be affected. The term moderate is used to described the results in Figure 3.5 as a comparative term to differentiate from the more severe scintillation shown in Figure 3.6. As seen in the plot of strong scintillation, during periods of deep amplitude fading the carrier phase can change by a half or full cycle over short time periods. This phenomenon is likely to cause cycle slipping in a traditional PLL and could cause complete loss of lock.

3.5 Clock Errors

GPS positioning requires precise time synchronization across all elements of the system. The satellite and receiver clocks are not generated with perfect frequency references, resulting in time bias and drift that must be estimated as part of the positioning solution. The oscillator dynamics are also important in the design of the carrier tracking loop. Satellite and receiver clock models are discussed in the next two subsections.

3.5.1 Receiver Clock

It is important to analyze the receiver clock accuracy in the time domain and frequency domain to understand the impact of clock errors on the position estimation and on the carrier tracking loop design. Typically, the clock in the GPS receiver is based on a low cost crystal oscillator which exhibits a variety of stochastic behaviors that result in time inaccuracies and signal dynamics. Time inaccuracies manifest in the pseudorange measurements from the receiver and degrade the navigation solution. The phase and frequency noise also cause apparent changes in the received signal which must be tracked in the carrier tracking

loop. The magnitude of the phase and frequency noise limits the range of noise equivalent bandwidths that are usable in the carrier tracking loop.

Frequency Domain Analysis

The clock in the GPS receiver is derived from a frequency generator typically provided by either a temperature controlled or ovenized crystal oscillator (TCXO or OXCO, respectively). The accuracy of these oscillators varies widely with the OXCO being a significantly more stable frequency source. Variations in the frequency of the oscillator create signal dynamics that must be tracked by the receiver tracking loops. Therefore, the frequency spectrum of the receiver oscillator should be considered when designing the receiver tracking loop. Phase noise specifications for commercial oscillators are typically provided at several key frequencies offset from the nominal frequency and allow the end user to reconstruct an approximate single sideband noise spectrum. The phase noise is reported in decibels relative to the carrier per one hertz bandwidth (dBc/Hz). Using specifications from [41], Figure 3.7 shows the single sideband phase noise for an OCXO and TXCO with frequency ranges consistent with common GPS front ends.

Using the data from the oscillator specifications, a polynomial is fit to the phase noise spectrum to determine the power law parameters normally used to characterize oscillators. The power law coefficients complete the model for the oscillator power spectral density seen in Equation (3.13).

$$S_\phi(f) = N^2(h_0 + \frac{h_1}{f} + \frac{h_2}{f^2} + \frac{h_3}{f^3} + \frac{h_4}{f^4}) \tag{3.13}$$

Note that N is the ratio of the frequency of interest (i.e. GPS L1) to the nominal frequency of the oscillator [46]. Polynomial fits for the power spectral densities of the two types of oscillators mentioned above are shown in Figure 3.8 and the resulting coefficients are compiled in Table 3.1. These values are consistent with typical GPS receiver clocks.

The design of the loop filter in the receiver tracking channels determines the degree to which the oscillator phase noise is suppressed. Since the oscillator phase noise introduces

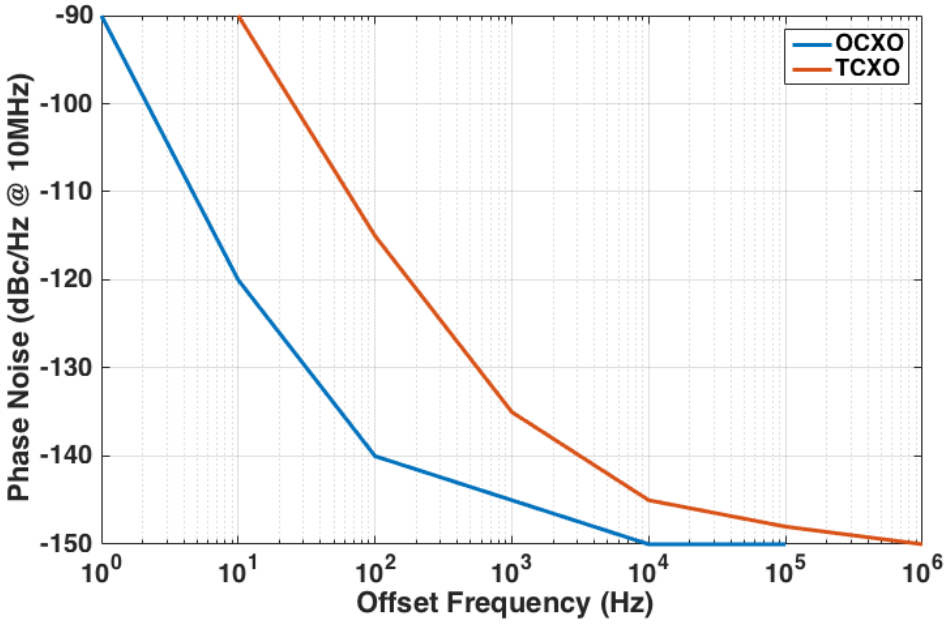

Figure 3.7: Single sideband phase noise spectrum for commercial OCXO and TCXO

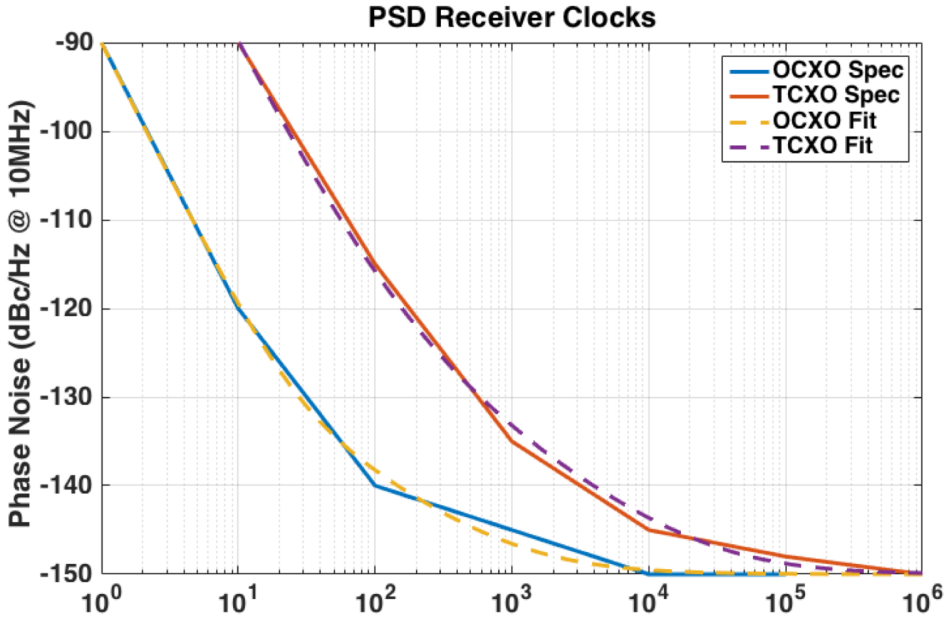

Figure 3.8: Polynomial fits provide parameters to further analyze receiver clock dynamics

Table 3.1: Power Law Coefficients Determined By Polynomial Fit To Oscillator Specifications

Coefficient	OCXO	TCXO
h_0	2.0×10^{-29}	2.0×10^{-29}
h_1	2.4×10^{-26}	6.4×10^{-25}
h_2	2.2×10^{-25}	2.8×10^{-22}
h_3	1.8×10^{-23}	1.8×10^{-20}
h_4	1.6×10^{-24}	2.4×10^{-24}

signal dynamics that must be tracked, the attenuation of the clock phase noise results in errors in the carrier phase estimates maintained in the tracking loop. The phase error is characterized by the order and noise equivalent bandwidth of the loop filter, and is calculated using Equation (3.14)

$$\sigma^2_{\phi_{rxo}} = \int_0^\infty |1 - H_\phi(f)|^2 S_\phi(f) df \tag{3.14}$$

where $H_\phi(f)$ is the closed loop transfer function of the PLL and $1 - H_\phi(f)$ is the error transfer function.

Equation (3.14) can be solved numerically over an expected range of frequencies, or in [31] a closed form solution for a second PLL is derived. The resulting one standard deviation error (or jitter) for the two oscillator models defined by the parameters given in Table 3.1 for second order and third order PLLs is shown in Figure 3.9 as a function of the noise equivalent bandwidth of the filter. In the figure, it is clear that as the bandwidth of the PLL decreases, the ability of the filter to track the receiver clock dynamics decreases. As a result, there is a lower bound on the PLL noise equivalent bandwidth that may be used for the tracking loop. The horizontal black line represents the one sigma phase error threshold where the PLL begins to slip cycles of the carrier. Therefore, a designer must select a bandwidth greater than approximately one half hertz when using an OCXO and greater than three hertz when using a TCXO. Later it will be clear that additional sources of signal dynamics will require the bandwidth to be even higher.

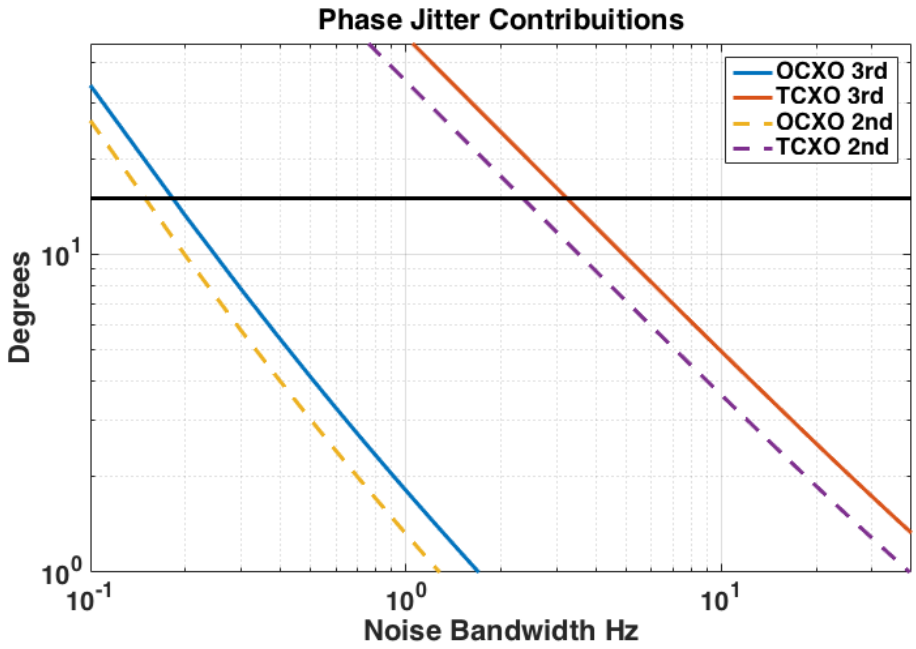

Figure 3.9: Tracking loop phase jitter introduced by typical OCXO and TXCO receiver clocks

Time Domain Analysis

To understand how the clock bias and clock drift terms affect the pseudorange and pseudorange rate measurements described in Section 2.5.5, it is valuable to analyze the receiver clock in the time domain. The Allan variance is normally used to analyze oscillator stability in the time domain and is calculated by Equation (3.15)

$$\sigma_y^2(\tau) = \frac{1}{2(M-1)} \sum_{k=1}^{M-1} (\bar{y}_{k+1} - \bar{y}_k)^2 \tag{3.15}$$

where $\bar{y}$ is the average frequency error over the averaging time, τ [3]. Typically, $M = 2$ is used to calculate the two sample Allan variance. For crystal oscillators, the power law coefficients determined from the single sideband phase noise (as described above) are also directly relatable to the Allan variance of the oscillator. Based on the definition of the Allan variance [13], it can be shown that the Allan variance can be approximated using the power

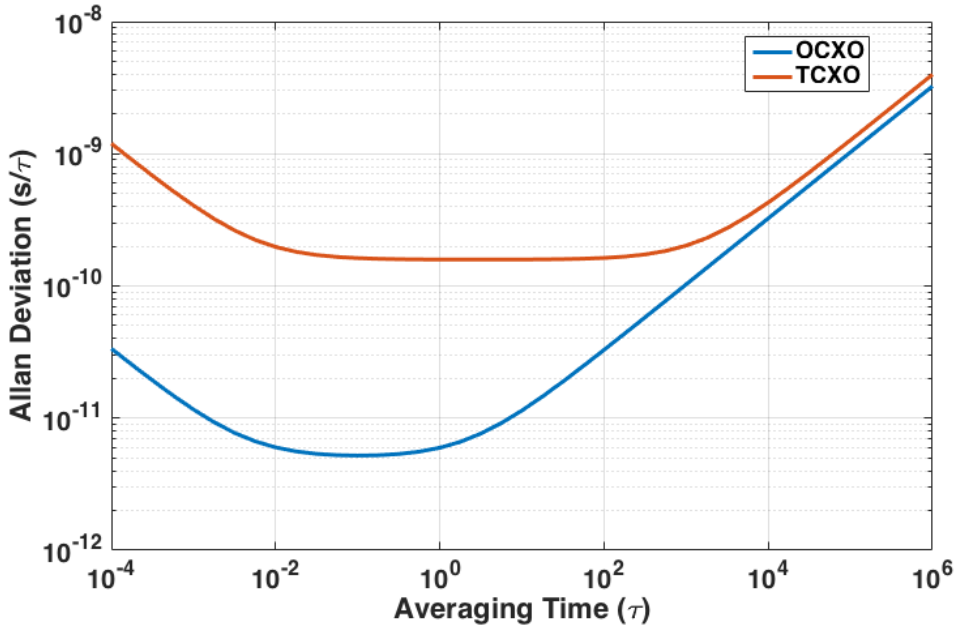

Figure 3.10: Allan deviation plot for the two oscillators with power law coefficients given in Table 3.1

law coefficients as seen in Equation (3.16).

$$\sigma_y^2(\tau) = h_2 \frac{1}{2\tau} + h_3 2 \ln 2 + h_4 \frac{2\pi^2}{6} \tag{3.16}$$

The impact of h_0 and h_1 on the Allan variance is minimal relative to the three terms seen in Equation (3.16), and accordingly, those terms have been omitted. From Equation (3.16) and the values found in Table 3.1, the Allan deviation (i.e. the square root of the Allan variance) for typical GPS OCXO and TCXO clocks are shown in Figure 3.10. The OCXO is clearly more precise than the TCXO.

As shown in [7], a simple two state clock model that neglects the flicker noise of the oscillator can be derived based on the Allan variance . Flicker noise causes the flat region of the Allan variance that is seen in Figure 3.10 which is particularly noticable in the variance of the TCXO. The states of this clock model are bias and drift, the two parameters that must be estimated along with position and velocity to form the GPS navigation solution.

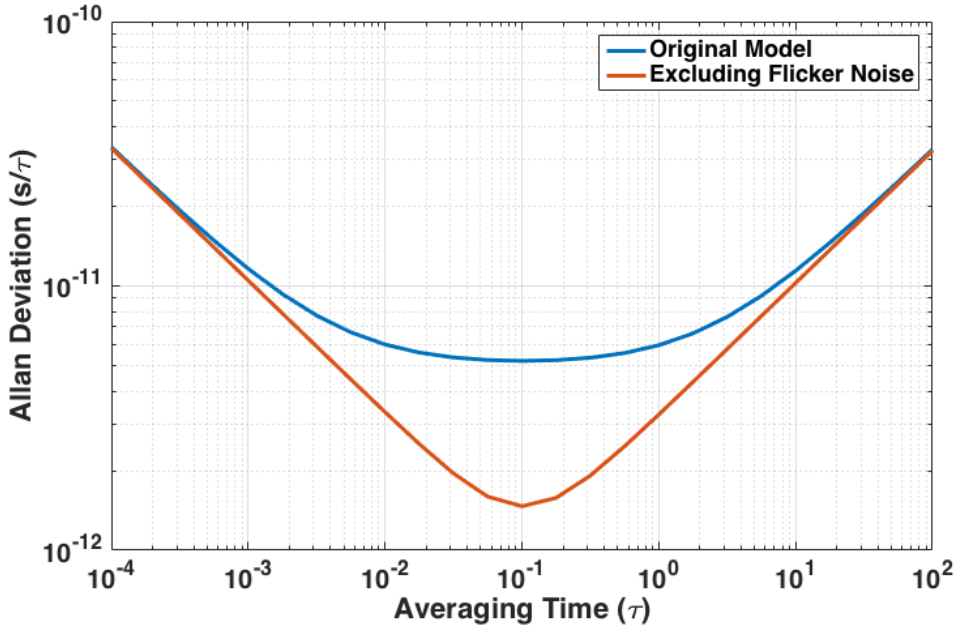

Figure 3.11: Allan deviation plot for the original OCXO model and the modeling excluding flicker noise.

The model assumes that the oscillator frequency and phase will exhibit random walk, and is given by Equation (3.17).

$$\begin{bmatrix} b \\ \dot{b} \end{bmatrix} = \begin{bmatrix} 1 & \Delta t \\ 0 & 1 \end{bmatrix} + \begin{bmatrix} w_b \\ w_{\dot{b}} \end{bmatrix} \tag{3.17}$$

where

$$E[ww^{\mathrm{T}}] = \begin{bmatrix} \frac{h_2}{2}\Delta t + \frac{2}{3}\pi^2 h_4 \Delta t^3 & \pi^2 h_4 \Delta t^2 \\ \pi^2 h_4 \Delta t^2 & 2\pi^2 h_4 \Delta t \end{bmatrix} \tag{3.18}$$

This optimistic model results in an Allan variance that underestimates the time uncertainty introduced by flicker noise. The optimistic model is compared to the original Allan variance model for the OCXO in Figure 3.11. Clearly, the expected deviation using the simple clock model is significantly lower than the likely error for averaging times between ten milliseconds and one second. One way to compensate for the flicker noise is to shift up the model excluding flicker noise, but that would result in a pessimistic model of uncertainty for shorter and longer averaging times. An alternative model was suggested in [13], which required a modest change

to the states in that the derivative state $\dot{b}$ was assumed to be an estimate of the average drift rather than the instantaneous drift. Making this assumption, the process noise model (i.e. $E[ww^{\mathrm{T}}]$) is modified to include a term modeling the flicker noise. This modification is necessary due to the fact that the filcker noise can not be modeled with a finite-order model [7]. The state transition matrix of this modified model is the same as Equation (3.17), and the new process noise model is given by:

$$E[ww^{\mathrm{T}}] = \begin{bmatrix} \frac{h_2}{2}\Delta t + \frac{2}{3}\pi^2 h_4 \Delta t^3 + 2h_3\Delta t^2 & \pi^2 h_4 \Delta t^2 + 2h_3\Delta t \\ \pi^2 h_4 \Delta t^2 + 2h_3\Delta t & 2\pi^2 h_4 \Delta t + 2h_3 \end{bmatrix} \tag{3.19}$$

A time series of the clock bias and drift values were simulated using the modified filter model and was compared to the original model of the expected Allan variance. The result is shown in Figure 3.12 along with the process noise uncertainty predicted by the new model. The simulated clock bias exhibits the expected characteristics, such that the process noise uncertainty matches well while slightly overestimating the flicker noise floor.

3.5.2 Satellite Clock

GPS satellites carry an atomic frequency standard and are therefore able to precisely maintain time over long periods. Additionally, the satellite clocks are periodically updated with timing information from the GPS ground station segment. Due to the long term accuracy and the minimal drift of the satellite clocks, the satellite clock bias can be accurately predicted using parameters from the satellite ephemerides provided in the navigation message. For high precision applications using the carrier phase measurements, any residual satellite clock bias is normally removed by differencing measurements from multiple receivers; this procedure will be discussed in Chapter 5. Also, the satellite clock drift is negligible when estimating the receiver velocities. This chapter will not focus on the effects of the satellite clock errors on receiver position and velocity estimation due to the long term stability and predictable accuracy of the satellite clock errors.

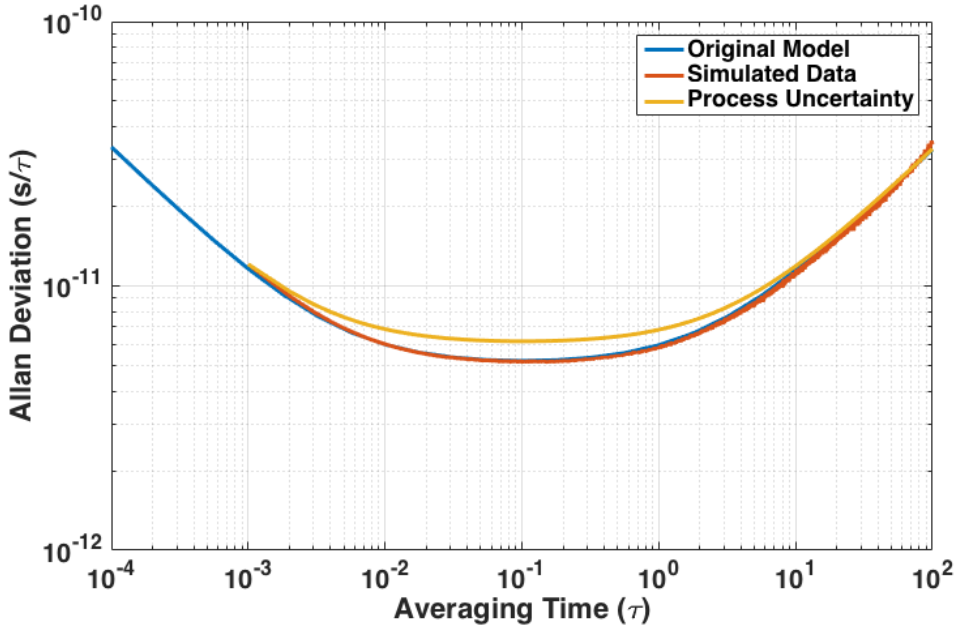

Figure 3.12: Allan deviation plot for the original model of the OCXO, for simulated data including flicker noise, and the process noise uncertainty based on the modified clock model.

While the satellite clock errors are readily mitigated in the navigation solution, the impact of satellite clock errors on carrier tracking should be considered when designing tracking loops. Based on the GPS standard positioning signal specification [48] and the analysis in [16], the power spectral density for the GPS satellite clock can be approximated maintaining the shape of a typical TCXO power spectral density and shifting it such that the new density passes through the signal data point given in the specification document. With a representative power spectral density, the expected one sigma phase jitter introduced in the carrier phase tracking loop by the satellite clock error can be calculated as a function of the noise equivalent bandwidth of the loop filter using Equation (3.14). Figure 3.13 shows the phase noise using third order and second order tracking loops due to the satellite clock with a phase tracking threshold of 15 degrees shown in black. The phase jitter due to satellite clock errors will be combined with additional phase jitter sources later in this chapter to illustrate the overall limitations on tracking loop bandwidths.

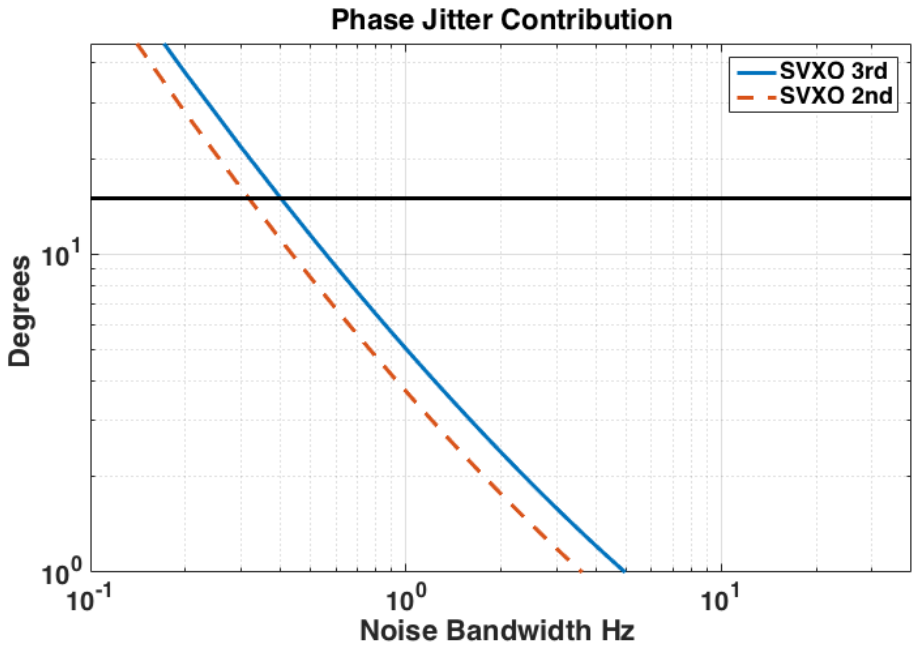

Figure 3.13: Tracking loop phase jitter introduced by satellite clock.

3.6 Dynamic Stress

Rapid changes in the position, velocity, or acceleration of the receiver stress the tracking capability of the PLL. Receiver motion along the line of sight vector to a satellite results in signal dynamics that must be tracked by the PLL. Step changes in frequency, frequency rate, and frequency acceleration cause transient responses in the PLL that may result in phase errors that exceed the reliable operating region of the tracking loop. As shown in previous figures, a rule of thumb value for the maximum allowable phase jitter is 15 degrees. The filter order and bandwidth determine the maximum phase error due to the various step changes listed above. For example, if the maximum line of sight change in acceleration between receiver and satellite is 2 m/s^2, a third order PLL can track the signal with zero steady error. The maximum phase error during the transient response of the filter is approximated by [32]:

$$\sigma_{\phi_{d,a}} = \frac{\Delta\ddot{x}}{(1.885B_n)^2}\frac{360}{3\lambda} \tag{3.20}$$

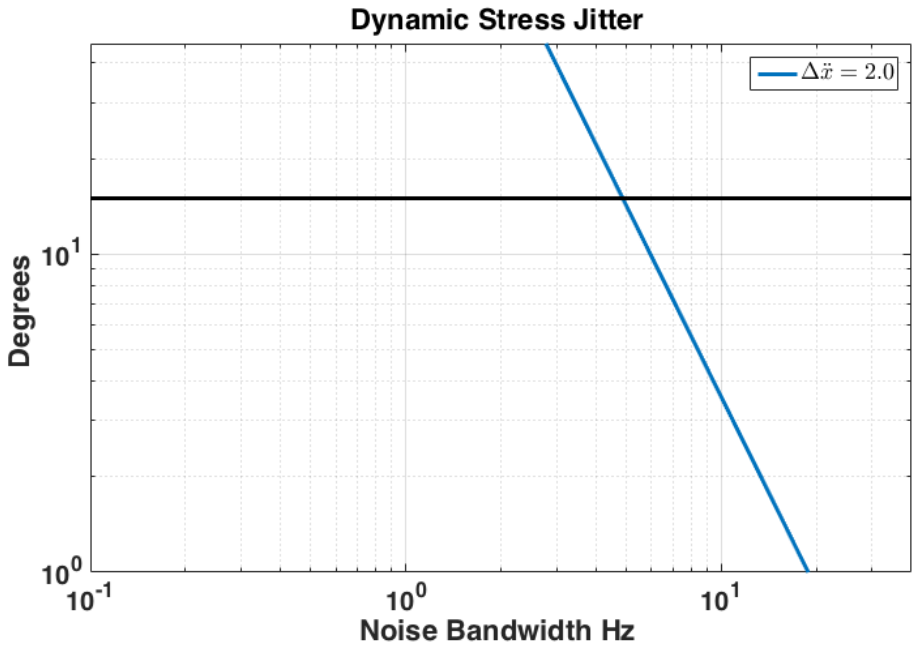

Figure 3.14: Tracking loop phase jitter due to line of sight acceleration

where B_n is the noise equivalent bandwidth of the PLL.

Figure 3.14 shows phase error as a function of the noise bandwidth for the example of a third order PLL with a line of sight acceleration of 2 m/s^2. Note that the acceleration in meters per second squared is converted to frequency rate by dividing by the wavelength (λ) of the GPS L1 signal. Also, the phase error has been converted to degrees and divided by three to calculate the one sigma phase error value. From the figure, it is clear that third order PLLs with a noise bandwidth less than approximately 5 Hz would likely cycle slips or lose lock in these conditions.

3.7 Thermal Noise

In this chapter, several errors sources and their impact on carrier tracking loop design have been discussed. Each of the factors described so far were related to signal dynamics that must be tracked by the tracking loop. Those factors combine to produce a lower bound for the tracking loop bandwidth as will be seen in the next section. Alternatively, the loop

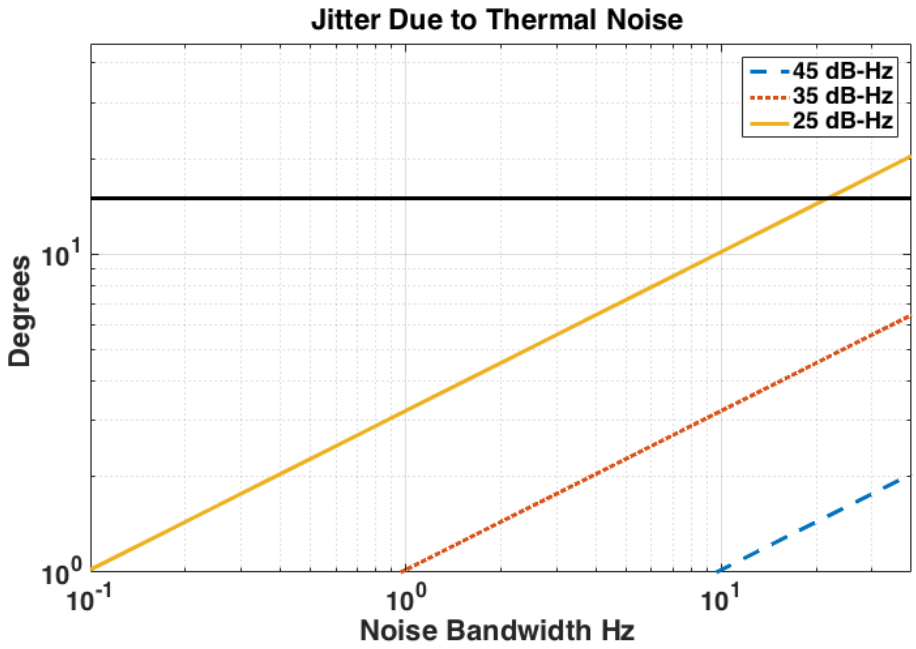

Figure 3.15: Tracking loop phase error due to thermal noise for three C/N_0 ratios.

filter is designed to reject thermal noise, and as the bandwidth increases the phase error due to thermal noise increases. For a carrier tracking loop using the two quadrant arctangent discriminator used in this dissertation, the phase error due to thermal noise can be predicted as a function of the filter noise bandwidth and the C/N_0 ratio using Equation (3.21).

$$\sigma_{\phi_t} = \frac{360}{2\pi}\sqrt{\frac{B_n}{C/N_0}(1+\frac{1}{2TC/N_0})} \tag{3.21}$$

From Equation (3.21), it is clear that σ_t increases monotonically as B_n increases for a given C/N_0 ratio. The phase error for three typical C/N_0 ratios is represented graphically in Figure 3.15.

The three carrier to noise ratios used to calculate phase error for Figure 3.15 represent approximately the full range of C/N_0 values for received satellite signals under normal operating conditions (i.e. without intentional interference). The highest C/N_0 ratio, 45 dB-Hz, is typical for a satellite signal receiver on a clear line of sight as the satellite passes overhead. The lowest value, 25 dB-Hz, is at or below the signal power for which a traditional receiver

can maintain tracking. A signal with this C/N_0 ratio would likely be very low on the horizon, or obstructed by the environment near the receiver.

3.8 Total Phase Jitter and Tracking Loop Design

The tracking loop design space combines each of the error sources described in this chapter. For a given loop filter order, bandwidth, and C/N_0 ratio, the total phase jitter includes the phase error from thermal noise, colored noise sources (i.e. oscillator dependent), and dynamic stress [32] as seen in Equation (3.22).

$$\sigma_\phi = \sigma_{\phi_t} + \sigma_{\phi_{rxo}} + \sigma_{\phi_{sxo}} + \sigma_{\phi_{d,i}} + \sigma_{\phi_{d,a}} \tag{3.22}$$

Recall, σ_{ϕ_t} represents the thermal noise jitter. $\sigma_{\phi_{rxo}}$ and $\sigma_{\phi_{sxo}}$ represent the jitter due to receiver and satellite clock errors respectively. Finally $\sigma_{\phi_{d,i}}$ and $\sigma_{\phi_{d,a}}$ represent the dynamic stress due to ionospheric disturbances and line of sight accelerations.

A graphical representation of the total phase jitter for a receiver using the OCXO described earlier in this section is provided in Figure 3.16. The data in the figure assumes that the maximum line of sight acceleration is 2 m/s^2 and that the maximum ionosphere induced frequency shift is 0.085 Hz. Phase errors are plotted for second and third phase locked loops. There is not a significant difference in the acceptable noise bandwidth between the second and third order loop filter. However, note that the results assume that the line of sight acceleration is zero mean and non-zero accelerations are short in duration. Using either a second or third order loop, the minimum noise bandwidth that would provide reliable tracking is approximately 6 Hz. Based on Figure 3.16, a PLL could not be designed to track a signal with a C/N_0 ratio of 25 dB-Hz with this clock and dynamic stress. That is consistent with the finding in [16] which shows a traditional PLL can not reliably maintain phase lock on signals with C/N_0 ratios below 28 dB-Hz.

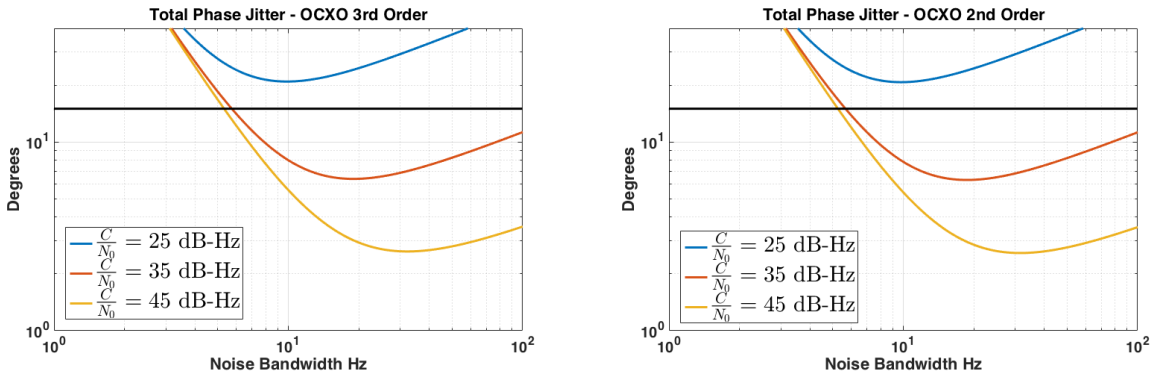

Figure 3.16: Total phase jitter assuming a third order PLL, an OCXO clock, and a maximum line of sight acceleration of 2 m/s^2.

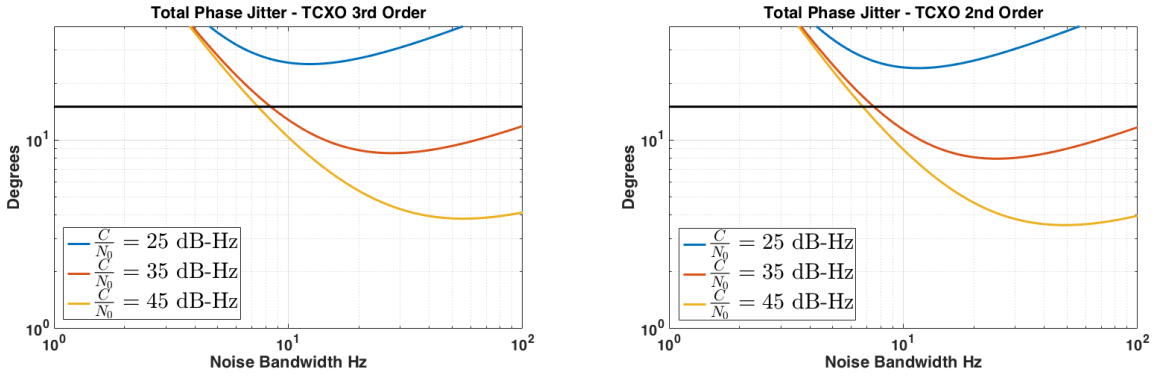

Figure 3.17: Total phase jitter assuming a third order PLL, a TCXO clock, and a maximum line of sight acceleration of 2 m/s^2.

The phase tracking performance of a receiver using the TXCO described in Section 3.5.1 was also analyzed. The results are compiled in Figure 3.17. All parameters other than the clock model remained the same as those used in Figure 3.16. The phase error profile is similar to that seen for the receiver using the OCXO, but the minimum reliable noise bandwidth is slightly larger at approximately 8 Hz. The minimum phase error is also higher than that of the OCXO as would be expected. Accordingly, the receiver using the OCXO would be able to maintain phase lock signals at a slightly lower C/N_0 ratio than the TXCO if the optimal bandwidth were used in both cases.

3.9 Conclusion

In this chapter, the factors affecting GPS signal tracking and position estimation were examined. The local environment, atmosphere activity, receiver and satellite clocks, and receiver motion are all important criteria to consider in designing the GPS receiver tracking and positioning module. In particular, the selection of the PLL noise bandwidth is a critical design decision. The design space for the traditional scalar tracking PLL was described in this chapter and will be considered again in Chapter 4 in the design of a vector tracking aided phase locked loop for improved carrier phase tracking.

Chapter 4

Doppler Aided Carrier Phase Tracking

Carrier phase tracking is vital to high precision GPS positioning solutions that exploit the accuracy of the carrier phase measurement. RTK GPS algorithms can provide position estimates with errors on the order of a few centimeters when using measurements from a local base station. Both the base station and rover receiver must maintain phase lock on five or more satellites to reliably provide this level of accuracy. In this chapter, advanced GPS tracking approaches are designed for implementation with a single receiver without external sensor aiding. Recall from the comparison of scalar and vector receiver architectures in the introduction that the vector tracking architecture provides improved tracking capability due to the over-constrained nature of the GPS navigation solution. Accordingly, the navigation solution is more robust to errors in one channel that is the scalar tracking loop. To leverage that improvement in tracking performance, a vector frequency locked loop aided phase lock loop is described and analyzed in terms of receiver dynamics and C/N_0 ratio. Next, an implementation intended for a static base station receiver operating in the presence of ionospheric scintillation is derived and the performance is analyzed in simulation.

4.1 Vector Frequency Locked Loop Aided Phase Tracking

There are two approaches to consider when designing the vector aided phase tracking loop. In each approach, the navigation processor is responsible for predicting the carrier frequency for each channel as a function of the current best estimates of the receiver states and the satellite states calculated from the ephemerides. The primary difference can be seen in the design of the tracking channel. Block diagrams of the two approaches that are considered are shown in Figures 4.1 and 4.2.

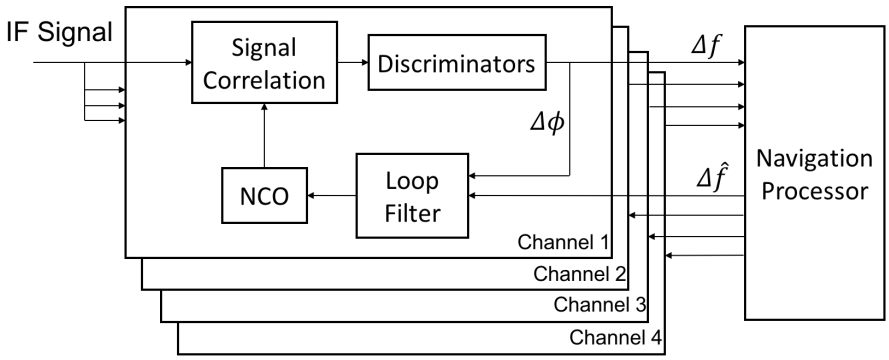

Figure 4.1: Vector frequency locked loop aided phase lock loop with fixed gain loop filter.

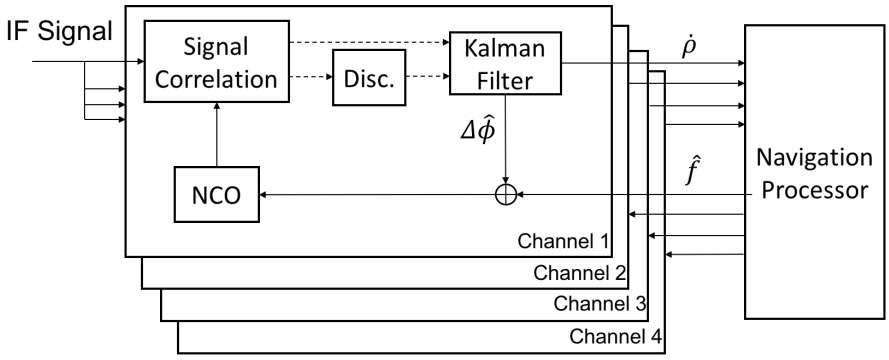

Figure 4.2: Vector frequency locked loop aided phase lock loop with local Kalman filter estimation.

In the two figures, the first approach uses a fixed gain loop filter to combine phase and frequency error estimates, and the second approach uses a local Kalman filter to estimate phase errors and the navigation processor to estimate frequency errors. In the first architecture, the phase discriminator output is combined with feedback from the navigation processor in a fixed gain loop filter. The navigation processor updates velocity and clock drift estimates with carrier frequency discriminators from each channel and returns filtered carrier frequency error estimates. The second implementation relies on a local Kalman filter to estimate the carrier phase errors. Typically, the states of this filter include phase rate errors and phase acceleration errors. Each channel provides a measurement of the pseudorange rate to update the state estimates of the navigator and receives feedback in the form of estimated carrier frequency.

Each of the alternatives offer advantages and disadvantages. The first approach is relatively simple to implement, and traditional loop filter design criteria can be leveraged in the design. Alternatively, by maintaining an accurate phase error estimate at the update rate of the correlation step, the update rate of the master filter can be reduced in the second implementation. However, when designing two Kalman filters to track common errors, time correlation and cross correlation of the estimated uncertainty within the two filters can result in an overly optimistic covariance estimate and filter divergence. Based on these criteria, the first approach was selected for implementation and analysis.

4.2 Vector Frequency Locked Loop

The vector frequency locked loop (VFLL) relies on a navigation processor that is implemented as an eight state Kalman filter. The states of the filter are given by Equation (4.1)

$$\mathbf{X} = \begin{bmatrix} \delta x \\ \delta \dot{x} \\ \delta y \\ \delta \dot{y} \\ \delta z \\ \delta \dot{z} \\ \delta cb \\ \delta \dot{cb} \end{bmatrix} \tag{4.1}$$

where x, y, and z are the Earth center Earth fixed (ECEF) position coordinates, $\dot{x}$, $\dot{y}$, and $\dot{z}$ are the velocity components, and b and $\dot{b}$ are clock bias and drift terms, respectively. The δ prefix indicates that the errors of the optimal estimates of each of these states are being maintained in the Kalman filter. Approximate initial values for position, velocity, clock bias, and clock drift are derived from a scalar tracking receiver which acquires the GPS signal, locks code and carrier phase, and decodes the navigation data message. The pseudorange and pseudorange rates are used to calculate estimated receiver states to initialize the Kalman filter. The state covariance matrix, $\mathbf{P_X}$, of the Kalman filter is initialized using the GPS error budget of the standard position service (SPS) solution as outline in [64].

4.2.1 VFLL Dynamic Model

The state dynamic equations, seen in Equation (4.2), are derived from the kinematic relationships of the states, and assumes that the receiver acceleration is zero mean and Gaussian distributed.

$$\dot{\mathbf{X}} = A\mathbf{X} + B_d w_d + B_c w_c \tag{4.2a}$$

$$A = \begin{bmatrix} \alpha & 0_{2x2} & 0_{2x2} & 0_{2x2} \\ 0_{2x2} & \alpha & 0_{2x2} & 0_{2x2} \\ 0_{2x2} & 0_{2x2} & \alpha & 0_{2x2} \\ 0_{2x2} & 0_{2x2} & 0_{2x2} & \alpha \end{bmatrix} \tag{4.2b}$$

$$B_d = \begin{bmatrix} 0 & 0 & 0 \\ 1 & 0 & 0 \\ 0 & 0 & 0 \\ 0 & 1 & 0 \\ 0 & 0 & 0 \\ 0 & 0 & 1 \\ 0 & 0 & 0 \\ 0 & 0 & 0 \end{bmatrix} \tag{4.2c}$$

$$B_c = \begin{bmatrix} 0_{2x2} \\ 0_{2x2} \\ 0_{2x2} \\ I_{2x2} \end{bmatrix} \tag{4.2d}$$

$$\alpha = \begin{bmatrix} 0 & 1 \\ 0 & 0 \end{bmatrix} \tag{4.2e}$$

$$w_d = \begin{bmatrix} w_x \\ w_y \\ w_z \end{bmatrix} \tag{4.2f}$$

$$w_d = \begin{bmatrix} w_b \\ w_{\dot{b}} \end{bmatrix} \tag{4.2g}$$

The basic two state clock model follows the derivation from Section 3.5.1.

The state transition matrix and discrete process noise model can be determined by truncating the Taylor series expansion of the dynamic equations to first order. The resulting discrete model, seen in Equation (4.3) is used to propagate the estimated mean and covariance in the standard Kalman filter time update.

$$\mathbf{X}_{k+1} = \Phi_{k,k+1}\mathbf{X}_k + Q_k \tag{4.3a}$$

$$\Phi_{k,k+1} = \begin{bmatrix} \alpha_k & 0_{2x2} & 0_{2x2} & 0_{2x2} \\ 0_{2x2} & \alpha_k & 0_{2x2} & 0_{2x2} \\ 0_{2x2} & 0_{2x2} & \alpha_k & 0_{2x2} \\ 0_{2x2} & 0_{2x2} & 0_{2x2} & \alpha_k \end{bmatrix} \tag{4.3b}$$

$$\alpha_k = \begin{bmatrix} 1 & \Delta t \\ 0 & 1 \end{bmatrix} \tag{4.3c}$$

$$Q_k = \begin{bmatrix} Q_x & 0_{2x2} & 0_{2x2} & 0_{2x2} \\ 0_{2x2} & Q_y & 0_{2x2} & 0_{2x2} \\ 0_{2x2} & 0_{2x2} & Q_z & 0_{2x2} \\ 0_{2x2} & 0_{2x2} & 0_{2x2} & Q_{cb} \end{bmatrix} \tag{4.3d}$$

$$Q_x = \begin{bmatrix} \sigma_x^2 \frac{\Delta t^3}{3} & \sigma_x^2 \frac{\Delta t^2}{2} \\ \sigma_x^2 \frac{\Delta t^2}{2} & \sigma_x^2 \Delta t \end{bmatrix} \tag{4.3e}$$

$$Q_y = \begin{bmatrix} \sigma_y^2 \frac{\Delta t^3}{3} & \sigma_y^2 \frac{\Delta t^2}{2} \\ \sigma_y^2 \frac{\Delta t^2}{2} & \sigma_y^2 \Delta t \end{bmatrix} \tag{4.3f}$$

$$Q_z = \begin{bmatrix} \sigma_z^2 \frac{\Delta t^3}{3} & \sigma_z^2 \frac{\Delta t^2}{2} \\ \sigma_z^2 \frac{\Delta t^2}{2} & \sigma_z^2 \Delta t \end{bmatrix} \tag{4.3g}$$

$$Q_{cb} = \begin{bmatrix} \frac{h_2}{2}\Delta t + \frac{2}{3}\pi^2 h_4 \Delta t^3 + 2h_3 \Delta t^2 & \pi^2 h_4 \Delta t^2 + 2h_3 \Delta t \\ \pi^2 h_4 \Delta t^2 + 2h_3 \Delta t & 2\pi^2 h_4 \Delta t + 2h_3 \end{bmatrix} \tag{4.3h}$$

In Equations (4.3e - 4.3g), Q_x, Q_y, and Q_z are the expected values of w_x^2, w_y^2, w_z^2 respectively. Each of the acceleration uncertainties can be tuned individually to reflect the likely vehicle dynamics if they are known to differ in certain directions. The h_2, h_3, and h_4 values are determined based on the specification of the receiver clock as described in Section 3.5.1. The Kalman time update of the state mean and covariance is calculated using Equations (4.4a) and (4.4b)

$$\mathbf{X}_{k+1} = \Phi_{k,k+1}\mathbf{X} \tag{4.4a}$$

$$\mathbf{P}_{\mathbf{X}_{k+1}} = \Phi_{k,k+1}\mathbf{P}_{\mathbf{X}_k}\Phi_{k,k+1}^{\mathrm{T}} + Q_k \tag{4.4b}$$

4.2.2 VFLL Filter Residuals

The estimates of position, velocity, and time are updated using pseudorange and pseudorange rate information from each tracking channel. The pseudorange information is used to update the position and clock bias estimates, and may be formulated as a standard GPS position estimation algorithm or a vector delay locked loop (VDLL). In this chapter, the focus is on the carrier tracking architecture; accordingly, the code tracking and pseudorange generation will be omitted from the discussion. The VDLL implementation couples with a vector carrier approach is discussed in Chapter 6.

The pseudorange rate information used to update a pure VFLL is normally the carrier frequency discriminator output from each channel scaled to convert to units of meters per second. That discriminator is also used in this VFLL aided PLL structure also. However, it cannot be applied directly as in the pure VFLL because the carrier frequency used in the tracking channel is not exactly the frequency that is predicted by the current state estimates. The difference is due to the combination of the VFLL feedback and the carrier phase discriminator in the loop filter. To account for the difference, the residuals are calculated by comparing the pseudorange rate predicted by the state estimates to the pseudorange rate

from the tracking channel which combines the carrier frequency and the frequency discriminator. This measurement equation is shown in Equation (4.5)

$$\tilde{\dot{\rho}} = (f_{IF} - f_{carr} - \Delta f)\lambda_{L1} \tag{4.5}$$

where

$$\Delta f = \frac{\text{atan2}(IP_1IP_2 + QP_1QP_2, IP_1QP_2 - IP_2QP_1)}{t_2 - t_1} \tag{4.6}$$

and where IP and QP are in the in-phase and quadrature prompt correlator outputs and the subscripts denote two consecutive integration periods. The predicted pseudorange rate is calculated as a function of the current state estimates and the satellite state information derived from the ephemerides as seen previous in Equation (2.28). The equation for the pseudorange rate residual was also given previously in Equation (2.29).

4.2.3 VFLL Residual Variances

The Kalman filter measurement update requires a measurement noise matrix to account for uncertainty in the measurements. Again, the code based position update will be discussed later in Chapter 6, so only the pseudorange rate residual variance is discussed here. The carrier frequency discriminator measurement variance is a function of the integration period and the C/N_0 ratio of the channel. Equation (4.7) shows the expected one sigma error of the pseudorange rate residual due to discriminator noise.

$$\sigma_{\dot{\rho}} = \frac{\lambda_{L1}}{\pi T}\sqrt{\frac{2}{T\frac{C}{N_0}}\left(1 + \frac{1}{T\frac{C}{N_0}}\right)} \tag{4.7}$$

The C/N_0 ratio must be estimated in the receiver to calculate the range and range rate residual covariances. Additional correlators are used to estimate the current noise level for comparison to the received signal power. The code phase of the additional noise correlators is intentionally set greater than one chip away for the prompt replica to minimize the C/A

code autocorrelation function and leave only an approximation of the noise power. The signal power and noise power are estimated in a moving average filter using the early/late and noise correlator outputs. The early and late correlators (rather than the prompt correlator) are used to estimate the receiver signal power to avoid variations in the prompt correlator output that results from tracking loop jitter. Equation (4.8) is used to estimate the square of the receiver signal power, P_{L1}.

$$P_{L1} = (IE + IL)^2 + (QE + QL)^2 \tag{4.8}$$

Note that the correlator outputs are also corrupted by noise; therefore the noise power of the four correlators is removed before calculating the C/N_0 ratio as seen in Equation (4.9).

$$\frac{C}{N_0} = 10 \log_{10} \left(\frac{P_{L1} - 4\eta^2}{\eta^2} \right) \tag{4.9}$$

The C/N_0 ratio is the ratio of the power of the received signal (in Watts) to the noise density (in W/Hz). The C/N_0 ratio is normally expressed in dB-Hz.

4.2.4 VFLL Measurement Update

The Kalman filter measurement update is performed once the state estimates have been propagated forward to the time of the current measurement and the residual and residual variance are calculated. The measurement matrix is derived by differentiating the residual from Equation (4.6) with respect to the state vector resulting in Equation (4.10).

$$H_k = \begin{bmatrix} 0 & a_x & 0 & a_y & 0 & a_z & 0 & -1 \end{bmatrix} \tag{4.10}$$

The standard Kalman filter measurement update is performed using Equation (4.11) [7].

$$K_k = \mathbf{P}_{\mathbf{X}_k} H_k^{\mathrm{T}} (H_k \mathbf{P}_{\mathbf{X}_k} H_k^{\mathrm{T}} + R_k)^{-1} \tag{4.11a}$$

$$\mathbf{X}_k = \mathbf{X}_k + K_k z_k \tag{4.11b}$$

$$\mathbf{P}_{\mathbf{X}_k} = (I - K_k H_k)\mathbf{P}_{\mathbf{X}_k} \tag{4.11c}$$

The satellite notation has been omitted from Equations (4.5 - 4.11), but note that residual and measurement updates are calculated from each channel at the end of the twenty millisecond integrate and dump period. An integration period of twenty milliseconds is chosen to maximize the effective C/N_0 ratio without needing *a priori* knowledge of the navigation data bits. Again, this discussion of the measurement update only describes the correction to the velocity and clock drift states using the carrier frequency discriminator. In a complete receiver implementation, an measurement update would be required to ensure that the position and clock bias states are observable. That update could come in the form of code discriminator (i.e. vector delay locked loop) or as pseudorange residuals (i.e. scalar delay locked loop).

4.3 Frequency Locked Loop Aided Phase Locked Loop

As shown previously in Figure 4.1, the VFLL aided PLL loop filter combines the estimated carrier frequency error from the navigation processor with the phase discriminator to update the NCO in each channel. The first step in closing the vector aided loop is to generate an estimate of the carrier frequency and compare it to the carrier frequency of the NCO to calculate an estimated error. The estimated carrier frequency is calculated using Equation (4.12).

$$\hat{f} = \left(\frac{1 - \frac{\hat{\dot{r}}}{c}}{1 + \frac{\hat{\dot{b}}}{c}}\right) f_{L1} + f_{IF} - f_{L1} \tag{4.12}$$

The carrier frequency error estimate, $\Delta\hat{f}$, is calculated by simply subtracting the current carrier NCO value from the estimated carrier frequency. The filtered carrier frequency discriminator is then used along with the phase discriminator to update the carrier NCO.

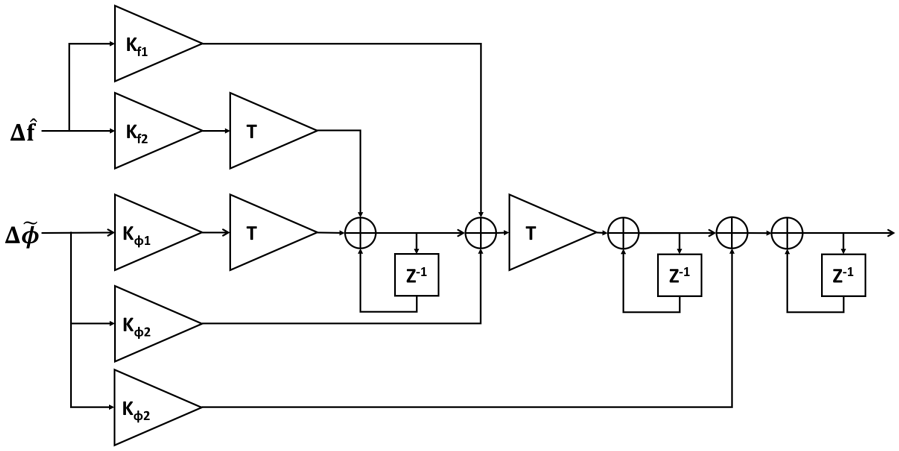

Figure 4.3: Loop filter and NCO integrator of a third order PLL aided by second order FLL with vector processor feedback.

Previously in Section 2.3.3, a second order FLL aided PLL was described, and that loop filter formulation was used to fuse the phase and frequency errors. A block diagram of the modified FLL aided PLL is shown in Figure 4.3. Note that in the figure the frequency discriminator is replaced with the estimated carrier frequency error from the navigation processor.

It is expected that the accuracy of the carrier frequency error estimates from the navigation filter will improve carrier phase tracking robustness when combined with the phase discriminator in the loop filter. The navigation filter provides accurate Doppler frequency estimates which degrade less than the carrier frequency discriminator as the received signal carrier to ratio decreases. To analyze the accuracy of the carrier frequency estimates as a function of decreasing C/N_0 ratio, the steady state performance of the navigation Kalman filter was simulated for varying signal powers. The first simulation was performed assuming that all satellite signals were strong and clear line of sight signals with C/N_0 ratios of 48 dB-Hz. Nine satellites were simulated with the satellite geometry shown in the azimuth and elevation plot shown in Figure 4.4. This geometry was selected to reflect the true satellite locations at the day and time of the simulation.

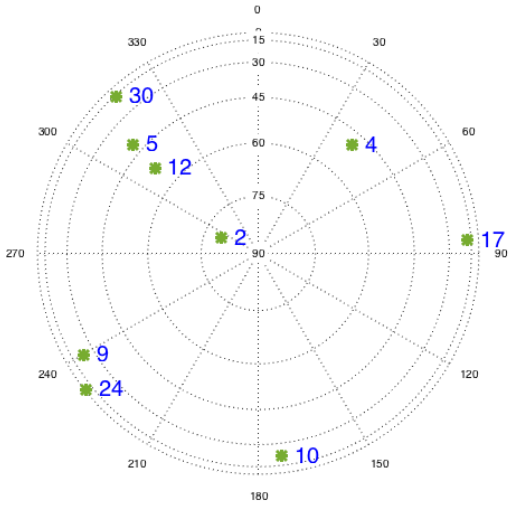

Figure 4.4: Satellite visibility and geometry for the simulation used to compare measurement accuracy for combinations of strong and weak signals.

The Kalman filter time and measurement updates were performed iteratively to update the state covariance estimates. Various dynamic uncertainties were simulated, and the measurement uncertainty was calculated using Equation (4.7). Once the state covariance converged to a steady state value, the variance of the *a posteriori* estimate of the carrier frequency was calculated using Equation (4.13).

$$\sigma_{\delta f}^2 = \frac{H\mathbf{P_{ss}}H^{\mathrm{T}}}{\lambda_{L1}^2} \tag{4.13}$$

The steady state one sigma frequency error for the raw discriminator and the estimated (feedback) frequency error are shown together in Figure 4.5. Both errors are plotted versus the dynamic uncertainty in units of Gs (1G = 9.81 m/s^2). Clearly, the filtered frequency error estimate is significantly more accurate than the raw discriminator, even with a platform dynamic uncertainty of one G in all directions. In this simulation, where all satellite signals are strong, the accuracy improvement is tangible, but the receiver demonstrates no problem maintaining carrier phase or frequency lock with a well designed scalar tracking loop.

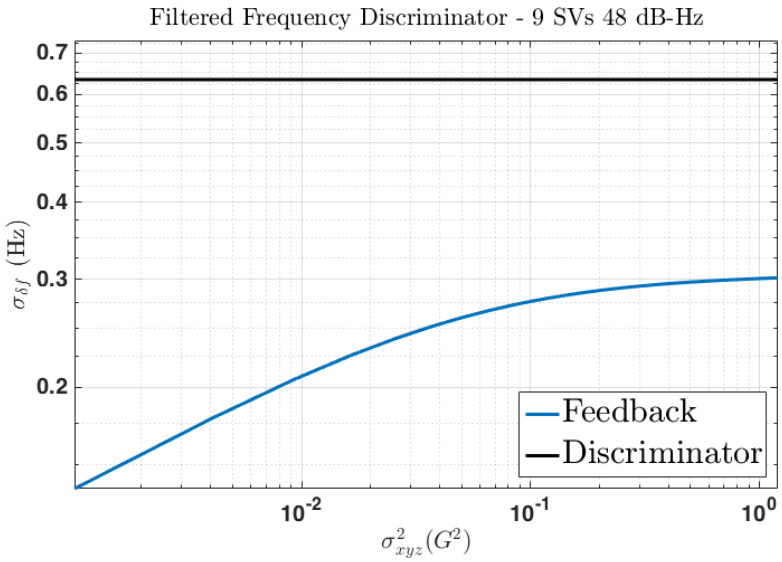

Figure 4.5: Filtered frequency discriminator shows improved accuracy over raw frequency discriminator.

Next, the simulation was repeated several times with the C/N_0 ratio for all satellite signals reduced in each simulation. The results are compiled in Figure 4.6. On the left, the filtered discriminator is shown versus C/N_0 ratio for five different process noise values. As expected, when the unmodeled platform dynamics are low, the Kalman filter provides accurate state estimates results and more accurate carrier frequency estimates. In all cases, the carrier frequency error estimates show improvement over the raw discriminator which is shown on the right. At C/N_0 ratios above 40 dB-Hz the improvement is marginal, but as the C/N_0 ratio drops below 30 dB-Hz the accuracy improvement becomes more significant.

It is important to note that the typical rule of thumb frequency error threshold for frequency lock is approximately 8.33 Hz [32]. Looking at the right plot in Figure 4.6, that threshold would indicate that a scalar FLL would be able to maintain frequency lock down to approximately 25 dB-Hz C/N_0 ratio. The vector tracking receiver using a VFLL to close the carrier frequency loop would be able to maintain frequency at C/N_0 ratios lower than those simulated here. Extrapolating the data in the plot on the left, the filtered discriminator standard deviation would likely exceed the 8.33 Hz threshold between 10 and 15 dB-Hz,

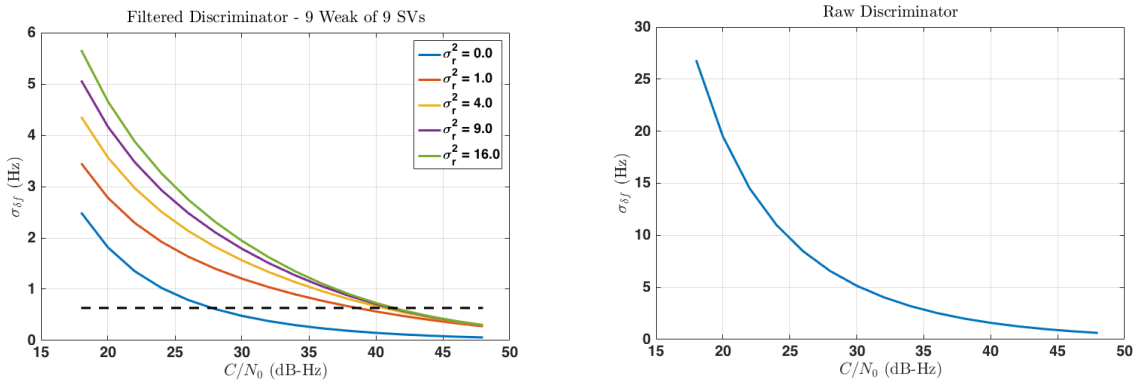

Figure 4.6: As C/N_0 ratio decreases, the filtered discriminator standard deviation increases. Reducing dynamic uncertainty improves filtering. The raw discriminator standard deviation is shown on the right for comparison.

which is consistent with results in [40]. This does not indicate that the vector aided PLL will be able to maintain phase lock at those C/N_0 ratios, but it does indicate that the receiver will likely not need to re-enter the acquisition phase until the C/N_0 ratio falls into this region.

One of the major benefits of the vector tracking receiver is the sharing of signal power across channels. More specifically, the satellite signals that are received with high power provide more accurate range and range rate information. The accuracy of the high power channels improves the accuracy of the navigation solution, and the accuracy of the navigation solution thereby improves the tracking performance. To analyze the accuracy of the estimated carrier frequency error accuracy, the steady state Kalman filter response was simulated again with varying numbers of weak satellite signals. The number of strong satellite signals that are present has a dramatic effect on the accuracy of the carrier frequency information for all channels, strong and weak. The simulation results of the worst combination of strong and weak signals (i.e. 8 of 9 weak signals with 1 of 9 strong signals) are shown in Figure 4.7.

In Figure 4.7, the average carrier frequency error standard deviation of the eight weak signal channels is shown on the left for various process noise tunings. On the right, the standard deviation of carrier frequency estimates for the one strong channel with a constant

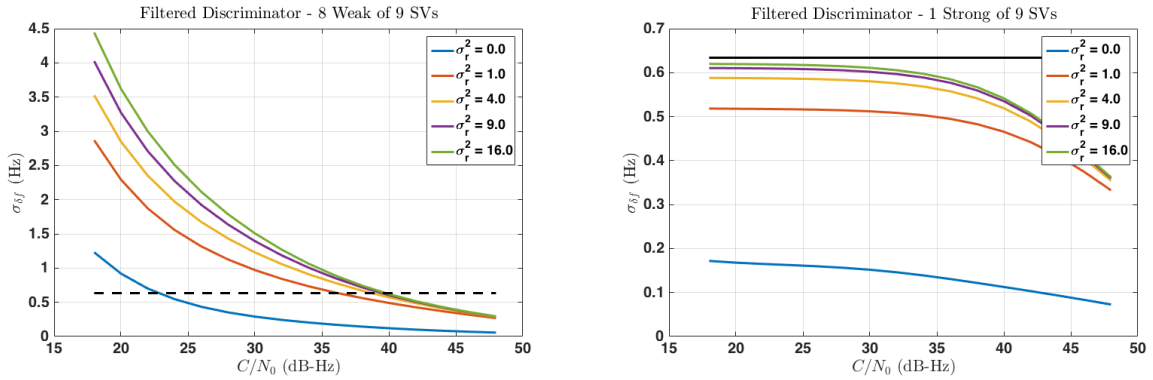

Figure 4.7: Strong signals from other satellites improve the navigation solution and improve the accuracy of the filtered discriminator. Discriminators from strong satellites are not degraded by weak signals when the dynamic uncertainty is bounded.

C/N_0 ratio of 48 dB-Hz is shown as a function of the carrier to ratios of the weak signals. Regardless of the strength of the weak signals or the process noise setting, the standard deviation of the filtered discriminator of the strong channel is lower than the nominal standard deviation of the raw discriminator (shown in black). By comparison to Figure 4.6, the standard deviation of the carrier frequency error estimate of the eight weak channels is improved by the inclusion of one strong satellite.

The navigation Kalman filter is responsible for estimating three coordinates of velocity and the receiver clock drift. Four pseudorange rate observations are required to accurately maintain the filter estimates. Therefore, a significant improvement in the accuracy of the carrier frequency estimates occurs when at least four strong satellite signals are available. In the case where four strong signals are present, the navigation solution may be maintained without information from the weak signals. The weak signal measurements improve the geometric dilution of precision, but the measurements may be removed using a fault detection and exclusion scheme if their inclusion threatens the stability of the filter [22]. The results of the simulation which include 5 of 9 weak signals and 4 of 9 strong signals are shown in Figure 4.8. The standard deviation of the carrier frequency estimates from the weak channels now appear to be bound even as the C/N_0 ratio drops below 20 dB-Hz. In previous simulations

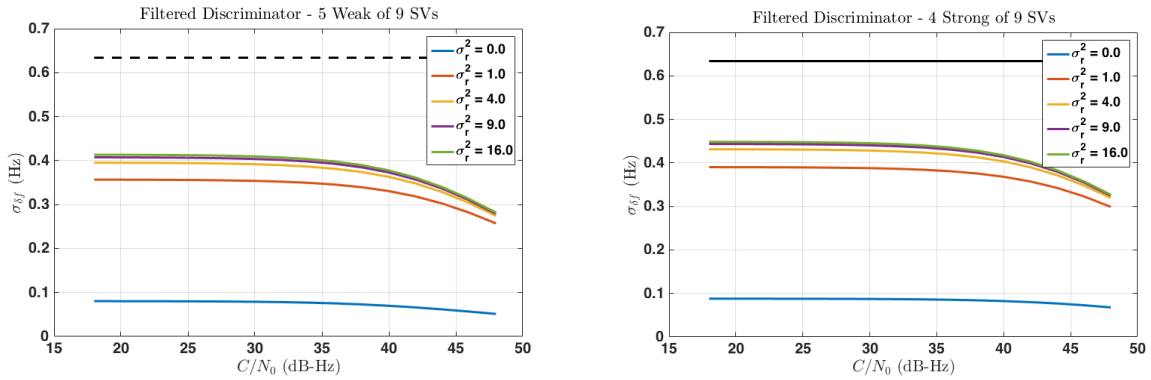

Figure 4.8: Significant improvement in the accuracy of filtered discriminators when four or more strong satellites are present.

where less than four strong signals were present, the standard deviation grew exponentially as the C/N_0 ratio of the weak signal decreased.

Recall that the filter residual is calculated using the frequency discriminator given in Equation (4.6). This discriminator has an effective range of -50 to 50 Hz. If the true frequency error is outside that range, or the discriminator is dominated by noise (a more likely event when four or more strong satellites are available) then the measurement does not provide useful information for updating the navigation filter. In that case, the measurement is likely to be detected as a fault and excluded from the Kalman filter measurement update. For this reason, the simulation does not include extremely inaccurate frequency discriminator measurements that may occur when signals are partially obstructed or reflected.

4.4 VFLL aided PLL Thermal Noise Performance

Figures 4.6 through 4.8 give insight into the accuracy of the carrier frequency feedback information that is used in the vector aided PLL, but do not directly predict the performance of the carrier phase tracking loop. Therefore, to better analyze the carrier phase tracking performance, a simulation environment was developed to evaluate the scalar and vector aided GPS receivers that have been described in this dissertation. The environment uses actual broadcast satellite ephemerides, user specified trajectories, and clock behaviors to simulate

the in-phase and quadrature correlator outputs that are used to drive the code and carrier NCOs. More details on the simulation environment are available in Appendix A.

The simulation environment was used to analyze the thermal noise performance of the VFLL aided PLL algorithm as compared to the traditional scalar tracking PLL which was described in Section 2.3.3. Each simulation included nine visible satellites and included random receiver dynamics based on the dynamic model given in Equation (4.3a) with the standard deviation on the acceleration set to 1 m/s^2. The clock model was simulated using the specification derived for the OCXO in Section 3.5.1. The scalar and vector aided PLL noise equivalent bandwidths were varied from a low of 6 Hz to a high of 18 Hz to cover the expected viable range. The C/N_0 ratio of the received signals ranged from a high of 30 dB-Hz to a low of 26 dB-Hz and were the same across all channels. The next several figures present the results of these simulations.

First, the variance of the carrier phase errors are shown as a function of the noise bandwidth (Bn) and C/N_0 ratio in Figures 4.9 and 4.10. It was expected that the vector aided PLL may be capable of maintaining phase lock at lower noise bandwidth because the VFLL would account for much of the receiver dynamics. However, the clock dynamics still demand a minimum noise bandwidth for the PLL. The effects of cycle slips on the phase error variance have been removed from the data in Figures 4.9 and 4.10 so that the phase jitter threshold comparison gives a reasonable representation of the tracking capability of the two approaches. In analyzing the figures, it appears that the optimal noise bandwidth for both the scalar and vector aided receivers is approximately 12 Hz. This would indicate that the clock dynamics, not the platform dynamics, are the dominant effect in this simulation. For both the scalar and vector aided receiver, the minimum achievable carrier to ratio is approximately 28 dB-Hz. In addition to the receiver clock dynamics, the performance of the VFLL aided PLL is limited by the correlations between the thermal noises of the frequency discriminator and the phase discriminator. The errors in the frequency estimates from the navigation process are then correlated with the errors in the phase discriminator. Both of

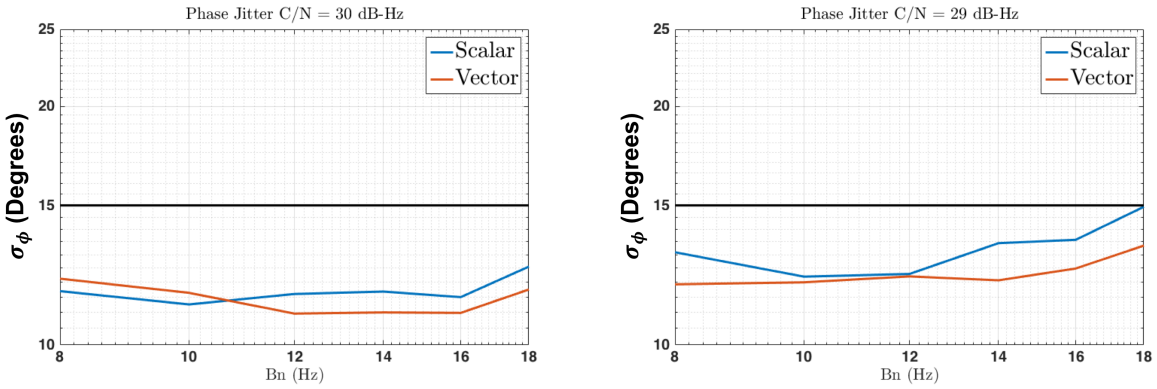

Figure 4.9: Both the scalar and vector aided phase locked loops have similar optimal noise equivalent bandwidth and have some tracking margin at 29-30 dB-Hz C/N_0 ratio.

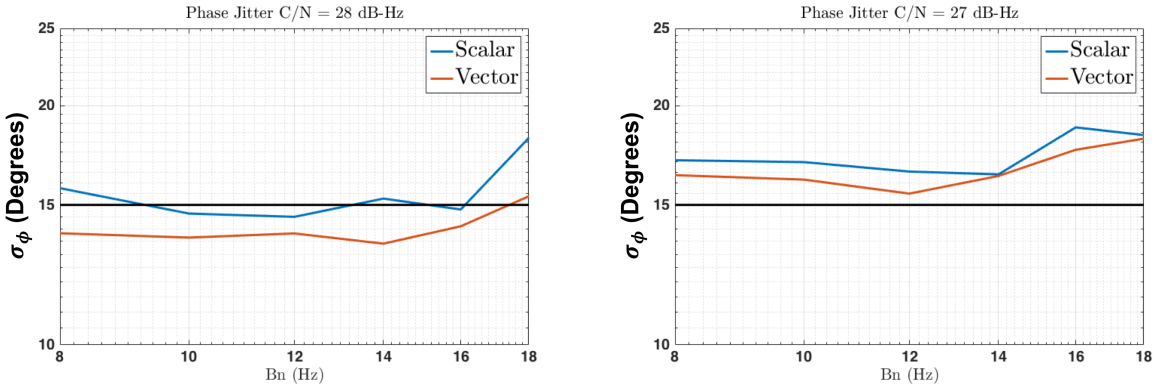

Figure 4.10: For C/N_0 ratios below 28 dB-Hz, both the scalar and vector aided phase locked loop exhibit one sigma phase jitter higher than the allowable threshold.

these are used to update the carrier NCO through the loop filter. Additional simulations were performed assuming that the velocity information used to update the navigation processor was provided by an external source (e.g. IMU), thereby decorrelating the frequency feedback noise from the phase discriminator noise. The results of those simulations are provided in Appendix B.

Despite the similarities seen in Figure 4.9 and 4.10, the VFLL aided PLL did outperform the scalar tracking receiver. As stated above, the effects of cycle slips were neglected in calculating the standard deviation of the phase error. Also, the standard deviations shown in those figures do not include the phase errors for channels that completely lost lock on the

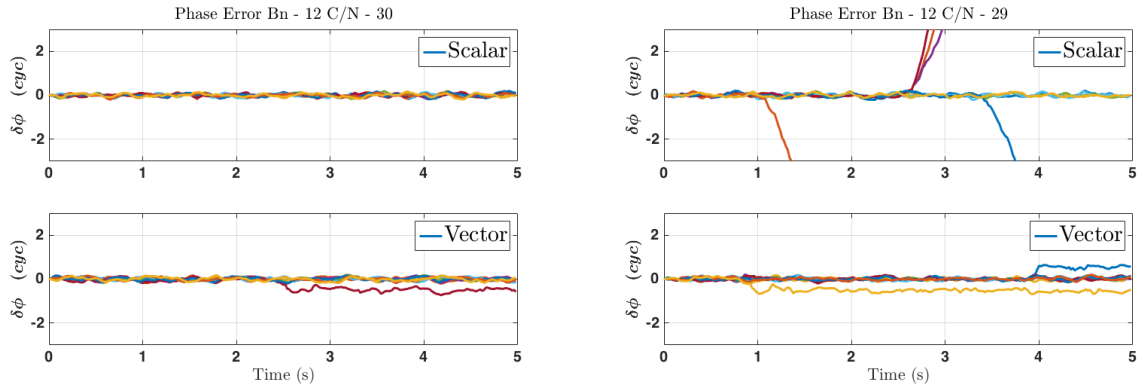

Figure 4.11: The scalar and vector aided phase locked loops typically track the carrier phase at C/N_0 ratios above 29 dB-Hz. The scalar receiver struggles to maintain lock at 29 dB-Hz in this particular simulation.

received phase. The next two figures, 4.11 and 4.12, show the phase error versus time for the scalar and vector aided tracking loops for each channel. The plots show the phase error for nine tracking channels over a period of five seconds. An integration period of 20 ms is used. The noise bandwidth of the phase loop filters for both receivers is set to 12 Hz. The two plots in Figure 4.11 show the results for C/N_0 ratios of 30 (left) and 29 (right) dB-Hz. At a C/N_0 ratio of 30 dB-Hz, both the scalar and vector receivers are able to maintain phase lock with one cycle slip on one channel seen in the vector tracking results. On the right, the scalar tracking receiver begins to loses lock on several channels at 29 dB-Hz. The vector tracking receiver experienced one cycle slip on two channels at 29 dB-Hz.

In Figure 4.12, the C/N_0 ratio of the simulated signal is reduced to 28 (left) and 27 (right) dB-Hz. At 28 dB-Hz the scalar tracking receiver loses lock on four channels and slips one cycle on another channel. The vector tracking receiver slips one cycle on two channels and has two separate cycle slips on another channel. The results for the scalar and vector tracking receivers are similar at 27 dB-Hz. These results show that the scalar tracking receiver does not reliably maintain phase lock for C/N_0 ratios less than approximately 29 dB-Hz. This is comparable to the results presented in [16] with some discrepancy related to the difference in the clock parameters used in the simulation. The vector tracking receiver

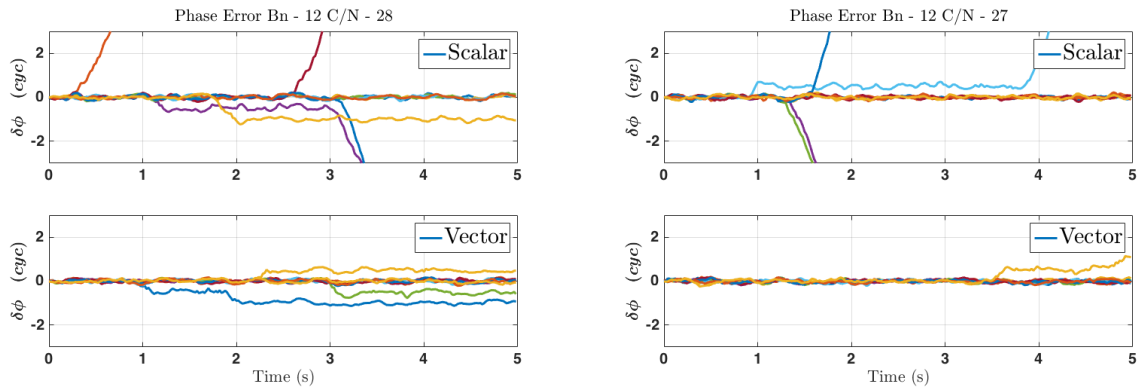

Figure 4.12: The phase errors for the scalar phase locked loop often diverge and would require reacquisition as the C/N_0 ratio approaches 26 dB-Hz. The vector aided phase locked loop exhibits cycle slips but does not completely lose lock.

does occasionally slip cycles on multiple channels, but it does not lose lock completely at these C/N_0 ratios.

The phase error results for the scalar and vector tracking receivers were also analyzed in terms of the time until cycle slip occurred. The time to slip for the scalar and vector tracking receivers for C/N_0 ratios of 28 (left) and 27 (right) dB-Hz are shown versus simulation time in Figure 4.13. The long time to cycle slips occur prior to the first slip on a channel. For the scalar tracking receiver, multiple additional slips happen often after the first slip. In this figure and in the tabulated results, the time to slip was no longer calculated once the total phase error was greater than ten cycles. At that point the channel was assumed to have lost lock.

The time to cycle slip results for the scalar and vector aided tracking algorithms are compiled in Table 4.4. Note that the mean time to slip (MTTS) was only calculated on channels that experienced at least one slip, and that these values are somewhat pessimistic. The comparison between the scalar and vector aided PLL, however, is instructive. It is clear that the vector aiding PLL drastically reduces both the number of cycle slips and the number of channels that lose lock on the carrier over the traditional scalar PLL. While the vector aided PLL does offer improved robustness, even a few cycle slips can be detrimental

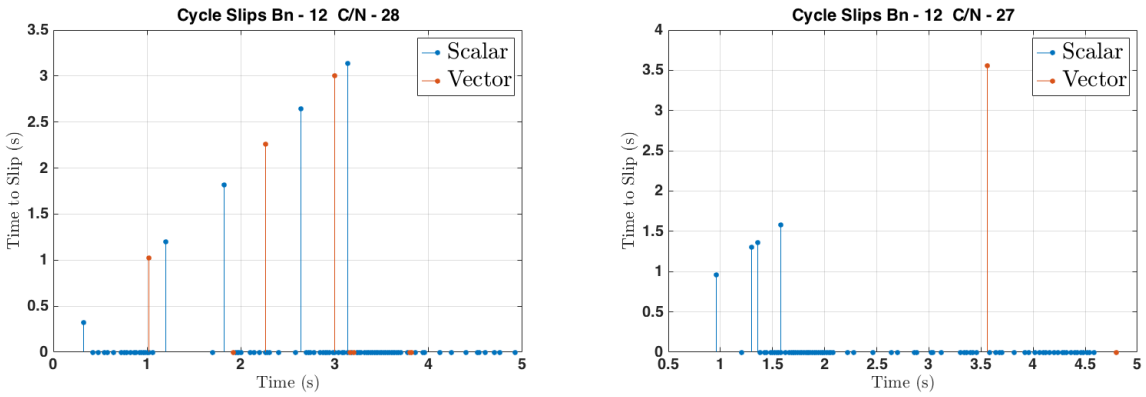

Figure 4.13: The time to cycle slip for the scalar tracking receiver is regularly on the order of one integration period for C/N_0 ratios of 27-28 dB-Hz as the channel loses phase lock. The vector receiver produces periodic cycle slips much less frequently.

Table 4.1: Cycle Slip Comparison of Scalar and Vector Aided PLL

	Scalar			Vector		
$\frac{C}{N_0}$	Number Slips	MTTS	Number Lost	Number Slips	MTTS	Number Lost
30	0	NA	0	3	0.83	0
29	99	0.13	4	4	1.22	0
28	73	0.12	3	8	0.79	0
27	82	0.06	4	2	1.78	0
26	72	0.22	2	17	0.89	0

to high precision carrier phase positioning, which relies on accurate estimation of a constant carrier ambiguity. The VFLL aided PLL is a viable option for improved carrier tracking by a stand alone mobile receiver. In Chapter 6 an alternative tracking approach is introduced that uses data from a static base station to provide high precision position estimation of a mobile rover receiver using a carrier phase vector tracking architecture.

4.5 Stationary Base Station Phase Tracking

GPS receivers are often mounted in specific locations to provide a variety of service. The static base receivers are used for surveying, precise timing, and as differential GPS base stations. Typically a GPS base station is mounted in an environment with a clear line of sight to the sky. In that environment, signal tracking with a traditional scalar tracking

receiver is normally sufficient. However there are scenarios that may limit the availability of accurate carrier phase measurements from the base station that are used in high precision GPS positioning. For example there are factors that may reduce received signal strength including intentional or un-intentional interference and an increase in natural interference as the satellite approaches the horizon. Also, at low latitudes the received signal may be corrupted by ionospheric scintillation as described in Section 3.4.2. In these cases, the tracking performance of the receiver may be improved by incorporating knowledge of the position and velocity of the receiver along with clock state estimates.

Unlike the VFLL aided PLL receiver architecture described above, the position and velocity of the static base station do not have to be estimated in the navigation filter, as those are known quantities for the base station or can be determined over time. Accordingly the navigation Kalman filter for the static base vector tracking receiver need only estimate the clock bias and clock drift state of the receiver. As a result, the discrete dynamic model originally shown in Equation (4.3a) can be reduced to:

$$\mathbf{X}_{k+1} = \Phi_{k,k+1}\mathbf{X}_k + Q_k \tag{4.14a}$$

$$\Phi_{k,k+1} = \begin{bmatrix} 1 & \Delta t \\ 0 & 1 \end{bmatrix} \tag{4.14b}$$

$$Q_{cb} = \begin{bmatrix} \frac{h_2}{2}\Delta t + \frac{2}{3}\pi^2 h_4 \Delta t^3 + 2h_3\Delta t^2 & \pi^2 h_4 \Delta t^2 + 2h_3\Delta t \\ \pi^2 h_4 \Delta t^2 + 2h_3\Delta t & 2\pi^2 h_4 \Delta t + 2h_3 \end{bmatrix} \tag{4.14c}$$

where

$$\mathbf{X} = \begin{bmatrix} \delta cb \\ \dot{\delta cb} \end{bmatrix} \tag{4.15}$$

The residual and Kalman filter measurement updates are calculated in the same manner as in the VFLL aided PLL architecture seen in Equations (4.6) and (4.11). The new architecture is analogous to the VFLL aided PLL receiver with near perfect line of sight

velocity prediction. Satellite ephemerides provide accurate but imperfect satellite velocity estimates. It is expected that the static base vector tracking architecture will improve the receiver tracking performance of degraded GPS signals. To analyzed the performance of the receiver, the thermal noise and ionosphere scintillation tracking performance of the static base vector tracking architecture is evaluated in simulation.

4.5.1 Thermal Noise Performance

The thermal noise performance of the static base vector tracking receiver is analyzed using the correlator simulation tool described in Appendix A. Nine satellites were simulated in each test using the geometry shown previously in Figure 4.4. The receiver position was set to a location on the Auburn University campus and the receiver velocity was set to zero. Receiver clock dynamics were again simulated using the model of the OCXO clock derived in Section 3.5.1. Originally, the simulation covered C/N_0 ratios of 26 dB-Hz to 30 dB-Hz with PLL noise equivalent bandwidths ranging from 4 Hz to 18 Hz. The optimal noise bandwidth was determined and the performance was evaluated for additional C/N_0 ratios.

As in Section 4.4, the standard deviation of the carrier phase errors for the static base vector tracking receiver are plotted as a function of the noise bandwidth of the PLL to determined the optimal noise bandwidth. In Figures 4.14 and 4.15 the carrier phase error standard deviations C/N_0 ratios ranging from 26 dB-Hz to 29 dB-Hz are shown. Clearly the static base vector receiver is easily capable of maintaining phase lock at each of these signal strengths. It also appears that a vector aided PLL with a noise equivalent bandwidth of 6 Hz provides the best performance. 6 Hz is considerably lower than the optimal bandwidth found for the unconstrained (i.e. mobile receiver) VFLL aided PLL architecture (12 Hz). The lower bandwidth allows the static base receiver to reject more thermal noise and maintain phase lock at lower C/N_0 ratios.

As seen in Section 4.4, the tracking performance of the VFLL aided PLL receiver began to degrade significantly at approximately 26 dB-Hz. However, the static base vector receiver

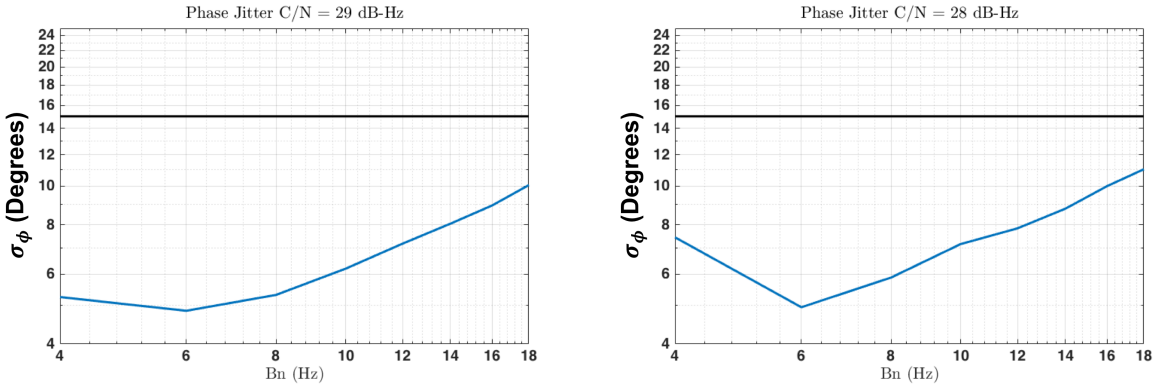

Figure 4.14: The static base vector tracking algorithm has no trouble tracking at 28-29 dB-Hz C/N_0 ratio.

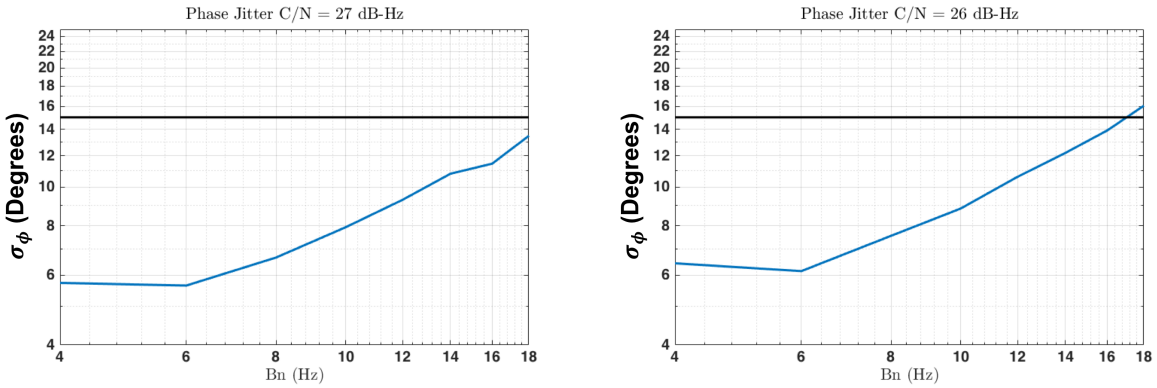

Figure 4.15: For higher noise equivalent bandwidths, the static base vector tracking approach begins to breakdown near 26 dB-Hz.

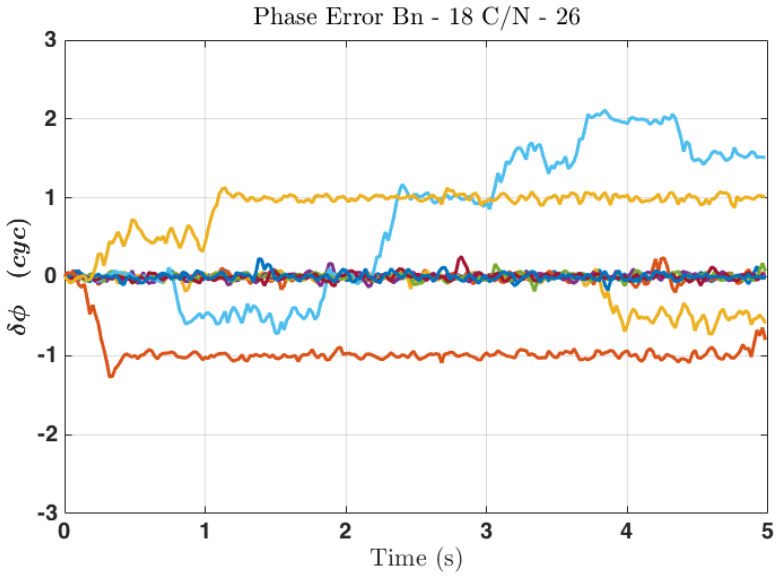

Figure 4.16: Static base vector tracking algorithm exhibits cycle slips at 26 dB-Hz with a noise equivalent bandwidth of 18 Hz.

is capable of tracking well below 26 dB-Hz when the noise bandwidth of the PLL is selected properly. In Figure 4.16, the vector receiver exhibits cycle slips at 26 dB-Hz with a noise bandwidth of 18 Hz. In normal conditions it would be reasonable to set the noise bandwidth considerably lower than 18 Hz, but the signal dynamics introduced by ionospheric scintillation (analyzed in the next section) will limit the PLL bandwidth to higher values. Figure 4.16 shows the lower limits of thermal noise performance for the static base vector tracking receiver with a PLL noise bandwidth of 18 Hz.

As expected, the noise bandwidth of the PLL has a lower bound. At very low bandwidth the PLL is unable to track the signal dynamics due to satellite motion and clock dynamics not captured by the navigation processor. The phase error for the static base receiver using a 4 Hz noise bandwidth with a signal strength of 28 dB-Hz is shown in Figure 4.17. The phase error is clearly not zero mean.

A PLL noise bandwidth of 6 Hz resulted in the best thermal noise performance of the static base vector tracking receiver. Since the receiver tracked successfully at 26 dB-Hz without cycle slips, the simulation was extended to lower C/N_0 ratios. Figure 4.18 shows

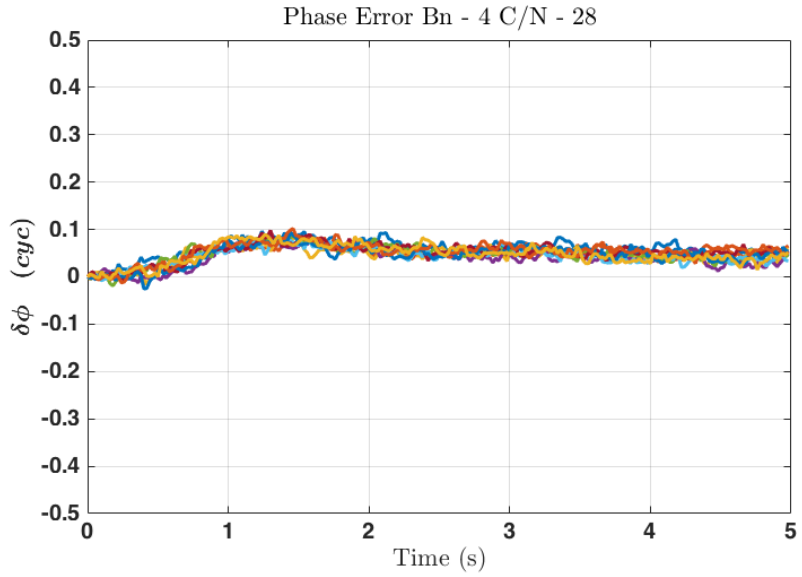

Figure 4.17: Static base vector tracking algorithm does not provide zero mean phase error when a loop noise bandwidth of 4 Hz is used.

the C/N_0 ratios where the static base vector tracking receiver begins to exhibit cycle slips. At a C/N_0 ratio of 18 Hz (plot on the left) the receiver slips one cycle on one channel. There are two cycle slips shown in the right plot were the simulated C/N_0 was 17 dB-Hz. This is almost 10 dB lower than the C/N_0 ratios tracked by the VFLL aided PLL. Some of this improvement can be attributed to the lack of receiver dynamics in this scenario in addition to the improvement in the line of sight velocity prediction.

Figure 4.19 shows the simulations where the receiver was unable to maintain phase lock. For C/N_0 ratios below 13 dB-Hz the carrier phase errors begin to drift without clear cycle slipping. With the signal power this low, the phase discriminator is no longer providing useful phase error information so the frequency aiding is primarily driving the tracking loop. The navigation processor does not have carrier phase error information since the frequency discriminator is used in the update step. As a result, the phase error grows slowly without correction.

There were few cycle slips for the static base receiver for C/N_0 ratios above 15 dB-Hz (there were no slips at 16 or 17 dB-Hz). The number of cycle slips for lower C/N_0 ratios are

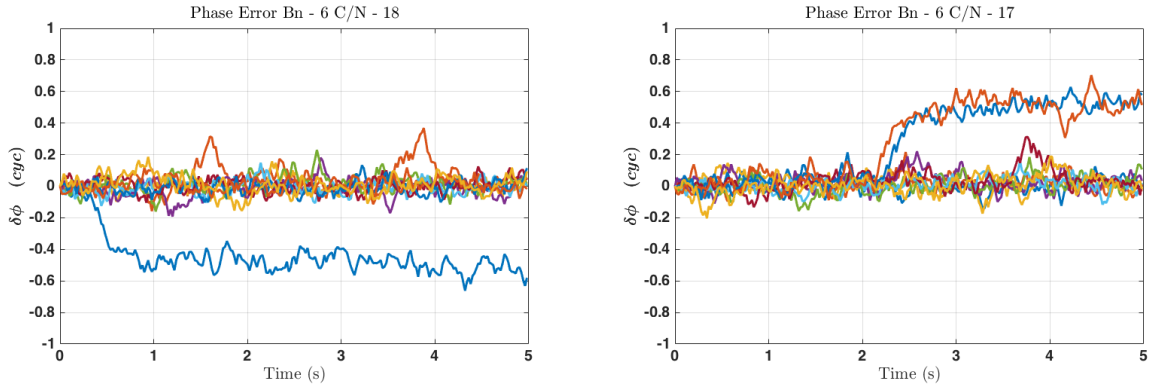

Figure 4.18: The static base vector tracking algorithm using a noise equivalent bandwidth of 6Hz exhibits minor cycle slips beginning at a C/N_0 ratio of 18 dB-Hz.

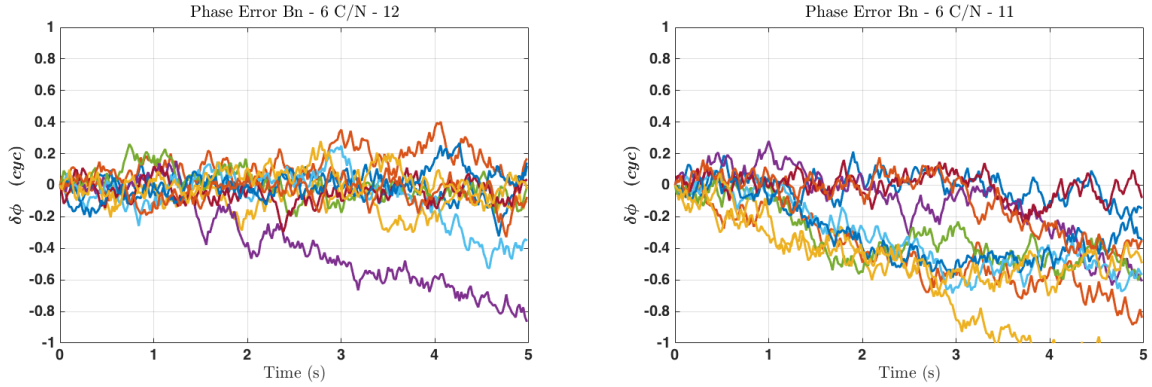

Figure 4.19: The static base vector tracking algorithm is no longer capable of maintaining phase lock as the received signal strength drops below 13 dB-Hz.

Table 4.2: Cycle Slip Analysis Static Base Vector Aided PLL

	Static Base		
$\frac{C}{N_0}$	Number Slips	MTTS (sec)	Number Lost
15	3	3.22	0
14	57	0.18	0
13	34	0.32	0
12	63	0.42	0
11	77	0.18	0

tabulated in Table 4.5.1. There were no scenarios where the phase error exceeded the 10 cycle threshold that has been used to indicate loss of lock. However, there is a significant decrease in the mean time to slip for the simulations of C/N_0 ratios below 15 dB-Hz. Based on this simulation, it is concluded that the static base vector tracking receiver reliably maintains phase lock down to 15 dB-Hz C/N_0.

4.5.2 Ionospheric Scintillation Performance

Real Time Kinematic (RTK) positioning requires consistent carrier phase tracking by the base station and the rover receiver. In certain regions, particularly at high and low latitude, ionospheric conditions can cause signal variations that disrupt carrier phase tracking on the ground. Scintillation results in rapid fluctuations in signal strength and in several cases can cause rapid changes to the phase of the receiver signal. In Section 3.4.2 the characteristics of amplitude and phase scintillation and a procedure for simulating scintillation as a function of S4 index and decorrelation time was described. The phase tracking performance of the static base vector receiver during mild, moderate, and strong scintillation is evaluated using the correlator simulator and the scintillation simulation procedure described in that section.

Due to the rapid phase changes caused by ionospheric scintillation, the 6 Hz PLL noise bandwidth used in the previous section does not provide the dynamic response needed to maintain phase lock. Several noise bandwidths were tested with strong and moderate scintillation and a noise bandwidth of 18 Hz provided the most consistent tracking performance. In the next several figures, the noise bandwidth of the static base vector aided PLL and of

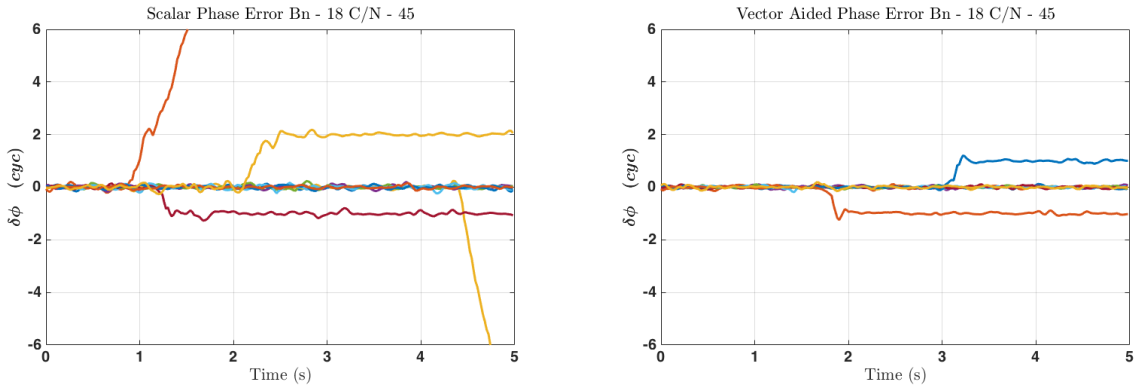

Figure 4.20: In **moderate** ionospheric scintillation, the scalar tracking PLL slips cycles and occasionally loses lock completely. The static base vector tracking receiver exhibits fewer slips and never loses lock.

the scalar tracking PLL (used for comparison) is set to 18 Hz. Three scintillation scenarios were simulated: mild scintillation (S4 = 0.5, tau = 1.0), moderate scintillation (S4 = 0.7, tau = 0.4), and strong scintillation (S4 = 0.9, tau = 0.2). The nomimal C/N_0 ratio for each satellite was set to 45 dB-Hz to represent normal signal conditions that are corrupted by scintillation only. Twenty Monte Carlo simulations of each scenario were performed with the receiver tracking nine satellites (all affected by scintillation) in each simulation.

The phase error results of one simulation of the moderate and strong scintillation cases are shown in Figures 4.20 and 4.21. In each figure, the plot on the left shows the phase error results for the scalar PLL and the plot on the right shows the static base vector tracking results. As seen in Figure 4.20 the moderate ionospheric scintillation causes several cycle slips in the scalar tracking receiver and two cycle slips in the vector receiver in this test. Two of the channels of the scalar receiver completely lose phase lock on the received signal while only single slips occur in the vector receiver.

Strong scintillation is more detrimental to carrier phase tracking. In strong scintillation, the scalar phase locked loop was not able to maintain lock on any channel. In Figure 4.21, the scalar receiver loses lock on all nine channels within one second. The static base vector receiver slips up to four cycles on any one channel, and experiences regular slips. However,

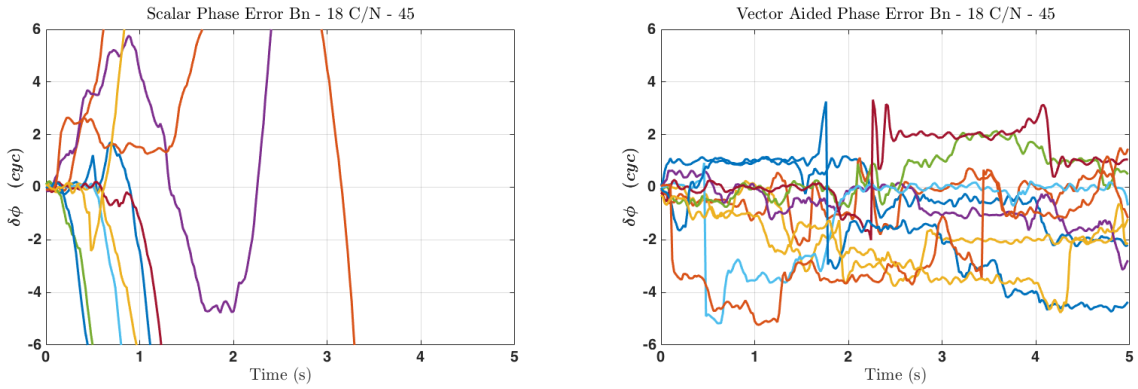

Figure 4.21: In **strong** ionospheric scintillation, the scalar tracking PLL loses lock completely on all satellites. The static base vector tracking receiver exhibits frequent cycles slips and never loses lock.

the vector receiver would not have to reenter the acquisition phase after the scintillation event subsided.

The statistical results of the scintillation study are given in Table 4.5.2. Both the scalar and static base vector receivers were able to maintain phase lock on all channels without cycle slips in mild ionospheric scintillation. The moderate scintillation caused a total of 53 cycle slips in the twenty simulations of the scalar tracking receiver. Those slips caused total loss of lock on an average of 2.3 channels per simulation. The static base vector receiver only experienced 6 total cycle slips in moderate scintillation. In strong scintillation, the scalar tracking receiver lost lock completely on all channels on all simulations. The number of slips were accumulated until the receiver reached ten cycles of total error. As a result, the number of slips for the scalar receiver is lower than the vector receiver for the strong scintillation simulations. However, the vector receiver does not reach ten cycles of error on any channel throughout the simulation.

4.6 Conclusion

A vector aided phase lock loop architecture for improved carrier phase tracking in low C/N_0 ratios and in ionospheric scintillation environment is described in this chapter. The

Table 4.3: Scintillation Induced Cycle Slip Comparison of Scalar and Static Base Vector Receiver

	Scalar			Static Base		
Scintillation	Number Slips	MTTS	Number Lost	Number Slips	MTTS	Number Lost
Mild	0	NA	0	0	NA	0
Moderate	53	0.14	2.3	6	0.6	0
Strong	268	0.01	10	336	0.02	0

vector receiver may be implemented on a standalone mobile receiver, on an IMU aided mobile receiver, or a static base station. The performances of the mobile receiver and the static base receiver are analyzed in simulation using a correlator simulator developed for this study. The thermal noise performance in low C/N_0 environments is investigated as is the performance of the static base vector receiver in ionospheric scintillation. The performance of the vector aided phase lock loop is dependent on the accuracy of the platform velocity estimates, and therefore the static base vector receiver is the most effective implementation discussed in this chapter. This VFLL aided PLL architecture does provide improved performance over the traditional scalar tracking receiver (particularly in loss of lock performance), but the VFLL aided PLL does exhibit numerous cycle slips in low C/N_0 simulations. These cycle slips cause changes to the carrier phase ambiguity that must be estimated as part of a RTK GPS position solution. Accordingly, a new RTK vector phase lock loop is developed in Chapter 6 to take advantage of the improved tracking capability of the static base vector receiver.

Chapter 5

Carrier Phase Differential GPS Positioning

Standalone GPS receivers use the pseudorange measurements from four or more satellites to estimate three dimensional position and receiver clock error. The pseudorange measurement is derived from the local replica of the code tracking loop which has an accuracy of approximately one to two percent of a chip, which translates to approximately 3 m. The received signal is also corrupted by atmospheric effects, satellite and receiver clock errors, multipath signals, and noise. Based on the accuracy of the pseudorange measurement, the position estimates are typically accurate to within one to two meters horizontally and a few meters vertically. In some applications, like automated vehicle navigation, these levels of errors can be unacceptable.

A common approach to reduce the effects of atmospheric error and satellite clock errors on position accuracy is to compare the receiver measurements to measurements from a static base receiver at a known location. The differential GPS concept is illustrated in Figure 5.1. The base station receiver is mounted at a known location near the area (within several kilometers) where the rover receiver is to operate. As depicted in the figure, the base receiver is mounted on a structure with a clear view of the sky and the rover receiver is mounted on a vehicle. The atmospheric corruption of the received signal from a common satellite is highly correlated for the rover and base receiver. Using the pseudorange measurements from the rover and base receivers, the position of the rover relative to the position of the base can be estimated more accurately (typically one order of magnitude) than the global position estimates of the standalone receiver. The relative position solution is then added to the known location of the base antenna to calculate the differential pseudorange position solution.

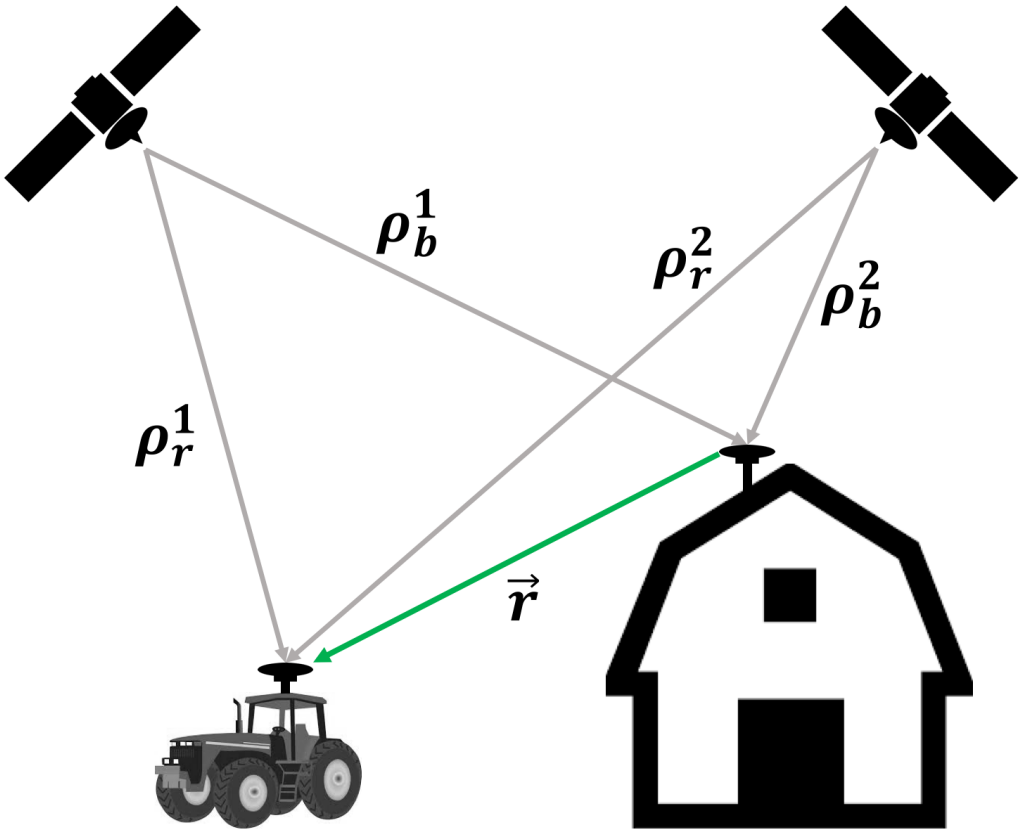

Figure 5.1: Differential GPS positioning uses pseudorange or carrier phase measurements from common satellites to reduce common mode errors and improve positioning accuracy.

The carrier phase replica, like the code replica, is accurate to approximately 1 - 2 % of a wavelength. For the GPS L1 signal that translates to an accuracy of 2 - 4 mm. The receiver carrier phase is corrupted by the same environmental and temporal effects as the CA code. Additionally, the carrier phase measurement is a function of the range from satellite to receiver, but as described in Chapter 2, the carrier phase measurement contains an ambiguous integer number of cycles that prevents it from being used directly as a range measurement.

The real time kinematic (RTK) GPS position solution is a differential GPS solution based on the carrier phase measurement. The RTK algorithm is a three step procedure for estimating the position of the rover receiver. First, the relative carrier phase ambiguities between the rover and base measurements are estimated as decimal numbers. Then, the decimal estimates of the ambiguities are intelligently rounded to integer values. Finally, the high precision relative position vector from the base station to the rover is calculated using the integer ambiguities. RTK GPS using commercial GPS receivers is well documented in the literature [10,43,58,67]. However, limited information is available on implementing RTK algorithms with software GPS receivers. In this dissertation, a detailed description of a software receiver based implementation of the RTK positioning is outlined. The accuracy of the software receiver positions is compared to a reference RTK solution using COTS survey grade hardware.

5.1 Software Receiver Carrier Phase and Pseudorange Measurements

The accuracy of the RTK solution is derived from the accuracy of the pseudorange and carrier phase measurements of the receiver. It is important that the measurements from the rover receiver and base station are taken synchronously to ensure that the satellite geometry, clock errors, and atmospheric effects are common to each receiver. Time synchronization and measurement generation algorithms used in the software receiver are discussed in this section.

5.1.1 Time Synchronized Measurements

Typically the measurements for an RTK positioning algorithm are updated on the order of 1 to 5 Hz. To synchronize measurements across receivers, each receiver will synchronize the measurements to whole GPS seconds. In the software receiver, time is propagated by counting samples from the front end. The front end attempts to sample the received signal at a nominal rate but differs slightly, resulting in the receiver clock bias and drift discussed throughout this dissertation. This clock error must be accounted for when synchronizing the measurement updates to GPS time. The synchronization procedure begins with the first GPS position solution.

As stated in Chapter 2, once the navigation data message has been decoded, the first set of pseudoranges are computed using a default value for the range to the nearest satellite. This default value sets the initial receiver time for the sample at which the initial position is calculated. When calculating the position solution using the initial pseudorange measurements, the error in the initial receiver time is estimated in the form of the initial clock bias estimate. The GPS time for that initial sample is then calculated using Equation (5.1)

$$t_{gps} = t_r - \frac{\hat{cb}}{c} \tag{5.1}$$

where t_r is the initial receiver time, $\hat{cb}$ is the clock bias estimate in meters, and c is the speed of light.

Once the GPS time of the initial position sample is calculated, the time of the next measurement is calculated as a function of the desired measurement update rate. The algorithm for calculating the desired time, t_n, of the next measurement is given by Equation (5.2)

$$t_n = t_{gps} + \alpha - \text{mod}(t_{gps}, \alpha) + \alpha(\text{round}(\text{mod}(t_{gps}, \alpha)/\alpha)) \tag{5.2}$$

where α is the desired update rate in seconds and mod returns the remainder after division. The sample that occurs closest to that time is predicted as a function of the estimated clock

drift from the navigation solution. The sample of the next update, S_n, is calculated by Equation (5.3)

$$S_n = \text{round}(S_c + f_s(t_n - t_{gps})(1 - \hat{\dot{cb}}/c)) \tag{5.3}$$

where S_c is the current sample count, f_s is the nominal sampling frequency of the front end, and $\hat{\dot{cb}}$ is the estimated clock drift.

It is important to note that the accuracy of the time synchronization is dependent on the accuracy of the clock bias and clock drift estimates. The clock bias estimates of a pseudorange based least squares solution are rather noisy as is the clock drift estimated using Doppler measurements. To improve the clock bias and drift estimate, an eight state Kalman filter is implemented to estimate position, velocity, clock bias, and clock drift. The Kalman filter is similar to the implementation described in Chapter 4, except the measurement update leverages the accuracy of the carrier phase measurements. The filter residuals are calculated using the pseudorange measurements and the differential carrier phase measurement given previously in Equation (2.20). The carrier phase measurement is significantly less noisy than the Doppler measurement, resulting in more accurate clock drift estimates. Since the drift estimates are used to propagate the bias estimates in the Kalman filter, the noise on the bias estimates is also significantly improved. Figure 5.2 shows the improved clock bias and drift estimates from the Kalman filter navigation solution over the least squares solution with pseudorange and Doppler measurements. The bias estimates are shown on the left with the Kalman filter results shown in orange.

The sampling frequency of the GPS front end determines the maximum residual timing error between the desired measurement time and the true measurement time. Depending on the drift rate of the oscillator, the offset between the desired GPS second and the closest sample will vary between $\pm\frac{1}{2f_s}$. The data shown in Figure 5.2 was calculated from IF samples taken with a GPS front end using a sampling frequency of 10 MHz. Assuming the optimal sample was selected for each measurement update, the residual time error should fall between $\pm 50ns$. The GPS time of each measurement update was calculated, and the error relative

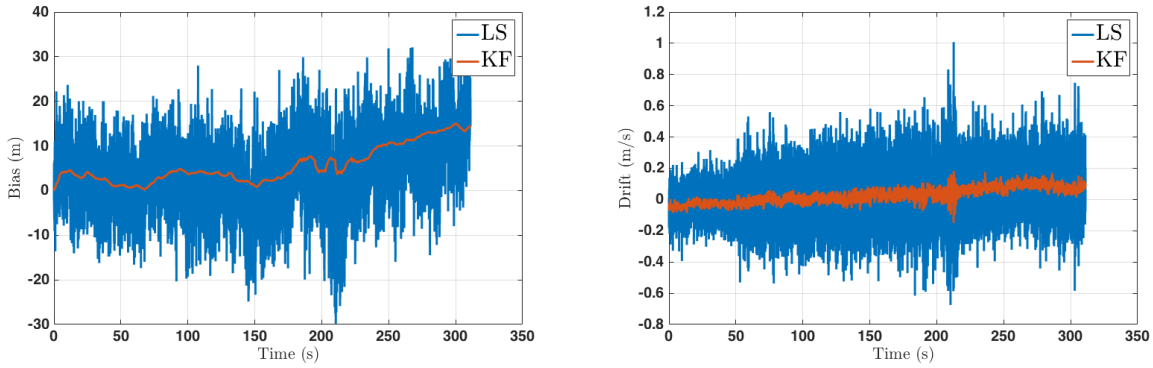

Figure 5.2: The Kalman filter using the differential carrier phase measurements signficantly improves the clock bias and drift estimates.

to the desired update time is plotted in Figure 5.3. Clearly, the residual time error is within the expected limits. This error does not represent the true time error but does indicate that the correct sample was selected based on the information available to the receiver.

5.1.2 Carrier Phase and Pseudorange Measurement Generation

At each measurement update, the receiver generates pseudorange and carrier phase measurements based on the local replicas of the code and carrier phase. The code tracking loop of the software receiver when operating in scalar tracking mode is a modified version of the DLL described in Chapter 2. The Doppler effect on the received code phase is proportional to the Doppler of the carrier frequency. This allows the carrier tracking loop to aid the DLL and greatly reduce the code phase noise, resulting in less noisy pseudorange measurements. The implementation is similar to the vector aided PLL described in later Chapter 6, except that the Doppler aiding from the carrier loop is applied directly. The bandwidth of the DLL is then set high enough that the dynamics of the residual code phase error are easily tracked ($1/2Hz$ is this dissertation).

The pseudorange measurements at each measurement update are calculated by comparing the receiver time from the sample counter to the transmit time of the signal calculated from the decoded navigation message. The pseudorange calculation is given by Equation

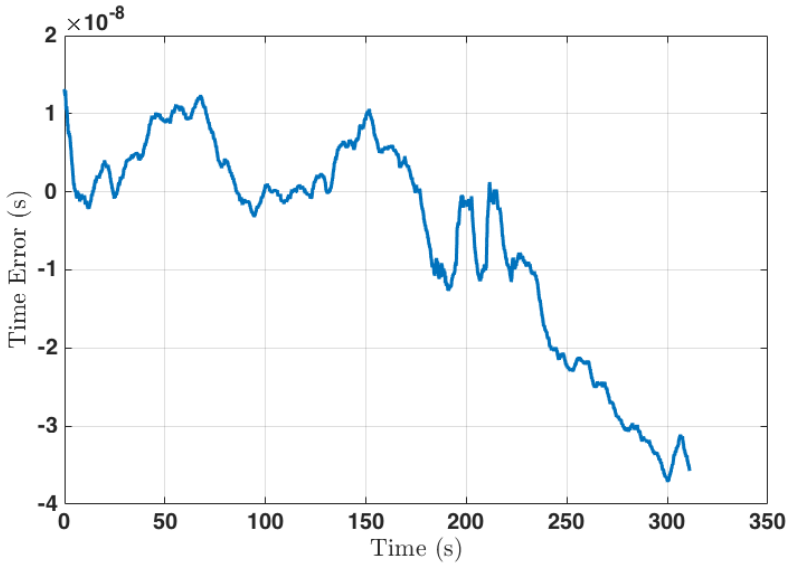

Figure 5.3: The residual time error indicates that the correct sample for the measurement update was selected.

(5.4).

$$\rho^1 = (t_r - t_t^1)c \tag{5.4}$$

The transmit time, t_t, is calculated using Equation (5.5)

$$t_t^1 = t_{tow}^1 + 0.001N_{CA}^1 + \frac{f_c^1 * N_s}{f_{CA}} \tag{5.5}$$

where t_{tow} is the time of week calculated from the decoded navigation message, N_{CA} is the number of code periods that have elapsed since the time of week calculation, f_c is current code NCO frequency, f_{CA} is the chipping rate of the GPS CA code, and N_s is the number of samples into the current integration period.

There is a thorough description of the carrier phase measurement generation in Chapter 2. Equation (5.6) is repeated here as a reminder of the key concepts of carrier phase positioning.

$$\phi^1 = \phi_{NCO} + N_{t,t_s} - f_{IF}(t - t_s) - f_{IF}(t_s - t_0) + \phi_{halfcycle} \tag{5.6}$$

The phase advance due to the IF mixer in the GPS front end (i.e. the third and fourth terms in Equation (5.6)) must reference the same initial time t_0 on all channels. This will ensure that the clock bias term is the same for all channels when the carrier phase measurements are used for positioning. The clock bias term may then be estimated using four or more measurements, or may be removed by computing the double difference observable that is discussed in the next section.

5.1.3 RTK Measurement Models

The RTK positioning algorithm relies on the pseudorange and carrier phase measurements from rover and base receivers. Each measurement is a function of the range from satellite to receiver, but is corrupted by atmospheric delays, clock errors, multipath, and noise. The mathematical models for the pseudorange and carrier phase measurements used to develop the software receiver single difference RTK algorithm are given in Equation (5.7a) and Equation (5.7b), respectively.

$$\rho^1 = r_u^1 + I_u^1 + T_u^1 + M_u^1 + ct_u + ct^1 + \eta_{\rho^1} \tag{5.7a}$$

$$\phi^1 = \frac{1}{\lambda}(r_u^1 - I_u^1 + T_u^1 + M_u^1 + ct_u + ct^1) + N_u^1 + \eta_{\phi^1} \tag{5.7b}$$

In the above equation the superscripts are used to designate the transmitting satellite and the subscripts designate the receiver. The ionosphere, troposphere, and multipath delays are represented by I, T, and M, respectively, and the satellite and receiver clock error are labeled with the appropriate script. Note that the carrier phase measurement is represented in units of cycles in Equation (5.7b), and that the carrier ambiguity N must be an integer value. The similarities in the two models allude to the principle behind the RTK algorithm. The difference between the pseudorange and carrier phase measurement is a good predictor of the carrier ambiguity with the exception of the noise and ionospheric delays.

5.2 Real Time Kinematic Positioning

As stated in the introduction to this chapter, the RTK algorithm is a three step procedure for estimating the high precision relative position vector (RPV) from base to rover antenna. The first step of the algorithm is to estimate the carrier ambiguities as decimal values. A Kalman filter is used to iteratively estimate the ambiguities along with the relative position vector and clock bias. The pseudorange and carrier phase measurements from rover and base are combined to perform the measurement update of the Kalman filter. The Kalman filter mean and covariance of the carrier ambiguities are then used to intelligently round the decimal estimate to integer values using an algorithm called the Least-squares Ambiguity Decorrelation Adjustment (LAMBDA) method. Finally, the high precision RPV is calculated using the integer value ambiguities and the carrier phase measurements from the two receivers.

5.2.1 Kalman Filter Ambiguity Estimation

The Kalman filter state vector, shown in Equation (5.8), includes the three dimensional RPV, the relative velocity, which is the rover velocity in the case of the static base station,

and relative clock bias and drift terms.

$$\mathbf{X} = \begin{bmatrix} \delta x_{r,b} \\ \delta \dot{x}_{r,b} \\ \delta y_{r,b} \\ \delta \dot{y}_{r,b} \\ \delta z_{r,b} \\ \delta \dot{z}_{r,b} \\ \delta cb_{r,b} \\ \delta \dot{cb}_{r,b} \\ N^1_{r,b} \\ \vdots \\ N^m_{r,b} \end{bmatrix} \tag{5.8}$$

In Equation (5.8) the pose and clock states are error states. The state vector also contains a carrier ambiguity for each satellite that is tracked by both the rover and the base receivers. The subscript r, b is used to denote that each state represents a difference between the global state of the rover and base (i.e. $x_{r,b} = x_r - x_b$ where x_r is the ECEF x coordinate of the position of the rover).

The state transition matrix is derived in the same manner as the state transition matrix used to estimate the standalone receiver position in Chapter 4. The dynamic model used in the Kalman filter time update is given in Equation (5.9).

$$\mathbf{X}_{k+1} = \Phi_{k,k+1}\mathbf{X}_k + Q_k \tag{5.9a}$$

$$\Phi_{k,k+1} = \begin{bmatrix} \alpha_k & 0_{2x2} & 0_{2x2} & 0_{2x2} & 0_{2xm} \\ 0_{2x2} & \alpha_k & 0_{2x2} & 0_{2x2} & 0_{2xm} \\ 0_{2x2} & 0_{2x2} & \alpha_k & 0_{2x2} & 0_{2xm} \\ 0_{2x2} & 0_{2x2} & 0_{2x2} & \alpha_k & 0_{2xm} \\ 0_{mx2} & 0_{mx2} & 0_{mx2} & 0_{mx2} & I_{2xm} \end{bmatrix} \tag{5.9b}$$

$$\alpha_k = \begin{bmatrix} 1 & \Delta t \\ 0 & 1 \end{bmatrix} \tag{5.9c}$$

$$Q_k = \begin{bmatrix} Q_x & 0_{2x2} & 0_{2x2} & 0_{2x2} & 0_{2xm} \\ 0_{2x2} & Q_y & 0_{2x2} & 0_{2x2} & 0_{2xm} \\ 0_{2x2} & 0_{2x2} & Q_z & 0_{2x2} & 0_{2xm} \\ 0_{2x2} & 0_{2x2} & 0_{2x2} & 2Q_{cb} & 0_{2xm} \\ 0_{mx2} & 0_{mx2} & 0_{mx2} & 0_{mx2} & Q_{N_{r,b}} \end{bmatrix} \tag{5.9d}$$

The kinematic relationship between the states are used to construct the discrete dynamic matrix (Equation (5.9a)), and the unmodeled acceleration of the rover is assumed to be zero mean with variance $\sigma^2_{x,y,z}$ (Equation (5.9c)). Also note in Equation (5.9c) that the clock model process noise is multiplied by two which assumes both receivers use clocks with the same model parameters and the stochastic components are uncorrelated. The term $Q_{N_{r.b}}$ in Equation (5.9d) is used to ensure that the ambiguity update continues to be corrected with the latest measurements. Without increased uncertainty in the time update, the variance estimates for the ambiguity states would converge to a low value, and the correction to the ambiguities from the latest measurements would approach zero.

5.2.2 Single Difference Measurements

The measurement models of the pseudorange and carrier phase measurements given in Equations (5.4) and (5.7b) show the similarity in the measurements. While the pseudorange is a noisier measurement, it can be used to approximate the carrier ambiguity when

accounting for the ionospheric error. To mitigate the ionosphere error, the single difference pseudorange and carrier phase observable is used to update the Kalman filter. The models of the single difference pseudorange and carrier phase measurements are given in Equation (5.10a) and Equation (5.10b), respectively.

$$\Delta\rho^i_{r,b} = r^i_{r,b} + ct_{r,b} + \eta_{\rho^i_{r,b}} \tag{5.10a}$$

$$\Delta\phi^i_{r,b} = \frac{1}{\lambda}(r^i_{r,b} + ct_{r,b}) + N^i_{r,b} + \eta_{\phi^i_{r,b}} \tag{5.10b}$$

Equations (5.10a) and (5.10b) assume that the residual atmospheric error after subtraction is small relative to the noise. The difference in multipath error and the satellite clock error is also assumed to be small. Now it can be seen that the difference between single difference pseudorange and single difference carrier phase is a good predictor of the carrier ambiguity when the measurements are expressed in common units.

The residuals for the Kalman filter measurement updates are computed by subtracting the predicted single difference pseudorange and carrier phase from the measurements. The predicted single differences are calculated as a function of the current best estimates of the states using Equation (5.11).

$$\begin{bmatrix} \Delta\hat{\rho}^i_{r,b} \\ \lambda\Delta\hat{\phi}^i_{r,b} \end{bmatrix} = \begin{bmatrix} a^i_x & a^i_y & a^i_z & -1 & 0_{1xm} \\ a^i_x & a^i_y & a^i_z & -1 & \lambda I_{1xm} \end{bmatrix} \begin{bmatrix} x_{r,b} \\ y_{r,b} \\ z_{r,b} \\ cb_{r,b} \\ N^1_{r,b} \\ \vdots \\ N^m_{r,b} \end{bmatrix} \tag{5.11}$$

In Equation (5.11), a^i_x, a^i_y, and a^i_z are the unit vector components point from the base receiver to the *ith* satellite. This formulation assumes that the unit vectors from the base

receiver to satellite i are equal to the unit vectors from the rover receiver to satellite i. This assumption is reasonable for the maximum baseline distance of 2 km (which is needed to minimize atmospheric errors).

The measurement matrix used in the update step of the Kalman filter is derived by differentiating Equation (5.11) with respect to the state vector. The measurement matrix is given by Equation (5.12).

$$H = \begin{bmatrix} a_x^i & 0 & a_y^i & 0 & a_z^i & 0 & -1 & 0 & 0 \\ a_x^i & 0 & a_y^i & 0 & a_z^i & 0 & -1 & 0 & \lambda I_{1xm} \end{bmatrix} \tag{5.12}$$

To complete the measurement update, the measurement noise matrix, R, is needed. The measurements are a combination of the pseudorange and carrier phase measurements from the rover and base receivers. Those measurements are derived from the code and carrier tracking loops, respectively, and therefore the measurement uncertainty is a function of the thermal noise of tracking loops, assuming all other errors are small. The measurement noise matrix is given by Equation (5.13)

$$R = \begin{bmatrix} \sigma_{r_{DLL}}^2 + \sigma_{b_{DLL}}^2 & 0 \\ 0 & \sigma_{r_{PLL}}^2 + \sigma_{b_{PLL}}^2 \end{bmatrix} \tag{5.13}$$

where σ_{DLL}^2 and σ_{PLL}^2 are the thermal noise induced variance of the pseudorange and carrier phase measurement respectively. Recall that σ_{PLL}^2 was previously discussed in Chapter 3 and was defined in Equation (3.21). The code phase error due to thermal noise is a function of the correlator spacing, loop filter bandwidth, and the C/N_0 ratio of the signal and is calculated using Equation (5.14) [32]

$$\sigma_{DLL}^2 = \beta^2 \frac{4d^2 B_n}{C/N_0} \left(2(1-d) + \frac{4d}{TC/N_0} \right) \tag{5.14}$$

where β is the CA code chip width and d is the early/late correlator spacing.

The common Kalman filter time update and measurement update equations were given previously in Equations (4.4) and (4.11) and are not repeated here for brevity. Also, note that in Equations (5.10 - 5.13) only the measurement from one channel have been included for clarity, but in the actual implementation at least four satellites are needed to estimate the states.

5.2.3 Integer Fixing using the LAMBDA Method

Since the carrier ambiguities remain constant as long as the receiver maintains phase lock, the carrier ambiguity estimates from the Kalman filter continue to improve with additional measurements. As the satellites move across the sky, the changing geometry improves the ambiguity uncertainty. Once the carrier ambiguities converge, the most straightfoward method of resolving integer estimates is to simply round the decimal values of the Kalman filter. However, directly rounding the ambiguity estimates does not take advantage of the uncertainty estimate from the Kalman filter state covariance matrix. The covariance matrix not only contains statistics on the uncertainty of each state estimate but also the statistical correlation between the error in state estimates. Ideally, this information should be used in the integer fixing process. However, searching the multi-demensional space defined by the ambiguity state vector and covariance for the optimal combination of integer is impractical.

The LAMBDA method improves the efficiency of the integer search by first decorrelating the ambiguity estimates to reduce the search space. A linear transform is calculated and used to reparameterized the state estimates and covariance matrix such that the covariance matrix in the new domain is nearly diagonal. This transformation is given by Equation (5.15)

$$N_{z_{r,b}} = ZN_{r,b} \tag{5.15a}$$

$$P_{z_{r,b}} = Z\mathbf{P}_{N_{r,b}}Z^{\mathrm{T}} \tag{5.15b}$$

where the Z transform is integer and volume preserving [65]. Once the transformation is performed, the integers are rounded starting with the estimate with the lowest variance in a sequential conditional least square adjustment. The complete set of integers are then transformed back into the original domain.

The set of integers produced by the LAMBDA method is the most likely set of integers based on the state and covariance matrices provided to the algorithm. However the integers are not guaranteed to be the correct set. The ratio test derived by Teunissan *et al.* [66] is designed to provide a decision criteria along with the proposed integer set. A test statistic is calculated by comparing the optimal integer set, $\breve{N}_1$, to the next more likely set of integers, $\breve{N}_2$. Equation (5.16) is used to calculate the deviation of each integer set from original decimal estimates and normalize it by the covariance.

$$d_i = (\hat{N} - \breve{N}_i) P_N^{-1} (\hat{N} - \breve{N}_i)^{\mathrm{T}} \tag{5.16}$$

The test statistic is then calculated by dividing d_2 by d_1. If the value is greater than the threshold value, the optimal integer set is accepted. The threshold value is set to three for the software receiver in this work based on the results in [66].

5.2.4 High Precision Relative Position Vector Estimation

Calculating the high precision RPV (HPRPV) is the final step in the RTK position estimation algorithm. Once the LAMBDA method ratio test is passed, the resulting integer carrier ambiguities are assumed to be constant as long as phase lock is maintained in each tracking channel. Therefore, the ambiguities are only updated when a cycle slip is detected in the carrier phase measurement from one or more channels. The time difference carrier phase and pseudorange measurements are used in combination to check for cycle slips.

There are two options for computing the RPV: using the single difference carrier phase measurements to estimate the relative clock bias and HPRPV or using the double difference

carrier phase observable to negate the relative clock bias term. In either case, the relative position vector is calculated using least-squares or weighted least-squares. The single difference measurement vector, seen in Equation (5.17), is constructed by subtracting the fixed integer estimates of the single difference carrier ambiguities from the single difference carrier phase measurements.

$$z = \begin{bmatrix} \lambda(\Delta\phi^1_{r,b} - \mathbf{N}^1_{r,b}) \\ \vdots \\ \lambda(\Delta\phi^m_{r,b} - \mathbf{N}^m_{r,b}) \end{bmatrix} \tag{5.17}$$

In Equation (5.17), $\mathbf{N}^i_{r,b}$ represents the fixed integer carrier ambiguities produced by the LAMBDA method.

The least squares measurement matrix is shown in Equation (5.18). The H matrix includes the unit vectors from satellite to receiver and a column of ones, which maps the range and clock information contained in the measurement vector to ECEF coordinates.

$$H = \begin{bmatrix} a^1_x & a^1_y & a^1_z & -1 \\ & \vdots & & \\ a^m_x & a^m_y & a^m_z & -1 \end{bmatrix} \tag{5.18}$$

The least squares estimates of the x, y, z, and clock bias are then calculated using the traditional least square algorithm $X = (H^{\mathrm{T}}H)^{-1}H^{\mathrm{T}}z$.

Alternatively, the double difference carrier phase observable can be computed by selecting one of the single difference measurements as a base measurement and subtracting it from all other single difference measurements. The second difference is used to remove the relative receiver clock bias from the single difference measurement, since it is common to all the single differences. The model from the double difference carrier phase measurement is given in Equation (5.19).

$$\nabla\Delta\phi^{2,1}_{r,b} = \frac{1}{\lambda}r^{2,1}_{r,b} + N^{2,1}_{r,b} + \eta_{\phi^{2,1}_{r,b}} \tag{5.19}$$

This measurement model represents the value calculated by subtracting the single difference measurement from satellite number 1 from the single difference measurement from satellite number 2.

The double difference measurement vector is calculated by subtracting the double difference fixed integer carrier ambiguity estimates from the double difference carrier phase measurements. The vector is shown in Equation (5.20)

$$z = \begin{bmatrix} \lambda(\nabla\Delta\phi_{r,b}^{2,1} - \mathbf{N}_{r,b}^{2,1}) \\ \vdots \\ \lambda(\nabla\Delta\phi_{r,b}^{m,1} - \mathbf{N}_{r,b}^{m,1}) \end{bmatrix} \tag{5.20}$$

where $\mathbf{N}_{r,b}^{2,1} = \mathbf{N}_{r,b}^{2} - \mathbf{N}_{r,b}^{1}$.

The measurement vector for the double difference RPV estimator is given in Equation (5.21).

$$H = \begin{bmatrix} a_x^2 - a_x^1 & a_y^2 - a_y^1 & a_z^2 - a_z^1 \\ & \vdots & \\ a_x^m - a_x^1 & a_y^m - a_y^1 & a_z^m - a_z^1 \end{bmatrix} \tag{5.21}$$

Note that the column of ones has been removed because the clock error has been removed by the double difference, and that the unit vector from satellite to receiver for the base measurement is subtracted from the remaining unit vectors to form the correct geometry.

The remainder of this chapter is dedicated to analyzing the performance of the RTK software receiver using experimental data. First, the accuracy of the carrier phase measurements of a single receiver is verified through analysis of the carrier phase delta position calculation of a static receiver. Next, two GPS front ends are used to collect intermediate frequency (IF) data for processing with the software receiver. The RTK algorithm is used to compute high precision solutions for two static scenarios and one dynamic scenario. Details on the experimental setup used for data collection are provided in Appendix C.

5.3 Carrier Phase Delta Position Estimation

To validate the accuracy of the carrier phase measurements generated by the software receiver, the change in position estimator described in Section 2.5.5 was implemented on the measurements generated from the recorded IF samples. Data from a static receiver was used so that the change in position estimated using the delta carrier phase measurements would be an observation of the error in the carrier phase mapped into the position domain. When accurately tracking the phase of the received satellite signal, the carrier phase measurement generated by the receiver should capture the satellite motion by tracking the change in range from satellite to receiver. Therefore, a delta carrier phase measurement should result in zero change in receiver position when the satellite motion is correctly accounted for using the satellite ephemerides.

The experimental data was collected using a roof antenna with a clear line of sight to the sky. The software receiver acquired and tracked seven satellites in the experiment used to validate the carrier phase measurement accuracy. The azimuth and elevation of the seven satellites are shown in Figure 5.4. The traces show the satellite motion during the ninety minute test.

The phase of the received signal is maintained in the carrier tracking loop, with an accuracy of approximately two percent of a cycle which translates to a one sigma phase error of approximately 4 millimeters. The expected horizontal and vertical errors of the delta position solution can be predicted by multiplying the expected one sigma phase error by the dilution of precision (DOP) which is given in Equation (5.22)

$$DOP = (H^{\mathbf{T}}H)^{-1} \tag{5.22}$$

where H is given in Equation (5.18). The East, North, and Up dilution of precision due to the satellite geometry during the test are shown in Figure 5.5. Based on the dilution of precision and the expected 4 millimeter phase error, the East and North position errors

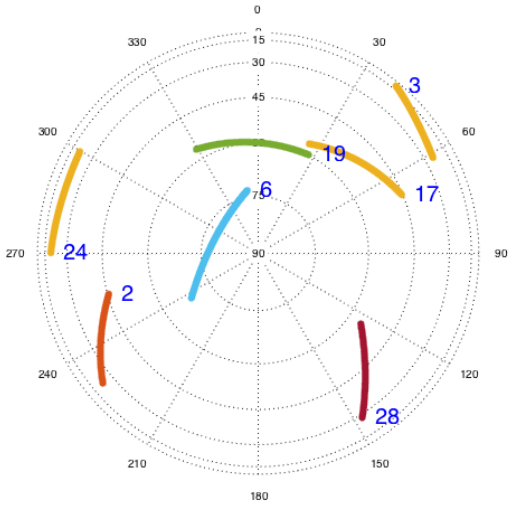

Figure 5.4: Azimuth and elevation of seven satellites during 90 minute delta position estimation test.

should be on the order of 3 millimeter (one sigma) and the vertical errors shown be on the order of 6 millimeters.

The delta position estimates from the software receiver are shown in Figure 5.6. The top plot shows the East and North components of the delta position. The horizontal components are typically more accurate than the vertical component, which is shown in the lower plot. As seen in the figure, the horizontal errors are less than 5 millimeters, which is consistent with the expected error. The vertical errors are less than one centimeter. These errors are within the expected range of RTK quality carrier phase measurements.

The statistics of the static delta position estimation test are compiled in Table 5.1. The East, North and Up mean errors are near zero mean with standard deviations at the millimeter level or better. These results are consistent with the dilution of precision analysis shown earlier. The accuracy of the carrier phase measurements used to estimate the delta position are promising for RTK positioning.

Next, the relative accuracy of the pseudorange and carrier phase measurements are compared. Recall that the RTK algorithm leverages the similarities of the pseudorange and

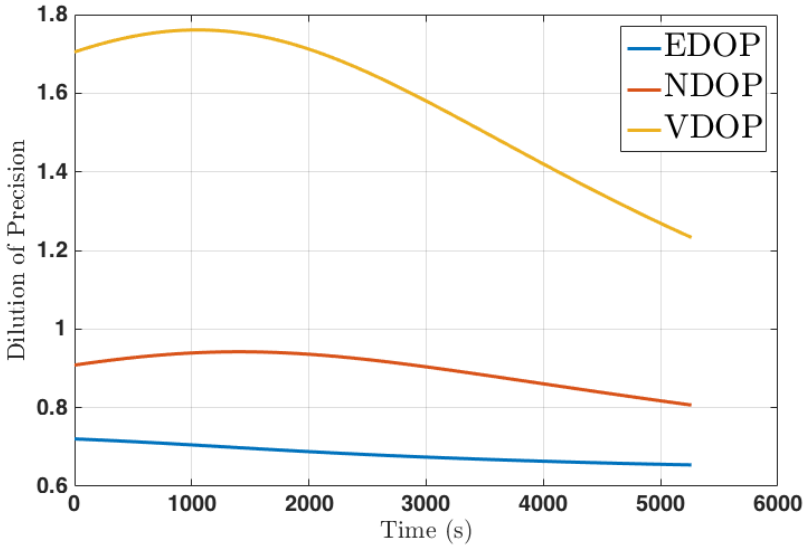

Figure 5.5: Dilution of precision for the satellite geometry during delta position estimation test.

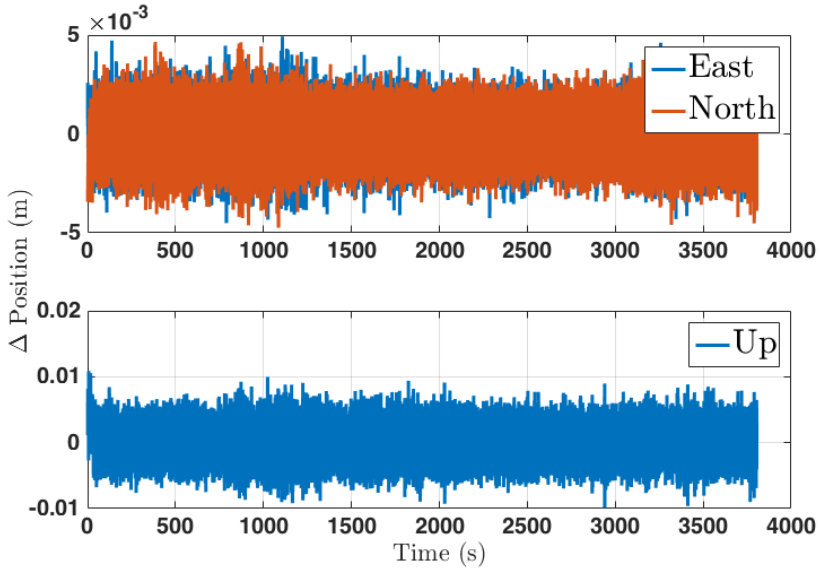

Figure 5.6: East, North, and Vertical change in position as estimated using delta carrier phase measurements.

Table 5.1: Error in Carrier Phase Delta Position Solution

Error	East	North	Up
Mean (cm)	4.4×10^{-4}	-4.5×10^{-4}	1.0×10^{-2}
STD (cm)	9.1×10^{-2}	9.2×10^{-2}	2.0×10^{-1}

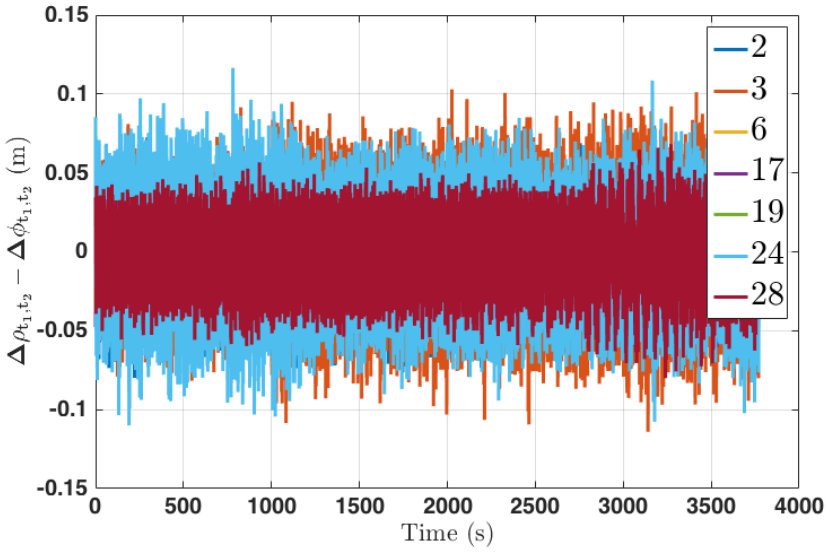

Figure 5.7: Time differenced pseudorange minus time difference carrier phase shows that RTK positioning is possible.

carrier phase to estimate the carrier ambiguities. A straightforward way to compare the pseudorange and carrier phase is to compare the change over one measurement epoch (often called the time difference). The difference between the time differenced pseudorange and the time differenced carrier phase for each satellite is shown in Figure 5.7. Refer back to the error sources in the pseudorange and carrier phase model in Equations (5.4) and (5.7b), respectively. The atomsphere errors are largely removed due the high correlation over short time periods when computing the time difference. The satellite clock is also very stable over short time periods and can be neglected. The carrier phase ambiguities are completely removed as long as the receiver has maintained phase lock over the measurement interval. The remaining terms are common to the pseudorange and carrier phase with the exception of the measurement noise. The difference between the two time differenced measurements should be zero mean with white noise proportional to the pseudorange noise since the carrier phase measurement noise is at least an order of magnitude lower. This is consistent with the data shown in Figure 5.7. Based on the accuracy of the pseudorange and carrier phase measurements, the software receiver should be capable of RTK positioning.

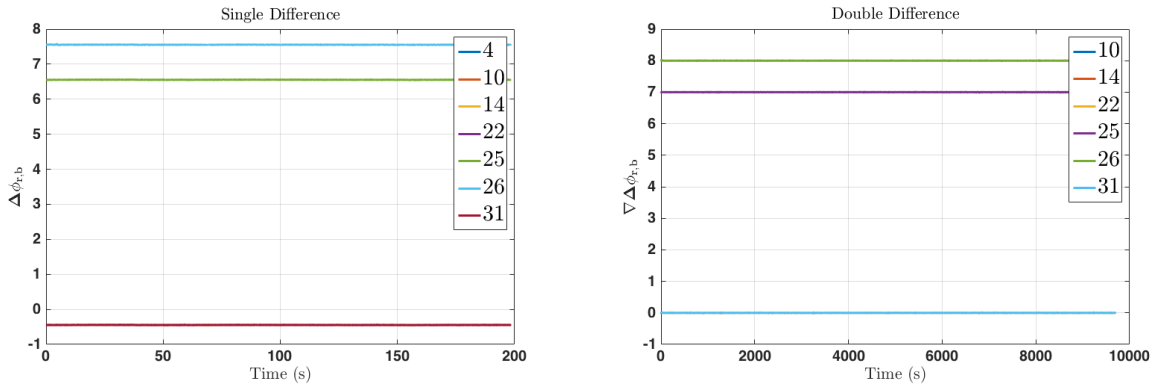

Figure 5.8: Single and Double difference carrier phase show relative clock bias and double difference ambiguities.

5.4 Software Receiver Carrier Phase RTK Results

Now that the accuracy of the raw measurements from the software receiver has been validated, the RTK positioning performance of the software receiver is analyzed with three tests. The tests include one static antenna feeding two GPS front ends, two static antennas separated by approximately 600 meters, and one static base receiver and one mobile rover receiver. The accuracy of the RTK position solutions are compared to a reference RTK solution computed using two commercial Novatel Propak survey grade GPS receivers.

First the RTK software receiver is tested with data from two GPS front ends connected to the same antenna. The data was collected using an antenna on the roof of the Woltosz Building on the Auburn University campus. Obviously, the correct RPV is zero meters in each direction so the RTK position errors are easily evaluated. Before analyzing the position estimates, it is informative to examine the single and double difference carrier phase measurements. Both measurements for each satellite in view are shown in Figure 5.8. In the figure, the plot on the left shows the single difference carrier phase measurements, which are clearly low noise. Three measurements are distinguishable with several of the measurements centered at approximately -0.5 meters. Due to the zero baseline, the single difference is only a function of the carrier ambiguity, the relative clock bias, and noise. The relative clock

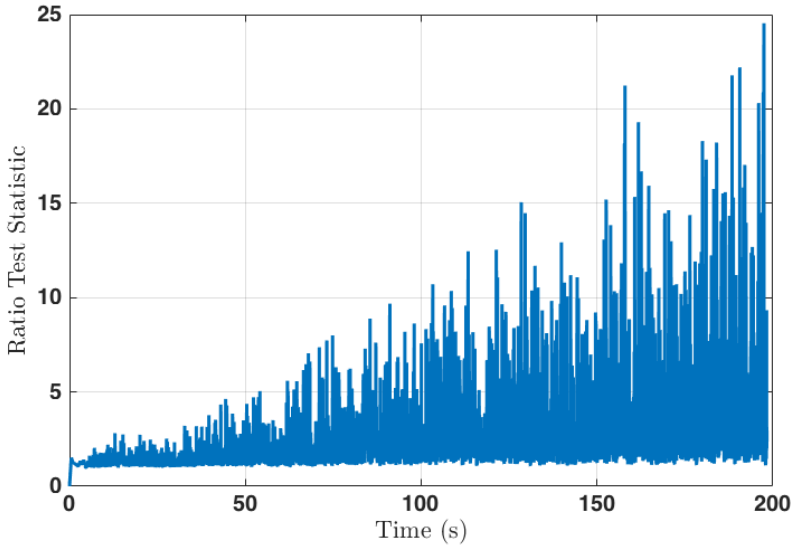

Figure 5.9: The ratio test statistic increases as decimal estimates approach true integers.

bias ensures that the single difference measurements do not fall on integer values. When the double difference is computed, the relative clock bias is removed and only the carrier ambiguity remains. This is seen in the plot on the right. Clearly all six double difference measurements are constant integer values, as expected.

To compute the HPRPV, the fixed integer carrier phase ambiguities must be determined by the LAMBDA method. In this ideal example, the double difference ambiguities can be determined rather easily by examining Figure 5.8, but in practice, the set of integer values will be selected once the LAMBDA ratio test is passed. The ratio test statistic increases as the decimal ambiguity estimates converge to the true values. That is seen clearly in the ratio test used on the this experimental data in Figure 5.9. In this test, the ratio test was passed after approximately twenty seconds.

Figure 5.10 shows a scatter plot of the Latitude and Longitude estimates of the software receiver (Sp - standard (pseudorange) precision, Hp - High (RTK) precision, Lp - Low (decimal ambiguity) precision). In the image on the left, only the standard pseudorange position solution is visible. The variance of the standard position solution is quite high due to a lack of carrier phase aiding. The image on the right shows a zoom in on the antenna used

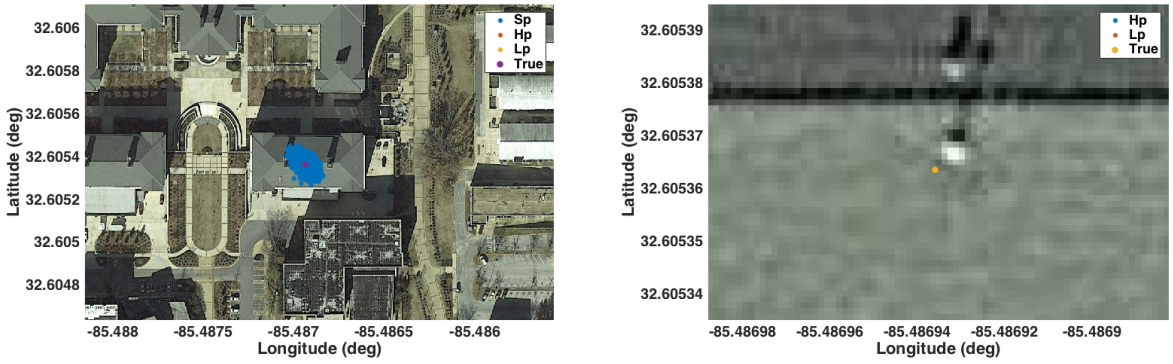

Figure 5.10: Scatter plot of standard, high, and low precision estimates of antenna position on map. Imagery by Google, DigitalGlobe.

for this test. The reference position, which was calculated using a commerical RTK receiver, is slightly offset relative to the map. The high and low precision solution are grouped tightly enough to be invisible on this scale.

Figure 5.11 shows the error in the RTK position solution compared to the reference position. The errors of the high precision and low precision position estimates are plotted in East and North coordinates in the left image. The vertical errors of each solution are shown in the image on the right. Clearly the HPRPV errors in each coordinate direction are near zero mean with millimeter level errors. The low precision solution is slightly biased during this three minute test, but would likely approach zero mean over longer test periods. Under these ideal conditions, the software receiver provides RTK level position solutions comparable with the survey grade GPS receivers.

Next the RTK performance was tested over a longer distance, again with two static receivers. The rover receiver was positioned in a parking lot approximately 600 meters west of the base antenna. The separation distance is seen on a map of the area in Figure 5.12. The horizontal and vertical components of the HPRPV and the low precision solution calculated by the software receiver are shown in Figure 5.13. On the left, a scatter plot of the East and North estimates are shown along with the reference location of the antenna calculated by the commerical survey grade receiver. The spread of the high precision solution covers

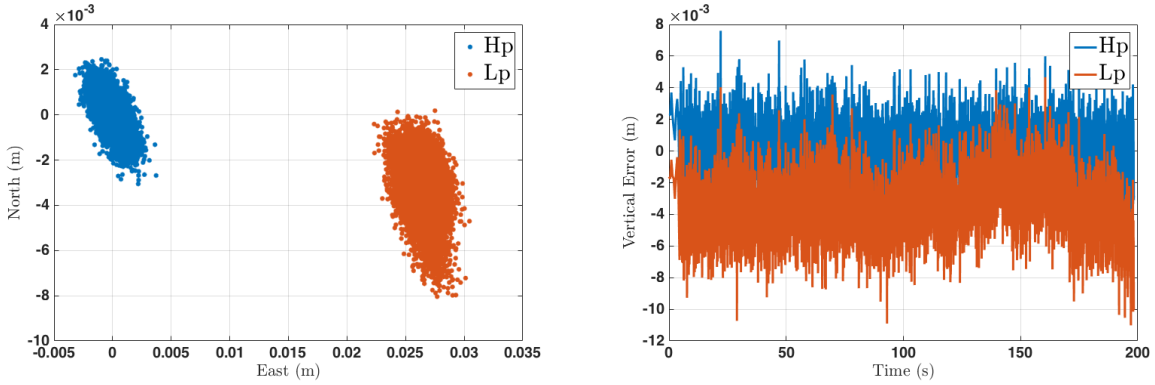

Figure 5.11: High and Low precision errors of zero baseline RTK test.

Figure 5.12: True location of the base antenna and the high and low precision estimates of the rover antenna location for long baseline static test of RTK receiver. Imagery by Google, DigitalGlobe.

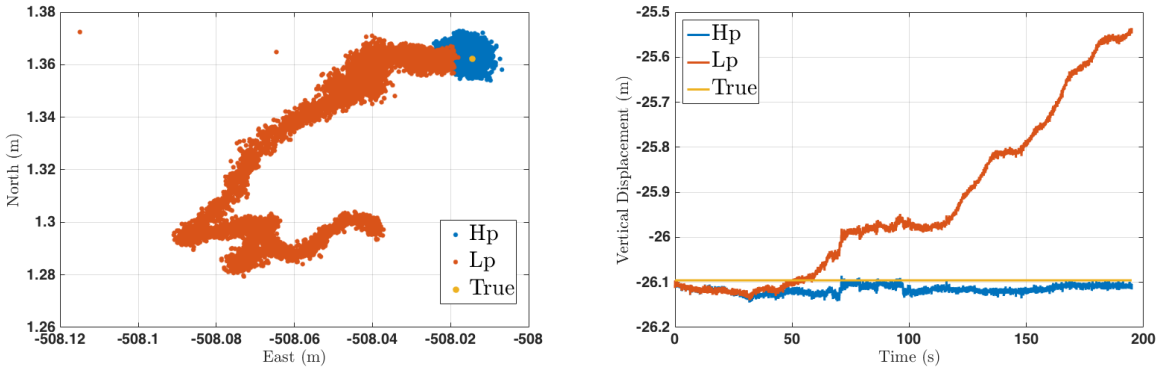

Figure 5.13: High and Low precision RPV for 600 meter baseline test compared to reference.

approximately one grid square, or about four square centimeters. The vertical component of the HPRPV is also accurate to within a few centimeters. The low precision solution is less well behaved, particularly in the vertical direction. Recall that the decimal estimates of the carrier ambigiuties are dependent on the pseudorange measurements. The low precision solution will drift due to noise in the pseudorange measurements but should approach zero mean over longer periods.

The statistics on the errors of the RTK solutions for the two static tests are provided in Table 5.2. The zero baseline and 600 meter baseline test results are reported separately to assess the performance as a function of separation distance. In both cases, the mean error was on the order of a few centimeters or less in the horizontal direction. During the long baseline test, the vertical error was slightly high when compared to the reference solution. The vertical direction is normally the least accurate, particularly when there is a significant height difference. The standard deviation of the errors was also at the centimeter level. That accuracy is consistent with commercially available RTK receivers.

A dynamic test was also performed to evaluate the software receiver RTK positioning performance. The rover receiver was driven in an open field in a winding route with the distance to the base receiver ranging from a few meters to several hundred meters. The base station was located at the southeast corner of the test area. The route can be seen on a map of the area in Figure 5.16. The high precision Latitude and Longitude position estimates of

Table 5.2: Error in RTK Position Solution in Static Tests

Static						
Distance	0 meters			600 meters		
Error	East	North	Up	East	North	Up
Mean (cm)	2.7	−0.33	−0.34	−0.17	0.11	2.0
STD (cm)	0.11	0.13	0.19	0.25	0.28	0.86

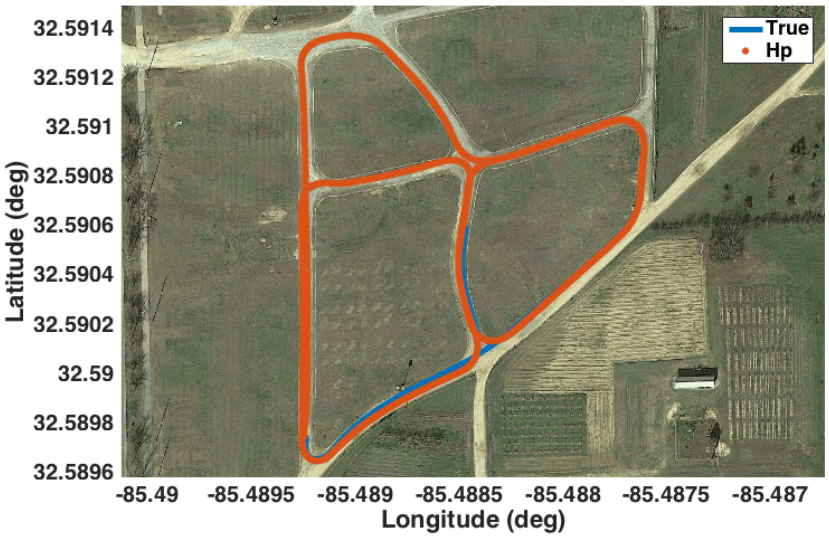

Figure 5.14: High precision solution lies directly over the reference solution in overhead view of route driven during dynamic RTK test. Imagery by Google, DigitalGlobe.

the software receiver and the reference receiver are shown in the figure. The reference is only seen under the RTK position solution for brief instances which will be examined shortly.

On closer inspection in Figure 5.15, it is clear that the software receiver position solution and the reference solution lie directly on top of one another through several turns. The left image shows the first turn made by the vehicle, and the two solutions are indistinguishable on this scale. The same is true for the image on the right where the vehicle makes several turns over multiple laps.

The software receiver reports RTK position estimates at 50 Hz, and the solutions were downsampled to the rate of the reference (1 Hz) to calculate the position errors. Two plots

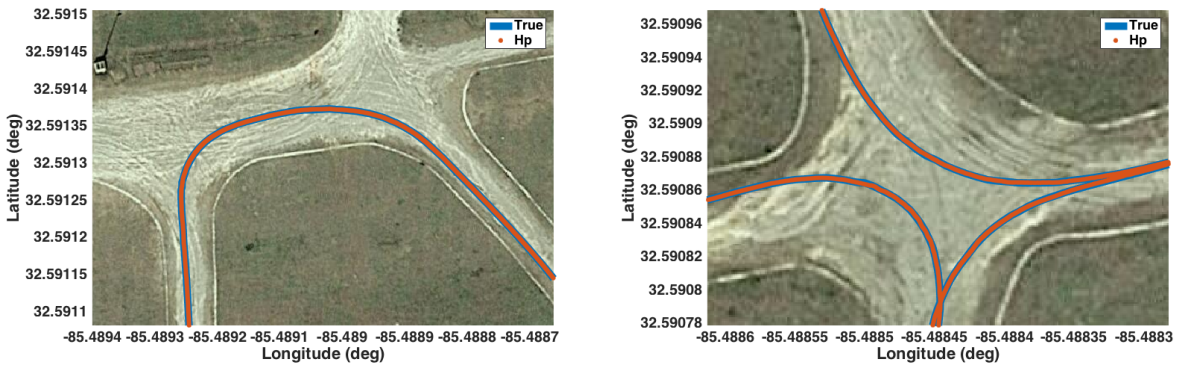

Figure 5.15: Reference and high precision solutions still indistinguishable in zoomed overhead view of RTK dynamic test. Imagery by Google, DigitalGlobe.

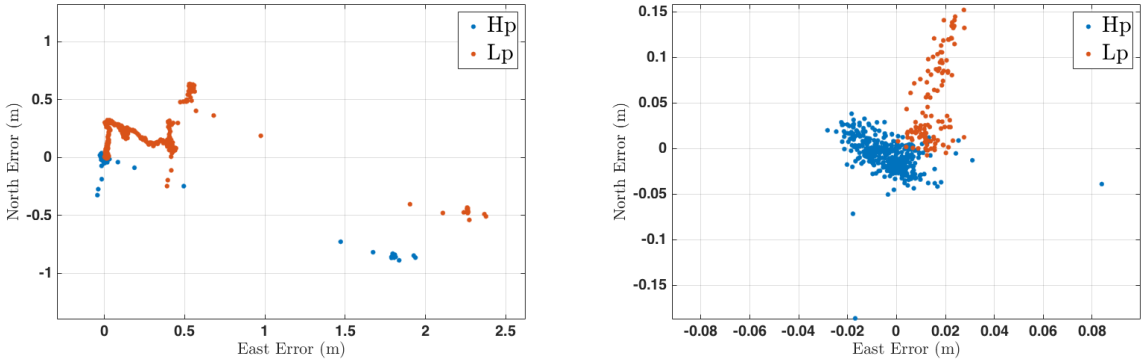

Figure 5.16: High and Low precision East and North errors for dynamic RTK test.

of the East and North errors are shown in Figure 5.16. The plot on the left shows all the low and high precision errors for the test. There are several errors that are near 2.5 meters in magnitude, but the majority of the errors (particularly for the high precision solutions) are much closer to centimeter level. The plot on the right shows a zoomed in view of the East and North errors. This cluster is more consistent with the RTK results from the static tests.

To understand the cause of the large errors seen in Figure 5.16, the three dimensional ECEF errors are shown in Figure 5.17 on the left. The majority of the errors are near zero mean with a standard deviation of a few centimeters. There is one section of approximately twenty seconds when the error jumps to several meters. The image on the right shows a

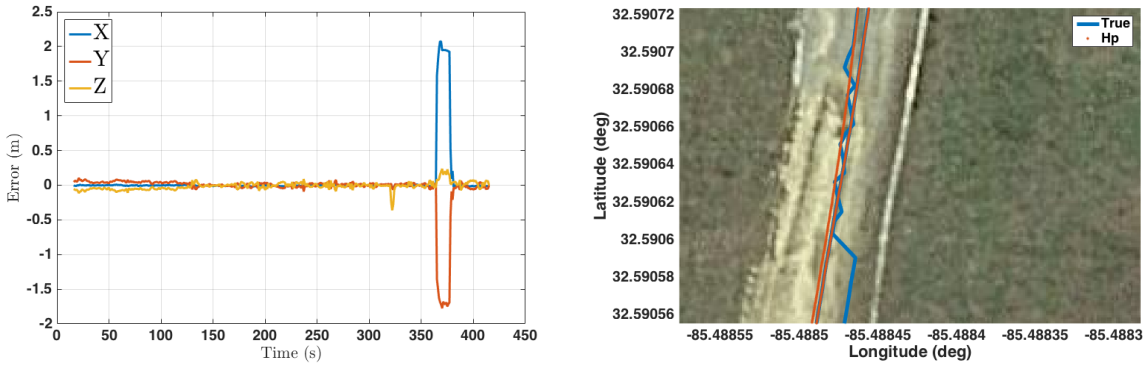

Figure 5.17: Temporary difference in reference and high precision solutions appears to be due to incorrect integer fix in reference solution. Imagery by Google, DigitalGlobe.

Table 5.3: Error in RTK Position Solution in Dynamic Tests

	Dynamic		
Distance	Variable		
Error	East	North	Up
Mean (cm)	−4.6	1.1	−1.8
STD (cm)	0.79	3.4	4.6

zoomed in view of the issue from overhead. The software receiver position shown in orange is clearly consistent with normal vehicle maneuvers. It is the reference receiver that begins to report erratic position estimates. The reference receiver appears to have trouble maintaining the fixed integer carrier phase solution and then begins reporting a bias solution. This section of the test was removed when analyzing the statistical performance of the software receiver. Table 5.3 provides the mean and standard deviation of the RTK software receiver positioning errors. Again, the statistics are comparable to a commercial RTK receiver.

5.5 Conclusion

This chapter discussed the design and testing of a software receiver based RTK positioning algorithm using the GPS carrier phase measurement. The procedure for calculating the high precision relative position vector between a base receiver and a rover receiver using

fixed integer carrier ambiguity estimates was described. The performance of the RTK software receiver is compared to a survey grade GPS receiver in static and dynamic tests. The receiver provided position solutions with accuracy consistent with commercial RTK receivers (2-3 cm). The RTK position algorithm described in this chapter is used as an initialization procedure and as the foundation for the RTK vector receiver described in the next chapter.

Chapter 6

Vector Tracking Receiver Architecture

High precision RTK GPS receivers require continuous carrier phase lock on multiple satellite signals by the rover and base receiver. The traditional scalar tracking GPS receiver normally maintains phase lock on several signals in environments where the rover receiver has a clear line of sight to the sky, and where the received signal is not disrupted by interference due to atmospheric affects or signal jammers. Applications such as precision surveying in heavy foliage, and autonomous vehicle operation in urban canyons strain the capabilities of the scalar tracking receiver. In this chapter, a software receiver vector tracking architecture is derived for improved code and carrier tracking in environments that disrupt the operations of a traditional receiver. The receiver combines a Doppler aided vector delay locked loop (VDLL) with a novel RTK vector phase locked loop (VPLL). A conceptual drawing of the system design is shown in Figure 6.1. The vector tracking software receiver is mounted on the rover vehicle (the tractor in the figure), and a local base station receiver is mounted in the area with a clear view of the sky. The carrier tracking algorithms of the software vector tracking receiver on the rover use measurement from the base antenna and the relative position vector, $\vec{r}$, to predict the received signal from each satellite. When measurements are available at the rover, the relative position vector estimates are updated.

The software receiver combines vector code and carrier tracking. In a vector receiver, the local replicas are driven by the navigation solution directly. Due to the differences in the precision of the discriminator based measurements used to update the navigation solution and possible code/carrier divergence due to ionospheric affects, the vector tracking receiver is designed with two navigation processors.

A block diagram of the receiver architecture is shown in Figure 6.2. In the figure,

Figure 6.1: The RTK VPLL receiver uses differential carrier phase positioning and base station measurements to improve phase tracking in degraded environments.

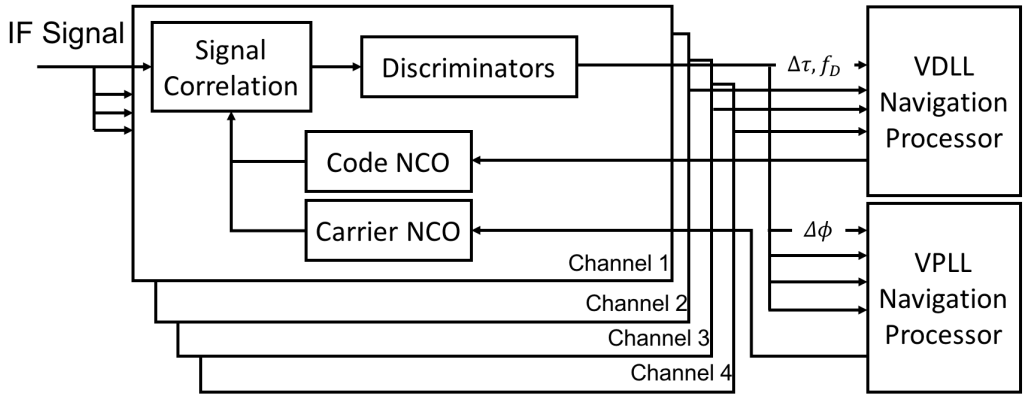

Figure 6.2: The software vector tracking receiver for the rover uses two navigation processors to track code and carrier phase independently.

the code discriminator and Doppler frequency from each channel feed the VDLL navigation processor. The carrier phase discriminator is used to update the VPLL navigation filter. The VDLL drives the code NCO, and the VPLL drives the carrier NCO. This architecture prevents the less accurate code discriminator measurements from degrading the accuracy of the carrier phase based navigation solution. The Doppler measurements are used to improve the velocity and clock drift state estimates in the VDLL navigation filter, and act like carrier smoothing or Doppler aiding in traditional scalar receivers. Also, the VDLL is not a differential navigation filter, meaning that the pseudorange measurements from the base station receiver are not used in the update or prediction step. This design was selected based on the following criteria: the VDLL navigation processor is robust without need of external data, the VDLL can maintain a navigation solution during a communication disruption since it does not rely on base station measurements, and the required communication bandwidth can be reduced by removing pseudorange measurements from the messages.

The navigation filter designs in this chapter use code and carrier phase errors calculated from correlator outputs to update the state estimates. Therefore, it is advantageous to review the correlator output model at this time. The mathematical model of the in-phase and quadrature correlators are given by Equation (6.1).

$$I(k,\gamma) = AR(\epsilon+\gamma)D(k)\cos(\pi f_e T + \delta\phi) + \eta_I(k) \tag{6.1a}$$

$$Q(k,\gamma) = AR(\epsilon+\gamma)D(k)\sin(\pi f_e T + \delta\phi) + \eta_Q(k) \tag{6.1b}$$

In the equations above, A is the received signal amplitude, ϵ is the code phase error, f_e is the carrier frequency error, and $\delta\phi$ is the carrier phase error. γ is the offset for the early and late replicas used to generate the code phase error measurement. Code phase and carrier phase error observables are used to update the VDLL and VPLL navigation processors as described in the following sections.

6.1 Vector Delay Locked Loop (VDLL)

The vector delay locked loop is implemented as an error state Kalman filter. The implementation described in the section follows the work in [40] and [9] with a modification to the measurement update. The states of this filter do not drive the carrier NCO, and the carrier frequency discriminator is not used to update the navigation states. The state vector includes three dimensional position and velocity errors, as well as clock bias and clock drift errors as seen in Equation (6.2).

$$\mathbf{X} = \begin{bmatrix} \delta x \\ \delta \dot{x} \\ \delta y \\ \delta \dot{y} \\ \delta z \\ \delta \dot{z} \\ \delta cb \\ \delta \dot{cb} \end{bmatrix} \tag{6.2}$$

The best estimate of position and velocity are maintained by applying the error correction to the state estimate after each time and measurement update of the Kalman filter. The position and velocity are estimated in ECEF coordinates, and the clock bias and clock drift are estimated in units of meters and meters per second, respectively.

6.1.1 VDLL Dynamic Model

A kinematic model is again used to propagate the Kalman filter state mean and covariance. The state transition and process noise matrices are defined in Equation (6.3).

$$\mathbf{X}_{k+1} = \Phi_{k,k+1}\mathbf{X}_k + Q_k \tag{6.3a}$$

$$\Phi_{k,k+1} = \begin{bmatrix} \alpha_k & 0_{2x2} & 0_{2x2} & 0_{2x2} \\ 0_{2x2} & \alpha_k & 0_{2x2} & 0_{2x2} \\ 0_{2x2} & 0_{2x2} & \alpha_k & 0_{2x2} \\ 0_{2x2} & 0_{2x2} & 0_{2x2} & \alpha_k \end{bmatrix} \tag{6.3b}$$

$$\alpha_k = \begin{bmatrix} 1 & \Delta t \\ 0 & 1 \end{bmatrix} \tag{6.3c}$$

$$Q_k = \begin{bmatrix} Q_x & 0_{2x2} & 0_{2x2} & 0_{2x2} \\ 0_{2x2} & Q_y & 0_{2x2} & 0_{2x2} \\ 0_{2x2} & 0_{2x2} & Q_z & 0_{2x2} \\ 0_{2x2} & 0_{2x2} & 0_{2x2} & Q_{cb} \end{bmatrix} \tag{6.3d}$$

Q_x, Q_y, Q_z, and Q_{cb} were defined previously in Equations (4.3e - 4.3h) and are not repeated here for brevity. The standard Kalman filter time update equations defined in Equation (4.4) are used to propagate the filter mean and covariance.

6.1.2 VDLL Filter Residuals

It is common to update the navigation processor of a vector tracking receiver with either correlator outputs or discriminator outputs. The VDLL navigation processor of the software vector tracking receiver uses code phase discriminator outputs to generate range error measurements to update the navigation filter. The current carrier NCO value is also used to calculate range rate residuals. Each channel provides range and range rate error residual to update the VDLL navigation processor at the end of each 20 ms integration and dump period. The filter residuals are described by the equations below.

The code phase error residual is calculated using Equation (6.4)

$$\delta\theta_{c_1} = \frac{1}{2}\frac{\epsilon_1}{A_1}\beta \tag{6.4}$$

where β is the CA code chip width ($\approx 293.05m$), which is used to β convert the code phase error from units of chips to meters. ϵ_1 is the early minus late power given by Equation (6.5a), and A_1 is the average received signal power given by Equation (6.5b).

$$\epsilon_1 = IE^2 + QE^2 - IL^2 - QL^2 \tag{6.5a}$$

$$A_1 = (IE + IL)^2 + (QE + QL)^2 - 4\eta^2 \tag{6.5b}$$

Unlike the vector delay and frequency locked loop (VDFLL) Kalman filter, the VDLL navigation processor does not control the carrier NCO. Instead of using the carrier frequency discriminator to update the velocity and clock drift states, a range rate residual is calculated using the current NCO value that is controlled by the RTK VPLL. The range rate residual is calculated by subtracting the range rate predicted by the current states of the navigation processor ($\hat{\dot{\rho}}$) from the measured range rate derived from the carrier NCO ($\tilde{\dot{\rho}}$) as seen in Equation (6.6).

$$\delta\dot{\rho}_1 = \tilde{\dot{\rho}}_1 - \hat{\dot{\rho}}_1 \tag{6.6}$$

The calculation of $\hat{\dot{\rho}}$ was previously described in Section 2.5.5 and is not repeated here. The measured range rate is calculated from the current carrier Doppler using Equation (6.7).

$$\tilde{\dot{\rho}}_1 = -\lambda f_{D_1} \tag{6.7}$$

The carrier Doppler measurement is calculating by subtracting the front end intermediate frequency from the current carrier NCO value.

6.1.3 VDLL Residual Variances

The expected variance of the range and range rate residuals is calculated as a function of the C/N_0 ratio from each channel. As described in [11], the variance of the code phase

discriminator based range residual is calculated using Equation (6.8).

$$\sigma_{\theta_c}^2 = \frac{\beta^2}{2(TC/N_0)^2} + \frac{\beta^2}{4TC/N_0} \tag{6.8}$$

Recall, β represents the CA code chip width and T is the integrate and dump period (20 ms in this dissertation).

Equation (6.9) is used to calculate the measurement noise on the range rate residual.

$$\sigma_{\delta\dot{\rho}}^2 = \left(\frac{\lambda_{L1}}{\pi T}\right)^2 \left(\frac{2}{(TC/N_0)^2} + \frac{2}{TC/N_0}\right) \tag{6.9}$$

The wavelength of GPS L1 carrier (λ_{L1}) is used to convert the carrier frequency error variance to units of meter squared per second squared. Equation (6.9) is also derived in [11], and assumes that the code phase error is small.

6.1.4 VDLL Measurement Update

At the end of the integrate and dump period on each channel, the range and range rate residuals are calculated to form the measurement vector for the Kalman filter update. The measurement vector is given in Equation (6.10).

$$z = \begin{bmatrix} \delta\theta_{c_1} \\ \delta\dot{\rho}_1 \end{bmatrix} \tag{6.10}$$

Differentiating the range and range rate predictions with respect to the state vector results in the measurement matrix, H, shown in Equation (6.11).

$$H = \begin{bmatrix} a_x & 0 & a_y & 0 & a_z & 0 & -1 & 0 \\ 0 & a_x & 0 & a_y & 0 & a_z & 0 & -1 \end{bmatrix} \tag{6.11}$$

a_x, a_y, and a_z comprise the line of sight unit vector from satellite to receiver. The end of the integration period is generally not synchronous across channels, and therefore a correction must be made to the measurement vector. The correction accounts for the change in the state vector that occurs between the code frequency prediction at the end of one integration period and the measurement update at the end of the next integration period. The correction is updated iteratively between measurement updates on each individual channel. For details on implementing the correction see [36] and [33].

6.1.5 Code Phase Prediction and NCO Calculation

The *a posteriori* state estimates are used to predict the received time of the start of the next code period and calculate the desired code frequency for the code NCO. First, a prediction of the state vector at the end of the current integrate and dump period is calculated using the state transition matrix. Note that the state mean and covariance estimates are not propagated forward in this step because the filter time update is performed at the end of each integration period. The Kalman filter time update is performed at the end of the integrate and dump period. The state vector prediction and the predicted satellite positions are used to calculate a prediction of the pseudorange at the end of the current integration period as seen in Equation (6.12).

$$\hat{\rho}_{k+1} = ||\vec{r}_{s_{k+1}} - \hat{\vec{r}}_{r_{k+1}}|| + \hat{cb}_{k+1} \tag{6.12}$$

The subscript $k+1$ is used to denote the end of the current integration period where k is the current time. $\vec{r}_{s_{k+1}}$ is the three dimensional satellite position calculated at time $k+1$ using the decode ephemerides. The predicted three dimensional receiver position is represented by $\hat{\vec{r}}_{r_{k+1}}$, and $\hat{cb}_{k+1}$ is the predicted clock bias. The operator $||\quad||$ represents the Euclidean norm.

The transmission time $t_{t_{k+1}}$ of the start of a code period is synchronized to GPS time, and is a known quantity based on the decoded navigation message and the code period counter in the receiver. The received time of the first sample of the code period starting at time $k+1$ is calculated using Equation (6.13).

$$\hat{t}_{r_{k+1}} = t_{t_{k+1}} + \hat{\rho}_{k+1} \tag{6.13}$$

At this point, the start time (i.e. current receiver time $t_{r_{k+1}}$) and the predicted end time (i.e. current receiver time $\hat{t}_{r_{k+1}}$) of the current integration period are available. The CA code chipping rate is 1.023×10^6, and the integration period T is 20 milliseconds. Therefore the desired code frequency is calculated by dividing the number of chips by delta time as seen in Equation (6.14).

$$f_c = \frac{1.023 \times 10^6 T - \theta_{c_k}}{\hat{t}_{r_{k+1}} - t_{r_k}} \tag{6.14}$$

The CA code chip transition does not happen on a whole sample from the front end, therefore the current code phase, θ_{c_k}, is subtracted from the total number of chips in the 20 milliseconds integration period.

6.2 RTK Vector Phase Locked Loop (RTK VPLL)

In a traditional vector receiver, the code and carrier NCO values are set using predictions derived directly from the navigation solution. The VDLL navigation processor is only responsible for updating the NCO value used to generate the local code replica. In this dissertation, a novel method using a separate navigation processor is used to drive the carrier NCO. As stated earlier, this architecture is chosen to prevent a degradation in the high precision navigation solution that would result from code phase error measurement updates. The block diagram of the separation of the code and carrier generation was shown previously in Figure 6.2. The block diagram in Figure 6.3 isolates the modules used in this new RTK

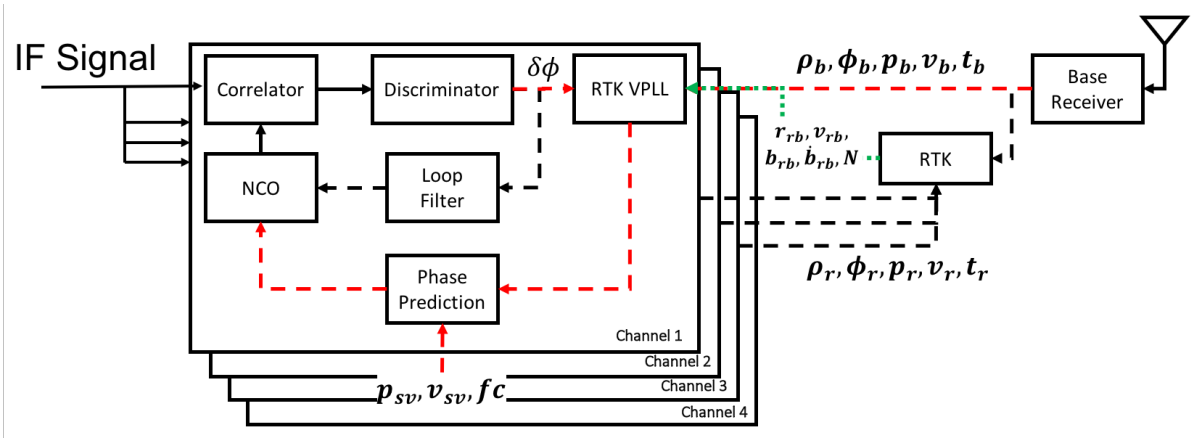

Figure 6.3: A block diagram of the RTK VPLL receiver architecture using carrier phase measurements from base station.

vector phase locked loop (VPLL) and highlights the different modes of the receiver from initialization through vector operation.

In the figure, the solid black lines represent the receiver operations that occur at all times, including the correlation and discrimination blocks. The black dashed lines connect the elements that are required to calculate the first receiver position and form an initial high precision relative position vector. The initialization of the RTK VPLL requires a scalar PLL in the rover receiver, measurements from the base receiver, and the RTK algorithm described in Chapter 5. The green dotted line shows the outputs of the RTK algorithm that are used to initialize the RTK VPLL, and the red dashed lines map the route of data through the RTK VPLL receiver components.

A Kalman filter is used to maintain high precision relative position estimates in the RTK VPLL navigation processors. The RTK VPLL state vector, seen in Equation (6.15), includes the three deminsional ECEF relative position vector errors, the relative velocity

errors, the relative clock bias error, and the relative clock drift error.

$$\mathbf{X} = \begin{bmatrix} \delta x_{r,b} \\ \delta \dot{x}_{r,b} \\ \delta y_{r,b} \\ \delta \dot{y}_{r,b} \\ \delta z_{r,b} \\ \delta \dot{z}_{r,b} \\ \delta cb_{r,b} \\ \delta \dot{cb}_{r,b} \end{bmatrix} \tag{6.15}$$

6.2.1 Initialization

The RTK algorithm described in Chapter 5 is used to estimate the relative position, velocity, and clock states used to initialize the RTK VPLL navigation processor. After the first integer fix is calculated using the LAMBDA method, the high precision relative position vector is calculated using the double difference least squares solution. The relative position states of the RTK VPLL are initialized with the HPRPV. The relative velocity and relative clock states are initialized using the single difference RTK Kalman filter estimates. The vector of fixed integer single difference carrier ambiguities, seen in Equation (6.16), is recorded and is used as a known quantity in the carrier phase prediction step of the RTK VPLL algorithm that is described later in Section 6.2.6.

$$\mathbf{N} = \begin{bmatrix} \mathbf{N}_{r,b}^{1} \\ \vdots \\ \mathbf{N}_{r,b}^{m} \end{bmatrix} \tag{6.16}$$

Since the relative velocity and relative clock states are estimated in the RTK algorithm along with the decimal estimates of the carrier ambiguities, the RTK VPLL navigation solution

is updated several times before the loop closure aspect of the vector PLL is initiated. The updates are performed at the update rate of the original RTK algorithm using the single difference carrier phase measurements from the rover and base receivers. This step allows the clock bias estimate in particular to converge to a more precise value that may be used to predict the received carrier phase and close the VPLL tracking loop.

6.2.2 RTK VPLL Dynamic Model

The RTK VPLL is designed assuming that the base receiver is able to maintain accurate carrier phase tracking (e.g. operating in a benign environment or using the static base vector aided receiver described in Section 4.5). Accordingly, the change in the relative position and velocity are the result of the motion of the rover receiver. Therefore, the dynamic model used in the Kalman filter time update is generally the same in the VDLL and the VPLL. The discrete dynamic model used in the RTK VPLL is shown in Equation (6.17).

$$\mathbf{X}_{k+1} = \Phi_{k,k+1}\mathbf{X}_k + Q_k \tag{6.17a}$$

$$\Phi_{k,k+1} = \begin{bmatrix} \alpha_k & 0_{2x2} & 0_{2x2} & 0_{2x2} \\ 0_{2x2} & \alpha_k & 0_{2x2} & 0_{2x2} \\ 0_{2x2} & 0_{2x2} & \alpha_k & 0_{2x2} \\ 0_{2x2} & 0_{2x2} & 0_{2x2} & \alpha_k \end{bmatrix} \tag{6.17b}$$

$$\alpha_k = \begin{bmatrix} 1 & \Delta t \\ 0 & 1 \end{bmatrix} \tag{6.17c}$$

$$Q_k = \begin{bmatrix} Q_x & 0_{2x2} & 0_{2x2} & 0_{2x2} \\ 0_{2x2} & Q_y & 0_{2x2} & 0_{2x2} \\ 0_{2x2} & 0_{2x2} & Q_z & 0_{2x2} \\ 0_{2x2} & 0_{2x2} & 0_{2x2} & 2Q_{cb} \end{bmatrix} \tag{6.17d}$$

Notice that the process noise matrix Q_k is changed to reflect the fact that the relative clock bias and drift includes the effects of both the rover and base clocks (by the use of a factor of 2). This model assumes that the clock model parameter are the same for the rover and base clocks and that the stochastic errors are uncorrelated.

6.2.3 RTK VPLL Filter Residuals

The navigation solution of the RTK VPLL is initialized with position information that is accurate enough to predict the received carrier phase. To maintain this level of accuracy, the Kalman filter residuals must be as accurate as the single difference carrier phase measurements used to estimate the HPRPV. As described in Chapter 2, the carrier phase discriminator provides a range error measurement with an accuracy of a few millimeters. The RTK VPLL Kalman filter residual is shown in Equation (6.18).

$$\delta\phi_1 = -\lambda_{L1}\text{atan}\left(\frac{QP}{IP}\right) \tag{6.18}$$

The Costas carrier discriminator is used to calculate the residual carrier phase error, and the wavelength of the GPS L1 signal is used to convert to units of meters.

6.2.4 RTK VPLL Residual Variances

The primary error source in the carrier tracking loop is thermal noise. Accordingly, the measurement uncertainty of the carrier discriminator is calculated as a function of the C/N_0 ratio of the signal from each channel. Equation (6.19) is used to calculate the carrier phase residual error variance.

$$\sigma^2_{\phi_1} = \left(\frac{\lambda_{L1}}{2\pi}\right)^2 \frac{B_n}{C/N_0}(1 + \frac{1}{2TC/N_0}) \tag{6.19}$$

Recall that Bn is the noise equivalent bandwidth of the PLL loop filter. The Kalman filter bandwidth is variable and does not include the integrator introduced by the NCO. One approach to calculating the residual error variance using Equation (6.19) is to select a nominal

filter bandwidth that is representative of the typical scalar PLL loop filter bandwidth. An alternative approach to modeling carrier phase error measurement noise was suggested in [45] and is given in Equation (6.20).

$$\sigma_{\phi_1}^2 = \left(\frac{\lambda_{L1}}{2\pi}\right)^2 \frac{1}{2TC/N_0} \tag{6.20}$$

The two equations give approximately the same variance when using a noise equivalent bandwidth of 18 Hz in Equation (6.19). As seen previously in Section 3.8, a noise equivalent bandwidth of 18 Hz is commonly a near optimal PLL bandwidth.

6.2.5 RTK VPLL Measurement Update

As in the VDLL navigation filter, the RTK VPLL measurement updates are performed at the end integrate and dump period on each channel. Therefore the measurement vector only includes a single carrier phase discriminator for the current channel as seen in Equation (6.21).

$$z = \begin{bmatrix} \delta\phi_1 \end{bmatrix} \tag{6.21}$$

The measurement matrix maps the state errors into the measurement domain using the line of sight unit vectors from satellite to receiver. The matrix is defined in Equation (6.22).

$$H = \begin{bmatrix} a_x & 0 & a_y & 0 & a_z & 0 & -1 & 0 \end{bmatrix} \tag{6.22}$$

The column of negative ones relates the relative clock error to the carrier phase residual. The Kalman filter measurement update is performed using the traditional equations defined previously in Equations (4.11).

6.2.6 Carrier Phase Prediction and NCO Calculation

To close the carrier tracking loop, the RTK VPLL state estimates as well as the carrier phase and Doppler measurements from the base station receiver are used to predict the carrier phase of the received signal at the end of the current integration period. The current integration period refers to the integration period that begins directly after the VPLL measurement update. The prediction step begins with the propagation of the base station carrier phase from the time t of the measurement to the end of the current integration period, t_{k+1}. The updated base station carrier phase is calculated by Equation (6.23).

$$\hat{\phi}_{b_{k+1}} = \phi_{b_t} + f_{D_{b_t}}(\hat{t}_{r_{k+1}} - t) \tag{6.23}$$

The k notation is not used with the base station carrier phase measurement because the base station measurements are synchronized to GPS time and are not synchronous with the end of an integration period in the rover tracking channels. In Equation (6.23), ϕ_{b_t} is the most recent base station carrier phase measurement $f_{D_{b_t}}$ is the most recent Doppler measurement from the base station, and $\hat{t}_{r_{k+1}}$ is the receive time of the end of the current integration period calculated in the VDLL predict step.

Next, the RTK VPLL navigation states are projected forward to time $\hat{t}_{r_{k+1}}$ using the state transition matrix defined in Equation (6.17). As in the VDLL, the estimated mean and covariance are not updated at this time. The predicted states are used along with the base receiver predicted carrier phase and the carrier ambiguity to calculate the predicted carrier phase at the rover at time $\hat{t}_{r_{k+1}}$ using Equation (6.18).

$$\hat{\phi}_{r_{k+1}} = \hat{\phi}_{b_{k+1}} + \frac{1}{\lambda}(\vec{a}_{k+1}\hat{\vec{r}}_{r,b_{k+1}} + c\hat{b}_{r,b_{k+1}}) + \mathbf{N}_{r,b} \tag{6.24}$$

The predicted state estimates are used to calculate the line of sight phase difference between the rover and base represented in the equation above by the second term. Note that $\vec{a}_{k+1}$

is the three dimensional line of sight unit vector, $\hat{\vec{r}}_{r,b_{k+1}}$ is the predicted three dimensional relative position vector, and $\hat{cb}_{r,b_{k+1}}$ is the predicted relative clock bias. The carrier ambiguity is initialized using the scalar RTK algorithm and is assumed to be constant during RTK VPLL operation.

The total phase change during the integration period of the sampled signal includes both the Doppler effect and the intermediate frequency of the GPS front end. To calculate the desired carrier frequency setting for the carrier NCO, the total phase change over the integration period is divided by the change in receiver time as defined in the Equation (6.25).

$$f_{\phi} = \frac{f_{IF}(\hat{t}_{r_{k+1}} - t_{r_k}) - (\hat{\phi}_{r_{k+1}} - \phi_{r_k})}{\hat{t}_{r_{k+1}} - t_{r_k}} \tag{6.25}$$

In the above equation, f_{IF} is the intermediate frequency of the GPS front end and ϕ_{r_k} is the current carrier phase measurement of the rover receiver. Note that the change in carrier phase is subtracted due to the fact that the Doppler frequency decreases for increasing range between transmitter and receiver.

6.2.7 Cycle Slip Check

Cycle slips in the carrier phase measurements of the rover receiver have the potential to cause the RTK VPLL navigation filter to diverge from the true relative position and clock states. A cycle slip will manifest as an error between the measured range and the predicted range (using the state vector) for rover to base. As a result, the navigation solution accuracy will be negatively affected, and the prediction of the received carrier phase will degrade. Alternatively, it is possible to correct the slip if it can be detected before the navigation solution is affected.

A cycle slip detection algorithm is designed to identify a cycle slip in a subset of the channels that are tracking satellite signals, and to remove the carrier discriminator provided

by those channels from the Kalman filter measurement update. The cycle slip check is performed at the update rate of the original RTK algorithm using the latest time synchronized rover and base station carrier phase measurements. The first step of the process is to propagate the RTK VPLL state estimates to the time of the current measurements using Equation (6.26).

$$\mathbf{X}(t) = \Phi_{t,t_k}\mathbf{X}_k \tag{6.26}$$

Recall that the state transition matrix, Φ_{t,t_k} was defined in Equation (6.17), and that t is the measurement epoch synchronized to GPS time and t_k is the current best estimates of the RTK VPLL state vector.

The cycle slip test statistic is calculated by comparing the measured single difference carrier phase to the single difference carrier phase predicted by the RTK VPLL state estimates using Equation (6.27).

$$\chi(t) = \Delta\phi_{r,b}(t) + \frac{1}{\lambda}(\vec{a}_t\hat{\vec{r}}_{r,b_t} + \hat{cb}_{r,b_t}) + \mathbf{N}_{r,b} \tag{6.27}$$

In this equation, $\Delta\phi_{r,b}$ is the single difference carrier phase measurement from the rover and base receivers. The middle term is the line of sight delta range as seen previously in Equation (6.24). Again, $\vec{a}_t$ represents the three dimensional line of sight unit vectors, $\hat{\vec{r}}_{r,b_t}$ represents the propagated relative position estimates, and $\hat{cb}_{r,b_t}$ represents the propagated relative clock bias estimate.

The test statistic $\chi(t)$ is calculated in units of cycles, and during normal operating conditions this value should be zero mean with a standard deviation of approximately one percent of a cycle. Recall that the Costas carrier phase discriminator has an effective range of one quarter of a cycle. Therefore, if the error of the carrier phase replica in one channel is larger than one quarter cycle the replica will converge to the next half cycle (i.e. a one half cycle slip). Based on the limits of the carrier discriminator, a threshold of one quarter cycle was selected for comparison with the test statistic. If the test value is greater than one

quarter cycle on a channel, the carrier discriminator from that channel is not used to update the RTK VPLL navigation solution. Assuming there are other channels that are capable of maintaining the accuracy of the RTK VPLL estimates, the fault channel should return to the cycle corresponding to the original carrier integer ambiguity.

6.2.8 Fault Detection and Exclusion

One additional fault detection approach is implemented to prevent large errors from impacting the receiver operation. This approach calculates the normalized innovation on each Kalman filter residual before it is used to update the state estimates. The normalized innovation is calculated by dividing the residual by the expected standard deviation of the residual as seen in Equation (6.28).

$$y_i = \left| \frac{z_i}{H_i P H_i^{\mathrm{T}} + R_{i,i}} \right| \tag{6.28}$$

The residual standard deviation is a function of the state uncertainty and measurement uncertainty. Ideally, the normalized residual follows a Gaussian distribution with unit variance. The test threshold is selected to produce a desired probability of false alarm. A threshold of 3 corresponds to a false alarm rate of approximately 0.3 percent. In the software receiver the cycle slip detection algorithm described previously is used as the precise fault detection method. The normalized innovation is used to detect large errors using very low false alarm rate and therefore the threshold was set to 5, which corresponds to a false alarm rate of approximately 1 in 1.75 million.

6.3 RTK VPLL Performance Analysis

The vector tracking software receiver combines the Doppler aided vector delay locked loop with the RTK VPLL to provide robust high precision positioning. Several have analyzed VDLL code tracking receivers with results available in the literature [9, 40, 51]. In this

dissertation, the performance of the phase tracking algorithm is the critical component. Therefore, the following sections focus on the performance of the carrier phase tracking algorithms. Simulation analysis results on the thermal noise and ionosphere scintillation tracking performance of the receiver are presented in Sections 6.3.1 and 6.3.2. The receiver is then analyzed with intermediate frequency data collected in live sky tests in clear sky, moderate foliage, and heavy foliage environments.

6.3.1 RTK VPLL Thermal Noise Performance

The nonlinear correlator simulator described in Appendix A was used to analyze the performance of the RTK VPLL algorithm as a function of the C/N_0 ratio of the received signal. Three different acceleration variances were simulated to analyze the response of the receiver to variable platform dynamics. The acceleration was modeled as a zero mean Gaussian random variable with standard deviations of either 0, 1, or 3 m/s^2. The three scenarios represent a static platform, a slow moving platform like a pedestrian or small robot, and a moderately dynamic platform like a ground vehicle. The C/N_0 ratio of the received signal was held constant during each simulation, and all channels were simulated with the same ratio. Simulations were performed with C/N_0 ratios ranging from 30 dB-Hz to 20 dB-Hz. During the simulations, it was assumed that the base station receiver had clear lines of sight to the satellites and that the receiver signals were quite strong. The C/N_0 ratios of the signals received by the base station receiver were set to 45 dB-Hz. Twenty simulations of each combination of acceleration variance and C/N_0 ratios were performed. The results of the simulations are summarized below.

First, the static receiver scenario is analyzed. Figure 6.4 shows the critical range of C/N_0 values where the RTK VPLL algorithm began to lose phase lock. In the figure, each plot shows the carrier phase error for all channels and for five simulations. Each simulation is represented by a different color in the figure (i.e. all channels from the first simulation are shown in blue). Clearly, the plot on the left shows that the RTK VPLL algorithm was

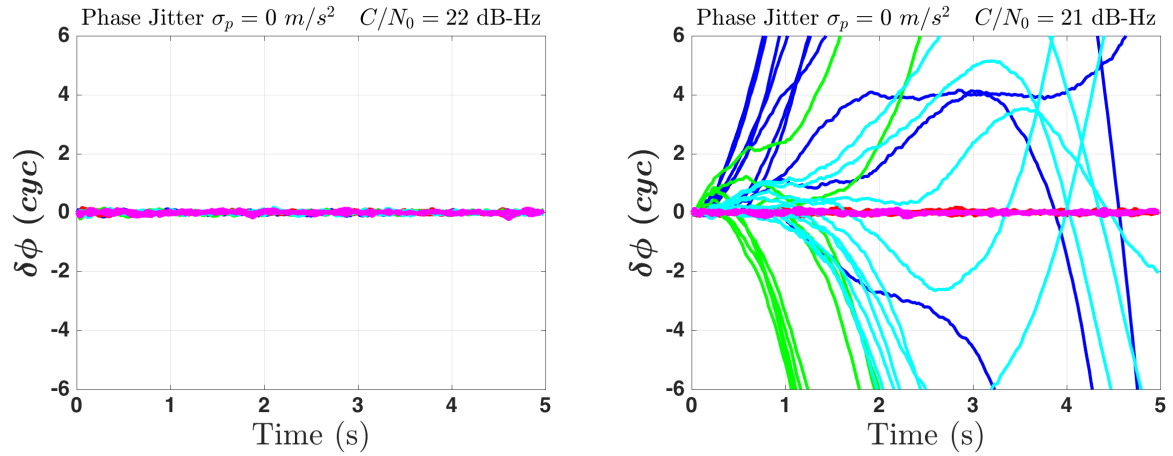

Figure 6.4: RTK VPLL phase tracking results for zero acceleration and C/N_0 ratios of 22 dB-Hz and 21 db-Hz.

able to maintain phase lock on all channels when the C/N_0 ratio of the simulated signal dropped to 22 dB-Hz. On the right we see the point were the RTK VPLL begins to fail at a C/N_0 ratio of 21 dB-Hz. Compared to the scalar PLL results presented in Chapter 4, this represents an improvement of approximately 8 dB. The RTK VPLL algorithm also shows significant improvement over the VFLL aided PLL which began to fail catastrophically at 26 dB-Hz.

The tracking performance of the RTK VPLL architecture is dependent on the accuracy of the navigation solution. To maintain phase lock, the VPLL position solution needs to be accurate to within approximately 5 centimeters. In Figure 6.5, the ECEF position error of the RTK VPLL navigation processor are shown for the same simulations shown in Figure 6.4. The navigation solution is clearly accurate enough to maintain phase lock when the C/N_0 ratio at the rover is 22 dB-Hz. When the C/N_0 ratio drops to 21 dB-Hz, the navigation solution rapidly degrades in three of the five simulations shown here. The three simulations that resulted in failure show the propensity of the receiver to fail catastrophically when it does fail. This is due to the fact that an error in one channel will affect all other channels. This was the motivating factor for the fault detection and cycle slip algorithms. Unfortunately, at low C/N_0 ratios it is difficult to distinguish faults in the carrier phase discriminators. Despite

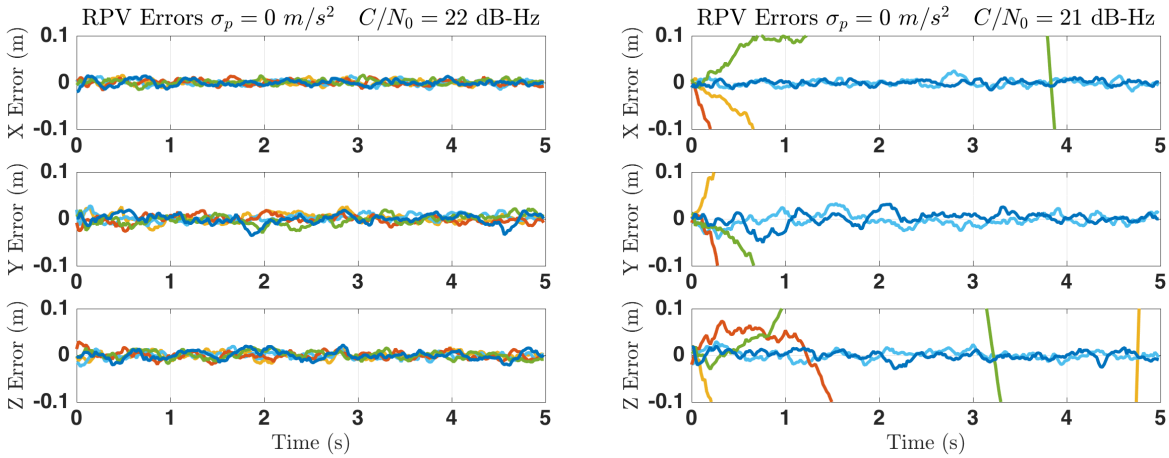

Figure 6.5: RTK VPLL relative positioning results for zero acceleration and C/N_0 ratios of 22 dB-Hz and 21 db-Hz.

this weakness, the RTK VPLL receiver shows considerable improvement in thermal noise performance over traditional tracking approaches. In two of the five simulations shown here, the RTK VPLL tracking algorithm was able to maintain an accurate navigation solution and maintain phase lock down to 21 dB-Hz.

Figure 6.6 shows the impact of adding receiver dynamics to the simulations. A modest random acceleration with a standard deviation of 1 m/s^2 was added for this study. In the figure, it is clear that the RTK VPLL performance is degraded slightly by the receiver motion. This is due to the fact that the process noise matrix values must be increased slightly to account for the unknown dynamics. As a result, the steady state Kalman gain is increased yielding a higher effective noise equivalent bandwidth of the vector loop filter. Under these conditions, phase lock was lost on two of five simulations at a C/N_0 ratio of 22 dB-Hz as seen in the plot on the right. In one of five simulations plotted on the left, the receiver experienced a cycle slip with the carrier to ratio at 23 dB-Hz, but this cycle slip did not cause catastrophic failure of the RTK VPLL tracking loop.

The impact of the cycle slip on the navigation solution can be seen in Figure 6.7. On the left, the blue line shows the ECEF x, y, and z position errors for that particular simulation. The solution does not diverge, but the error settles to approximately 0.5 centimeter in the

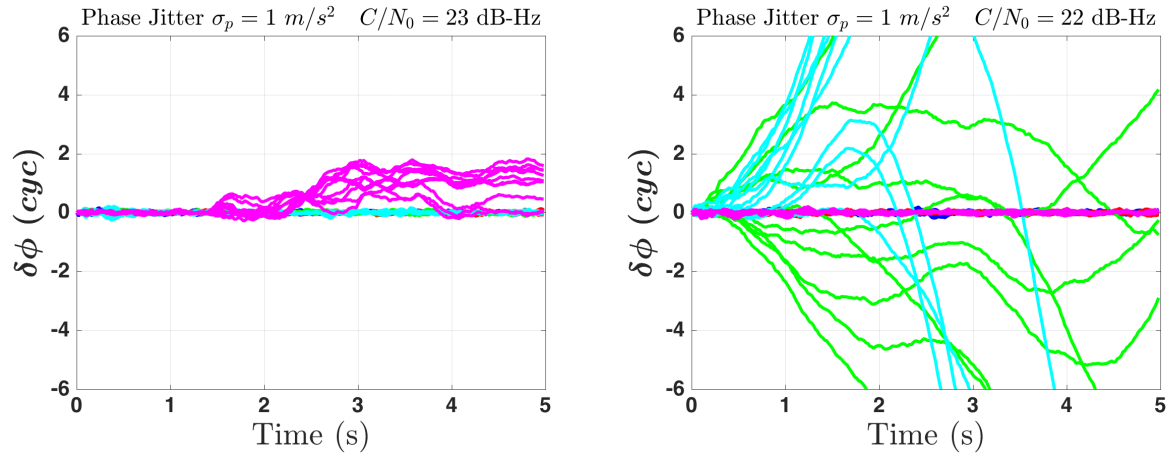

Figure 6.6: RTK VPLL phase tracking results for low acceleration and C/N_0 ratios of 23 dB-Hz and 22 db-Hz.

x direction and approximately 2 cm in the y and z directions. In this case, the RTK VPLL carrier phase prediction is accurate in terms of the fractional phase, but the carrier ambiguity has increased by one cycle on all channels. This indicates that the RTK VPLL receiver is capable of operating with small errors in the fixed carrier phase ambiguities at the expense of increased navigation solution errors. As with the carrier phase error plots in Figure 6.6, it is clear in the plot on the right that the navigation solution has diverged from the true RPV resulting in loss of phase lock in two of the five simulations at 22 dB-Hz C/N_0.

As the platform accelerations increase, so to does the minimum C/N_0 ratio that the RTK VPLL receiver can track. In the next set of simulations the standard deviation of the simulated acceleration was increased to 3 m/s^2. The process noise matrix of the RTK VPLL Kalman filter was adjusted to account for the increase in model uncertainty. The carrier phase errors for five simulations showing the limits of the RTK VPLL tracking performance are provided in Figure 6.8. The results for two different C/N_0 ratios are shown in the figure, 25 dB-Hz and 24 dB-Hz. The plot on the left shows that the receiver struggles to maintain phase lock when the C/N_0 ratio is 25 dB-Hz. At that signal strength, the receiver loses lock on the carrier phase in two of the five simulations that are shown in the figure. At 24 dB-Hz, the receiver loses lock in three of five simulations. These results represent an improvement

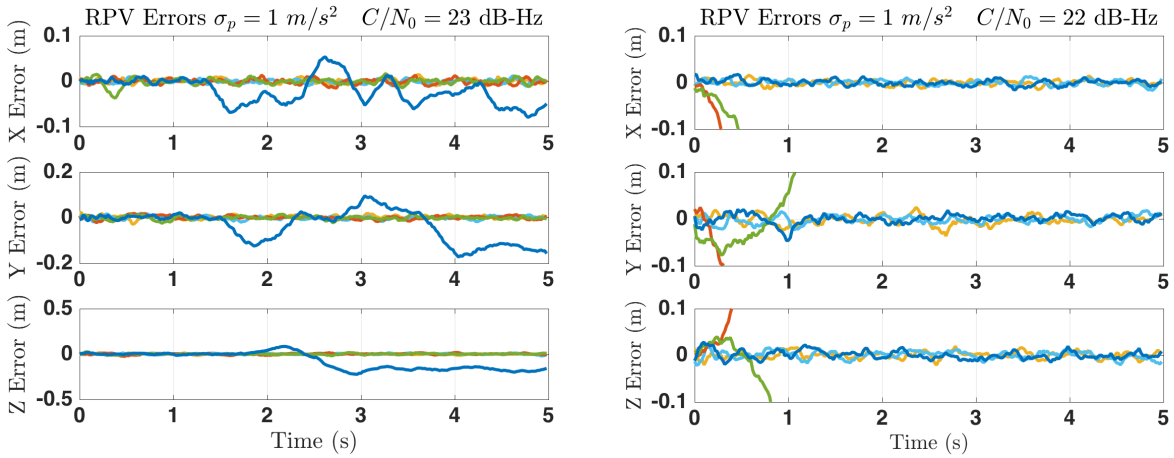

Figure 6.7: RTK VPLL relative positioning results for low acceleration and C/N_0 ratios of 23 dB-Hz and 22 db-Hz.

over the VFLL aided PLL architecture (shown in the previous chapter) which began to slip cycles at 29 dB-Hz and failed at 26 dB-Hz.

The RPV estimation results for the moderate acceleration simulations are shown in Figure 6.9. Again, the limits of the tracking capability of the receiver at low signal strengths is shown. When the receiver maintains phase lock, the accuracy of the RPV estimates appears consistent with the expected RTK accuracy (e.g. centimeter level). However, the RTK VPLL receiver does not often slip cycles without completely losing lock on the carrier phase of the received signal. The RTK VPLL receiver has been shown to provide superior performance in terms of maintaining carrier phase lock at lower C/N_0 ratios. It also has been shown to fail catastrophically when operating beyond the limits algorithm.

To better analyze the loss of phase lock condition of the RTK VPLL algorithm, the accuracy of the Kalman filter RPV estimates are examined in the measurement domain. In order for the carrier phase discriminator from each channel to provide accurate phase error information, the carrier NCO must provide a carrier replica that is accurate within the range of the discriminator (one quarter cycle for the Costas phase discriminator). The RPV errors are estimated in ECEF coordinates, and are mapped onto the line of sight vector from receiver to satellite using the unit vectors calculated in the Kalman filter. It is

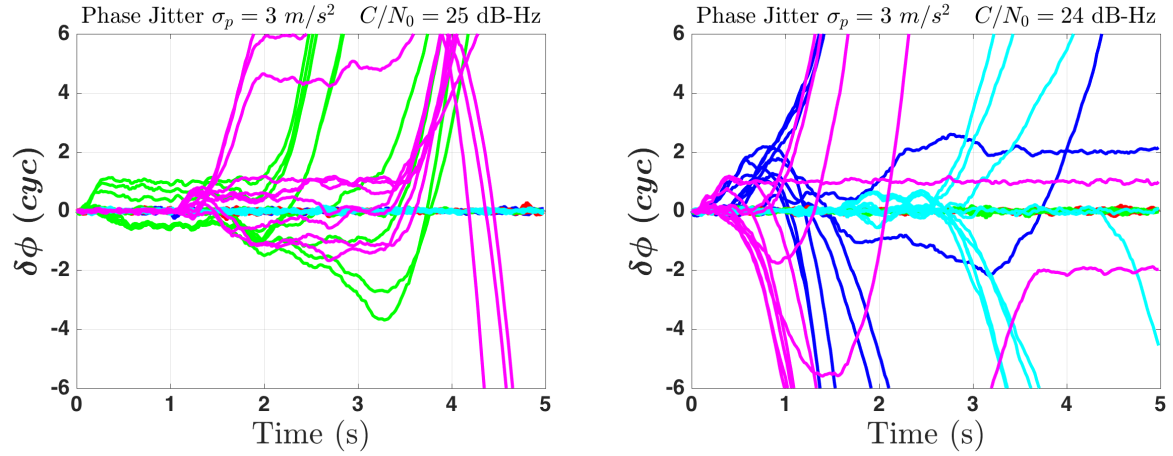

Figure 6.8: RTK VPLL phase tracking results for moderate acceleration and C/N_0 ratios of 25 dB-Hz and 24 db-Hz.

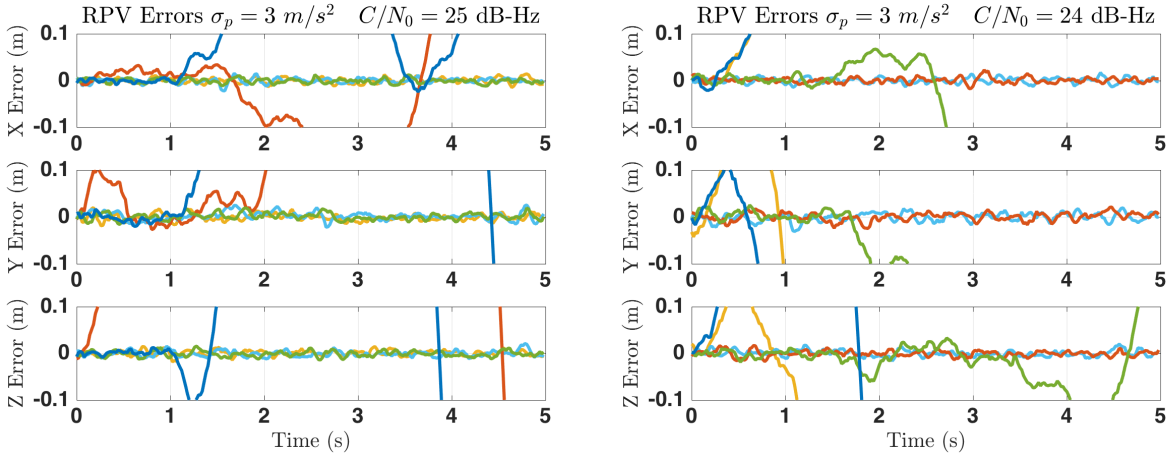

Figure 6.9: RTK VPLL relative positioning results for moderate acceleration and C/N_0 ratios of 25 dB-Hz and 24 db-Hz..

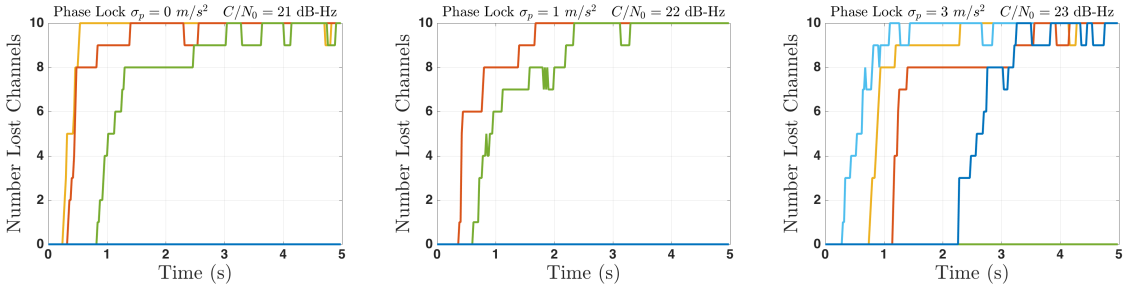

Figure 6.10: RTK VPLL lock detection for zero, low, and moderate acceleration near the limit of tracking capability.

assumed that the RTK VPLL algorithm will maintain phase lock as long as four or more local carrier replicas are generating accurate carrier phase discriminators. This means that the RPV error map into the measurements domain must be less than one quarter cycle for at least four satellite signals that are being tracked. Loss of lock occurs when less than four channels have line of sight phase errors that are less than one quarter cycle. To evaluate the RTK VPLL loss of lock performance, the number of channels with errors greater than one quarter cycle are shown in Figure 6.10. Each plot shows five of the twenty simulations. The three separate plots show the result for the static, low dynamic, and moderate dynamic simulations. Only the results for one C/N_0 ratio are presented. Note that nine satellites are being tracked in each simulation. This means that six or more lost channels indicates a loss of phase lock for the vector receiver. In the figure, vector loss of lock typically occurs quickly after the phase error exceeds the one quarter cycle threshold on one channel. In most cases, the number of lost channels reaches six within one tenth to two tenths of a second after the first channel is lost. Again, this is due to the fact that errors in one channel affect the accuracy of the navigation filter, and indirectly degrade the carrier replicas of the other channels.

For each simulated C/N_0 ratio, the average phase error was calculated for the three different acceleration models. The results are compiled in Figure 6.11. This figure gives an indication for the carrier phase tracking capability of the RTK VPLL for these dynamic scenarios. Clearly, increasing the standard deviation of the simulated acceleration degraded

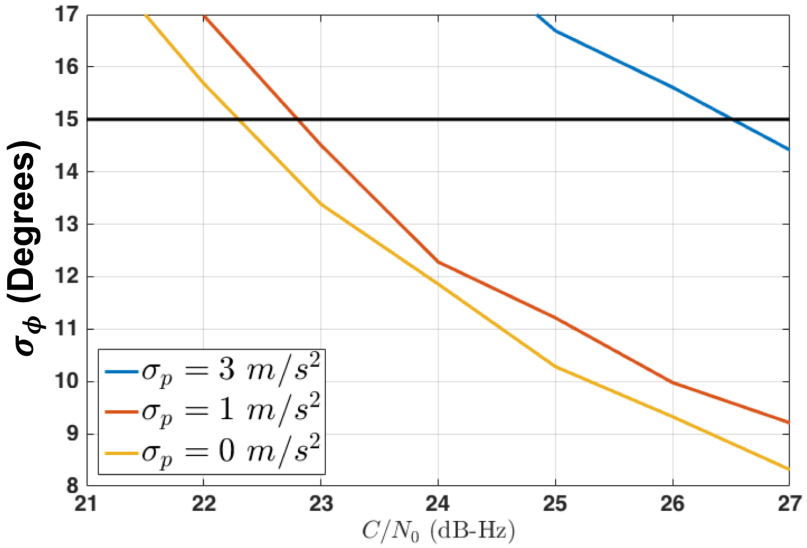

Figure 6.11: Standard deviation of carrier phase error of RTK VPLL receiver as a function of C/N_0 and platform acceleration.

the performance of the RTK VPLL receiver. At low dynamics, the RTK VPLL receiver was able to maintain phase lock at significantly lower C/N_0 ratios than the VFLL aided PLL receiver. The improved tracking sensitivity was more modest for higher accelerations, but recall that the VFLL aided PLL tests only included static receiver simulations. Figure 6.11 shows the RTK VPLL receiver can maintain phase lock reliably at C/N_0 ratios of approximately 22 to 23 dB-Hz with low platform dynamics.

The mean and standard deviation of the RPV estimate errors were also calculated for each C/N_0 ratio. The results are presented in Figure 6.12. The statistics were calculated for those simulations in which the receiver maintained phase lock on at least four satellite signals. In the plot on the left, the mean RPV errors for each of the dynamic scenarios are approximately zero mean with centimeter level standard deviations. The standard deviations plotted in the image on the right show that error variances increase as a function of decreasing C/N_0, and that the standard deviations increase faster for the simulations of higher dynamics. Overall, the figure demonstrates that the RPV estimation errors are zero mean with standard deviations on the order for centimeters for all scenarios wherein the

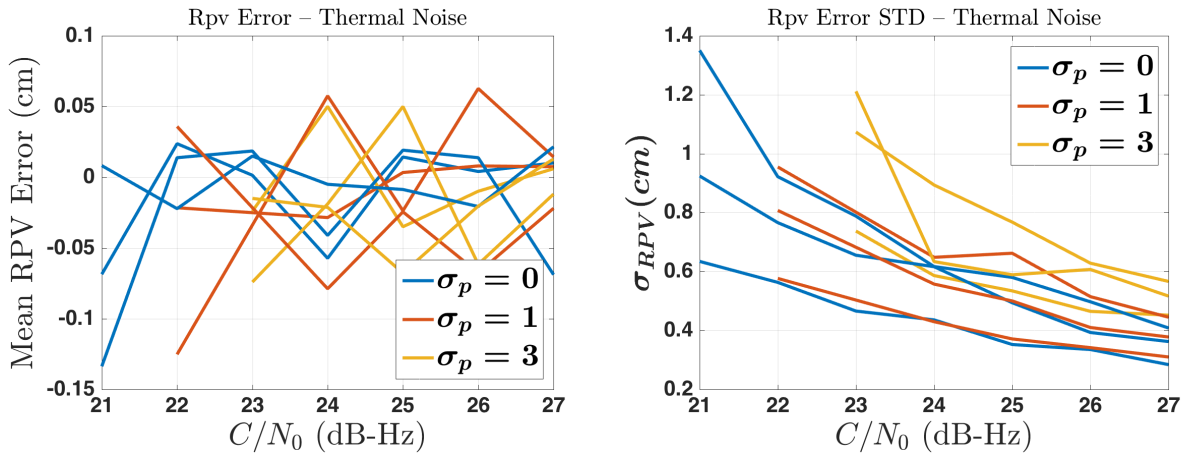

Figure 6.12: RTK VPLL relative positioning error means and standard deviations as a function of C/N_0 ratio and platform acceleration.

receiver is able to maintain phase lock. This is true regardless of the carrier to ratio of the received signal.

The statistical results of the RTK VPLL thermal noise performance analysis are compiled in Table 6.1. Included in the table are the C/N_0 ratios that were simulated, the phase standard deviations (σ_ϕ) in units of degrees, the percentage of simulations in which vector phase lock was lost, and the mean time to failure of those simulations. The results are shown for the static, low platform dynamics, and moderate platform dynamics simulations. Overall, the RTK VPLL phase tracking performance degrades slightly as the receiver dynamics increase as seen in previous figures. For lower dynamic scenarios, the receiver maintains phase lock at C/N_0 ratios as low as 22 dB-Hz.

6.3.2 RTK VPLL Scintilllation Performance

The nonlinear correlator simulator was also used to analyze the carrier phase tracking performance of the RTK VPLL vector tracking receiver in the presence of ionospheric scintillation. Ionospheric scintillation was simulated using the technique described in Section 3.4.2 for both the rover and base station receivers. In the simulation, all satellite signals were assumed to be corrupted with either mild, moderate, or strong scintillation with the

Table 6.1: RTK VPLL Thermal Noise Performance Simulation Results

	$\sigma_p = 0\ m/s^2$			$\sigma_p = 1\ m/s^2$			$\sigma_p = 3\ m/s^2$		
$\frac{C}{N_0}$	σ_ϕ	% *Lost*	MTTF	σ_ϕ	% *Lost*	MTTF	σ_ϕ	% *Lost*	MTTF
26	9.3	0.0	0.0	10.0	0.0	0.0	15.6	0.0	0.0
25	10.3	0.0	0.0	11.2	0.0	0.0	16.7	40.0	0.35
24	11.9	33.0	0.48	12.3	10.0	0.11	18.6	60.0	0.73
23	13.4	20.0	0.28	14.5	10.0	0.47	23.8	80.0	0.90
22	15.7	0.0	0.0	17.0	40.0	0.25	*NA*	100.0	0.82
21	18.3	40.0	0.39	*NA*	100.0	0.46	*NA*	100.0	0.64
20	*NA*	100.0	0.35	*NA*	100.0	1.07	*NA*	100.0	0.49

same decorrelation times and S4 indexes used in the simulation study presented in Chapter 4. The scintillation induced amplitude fades and carrier phase variations were simulated based on the transmit time of the signal from each satellite in view. The changes in the received signals of the rover and base receiver were therefore highly correlated with slight variations due to differences in the true received time of the signal. As in the thermal noise simulation analysis, three different receiver acceleration variances were simulated to emulate static, low dynamic, and moderate dynamic trajectories for the rover receiver. The base station receiver was modeled as a static receiver. Twenty simulations of each scenario were performed, and the results of the simulation study are presented in the next several figures and tables. Note that only the moderate scintillation experiments are discussed in detail below due to the fact that the mild scintillation did not significantly impact receiver operation, and the strong scintillation caused loss of lock in all twenty simulations.

First, the carrier phase errors for each simulation are shown in Figure 6.13. Each plot shows the results for one acceleration model with the static results on the left, the low dynamic results in the middle, and the moderate dynamic results on the right. Both the rover and base station carrier phase errors are shown in the figure to highlight any cycle slips that occur in the base station receiver. Note that yhe base station receiver is operating in the static base vector aided mode that was described in Section 4.5. In the figure, there are two

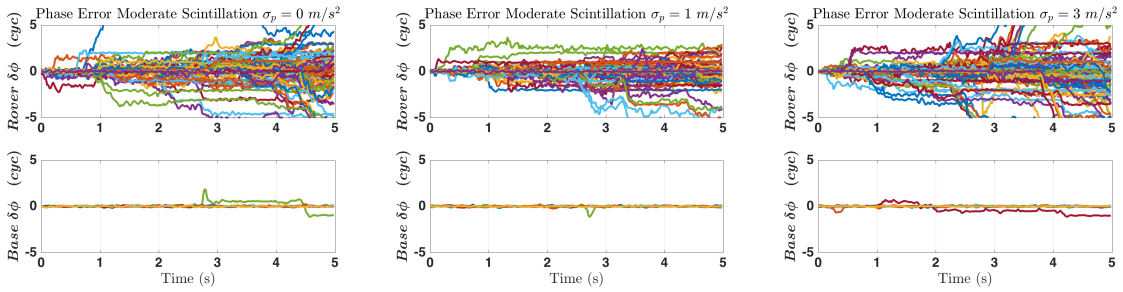

Figure 6.13: Carrier phase tracking errors for rover RTK VPLL receiver and base receiver in moderate ionosphere scintillation.

simulations in which there is cycle slip at the base station receiver. The carrier phase error for the rover receiver shows several cycle slips, but the receiver rarely fails catastrophically. There is little difference in the results of the static and low dynamic simulations, but the moderate dynamic simulations show increased error and cycle slipping.

Table 6.2 shows the numerical carrier phase tracking performance results of the mild, moderate, and strong scintillation simulations. As stated previously, the mild scintillation had no impact of the receiver performance, and the strong scintillation caused catastrophic failure in all simulations. The carrier phase error standard deviation (σ_ϕ) of 45.4 degrees is well beyond the reliable tracking threshold. In the moderate scintillation simulations, the standard deviation of the carrier phase errors is nearly 20 degrees. This is slightly higher than the rule of thumb 15 degrees threshold for reliable tracking, but this does include some cycle slip that result in errors of one or two cycles. These small errors do not always cause the RTK VPLL filter to break down. To prevent long term accuracy issues, these cycle slips would need to be corrected. A secondary RTK algorithm could be used to track changes in the carrier ambiguities, and the fixed integers used in the RTK VPLL prediction stage could be updated to reflect the changes.

The table also shows that 25 percent of the static and low dynamic simulations and 45 percent of the moderate dynamic simulations resulted in loss of lock. These numbers are also somewhat pessimistic due to the fact that a few cycle slips could result in enough error to cause the receiver to fail the vector loss of lock test. While it is true that the carrier

Table 6.2: RTK VPLL Scintillation Tracking Performance Simulation Results

	Mild	Moderate			Strong
	$\sigma_p = 1m/s^2$	$\sigma_p = 0m/s^2$	$\sigma_p = 1m/s^2$	$\sigma_p = 3m/s^2$	$\sigma_p = 1m/s^2$
σ_ϕ	8.5	21.6	21.4	23.9	45.4
$\%Lost$	0	25.0	25.0	45.0	100.0
MTTF	NA	0.28	0.21	0.30	0.17

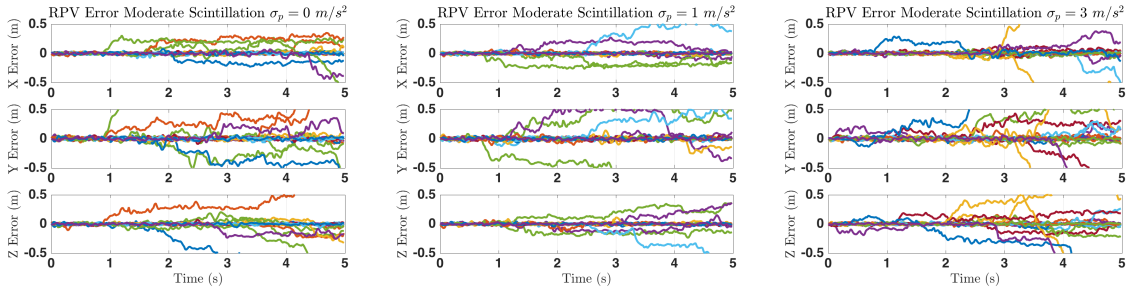

Figure 6.14: RTK VPLL relative positioning results for moderate ionosphere scintillation at zero, low, and moderate accelerations.

ambiguity has changed and the RPV estimates are degraded, it does not indicate that the receiver phase tracking has completely failed. Again, it may be possible to correct the carrier ambiguities in run to correct the navigation solution.

Next, the accuracy of the RPV estimates of the RTK VPLL navigation processor are examined. The RPV errors for the three dynamic scenarios and the moderate scintillation simulations are shown in Figure 6.14 where it is clear that the RPV estimates are maintained with centimeter level accuracy in several simulations for each of the dynamic cases. There are also several simulations where cycle slips degrade the RPV accuracy. Overall, the RPV errors are largely bounded between plus and minus one half meter.

The RPV estimation error was again mapped onto the line of sight vectors from the rover receiver to each satellite to analyze the loss of lock. The number of channels for which the line of sight navigation errors was greater than one quarter cycle are shown in three plots in Figure 6.15. Each simulation is represented by a different color in Figure 6.15. Unlike the loss of lock analysis for the thermal noise simulations, in this scenario the number of

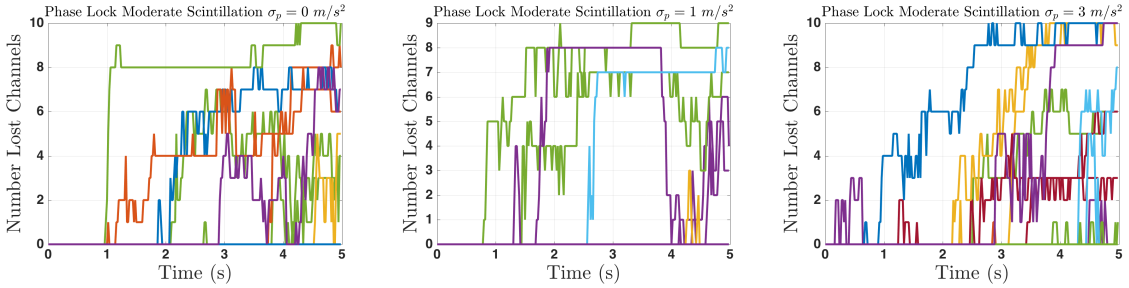

Figure 6.15: RTK VPLL phase lock detection for moderate ionosphere scintillation at zero, low, and moderate accelerations.

lost channels does not increase monotonically. The number of lost channels varies rapidly with increases and decreases. This is due to the rapid phase and amplitude changes that are caused by the ionospheric scintillation. In some cases, the phase can change by a whole cycle over one or two integration periods. The receiver may temporarily lose lock on a channel only to recover phase lock after several integration periods. Often the receiver will have slipped one or more cycles in that time. In the static and low dynamic plots, approximately five of twenty simulations result in more than five lost channels and loss of vector phase lock.

The mean and standard deviations of the ECEF x, y, and z RPV estimation errors are tabulated in Table 6.3 (in units of centimeters). Note that the statistics are calculated for the simulation in which vector phase lock was maintained to assess the accuracy of the algorithm when phase locked. The RTK VPLL algorithm maintained phase lock in approximately 68 percent of the moderate scintillation simulations including the static, low, and moderate acceleration profiles. The mean RPV error is less than one centimeter in each direction, and the standard deviation is on the order of a few centimeters. This level of accuracy is consistent with typical RTK GPS positioning.

One additional note on the RTK VPLL scintillation study is included. In several simulations, the base station receiver experienced a cycle slip. As a result, the fixed integers used by the RTK VPLL algorithm were incorrect by one or more cycles. Several of these instances did not result in errors in the RPV estimates of the RTK VPLL navigation processor. One

Table 6.3: RTK VPLL Scintillation RPV Estimation Simulation Results

Moderate

(cm)	$\sigma_p = 0m/s^2$	$\sigma_p = 1m/s^2$	$\sigma_p = 3m/s^2$
μ_x	0.10	0.10	0.19
μ_y	0.95	-0.33	0.34
μ_z	0.36	-0.36	-0.55
σ_x	1.30	1.30	1.60
σ_y	2.20	2.50	3.20
σ_z	1.50	1.40	2.70

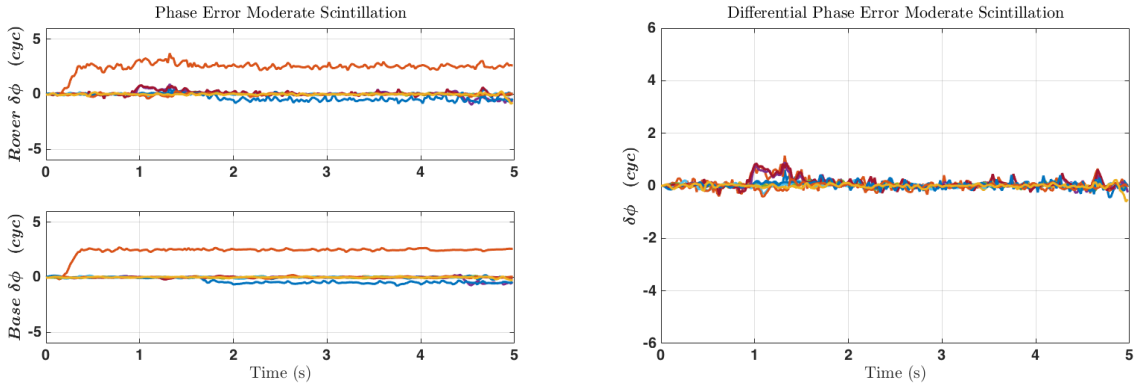

Figure 6.16: Common cycle slips by rover and base receivers do not cause loss of lock in RTK VPLL receiver.

such incident is shown in Figure 6.16. In the figure, the cycle slips at the base station receiver are clear. In response, the rover receiver also slips cycles to match the base station receiver. In this case the inherent carrier ambiguities in the carrier phase measurements of the rover and base have changed be two and one half cycles on one channel (seen in orange) and one half cycle on another channel (seen in blue). Due to the fact the both receivers contain the same cycle slip, the differential carrier phase error is still zero mean, as seen in the right hand plot in Figure 6.16. The RPV estimation error from this simulation is shown in Figure 6.17. Clearly, the RPV estimates are maintained with centimeter level accuracy, and the RTK VPLL algorithm is able to predict the rover carrier phase with phase lock precision. Recall

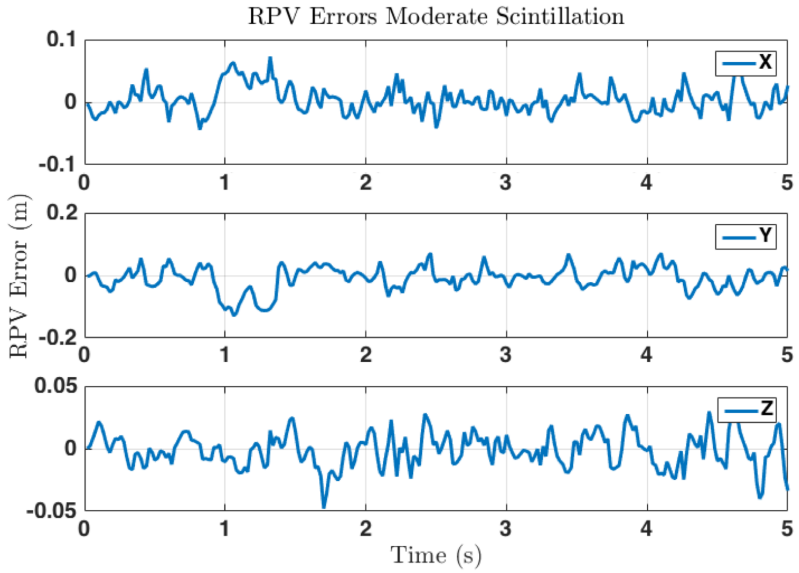

Figure 6.17: RTK VPLL relative positioning results for moderate scintillation induced cycle slips at the base receiver.

that the correlator only requires that the fractional phase be accurate enough to generate an accurate carrier phase discriminator.

6.3.3 RTK VPLL Experimental Performance

Intermediate frequency (IF) GPS data was collected and post processed in a variety of conditions to analyze the performance of the RTK VPLL vector tracking receiver in real world settings. Three clear sky tests, two static and one dynamic, were conducted to analyze the accuracy of the differential carrier phase based navigation solution as compared to a RTK reference solution. These experimental tests mirror the tests of the software RTK receiver seen in Chapter 5, but the results present here are generated using the RTK VPLL receiver. Data was also collected while driving near the Auburn University campus in areas where tree covers and buildings affected the sky visibility. The degraded GPS environment tests were conducted in areas that are designated as moderate or heavy foliage environments in this dissertation. The moderate foliage environments are characterized primarily by tree lined multi-lane roads where the sky view was regularly disrupted by trees, particularly to one

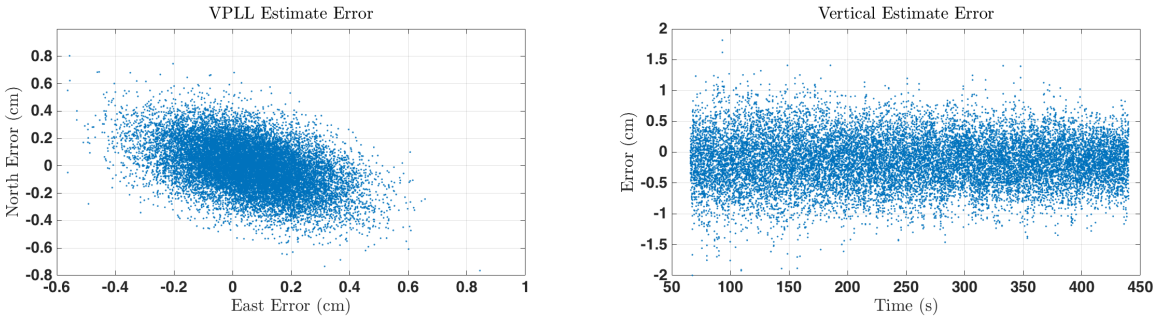

Figure 6.18: The horizontal and vertical errors of the RTK VPLL receiver are consistent with the high precision positioning of a carrier phase differential GPS solution.

side of the vehicle. In the heavy foliage environments, large portions of the sky were blocked by dense tree cover on narrow neighborhood streets. For more details on the data collection, test vehicle, reference solution, and environments see Appendix C.

The first experimental analysis of the RTK VPLL architecture was performed under ideal conditions. The signal from one antenna mounted on the roof of the building was recorded by two GPS front-ends. The sample clocks of the front-ends were synchronized to a common reference signal, and approximately ten minutes of data was collected. The intermediate frequency samples were post processed using the vector tracking software receiver that incorporated the VDLL and RTK VPLL code and carrier tracking loops. In this scenario, the true relative position vector and relative clock drift are known to be zero. Therefore, it is straightforward to analyze the accuracy of the relative position and relative clock estimates.

First in Figure 6.18, the horizontal and vertical relative position estimation errors are provided. The plot on the left shows the errors in the East and North directions in units of centimeters. On the right, the error in the vertical direction is plotted versus time. In both plots, the vast majority of the errors are sub-centimeter which is consistent with RTK GPS positioning accuracy. The errors also appear to be zero mean. The error statistics are presented later in Table 6.4 along with the other clear sky results.

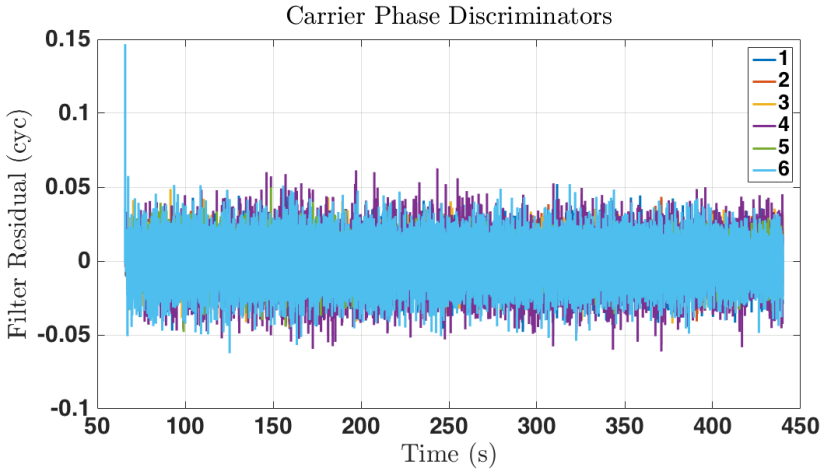

Figure 6.19: Carrier phase discriminator outputs shows the accuracy of the local replicas generated by the RTK VPLL receiver.

The RTK VPLL Kalman filter residuals, seen in Figure 6.19, show the accuracy of the carrier phase tracking algorithm. The carrier phase errors are calculated using the in-phase and quadrature correlator outputs and the Costas discriminator. This figure shows the accuracy with which the RTK VPLL is able to predict the carrier phase of the received signals at the rover receiver using the base station measurements and the estimated relative position and clock bias. The errors in the local carrier replicas generated by the vector receiver are less than five percent of a cycle (corresponding to approximately 1 cm).

Since a common reference oscillator was used to drive the sample clocks of each GPS front-end during the data collection, the true relative clock drift is approximately zero (small variations are possible due to the separate front-end hardware). Therefore, the accuracy of the relative clock estimates are easily identified by the estimated relative clock drift. The relative clock drift estimate from the RTK VPLL navigation processor is shown in Figure 6.20, showing that the relative clock drift error is on the order of a few millimeters per second. This is consistent with the clock drift errors calculated from the delta carrier phase estimator described in Chapter 5 when the software receiver was operating in scalar tracking mode.

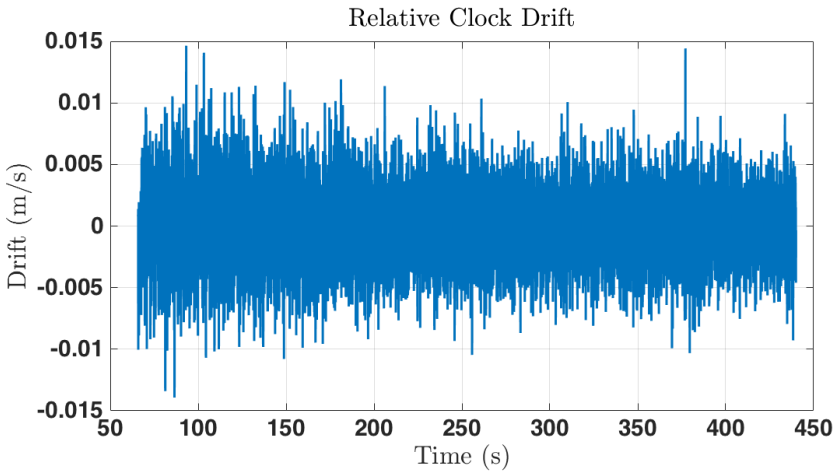

Figure 6.20: The RTK VPLL relative clock drift estimates are zero mean with a standard deviation on the order of a few millimeter per second when using a common reference oscillator.

A second static test was performed to analyze the RTK VPLL accuracy over a longer separation distance. In this test, the base station and rover receivers were located approximately 600 meters apart with a vertical displacement of approximately 30 meters. The reference relative position vector was calculated by averaging ten minutes of high precision RTK position solutions from a survey grade GPS receiver. The RTK VPLL algorithm was initialized with the first integer fixed from the scalar RTK algorithm as described in Section 6.2.1. The relative position vector estimation error in the horizontal and vertical directions is presented graphically in Figure 6.21. The errors in the East and North directions are shown in the scatter plot on the left in units of centimeters. Clearly, the accuracy of the RTK VPLL navigation processor was not significantly impacted by the separation distance. The error is again centimeter level and approximately zero mean. The relative vertical position estimates are also accurate to within a few centimeters, but show a slight bias relative to the reference solution. This is approximately the same bias calculated previously using the carrier phase measurement from the scalar software receiver in Chapter 5.

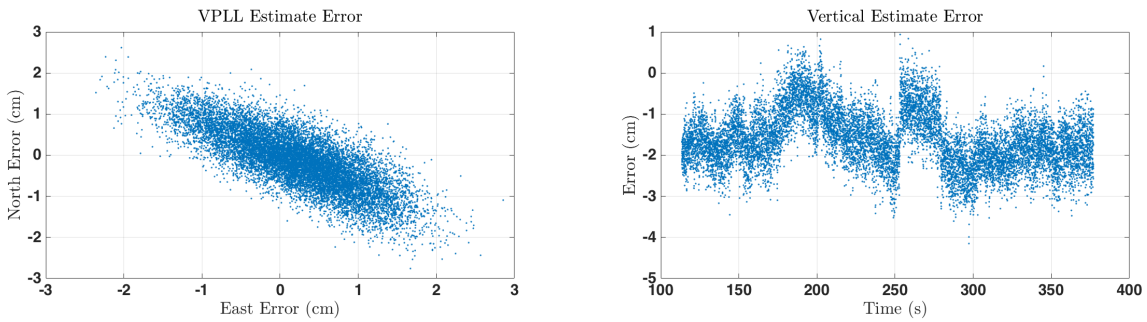

Figure 6.21: The RTK VPLL position solution accuracy is maintained over longer static 600 meter baseline.

In Figure 6.22, the carrier phase discriminator values are shown for the long baseline static test. The residuals are slightly larger than in the ideal case, and show signs of a random walk. It is important to note that the residual shown in the figure is a combination of the carrier phase discriminator and a correction term used to account for the asynchronous updates of the Kalman filter. As described in Section 6.1.4, the discriminator output is referenced to the Kalman filter state estimate at the start of the integration period. Between the start and the end (when the discriminator is calculated) of an integration period, the Kalman filter state estimates are updated by discriminators from other channels. A correction term is applied to account for the change in the state estimate during the integration period. This correction causes the appearance of correlated noise in the filter residuals.

A plot of the relative clock drift is included for the long baseline test in Figure 6.23. The relative clock drift of the rover and base station receivers is not zero mean when a common reference oscillator is not used. The RTK VPLL must estimate the relative clock drift and bias to accurately predict the carrier phase of the received signal at the rover receiver. For comparison, the relative clock drift was calculated using the Kalman filter clock drift estimates from scalar tracking software receiver. The magnitudes are consistent between the two solutions; however, the RTK VPLL estimates are considerably less noisy.

One additional experiment was performed to assess the accuracy of the RTK VPLL navigation solution accuracy during motion in a clear sky environment. Data was collected

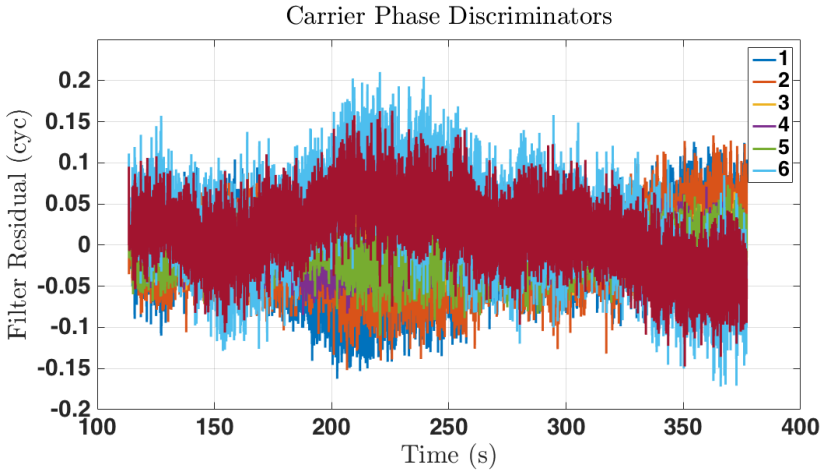

Figure 6.22: Carrier phase residuals are on the order of ten percent of a cycle for the longer 600 meter baseline.

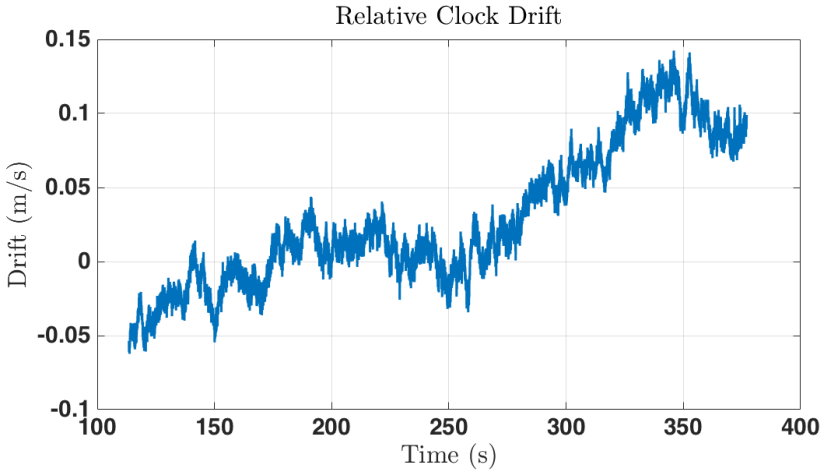

Figure 6.23: The relative clock drift is not zero mean for the base station and rover receiver when they are not driven by a common clock.

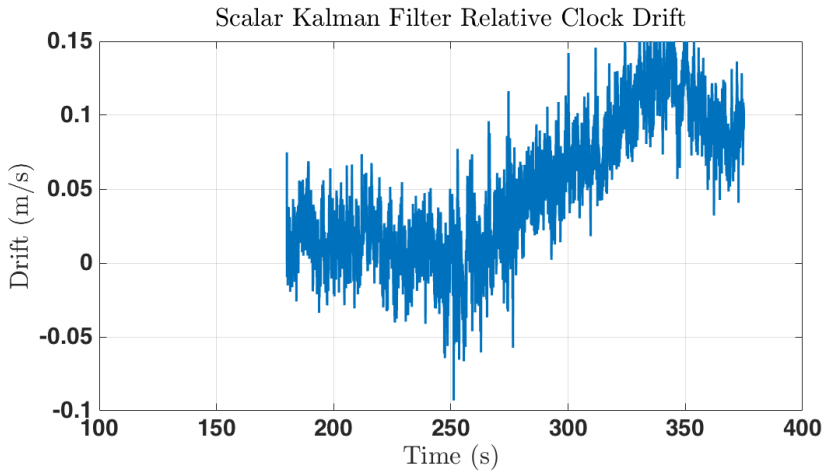

Figure 6.24: The relative clock drift calculated using the scalar Kalman filter clock drift estimates illustrates the accuracy of the RTK VPLL estimates.

using the intermediate frequency data recorder while the test vehicle traversed at slow speeds around an open field. The vehicle was driven at speeds ranging from three to five meters per second around the field for approximately six minutes. The base station receiver was mounted on the roof of a static vehicle location at the southwest corner of the test site. The separation distance between the base station and the rover receiver varied during the test from 5 to 210 meters.

The horizontal and vertical errors in the RPV estimates from the RTK VPLL navigation processor are shown in Figure 6.25 in units of meters. The scatter plot on the left shows the East and North RPV errors relative to the RTK reference solution. The majority of the errors are less than four centimeters with occasional larger errors near eight centimeters. Note that the accuracy of the reference solution is approximately 2 cm. The vertical error, shown in the plot on the right, shows some transient behavior before the figure converges to a zero mean error solution. The majority of the vertical errors are less than five centimeters.

Figure 6.26 shows the carrier phase residuals used to update the RTK VPLL navigation filter during the dynamic test. The residuals included the carrier phase discriminator and the correction term that accounts for the asynchronous measurement updates as described

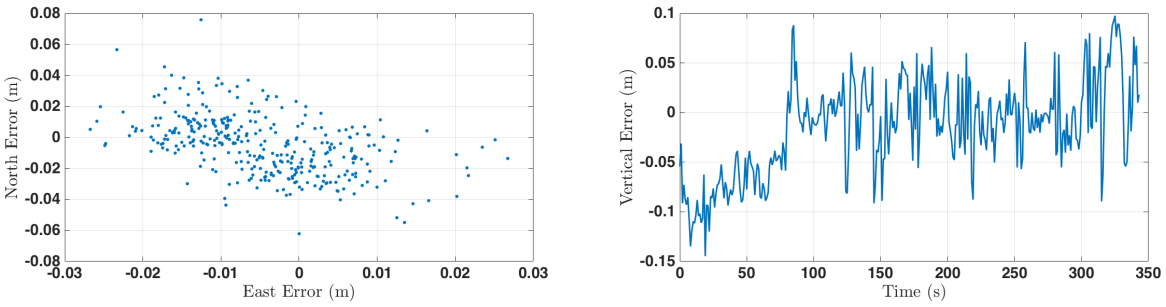

Figure 6.25: The RTK VPLL receiver provides centimeter level positioning during dynamic test.

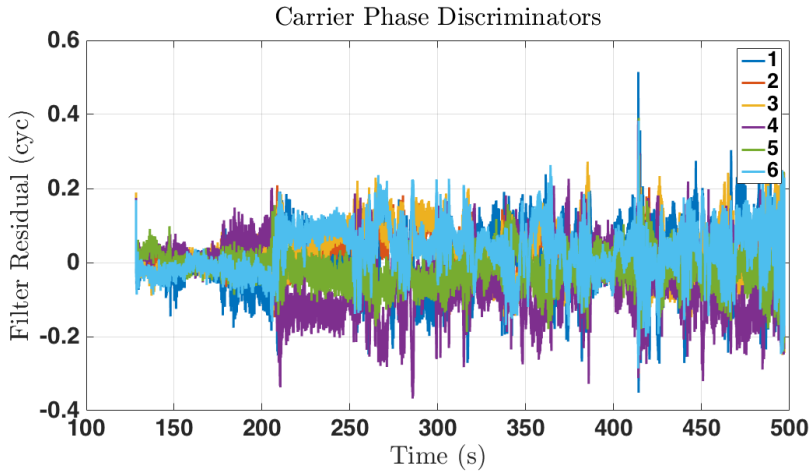

Figure 6.26: RTK VPLL carrier phase discriminator exhibit larger variances during dynamic testing.

above. This is the reason that some errors are larger than the one quarter cycle range of the Costas discriminator. Generally speaking the residual variance is larger during the dynamic testing due to larger differences between the local carrier replica and the receiver carrier signal that are caused by receiver motion. Also, there is a large residual that occurs at approximately the 410 second mark. This larger error was removed by the fault detection and exclusion algorithm, which was described in Section 6.2.8, prior to the measurement update.

A qualitative comparison of the RTK VPLL navigation solution and the reference RTK solution is provided in Figures 6.27 and 6.28. The first images show the Novatel RTK

Figure 6.27: The RTK VPLL position solution is indistinguishable from the reference RTK solution in the first turn of the dynamic test. Imagery by Google, DigitalGlobe.

reference solution along with the RTK VPLL position estimates for the vehicle during the first turn of the dynamic test. The satellite imagery gives an indication of the global accuracy of the two solutions showing that the vehicle followed the gravel path. The figure shows the route of the vehicle as it makes a wide right turn, and then travels down the right hand side of the gravel path as it moves south. This is consistent with the true route driven in the vehicle. Figure 6.28 shows the intersection of three different laps that vehicle made around the gravel path. In all three cases, the reference position estimates and the RTK VPLL position estimates are virtually identical. Note that the reference solution is shown with a bolder line so that both solution are visible in the figure.

Statistics on the position estimation errors of the RTK VPLL receiver, as compared to the RTK reference solution, are compiled in Table 6.4. The mean and standard deviations of the errors during the signal antenna, 600 meter baseline, and dynamics tests are provided. In the table, the mean horizontal errors in the East and North directions are sub-centimeter in both directions for all three tests. The mean vertical error was just over one centimeter in magnitude for the longer baseline and dynamic tests. The standard deviations of the errors

Figure 6.28: The RTK VPLL position and the reference RTK solutions are virtually identical in the image that shows the convergence of multiple laps. Imagery by Google, DigitalGlobe.

are also centimeter level or better. The accuracy of the software vector tracking receiver operating in RTK VPLL mode is consistent with survey grade GPS receivers using RTK corrections from a local base station.

To further evaluate the capabilities and improvement of the software vector tracking receiver, data was collected while driving the test vehicle around the Auburn University campus. The test route traversed areas where the line of sight to the sky was disrupted by tree cover and buildings. The reference antenna was located on the roof of the building in the north central portion of campus. Separation distances between the rover and base station antennas ranged from approximately 100 meters to 1 kilometer. The maximum vehicle speed was approximately 14 m/s. The roads of the test route were mostly tree lined multi-lane roads where the sky view of the antenna was obstructed by trees up to 75 degrees above the horizon.

Figure 6.29 shows the complete test route. The orange dots show the position solution as calculated by the software receiver using the RTK VPLL algorithm. The solution is clearly continuous throughout the route, and following the roads driven during the test. The

Table 6.4: RTK VPLL Experimental Error Statistics

	Separation Distance		
Mean Error	0 meters	600 meters	Variable
East (cm)	0.0563	0.210	−0.473
North (cm)	−0.00538	−0.134	−0.489
Up (cm)	−0.142	−1.61	−1.50
STD Error	0 meters	600 meters	Variable
East (cm)	0.166	0.737	0.955
North (cm)	0.177	0.706	1.89
Up (cm)	0.408	0.685	4.76

blue dots show the high precision RTK reference solution. There are several areas where the reference receiver was unable to maintain phase lock on enough satellite signals to produce a high precision position solution. In some areas, the reference solution appeared to be degraded, possibly due to multipath signals corrupting the carrier phase measurements.

A closer look at the RTK VPLL navigation solution is provided in Figure 6.30 and Figure 6.31. First, the lane level accuracy of the RTK VPLL navigation solution is shown in Figure 6.30. The tree cover at the intersection prevents the reference receiver from reporting a high precision solution. Note that the antenna is mounted on the driver side of the vehicle just outside the frame of the vehicle, and that the vehicle is driving north in the image. The antenna mounting location is consistent with the location of the navigation solution relative to the satellite imagery shown in the figure.

In Figure 6.31, the navigation solution of the RTK VPLL algorithm is shown for the vehicle as it passes Jordan-Hare Stadium. The upper deck of the stadium overhangs the road slightly, blocking a large portion of the sky. As the vehicle passes the stadium, the RTK VPLL navigation processor is not able to maintain position solution accuracy due to a lack of quality carrier phase discriminator. The solution drifts from the correction position of the left edge of the right edge of the lane. This drift is attributable to cycle slips which change the true carrier ambiguities. The RTK VPLL algorithms assumes that the carrier

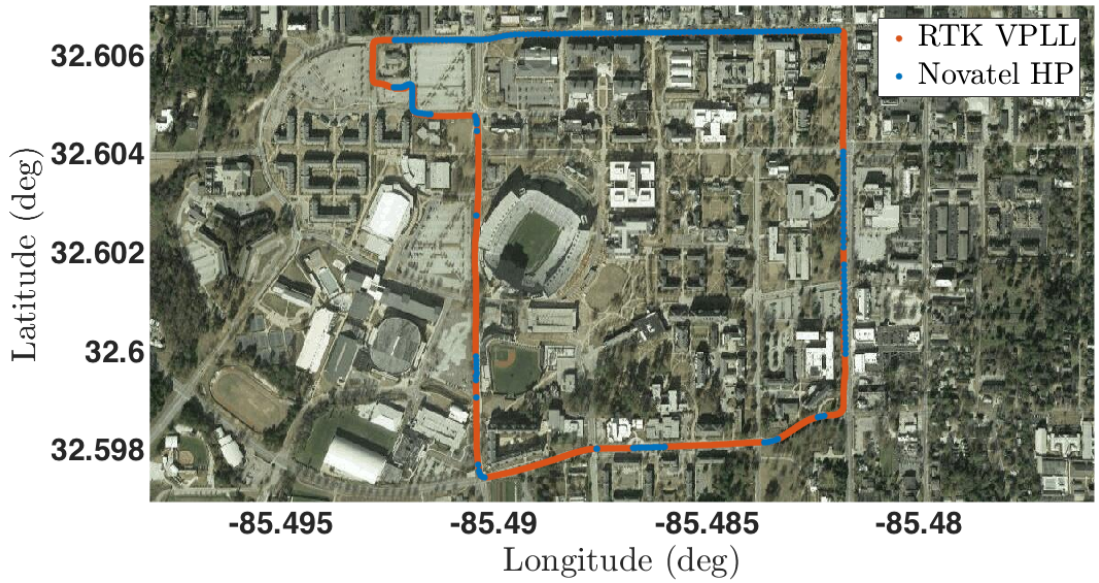

Figure 6.29: The RTK VPLL receiver provided carrier phase positioning throughout the moderate foliage while the reference receiver experienced significant outages. Imagery by Google, DigitalGlobe.

Figure 6.30: The RTK VPLL navigation filter provided lane level accuracy through intermittent heavy tree cover. Imagery by Google, DigitalGlobe.

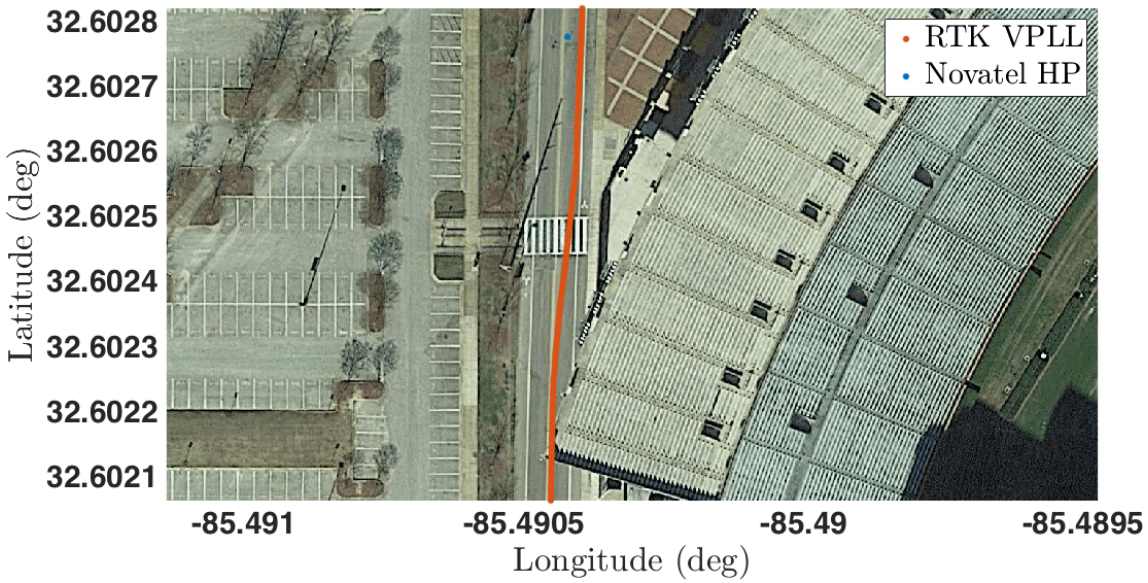

Figure 6.31: The RTK VPLL carrier tracking loop experience cycle slips due to the blockage of a large portion of the sky near Jordan-Hare Stadium. Imagery by Google, DigitalGlobe.

ambiguities are constant, and the algorithm reports a biased solution after the cycle slips. In the image, there is one high precision solution (near the north edge of the plot) for the reference receiver after the vehicle emerges from the shadow of the stadium. The blue dot appears to be an accurate representation of the position of the vehicle.

As a result of the cycle slips that occur in the RTK VPLL algorithm as the vehicle passes the stadium, the estimated position of the vehicle at the end of test is biased from the true position. The estimated positions from the reference receiver and the RTK VPLL receiver are shown in Figure 6.32. The RTK VPLL solution is offset from the true position by approximately 4 to 5 meters. Despite the error in the navigation solution, the RTK VPLL filter was in phase lock at the end of the test. During the test, cycle slips in the carrier phase estimates caused changes to the carrier ambiguities. Since the RTK VPLL navigation solution is dependent on the carrier ambiguity, the ambiguity error causes a bias in the navigation solution. In future versions of the algorithm, a carrier ambiguity correction algorithm can be implemented to correct the erroneous integer estimates in real time.

Figure 6.32: Due to cycle slips, the RTK VPLL navigation solution was in error by several meters at the end of the moderate foliage test. Imagery by Google, DigitalGlobe.

To give context to the positioning results shown above, the number of satellites that were tracked by the reference receiver during the test are shown as a function of time in Figure 6.33. The carrier phase discriminator used to update the RTK VPLL navigation filter are shown in the figure as well. Clearly, the reference receiver was not able to track four or more satellites throughout the run. It is important to note that the number of observations is determined by the number of satellite signals on which the receiver has code phase and carrier frequency lock. There are several additional times when the receiver loses phase lock or slips cycles. On the right, it is clear that the carrier phase discriminator becomes extremely noisy near the 700 second mark of the test. This coincides with the vehicle passing near the stadium. Despite the lack of useful error measurements, the RTK VPLL algorithm is able to recover carrier phase lock after several cycle slips.

The final analysis of the RTK VPLL tracking performance used data collected on narrow neighborhood streets with dense tree cover. In some areas, trees from each side of road met overhead preventing a clear view of any portion of the sky. The antenna mounted on the

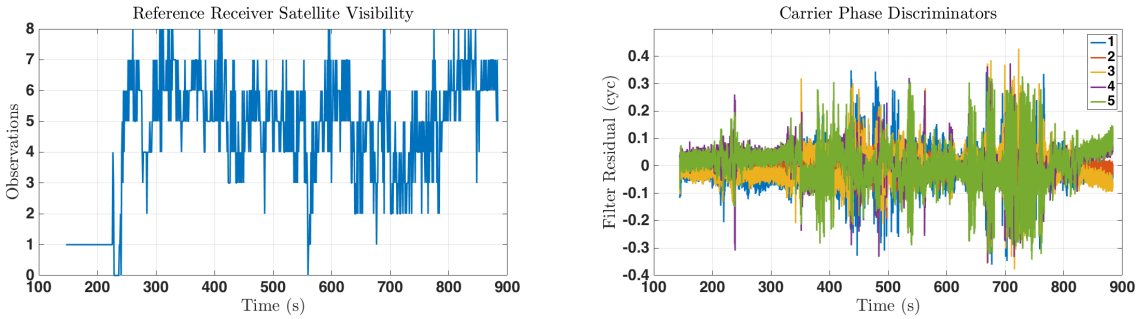

Figure 6.33: The reference receiver was not able to report a pseudorange navigation solution for portions of the moderate foliage test route. The carrier discriminator of the RTK VPLL saturated when the vehicle passed near Jordan-Hare Stadium.

roof of the building was used as the base station, and the distance from the vehicle to the base station ranged from approximately 100 meters to just over 3 kilometers. Data was collected for approximately twenty-five minutes as the test vehicle was driven through the area of heavy foliage. The maximum speed of the test vehicle was approximately 15 m/s during the test.

The complete heavy foliage test route is shown in Figure 6.34. In the figure, the path of the vehicle begins in the north west corner of the image in a large parking lot with a clear view of the sky. For the first third of the route, the reference receiver reports a high precision solution with short disruptions. As the vehicle moves into the heavily wooded neighborhood, the reference receiver is not able to maintain carrier phase lock on enough satellite signals to calculate a high precision solution. The RTK VPLL receiver is able to maintain a navigation solution throughout the test although the solution accuracy is degraded in some areas as seen below.

The robustness and accuracy of the RTK VPLL navigation solution can be seen in Figure 6.35. The estimated position of the vehicle remains within the lane as shown by the satellite imagery as the vehicle moves along a densely wooded street. As noted previously, the antenna was mounted on the driver's side of the vehicle. In the image, the position estimates appear to trace the left edge of the lane as the vehicle moves to the south. The reference receiver was unable to calculate a pseudorange based navigation solution in this environment,

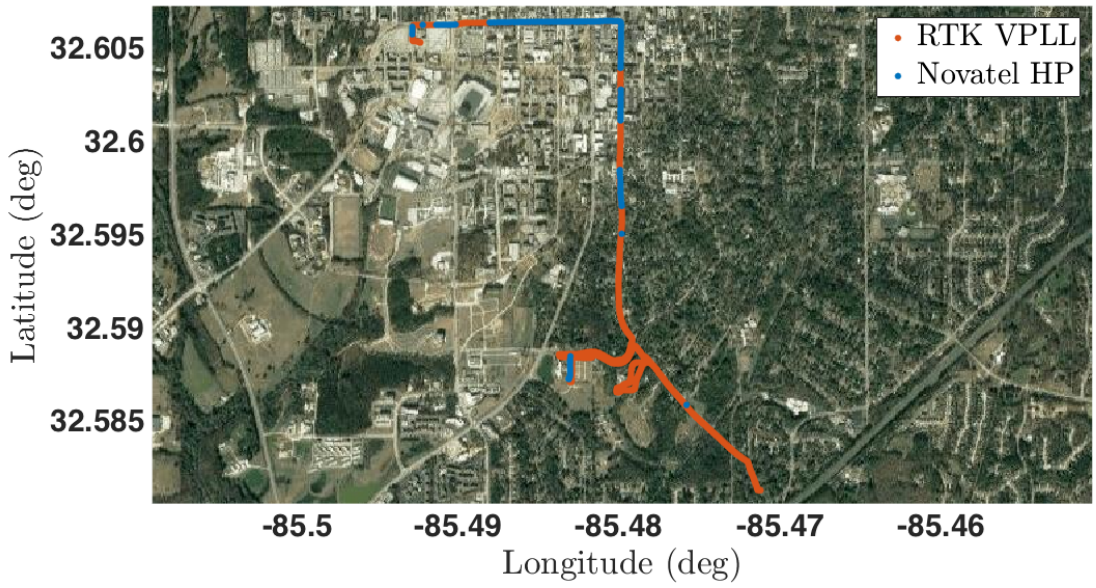

Figure 6.34: The RTK VPLL receiver continues to track the carrier phase throughout the heavy foliage test route while the reference receiver experienced lengthy outages. Imagery by Google, DigitalGlobe.

and had not reported a high precision carrier phase estimate for several hundred meters by this point.

In the weakest signal environments where tree cover blocks the majority of the sky, the RTK VPLL receiver was not able to maintain the phase of the received signals without carrier cycle slips. The errors in the RTK VPLL navigation solution resulting from the cycle slips are apparent in Figure 6.36. In the figure, the vehicle is moving south east before turning right onto a densely wooded narrow street (near Latitude 32.5895 and Longitude -85.48). The vehicle is driven through a parking lot as seen on the far west portion of the route where the reference receiver briefly reported a solution. Then the vehicle was turned back to the east, and returned to the original street traveling southeast. The vehicle was driven on another loop through a second parking lot before again returning to the original street (The second loop begin and ends near Latitude 32.5885 and Longitude -85.479). In the heavy foliage, the carrier phase discriminators used by the RTK VPLL Kalman filter to update the navigation solution do not provide the needed accuracy to maintain the centimeter level

Figure 6.35: The RTK VPLL navigation filter provided lane level positioning through densely wooded neighborhood streets. Note that the Novatel reference solution is not available in this area. Imagery by Google, DigitalGlobe.

precision. There is some improvement in the navigation solution as the vehicle moves away from the densest foliage seen in the figure on the south eastern section (near Latitude 32.587 and Longitude -85.478). The position estimates return to the road as seen on the satellite imagery.

The end of the test route is shown in Figure 6.37. The true final position of the vehicle was in the drive way in the image just south of the final estimated position. This represents an error of approximately six meters. As seen in the image, the reference receiver was not able to provide a high precision solution in this environment. The results of the moderate and heavy foliage test demonstrate that the RTK VPLL navigation algorithm provides improved carrier phase tracking over the reference receiver in some environments. However, in the most challenging environments the RTK VPLL receiver experienced cycle slips which degraded the navigation solution. It is promising that the RTK VPLL receiver was able to recover phase lock after the signal blockage. Additional work is needed to develop cycle slip correction

Figure 6.36: The RTK VPLL carrier phase tracking algorithm experience significant cycle slips in the most densely wooded areas. Imagery by Google, DigitalGlobe.

capability to improve the accuracy of the navigation solution after pronounced periods of signal blockage.

Figure 6.38 gives an indication of the severity of the environment during the heavy foliage test. The plot on the left shows the number of satellite signals that were tracked by the reference receiver during the test. For more than half of the test, the reference receiver was not able to track four or more satellites and report a position solution. It is reasonable to assume that the receiver was unable to maintain carrier phase lock on the few satellites that were tracked through the most difficult environments. There was an extended period of time where only one channel was reporting pseudorange measurements. The carrier phase residuals of the RTK VPLL receiver are shown on the right, and also illustrate the difficulty in maintain carrier phase lock in this environment. During the period from approximately 800 seconds to 1100 seconds, several channels appear to be slipping cycles as seen by the linear trend seen from channels 4, 5, and 6.

Figure 6.37: Despite difficultly of carrier phase tracking in the heavy foliage environment, the RTK VPLL algorithm provided a stable navigation solution with a bias of several meters in the final position estimates. The reference receiver was unable to calculate a high precision solution and is not seen in the figure. Imagery by Google, DigitalGlobe.

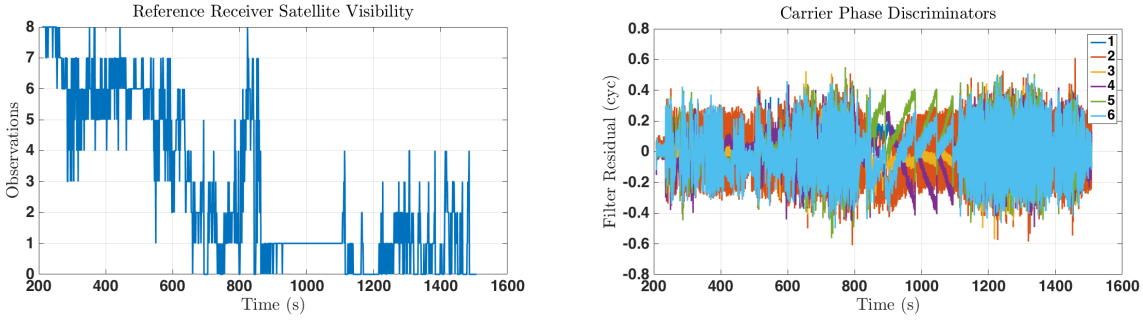

Figure 6.38: For large portions of the heavy foliage test route, the reference receiver was tracking two or fewer satellite signals. The carrier discriminator of the RTK VPLL were near the saturation level on two or more channels for much of the test.

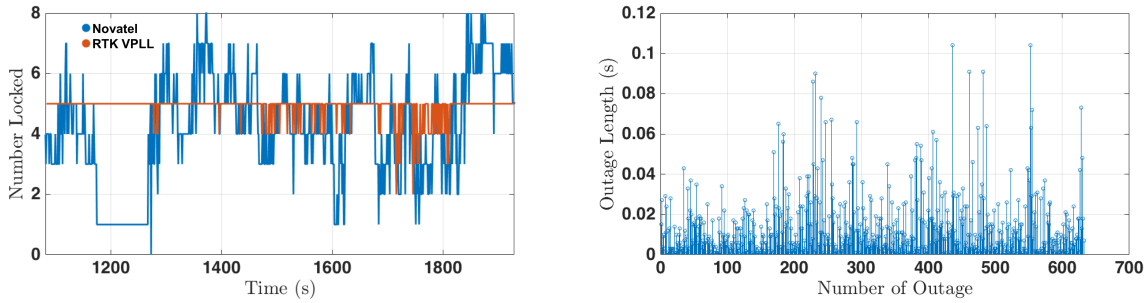

Figure 6.39: Number of phase locked channels for the RTK VPLL receiver and the reference receiver in the moderate foliage environment (left). Length of time when less than four channels of the RTK VPLL receiver pass the phase lock test in the moderate foliage environment (right).

To further analyze the experimental performance of the RTK VPLL receiver, the correlator outputs from each channel were used to calculate a phase lock indicator as described in [64]. The phase lock indicator is a ratio of the relative power in the inphase and quadrature prompt branch to total power of the prompt correlators. If the phase lock indicator exceeds the lock threshold, the channel is considered phase locked. For additional details on the phase lock indicator see [64]. The phase lock results for the moderate foliage test are shown in Figure 6.39. In the image on the left, the number of locked channels is plotted verses time. The number of locked channels in the reference receiver is also shown for comparison. It is clear in the figure that the RTK VPLL often has lock on a larger number of channels particularly at times when the conditions are difficult. Notice that the maximum number of locked channels does not increase for the RTK VPLL receiver because the receiver does not continue to run acquisition after startup.

The length of time of each outage of the RTK VPLL receiver is also shown in the figure. An outage is defined as a measurement interval (20 ms) during which there are less than 4 channels that pass the phase lock test. In the figure, the length of the longest outage is approximately 100 ms, and most outages are less than 50 ms. Cycle slips are more likely to occur during longer outages. As shown later in this chapter, the RTK VPLL Kalman filter

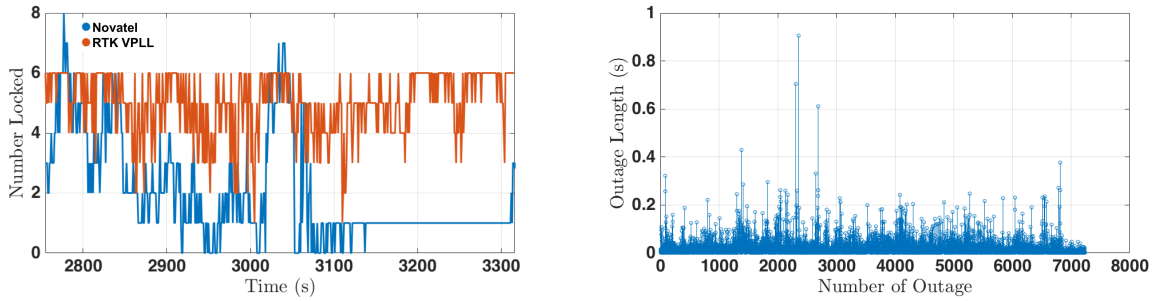

Figure 6.40: Number of phase locked channels for the RTK VPLL receiver and the reference receiver in the moderate foliage environment (left). Length of time when less than four channels of the RTK VPLL receiver pass the phase lock test in the moderate foliage environment (right).

is able to "dead-reckon" through short outages with limited satellite signals depending on the satellite geometry.

The phase lock performance and outage lengths for the RTK VPLL receiver operating in the heavy foliage environment are shown if Figure 6.40. Comparing Figures 6.39 and 6.40, it is clear that the heavy foliage environment had a more dramatic effect on tracking performance. There are times during the test when only one channel in the RTK VPLL receiver passes the phase lock test. The reference receiver often only maintains phase lock on zero or one channel. The length of the outages for the RTK VPLL receiver increases significantly in the heavy foliage environment. This is reflected with the qualitative results shown previously where a bias in the navigation solution suggests numerous cycle slips. The longest outage is nearly one second, which translates to nearly 50 iterations when the navigation solutions was not fully constrained (i.e. 4 or more phase locked channels).

In Table 6.5, the phase lock performance of the reference receiver and the RTK VPLL receiver are quantitatively characterized by the percentage of time during each test that each channel did not pass the phase lock test. The results are shown for 6 satellites that were tracked by each receiver during one or both of the tests. As expected, each receiver performed better during the moderate foliage test. On average, the RTK VPLL receiver lost lock 1.9 percent of the time in the moderate foliage environment compared to 9.5 percent of the time

Table 6.5: RTK VPLL Experimental Phase Lock Data

Percentage of Time Not Locked				
	Moderate Foliage		Heavy Foliage	
PRN	Novatel	RTK VPLL	Novatel	RTK VPLL
2	45.7	2.5	42.1	6.1
3	NA	NA	58.5	NA
6	2.6	0.7	15.8	2.2
17	23.6	1.8	43.3	13.7
19	15.7	1.6	32.8	15.3
28	42.5	3.6	68.1	10.2

in the heavy foliage environment. The RTK VPLL receiver maintained lock more often (i.e. lower percentage of time not lock) than the reference receiver on every channel during both tests. The improvement ranged from 2 percentage points to 58 percentage points.

The phase lock indicator give some insight into the quality of the discriminator outputs provided by each channel, but it does not necessary indicate that the vector tracking receiver has lost lock on a channel. The carrier tracking loop is closed by the navigation processor; therefore, the receiver can accurately close the tracking loop as long as the navigation solution is accurate enough to predict the phase to within the effective range of the discriminator. Take for instance the case where the receiver is tracking 6 satellite in vector mode, and at some point in time two of those signals are blocked by obstructions. The states of the navigation filter are still observable with the measurements from the remaining 4 satellite signals.

Consider the azimuth and elevation plot for the 6 satellites tracked during the foliage tests as shown in Figure 6.41. The signals from satellite 3 and satellite 28 are likely to be obstructed due to their height above the horizon. A covariance analysis was performed to show the observability of the navigation solution when only measurements from satellites 2, 6, 17, and 19 were using in the measurement update. The line of sight uncertainty was calculated using the satellite to receiver unit vectors and the state covariance matrix and

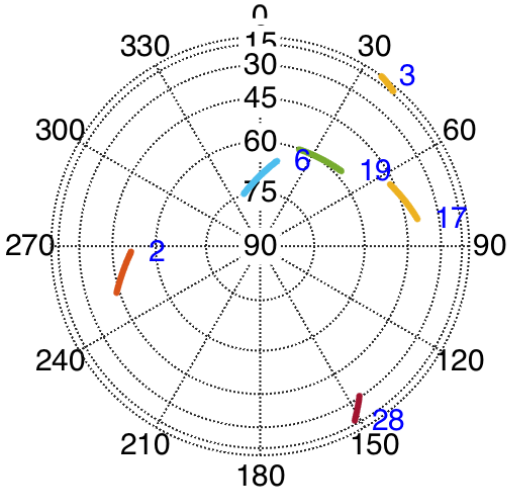

Figure 6.41: Satellite geometry during heavy foliage test.

was converted to units of degress. The results are shown in Figure 6.42. In the figure, the one standard deviation line of sight phase uncertainty is shown verses time. At the 20 second mark, the number of measurements used in the correction step of the Kalman filter was reduced from 6 to 4 measurements to simulate an outage of the signals from satellites 3 and 28. Clearly, the line of sight uncertainty increases (particularly for satellite 3), but the uncertainty along all 6 lines of sight remains well below the 15 degrees threshold. Accordingly, the local replica carrier for satellites 3 and 28 should be accurate when the signal returns to view, and the carrier phase discriminator should provide quality measurements of the phase error. Note that this analysis assuming that the phase discriminators from the channels tracking satellite 3 and 28 are ignored during the outage.

The covariance analysis above is the reason for defining an outage as a measurement update cycle during which less than 4 channels pass the phase lock test. Based on that criteria (i.e. 4 or more channels were phase locked), the RTK VPLL was in "vector" lock 98.7 % of the time in the moderate foliage environment and 90.3 % of the time in the heavy foliage environment. These percentages may be slightly optimistic because they assume that

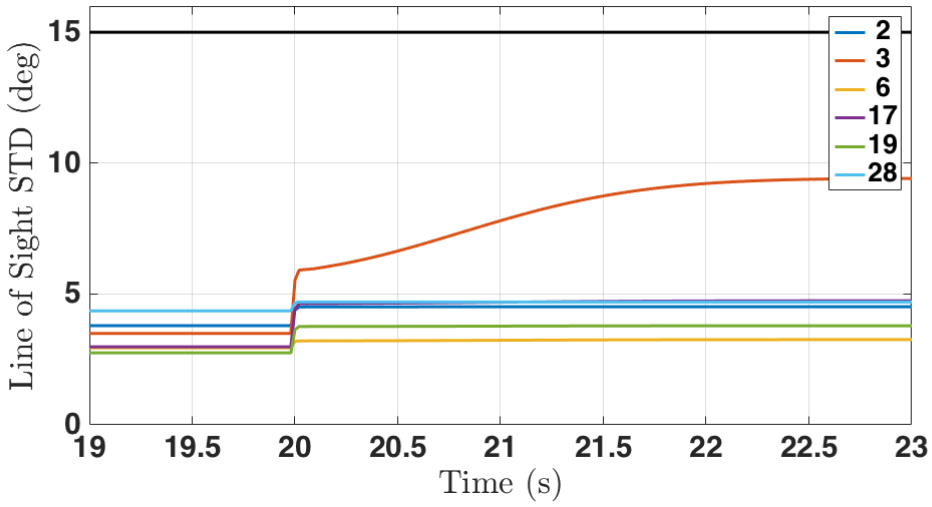

Figure 6.42: Covariance analysis shows that the expect line of sight error does not exceed the vector lock limit for any satellite when 4 channels are providing measurements.

the carrier phase discriminators for the unlocked channels were successfully excluded from the navigation solution by the fault detection algorithms.

Additionally, the navigation solution accuracy during an outage depends on the motion of the receiver and the number of channels that are reporting quality carrier phase discriminators. For example, a slow moving or stationary receiver that is tracking 3 satellites may be able to maintain an accurate navigation solutions for a few seconds before the error causes a loss of vector lock. Consider the two plots in Figure 6.43. The two plots are again constructed based on a covariance analysis of the growth in uncertainty during a measurement outage. In this case, only 3 measurements are used to update the navigation solution starting at the 20 second mark. At that point, the states of the filter are no longer fully observable. The plot on the left shows the simulation results when using measurements from 3 satellites that result in a "good" dilution of precision, and the plot on the right shows the result of a "bad" dilution of precision (DOP). Referring back to Figure 6.41, the good DOP satellites are 2, 19, and 28 and the bad DOP satellites are 2, 6, and 19. In the figure, it is clear that the satellite geometry is an important factor when navigation with less than 4 satellites. The navigator maintains a position solution that is accurate enough to maintain vector phase

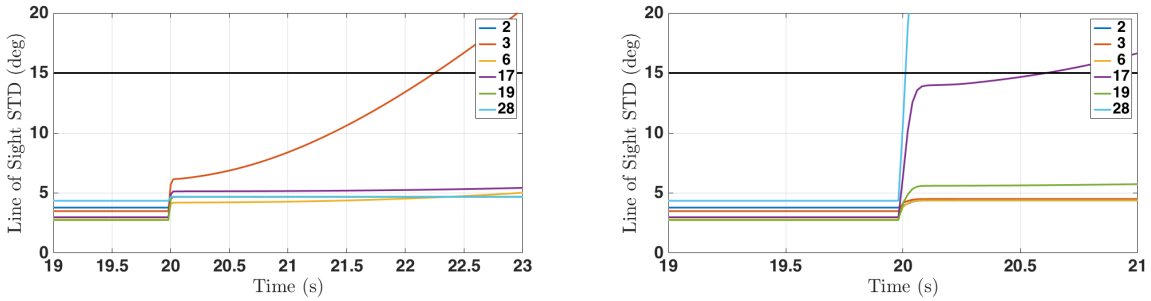

Figure 6.43: Covariance analysis shows that satellite geometry has a large impact of how long vector lock is maintained when only 3 satellites are providing measurements.

lock for more than 2 seconds with the better satellite geometry. Using the poor geometry, the filter loses vector phase lock almost instantly.

6.4 Conclusion

A novel software RTK receiver vector tracking architecture was described in this chapter. The receiver combines a vector delay locked loop with a differential carrier phase based vector phase locked loop that closes the phase tracking loop with relative position vector estimates, base station measurements, and fixed carrier ambiguities. This RTK VPLL algorithm uses carrier phase measurements from the base station receiver, and the states of the navigation filter to predict the phase of the received satellite signal and drive the carrier NCO. A RTK algorithm was used to estimate the carrier ambiguities off-line prior to the initialization of the RTK VPLL filter. The performance of the RTK VPLL algorithm was evaluated using nonlinear simulations and experimentally collected GPS samples. Simulation analysis focused on the performance of the RTK VPLL receiver in the presence of thermal noise and ionospheric scintillation. The RTK VPLL algorithm was shown to maintain phase lock at C/N_0 ratios 4 to 8 dB lower than a traditional scalar tracking phase locked loop and 2 to 6 dB lower than the VFLL aided PLL architecture described in Chapter 4. Using data collected during static and dynamic tests in clear sky environments, the accuracy of the RTK VPLL navigation solutions was shown to be comparable to a survey grade GPS receiver

operating in RTK mode. The RTK VPLL receiver was then shown to outperform the survey grade reference receiver in moderate foliage environments. A need for a cycle slip correction algorithm in the software receiver was identified during testing in dense foliage environments. Finally, the phase lock performance of the RTK VPLL receiver and the reference receiver were compared in the moderate and heavy foliage environments. The RTK VPLL receiver showed a 2 to 58 percentage point improvement in phase lock availability as a percentage of total test time.

Chapter 7

Multi-Antenna GPS Attitude Determination

Platform attitude determination is a key component of navigation systems for manual and autonomous ground, sea, and air vehicles. A variety of sensors are used to track the orientation of the platform including inertial measurement units (IMUs), magnetometer, camera, and lidar. IMUs in particular are often used in combination with GPS receivers to provide position, velocity, and orientation information. Unfortunately, the GPS/INS navigation system requires excitation in the form of platform motion to accurately estimate the full pose of the vehicle. Alternatively, the attitude of the platform can be estimated using position measurements from multiple GPS receivers. Since the multi-antenna attitude solution is based on positions rather than a velocity vector (as in the GPS/INS system) the accuracy is not dependent on platform motion. Rather, the multi-antenna attitude accuracy is dependent on the accuracy of the position solutions and the distance between the antennas.

7.1 Description of Attitude Calculation

The attitude of the platform is defined by a set of three rotations that relate two coordinate systems. The two coordinate systems are the body frame of the vehicle and a reference coordinate frame, which is often assumed to be a local level frame. For a given point on the Earth, the local level X-Y plane is tangential to the surface with the x-axis pointing north and the y-axis pointing east. The z-axis points down into the Earth to complete the right-handed coordinate system. The local level coordinate frame, also referred to as the north-east-down (NED) frame, is shown graphically in Figure 7.1. Note that the figure also shows the Earth Centered Earth Fixed (ECEF) coordinate frame in which the GPS position or RPV is normally represented.

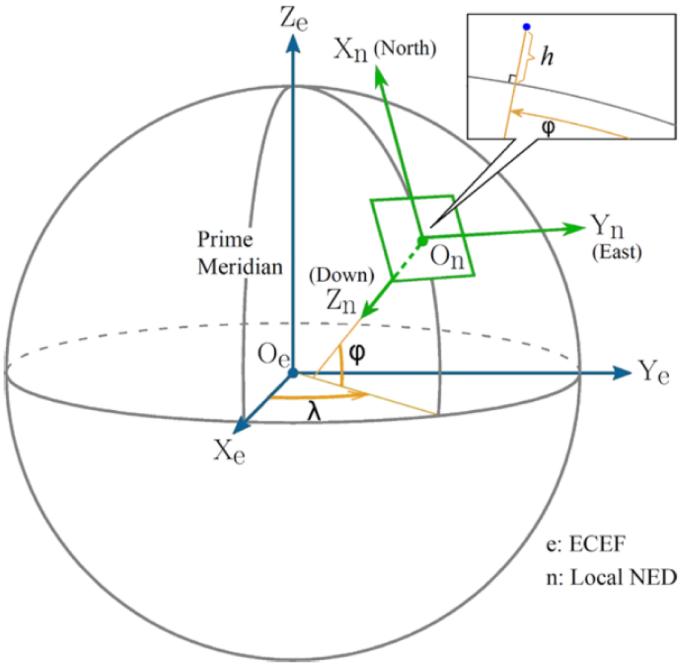

Figure 7.1: Local level coordinate frame defined for a location on the Earth and the ECEF coordinate frame. [8]

The body frame of the platform for which the attitude is to be determined is defined by longitudinal, lateral, and vertical axes. The longitudinal axis (x-axis) is aligned with the forward direction of the platform and the lateral axis (y-axis) points to the right of the platform. The vertical axis is positive in the downward direction to complete the right-handed coordinate frame. For the remainder of this chapter, it is assumed that three GPS antennas are mounted along the x-axis and y-axis of the platform body frame. The configuration is shown in Figure 7.2 along side a north, east, down coordinate system. In this configuration, the RPV from antenna one to antenna two ($RPV_{1,2}$) is parallel to the x-axis (longitudinal) of the body frame. The RPV from antenna one to antenna three ($RPV_{1,3}$) runs parallel to the y-axis (lateral) of the body frame.

In the figure, the vertical axis is orthogonal to x-y plane, and is nearly parallel to the down direction of the local NED frame. Recall that $RPV_{1,2}$ and $RPV_{1,3}$ are assumed to be parallel to the platform x-axis and y-axis, respectively. Consider an automobile with the

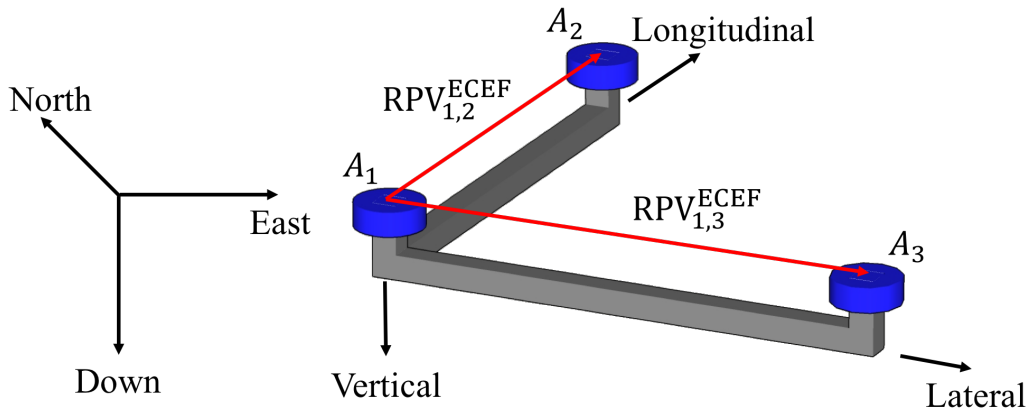

Figure 7.2: A local level NED coordinate system shown with three rigidly mounted GPS antenna that are aligned to the x-axis and y-axis of the vehicle body frame.

antennas mounted on the roof in the assumed configuration. The body (antenna) frame is related to the NED frame through a rotation about the vertical axis. This rotation about the vertical is called yaw. Assuming the x-y plane and the north-east plane are coplanar, no additional rotations are required to align the body frame and the NED frame. In this case, the pitch (i.e. a rotation about the y-axis) and the roll (i.e. a rotation about the z-axis) of the body frame relative to the NED would be equal to zero. Zero pitch and zero roll would indicate that the vehicle is sitting on flat ground.

In general, the attitude of the platform relative to the navigation frame is not defined by a rotation about a single body frame axis. Accordingly, the attitude of the platform is defined by a series of rotations that relate the two frames. The sequences of rotations can be arbitrarily defined. One customary series of rotations is the 3-2-1 sequence [15]. The first rotation is about the vertical axis of the navigation frame which is defined by Equation (7.1).

$$\begin{bmatrix} x' \\ y' \\ z' \end{bmatrix} = \begin{bmatrix} \cos(\psi) & \sin(\psi) & 0 \\ -\sin(\psi) & \cos(\psi) & 0 \\ 0 & 0 & 1 \end{bmatrix} \begin{bmatrix} N \\ E \\ D \end{bmatrix} \tag{7.1}$$

In the equation, ψ is the yaw or heading angle of the body frame relative to the NED frame. The heading angle defines the rotation that is required to align the north axis of the local tangent plane with the projection of the x-axis of the vehicle onto the NED frame. The second rotation, shown in Eqution (7.2), is the pitch rotation about the new y'-axis.

$$\begin{bmatrix} x'' \\ y'' \\ z'' \end{bmatrix} = \begin{bmatrix} \cos(\theta) & 0 & -\sin(\theta) \\ 0 & 1 & 0 \\ \sin(\theta) & 0 & \cos(\theta) \end{bmatrix} \begin{bmatrix} x' \\ y' \\ z' \end{bmatrix} \tag{7.2}$$

The final rotation about the x'' axis completes the alignment procedure. This angle of rotation is the roll value, ϕ and the rotation is shown in Equation (7.3).

$$\begin{bmatrix} x \\ y \\ z \end{bmatrix} = \begin{bmatrix} 1 & 0 & 0 \\ 0 & \cos(\phi) & \sin(\phi) \\ 0 & -\sin(\phi) & \cos(\phi) \end{bmatrix} \begin{bmatrix} x'' \\ y'' \\ z'' \end{bmatrix} \tag{7.3}$$

The three angles used in the complete rotation, ϕ, θ, ψ, are called the Euler angles, and the product of the three rotations in Equations (7.1) through (7.3) is called the rotation matrix.

The completed rotation matrix is used to map vectors represented the NED (i.e. navigation frame) into the body frame of the vehicle. Equation (7.4) shows the complete rotation matrix for the 3-2-1 rotation sequence.

$$\mathbf{r}_b = \begin{bmatrix} \cos(\psi)\cos(\theta) & \sin(\psi)\cos(\theta) & -\sin(\theta) \\ -\sin(\psi)\cos(\phi) + \cos(\psi)\sin(\theta)\sin(\phi) & \cos(\psi)\cos(\phi) + \sin(\psi)\sin(\theta)\sin(\phi) & \cos(\theta)\sin(\phi) \\ \sin(\psi)\sin(\phi) + \cos(\psi)\sin(\theta)\cos(\phi) & -\cos(\psi)\sin(\phi) + \sin(\psi)\sin(\theta)\cos(\phi) & \cos(\theta)\cos(\phi) \end{bmatrix} \mathbf{r}_n \tag{7.4}$$

The rotation matrix given in Equation (7.4) is often labeled R_n^b where the subscript denotes the initial frame and the superscript denotes the final frame. Using this notation for the rotation matrix, note that the roll, pitch, and yaw can be extracted from a given numerical

rotation matrix using Equation (7.5).

$$\phi = \tan^{-1}\left(\frac{R_n^b(2,3)}{R_n^b(3,3)}\right) \tag{7.5a}$$

$$\theta = -\sin^{-1}(R_n^b(1,3)) \tag{7.5b}$$

$$\psi = \tan^{-1}\left(\frac{R_n^b(1,2)}{R_n^b(1,1)}\right) \tag{7.5c}$$

Equation (7.5) will be useful when calculating the vehicle attitude angle using the estimated GPS antenna relative position vectors.

In previous chapters, high precision relative positioning algorithms were derived and tested showing accuracy on the order of centimeters or better. By mounting three antenna on a vehicle as described above, the high precision RPV estimates can be used to estimate the vehicle attitude. The Euler angles that must be estimated relate the vehicle body frame to the local NED frame. By defining one antenna as a base antenna for the RPV estimation and as the origin of a local NED frame, the locations of the two auxiliary antennas are easily expressed in both the body frame and the NED frame. It is assumed that any misalignment between the antenna mount and the vehicle body frame is negligible. Therefore, it is straightforward to define the location of antenna two and antenna three in the body frame with coordinates $[b_{12}\ 0\ 0]$, and $[0\ b_{13}\ 0]^{\mathbf{T}}$ respectively. Note that b_{12} and b_{13} are the magnitudes of the baseline vectors. These magnitudes are constants and may be determined *a priori* by hand measurement or surveying with RTK GPS.

The NED coordinates are determined in real-time using the estimated high precision relative position vectors. As shown previously, the RPV is typically estimated in the ECEF frame. The RPV is easily rotated from the ECEF to a local NED frame for a given location. For details on this transformation see [15]. The relative position vector relating antenna one to antenna two represented in the NED coordinate frame will be referred to by the label r_{12}^n,

and is defined by the three coordinates in Equation (7.6)

$$r_{12}^{n} = \begin{bmatrix} n_{12} & e_{12} & d_{12} \end{bmatrix}^{\mathbf{T}} \tag{7.6}$$

With two representations of the locations of antenna two and antenna three, the relationship between the two vectors is exploited to determine the attitude of the vehicle relative to the navigation frame. The two vectors are related through the rotation matrix as seen in Equation (7.7).

$$\begin{bmatrix} b_{12} \\ 0 \\ 0 \end{bmatrix} = R_{n}^{b} \begin{bmatrix} n_{12} \\ e_{12} \\ d_{12} \end{bmatrix} \tag{7.7}$$

Rotation matrices are known to be orthogonal (i.e. $R_{n}^{b^{-1}} = R_{n}^{b^{\mathbf{T}}}$) which means that Equation (7.7) can be rewritten as

$$\begin{bmatrix} n_{12} \\ e_{12} \\ d_{12} \end{bmatrix} = R_{n}^{b^{\mathbf{T}}} \begin{bmatrix} b_{12} \\ 0 \\ 0 \end{bmatrix} \tag{7.8}$$

It is clear from Equation (7.8) and Equation (7.5) that the pitch angle and yaw angle can be calculated directly using Equation (7.9).

$$\theta = -\sin^{-1}\left(\frac{d_{12}}{b_{12}}\right) \tag{7.9a}$$

$$\psi = \tan^{-1}\left(\frac{e_{12}}{n_{12}}\right) \tag{7.9b}$$

To calculate the roll angle, first the relative position vector relating antenna one and antenna three is transformed using the yaw rotation and pitch rotation derived from Equations (7.1), (7.2), and (7.9).

$$r_{13}'' = R_{\prime}'' R_{n}' r_{13}^{n} \tag{7.10}$$

Using Equation (7.10) and Equation (7.3), the equation for the final rotation is given by Equation (7.11)

$$\begin{bmatrix} 0 \\ b_{13} \\ 0 \end{bmatrix} = \begin{bmatrix} 1 & 0 & 0 \\ 0 & \cos(\phi) & \sin(\phi) \\ 0 & -\sin(\phi) & \cos(\phi) \end{bmatrix} r''_{13} \tag{7.11}$$

By examination of the last row of Equation (7.11), the roll angle is calculated using Equation (7.12) [42].

$$\phi = \tan^{-1}\left(\frac{z''_{13}}{x''_{13}}\right) \tag{7.12}$$

From Equations (7.9) and (7.12), only the relative position vectors from the base antenna to the two auxiliary antennas are needed to estimate the attitude of the platform. Previous chapters described algorithms for determining the relative position vector between two receivers using the GPS carrier phase measurements. The algorithms were developed with accuracy and robustness being the primary considerations. The remainder of this chapter will be used to investigate the possible performance improvements from two methods that leverage the hardware implementation of the three antenna attitude system. The first approach uses the knowledge of the fixed baseline length of the antenna mounts to improve carrier phase ambiguity resolution. The second approach seeks to improve the carrier phase tracking performance of the RTK VPLL algorithm developed in Chapter 6 by including the locations of two rover antennas in the navigation solution and assuming that the receiver front-ends are driven by a common clock. *A priori* knowledge of the baseline length is included in this algorithm as well.

7.2 Fixed Baseline RTK

Since the antennas used in the attitude system are rigidly mounted to the vehicle, the baseline distance between the antennas is a known constant value. The magnitude of the baseline provides an additional constraint that can be used to improve the initialization

procedure of the RTK VPLL receiver. Recall that integer value estimates of the carrier ambiguities are needed to initialize the RTK VPLL tracking algorithm. These ambiguities are determined using the procedure outline in Chapter 5. First, a Kalman filter is used to estimate the low precision floating point estimate of the ambiguities. In the Kalman filter, the floating point estimates of the carrier ambiguities are improved by including a measurement of the distance between antennas as seen in the next section. Then the LAMBDA method calculates the best integer fit as a function of the float estimates and the covariance matrix of the Kalman filter.

7.2.1 Carrier Ambiguity Estimation with Fixed Baseline

The distance between two antennas mounted at a fixed distance can be determined in a number of ways. It may be sufficient to simply measure the distance between the antenna with a tape measure. The distance may also be determined by processing several minutes of GPS carrier phase measurements and averaging the magnitude of the RTK high precision relative position vector. In either case, a measurement of the baseline is obtained with accuracy ranging from a few inches (e.g. coarse measurement by hand) to a few millimeters (e.g. RTK survey).

The baseline measurement is equal to the norm of the relative position vector that is estimated as part of the float carrier ambiguity estimation algorithm. A mathematical model of the baseline magnitude is shown in Equation (7.13).

$$\rho_b = \sqrt{x_{r,b}^2 + y_{r,b}^2 + z_{r,b}^2} \tag{7.13}$$

A baseline residual is calculated by subtracting the predicted baseline from the measured baseline. The predicted baseline is calculated by evaluating Equation (7.13) at the current best estimate of the relative position vector in the Kalman filter. Referring back to Section

5.2.2, the Kalman filter measurement vector is composed of the single difference pseudorange and carrier phase measurement from two receivers. To include the known baseline information, the baseline residual is appended to the measurement vector.

The measurement matrix must also be amended to include the relative position vector geometry. The new row of the measurement matrix is derived by differentiating the measurement model with respect to the state vector. Differentiating Equation (7.13) with respect to Equation (5.8) results in the unit vector that points from antenna r to antenna b as seen in Equation (7.14).

$$H = \begin{bmatrix} \frac{x_{r,b}}{\rho_b} & 0 & \frac{y_{r,b}}{\rho_b} & 0 & \frac{z_{r,b}}{\rho_b} & 0 & 0 & 0 & 0_{1\mathbf{x}m} \end{bmatrix} \tag{7.14}$$

The components of the unit vector are seen in the first, third, and fifth column of the measurement matrix corresponding to the $x_{r,b}$, $y_{r,b}$, and $z_{r,b}$ components of the relative position vector. The measurement noise matrix, R, which was originally defined in Equation (5.13) is augmented with the variance of the measurement of the baseline. For a RTK surveyed measurement, the variance of the baseline measurement is set to approximately 0.01 cm^2.

By adding a measurement of the baseline with low uncertainty, the low precision estimates of the relative position vector are constrained to a circle with the radius equal to the baseline magnitude. Changes in the single difference pseudorange measurements and the satellite geometry result in variations along the circle. As the number of pseudoranges increases, the low precision estimates converge to the true relative position vector. The measurements of the baseline significantly reduces the variance of the low precision relative position vector estimates.

To test the constrained baseline carrier ambiguity estimator, pseudorange and carrier phase measurement outputs from a Novatel Propak V3 receiver were recorded in a clear sky environment. Two antennas were placed about 10 meters apart, and two sets of measurements were recorded for approximately 10 minutes each. The first set of data was used to calculate the measurement of the baseline using GPS L1 and L2 frequency measurements.

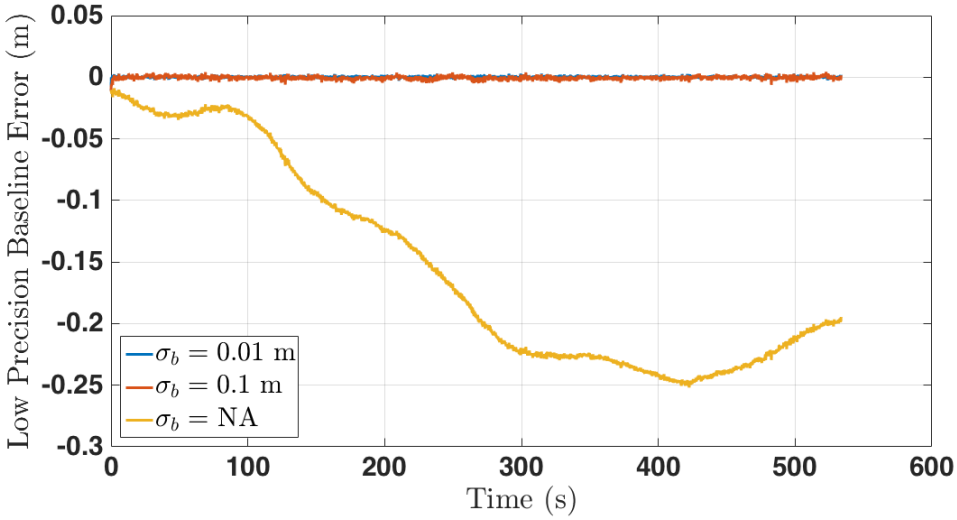

Figure 7.3: Low precision baseline estimate significantly improved by including know baseline length.

The surveyed baseline measured 11.32 meters. The baseline measurement was then used in the RTK estimation algorithm described above. Only the L1 frequency measurements were used during the constrained baseline test. The error of the low precision estimates (i.e. float ambiguity) of the constrained baseline estimator compared to the measured baseline are shown in Figure 7.3. In the figure, two fixed baseline estimator error vectors are shown in blue and orange. The data plotted in blue was calculated assuming the baseline measurement error was RTK level. The data plotted in orange assumes that the baseline measurement was a coarse hand measured value. In both cases, the low precision baseline error standard deviation is on the order of millimeters. The error of the low precision baseline estimate calculated without knowledge of the baseline magnitude is shown in yellow. The unconstrained low precision estimate is accurate to within 20 to 30 centimeters which is consistent with the expected accuracy.

Due to the improved accuracy of the low precision estimates, the estimated floating point carrier ambiguities are more accurate. Since the floating point ambiguity estimates are more accurate, it is easier to distinguish the correct set of integers from other candidates.

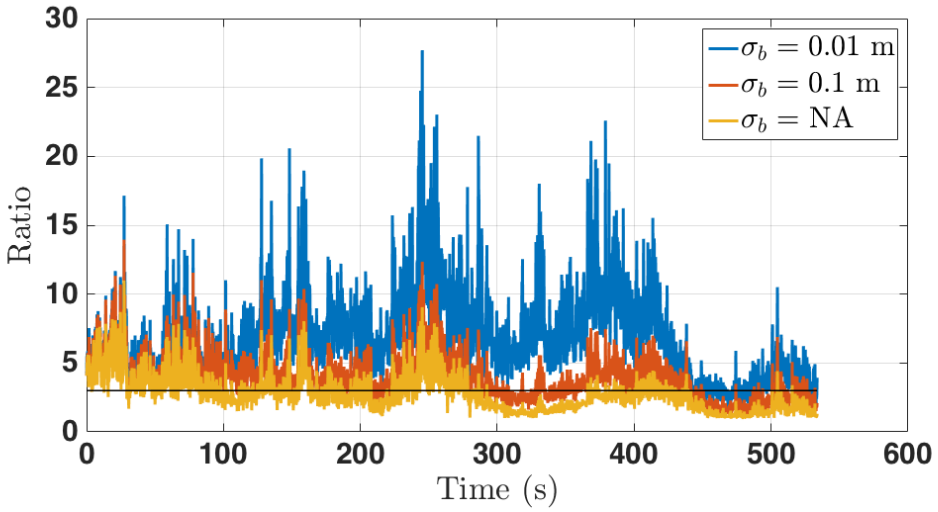

Figure 7.4: Ratio test comparing best integer fit to second best fit improved by including known baseline length in estimator.

Therefore, the LAMBDA ratio test is passed more often. The results of the ratio test for the three estimates (e.g. RTK measured baseline, hand measured baseline, no baseline) are shown in Figure 7.4. From the figure, it is clear that ratio test is passed often for all three estimators. However, it is clear that the ratio is consistently improved by incorporating measurements of the baseline. Notice the ratios for times 300 to 360 seconds. The estimates calculated without measurements of the baseline never passes the ratio test during that minute. Using the coarse hand measurement, the ratio test is passed on most iterations during the minute, and the test is passed on every iteration using the RTK surveyed baseline.

In further analysis, the time required to calculate the first set of fixed integers was calculated for the three scenarios. To calculate time to fix, the estimator was initialized as described in Chapter 5 and the time in GPS seconds was recorded. When the ratio test was passed the initial time was subtracted from the current time to result in the time to fix. In order to obtain multiple data points, after each fix the estimate was initialized using the data from the next measurement epoch and the process was repeated. The results of the time to fix test are shown in Figure 7.5. Notice the disparity in the scale of the y-axis in the figure. The maximum time to fix increased from approximately 10 seconds for the RTK surveyed

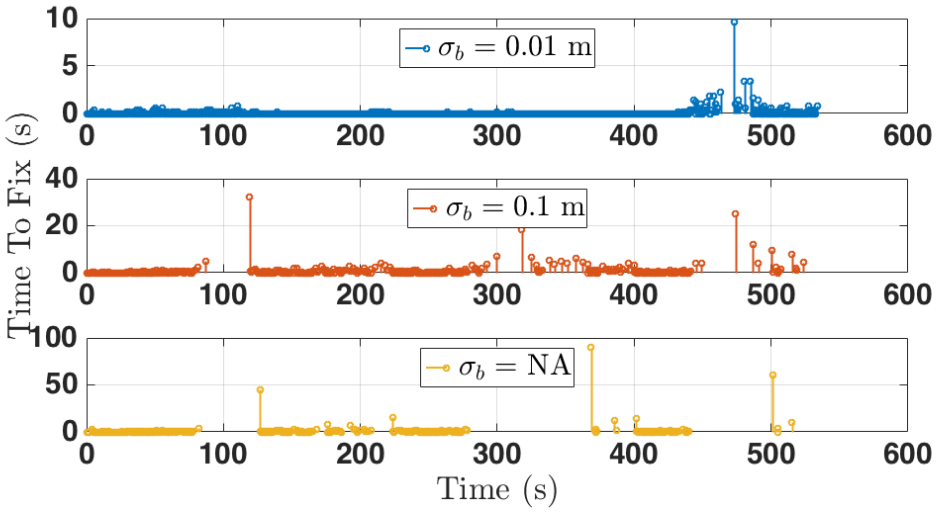

Figure 7.5: Time to fix integers is reduced using unknown and known baseline length.

baseline measurement, to approximately 35 seconds using the coarse baseline measurement. For the scenario where a baseline measurement was unavailable, the maximum time to fix was nearly 100 seconds. The pseudorange and carrier phase measurements were recorded at 5 Hz, so 100 seconds covered 500 measurement epochs. The mean time to fix for the three scenarios was 0.03 seconds, 0.50 seconds, and 0.74 seconds for the RTK baseline, hand measured baseline, and no baseline tests, respectively. On average, the estimator using the coarse baseline measurement took approximately 2.5 more measurement updates than the estimator using the RTK baseline measurement to fix the carrier ambiguities. Without any baseline measurement, the estimator took one additional measurement update to fix integers on average.

7.2.2 Incorrect Fix Detection

In addition to improving the accuracy of the low precision RPV estimates, the baseline measurement also adds an integrity monitoring capability to the RTK algorithm. Knowing the fixed baseline length allows the user to validate a new carrier ambiguity fix prior to reporting a high precision relative position vector. The integrity monitor is implemented by

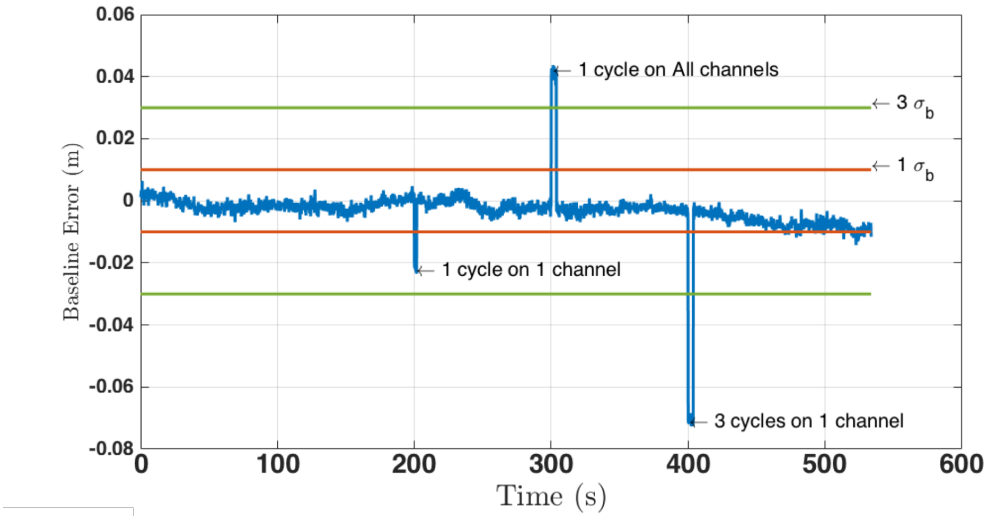

Figure 7.6: Errors in estimated fixed integers are detectable using known baseline length.

comparing the magnitude of the high precision relative position vector to the known baseline length. An incorrect integer fix will lead to a deviation between the true and estimated baseline. When an erroneous fix is detected, the carrier ambiguities are removed from the filter, and the next set of pseudorange and carrier phase measurements are processed.

The ability to detect incorrect integer fixes is dependent on the accuracy with which the fixed baseline is known. To analyze the sensitivity of the baseline integrity check, incorrect integer fixes were simulated during the processes of the pseudorange and carrier phase measurements described above. The incorrect ambiguities were simulated by adding integers to the correct carrier ambiguities fixes that were found using the LAMBDA method and ratio test. Three separate faults were simulated. The results are shown in Figure 7.6. The first incorrect fix was simulated at the 200 second mark seen in the figure. A one cycle error was added to the carrier ambiguity for one channel. This is the smallest possible error for the fixed carrier ambiguities. The error is clear in the figure because the correct integer values are available for every iteration before and after the fault. In practice, this incorrect ambiguity must be identified by comparing the estimated baseline length to the true (i.e. measured) baseline length. Since both the reference baseline length and the estimated baseline length

are corrupted by measurement uncertainty, a detection threshold must be selected that considers the uncertainty. In the figure, lines are provided showing the one sigma and three sigma RTK surveyed baseline uncertainty values. Recall the RTK surveyed baseline error was assumed to be accurate to 1 centimeter (one standard deviation). It appears that a one sigma threshold would allow for detection of a single cycle fault on one channel. However, at the end of the test at the 500 second mark, the correctly fixed high precision baseline estimation error exceeds the one sigma boundary. Based on the expected accuracy of the RTK solution, the error would exceed the one sigma threshold approximately 30 percent of the time. By comparison, the baseline estimate using the correctly fixed carrier ambiguity never exceeds the three sigma threshold.

Two additional integer fixing errors were simulated at 300 seconds and at 400 seconds. At the 300 second mark an error of one cycle was added to every channel. In previous simulation studies this was the most prevalent integer fixing error. An error of one cycle on all channels is clearly detectable using the three sigma detection threshold. The final error simulated at 400 seconds was the addition of 3 cycles to the true ambiguity on one channel. Since this error occurs along a single line of sight (because it only affects one channel), the error is easily detectable using either detection threshold.

This section has shown methods using the known mounting parameters of two antennas on a fixed baseline to improve the accuracy of the low precision baseline estimates, and the time required to calculate integer carrier ambiguity estimates. The known baseline also provides a method for validating the carrier ambiguity integer fixes. Based on the results shown above, a three sigma detection threshold should be selected to prevent false alarms. Next, a study is performed to analyze a deeper integration of the known mounting parameters of the body fixed antennas.

7.3 Modified Two Antenna RTK VPLL Receiver

The known baseline clearly improves the performance of the RTK algorithm used to estimate the carrier ambiguities. The next study focuses on improving the carrier phase tracking ability of the RTK VPLL architecture described in Chapter 6. When designing a multi-antenna system for estimating the attitude of a platform, it is common to drive the GPS front-end attached to each antenna with a common oscillator. Therefore, the signals that reach the correlators of each receiver are corrupted by a common clock error. In this section, a modified two antenna RTK VPLL receiver design is derived, and the performance of the new receiver is analyzed using the nonlinear correlator simulator described in Appendix A.

7.3.1 Two Antenna RTK VPLL Filter Time Update

Before deriving the modified two antenna RTK VPLL architecture, consideration must be made regarding which relative position vectors to estimate. As in the single receiver case, the algorithm begins with the definition of the base station receiver. Modified "two antenna" RTK VPLL refers to the two antennas on the rover platform. The base station remains at a fixed known location as before to provide the global accuracy of the RTK solution. Now there are three possible relative position vectors that may be estimated. The possible RPVs are base to rover1, base to rover2, and rover1 to rover2. While estimating the RPV relating rover1 and rover2 seems to provide the advantage of incorporating the known baseline length, estimating the two RPVs related to the base receiver does not preclude the use of the integration of the baseline measurement. There is a disadvantage to estimating the RPV relating rover1 and rover2. Recall that the main benefit of the RTK VPLL receiver is that it leverages the consistency of the carrier phase measurements from the base station receiver to predict the received phase at the rover. In the case where the RPV between rover1 and rover2 is estimated, both receivers are mounted on a common platform and will likely be impacted by the same environmental factors. This reduces that potential for improved carrier

phase tracking by the receiver that is designated as the rover in this pairing. Accordingly, the modified two antenna RTK VPLL receiver is designed to estimate the relative position vectors between the base station antenna and the two rover antennas. As in the original design, the carrier phase tracking loop is closed by predicting the receiver carrier phase as a function of the measurements from the base receiver and the navigation solution of the RTK VPLL Kalman filter.

The RTK VPLL navigation filter is now responsible for maintaining estimates of two relative position vectors, base to rover1 and base to rover2. As stated previously, it is assumed that the same clock is used in the two GPS front-ends to sample the received signal at the two rover antennas. The state vector of the Kalman filter is expanded to include estimates of the second relative position vector as seen in Equation (7.15).

$$\mathbf{X} = \begin{bmatrix} \delta x_{r_1,b} \\ \delta \dot{x}_{r_1,b} \\ \delta y_{r_1,b} \\ \delta \dot{y}_{r_1,b} \\ \delta z_{r_1,b} \\ \delta \dot{z}_{r_1,b} \\ \delta x_{r_2,b} \\ \delta \dot{x}_{r_2,b} \\ \delta y_{r_2,b} \\ \delta \dot{y}_{r_2,b} \\ \delta z_{r_2,b} \\ \delta \dot{z}_{r_2,b} \\ \delta cb_{r,b} \\ \delta \dot{cb}_{r,b} \end{bmatrix} \tag{7.15}$$

The modified state vector results in a minor change to the dynamic model given by Equation (7.16).

$$\mathbf{X}_{k+1} = \Phi_{k,k+1}\mathbf{X}_k + Q_k \tag{7.16a}$$

$$\Phi_{k,k+1} = \begin{bmatrix} \alpha_k & 0_{2x2} & 0_{2x2} & 0_{2x2} & 0_{2x2} & 0_{2x2} & 0_{2x2} \\ 0_{2x2} & \alpha_k & 0_{2x2} & 0_{2x2} & 0_{2x2} & 0_{2x2} & 0_{2x2} \\ 0_{2x2} & 0_{2x2} & \alpha_k & 0_{2x2} & 0_{2x2} & 0_{2x2} & 0_{2x2} \\ 0_{2x2} & 0_{2x2} & 0_{2x2} & \alpha_k & 0_{2x2} & 0_{2x2} & 0_{2x2} \\ 0_{2x2} & 0_{2x2} & 0_{2x2} & 0_{2x2} & \alpha_k & 0_{2x2} & 0_{2x2} \\ 0_{2x2} & 0_{2x2} & 0_{2x2} & 0_{2x2} & 0_{2x2} & \alpha_k & 0_{2x2} \\ 0_{2x2} & 0_{2x2} & 0_{2x2} & 0_{2x2} & 0_{2x2} & 0_{2x2} & \alpha_k \end{bmatrix} \tag{7.16b}$$

$$Q_k = \begin{bmatrix} Q_x & 0_{2x2} & 0_{2x2} & 0_{2x2} & 0_{2x2} & 0_{2x2} & 0_{2x2} \\ 0_{2x2} & Q_y & 0_{2x2} & 0_{2x2} & 0_{2x2} & 0_{2x2} & 0_{2x2} \\ 0_{2x2} & 0_{2x2} & Q_z & 0_{2x2} & 0_{2x2} & 0_{2x2} & 0_{2x2} \\ 0_{2x2} & 0_{2x2} & 0_{2x2} & Q_x & 0_{2x2} & 0_{2x2} & 0_{2x2} \\ 0_{2x2} & 0_{2x2} & 0_{2x2} & 0_{2x2} & Q_y & 0_{2x2} & 0_{2x2} \\ 0_{2x2} & 0_{2x2} & 0_{2x2} & 0_{2x2} & 0_{2x2} & Q_z & 0_{2x2} \\ 0_{2x2} & 0_{2x2} & 0_{2x2} & 0_{2x2} & 0_{2x2} & 0_{2x2} & 2Q_{cb} \end{bmatrix} \tag{7.16c}$$

As in the previous derivation, the velocity of each antenna is assumed to be driven by zero mean Gaussian noise. In Equation (7.16), only one clock bias and clock drift is estimated in the modified two antenna RTK VPLL Kalman filter. Also note that α_k, Q_x, Q_y, Q_z, and Q_{cb} were defined previously in Equation (6.17) and are not repeated here for brevity.

7.3.2 Two Antenna RTK VPLL Filter Measurement Update

The navigation filter measurement update is performed as each channel from either receiver completes an integrate and dump period. Again, the measurement residual is given by

the carrier phase discriminator calculated using the correlator outputs after each integration period. The measurement vector is not changed by the addition of a second antenna because the update is performed on a channel by channel basis. There are additional tracking channels which trigger updates, and the filter must determine which relative position vector states are directly related to the measurements. Therefore, the measurement matrix takes two distinct forms depending on which receiver is triggering the update. The two possible measurement matrices are shown in Equation (7.17).

$$H_{r_1,b} = \begin{bmatrix} a_x & 0 & a_y & 0 & a_z & 0 & 0 & 0 & 0 & 0 & 0 & 0 & -1 & 0 \end{bmatrix} \tag{7.17a}$$

$$H_{r_2,b} = \begin{bmatrix} 0 & 0 & 0 & 0 & 0 & 0 & a_x & 0 & a_y & 0 & a_z & 0 & -1 & 0 \end{bmatrix} \tag{7.17b}$$

Equation (7.17a) is used to update the navigation solution when a measurement from rover1 is available. The discriminator values from rover1 are a function of the relative position vector between rover1 and the base receiver. When rover2 triggers a measurement update, Equation (7.17b) is used.

In addition to the discriminator update, a measurement update is performed using the known baseline between the two rover antennas. The relative position vector relating rover1 and rover2 is easily computed using the estimated relative position of each rover antenna and the base station antenna. A prediction of the baseline magnitude is made from the estimated RPV using Equation (7.18).

$$\rho_{r1,r2} = \sqrt{(x_{r_1,b} - x_{r_2,b})^2 + (y_{r_1,b} - y_{r_2,b})^2 + (z_{r_1,b} - z_{r_2,b})^2} \tag{7.18}$$

The measurement residual used to update the Kalman filter is computed by subtracting the predicted baseline magnitude from the *a priori* baseline measurement.

The measurement matrix associated with the baseline residual is computed by differentiating Equation (7.18) with respect to the state vector given in Equation (7.15). The

resulting measurement matrix is shown in Equation (7.19).

$$H = \begin{bmatrix} \frac{x_{r_1,b}-x_{r_2,b}}{\rho_{r1,r2}} & 0 & \frac{y_{r_1,b}-y_{r_2,b}}{\rho_{r1,r2}} & 0 & \frac{z_{r_1,b}-z_{r_2,b}}{\rho_{r1,r2}} & 0 & \frac{x_{r_2,b}-x_{r_1,b}}{\rho_{r1,r2}} & 0 & \frac{y_{r_2,b}-y_{r_1,b}}{\rho_{r1,r2}} & 0 & \frac{z_{r_2,b}-z_{r_1,b}}{\rho_{r1,r2}} & 0 & 0 & 0 \end{bmatrix} \tag{7.19}$$

The baseline update is performed along with the carrier phase discriminator update each time a channel triggers a measurement update. Note that the derivative of Equation (7.18) with respect to the components of the two RPVs is opposite in sign, and the order of the subtraction in Equation (7.19) is reversed to reflect the change.

Other than the changes highlighted in Section 7.3.1 and 7.3.2, the RTK VPLL receiver architecture operates the same with one antenna or two. The filter is initialized by computing the high precision relative position vector using RTK and recording the carrier phase ambiguities. A matrix of correction values to the measurement vector is maintained to account for state changes due to asynchronous measurement updates. The correction matrix must be expanded to include a column for each new channel that is added by the second receiver. In the next section, the performance of the two antenna RTK VPLL receiver is analyzed using simulated correlator outputs under weak signal conditions.

7.4 Two Antenna RTK VPLL Performance

The performance of the two antenna RTK VPLL receiver is analyzed by simulating the code phase and carrier phase of the received signal at the two antenna with C/N_0 ratios ranging from 25 dB-Hz to 20 dB-Hz. The trajectory of antenna 1 was simulated in the same manner as the tests performed in Chapter 6. An initial position, velocity, clock bias, and clock drift were selected, and the acceleration of the vehicle was updated at each iteration of the simulation by selecting a random sample from a zero mean Gaussian distribution with a variance of one meter per second squared. In order to maintain the correct baseline distance, the position and velocity of antenna 2 were calculated as a function of the position and velocity of antenna 1 and the simulated heading of the vehicle. The yaw rate of the vehicle

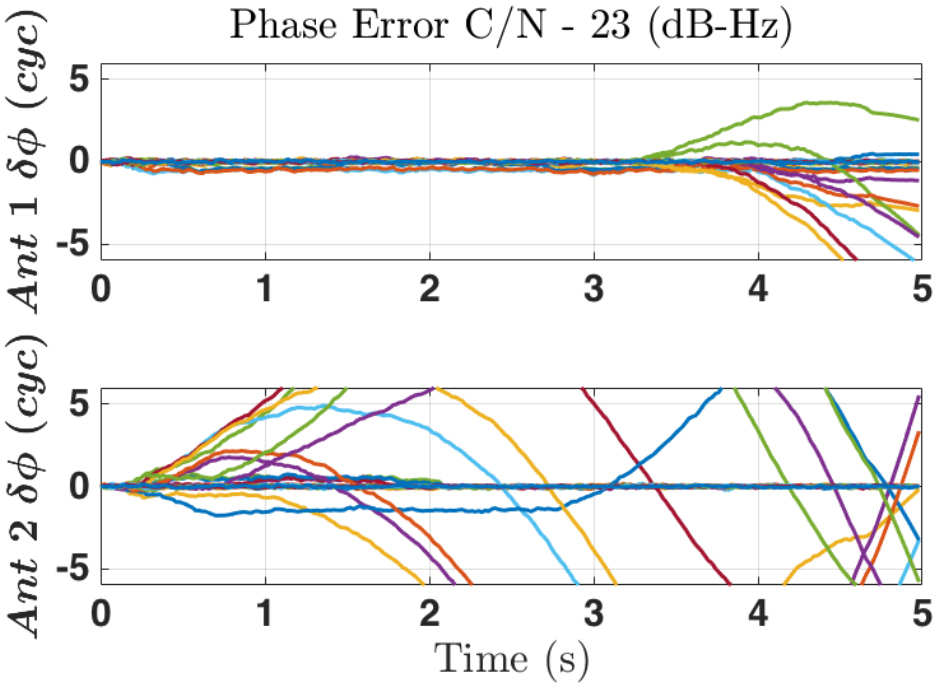

Figure 7.7: Carrier phase error from five simulation of the two antenna RTK VPLL receiver with a signal strength of 23 dB-Hz at each antenna. Each color represents a different channel.

was assumed to be constant with a magnitude of 2 revolutions per minute (a car driving in a circle). Each scenario was simulated twenty times, and the results of the analysis are presented in the next three figures.

The two antenna RTK VPLL algorithm was designed to exploit the use of the common clock to drive the two receiver front-ends and the knowledge of the fixed baseline distance. However, the simulation results do not suggest a significant improvement in the carrier phase tracking capability of the receiver at low C/N_0 ratios. Figure 7.7 shows the carrier phase errors for all satellite signals for five simulations using a C/N_0 ratio of 23 dB-Hz. The two plots separate the results for antenna 1 and antenna 2. This was the critical C/N_0 ratio in terms of the carrier phase tracking performance. In all the tests of higher C/N_0 ratios, the receiver was able to maintain carrier phase lock on all signals without cycle slips. The figure clearly shows that the receiver is unable to maintain phase lock consistently when the received signal strength is 23 dB-Hz. In all, the receiver lost phase lock on both antennas

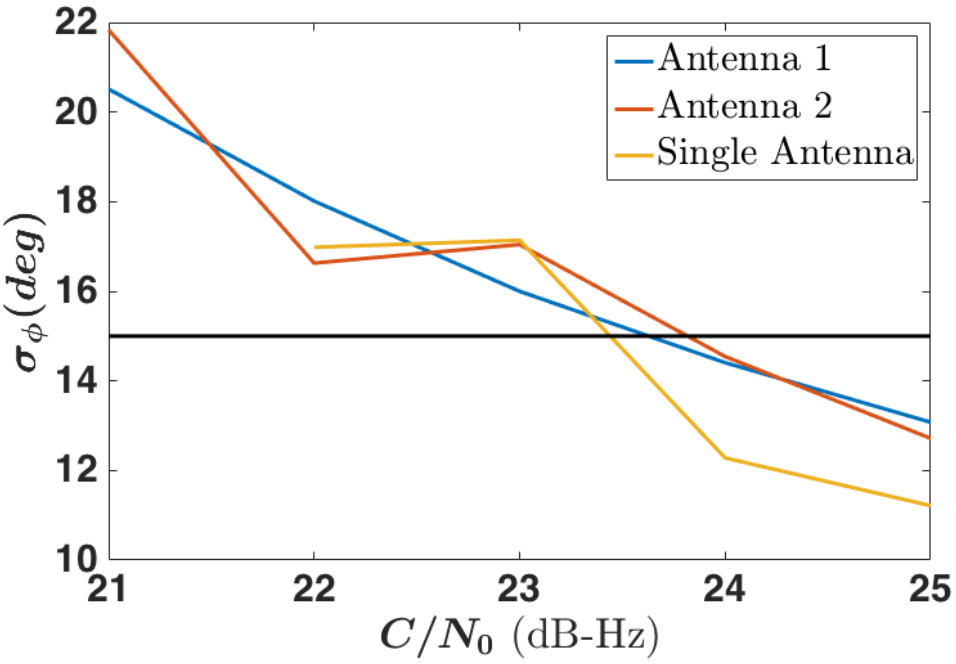

Figure 7.8: Phase error standard deviation as a function of the C/N_0 ratio for the single antenna, and two antenna RTK VPLL receiver.

on 40 percent of the simulations. Recall from Chapter 6 that lost phase lock occurs when less than four channels have a carrier phase error that is less than one quarter cycle. In that case, less than four channels are calculating accurate carrier phase error measurements. When the C/N_0 ratio was reduced to 22 dB-Hz, the receiver lost phase lock in 40 percent of the simulation again. At 21 dB-Hz, phase lock was lost in every simulation.

For comparison, the average phase error standard deviation for the Monte Carlo simulations is shown in Figure 7.8 for the two antenna tests and for the single antenna test described in Chapter 6. The phase error standard deviation is shown for each antenna of the two antenna RTK VPLL estimator. The figure shows that the minimum C/N_0 ratio that was reliably tracked by each estimator was 24 dB-Hz. It also appears that the standard deviation of the phase error was lower when the RTK VPLL receiver was estimating the relative position vector of a single rover antenna relative to the base station.

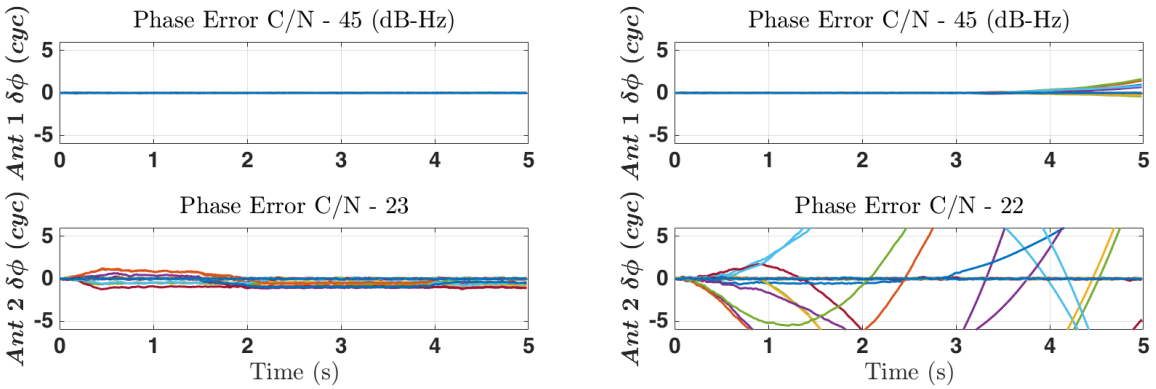

Figure 7.9: One of two receivers with low strength degrades the navigation solution for both receivers.

The simulation analysis does not demonstrate an improvement in the RTK VPLL receiver despite the use of an additional measurement of the fixed baseline distance and estimating the clock bias and drift of a single oscillator using measurement from two antennas. A major challenge to maintaining carrier phase lock in low signal strengths is the quality of the carrier phase discriminator measurement. At low C/N_0 ratios, detecting a fault in the measurement update is difficult due to increased measurement uncertainty. A fault on a single channel degrades the navigation solution and impacts the accuracy of the carrier phase replica on all channels. By adding channels to track the received signal at the second rover antenna, there is higher potential of an erroneous measurement to degrade the solution. Since the navigation solutions of the two antennas are correlated through the common clock bias and drift estimates, an error in any one channel threatens the tracking performance of all channels on both antennas.

An additional simulation study was performed to investigate the scenario where one rover antenna received strong signals and the second rover antenna received degraded signals. While this scenario is unlikely in a real world setting, it illustrates the danger of deeply coupling the carrier phase tracking performance of the two antenna receiver architecture. The carrier phase errors for two simulations are shown in Figure 7.9. In each simulation, the signals received at antenna 1 were given a C/N_0 ratio of 45 dB-Hz. The signals received by

antenna 2 were simulated with a C/N_0 ratio of 23 dB-Hz and of 22 dB-Hz for the left plot and right plot respectively. The plot on the left shows that the two antenna RTK VPLL receiver was able to continue to track the carrier phase of the received signal for both antennas. There are clear cycle slips shown in the plot of the low signal strength antenna, but the receiver does not lose lock. In this case, the channel tracking the stronger received signal from antenna 1 is able to track perfectly as expected. However on the right, the channels tracking the low C/N_0 ratio signals diverge from the true carrier phase, and the receiver loses phase lock. As a result, the carrier phase errors of the channels tracking the stronger signals begin to increase after approximately 4 seconds. The error introduced in the RTK VPLL navigation processor by the weak signal channels causes a degradation in the relative position vector estimates for antenna 1. The degraded navigation solution results in a loss of phase lock in the tracking channel.

Based on the results shown in this section, the RTK VPLL receiver should not be implemented in the two antenna configuration. The carrier phase tracking performance is not significantly improved by sharing measurements in a common navigation filter. Also, it is possible to degrade the navigation solution of one antenna, causing loss of lock in conditions that would otherwise not threaten loss of lock. Separating the navigation filters does not prevent the use of the baseline measurement. A periodic measurement update may be performed using the estimated relative position vectors to calculate a measurement residual and performed a correction to the navigation state. The measurement update may be perform in the navigation process for either antenna.

7.5 Heading Estimation with Experimental Data

Data was collected using the two antenna USRP intermediate frequency (IF) data recorder described in Appendix C to validate the heading estimation capability of the software receiver. The IF samples were processed using the software receiver operating in RTK VPLL mode on each antenna independently. The test vehicle was equipped with two GPS

Figure 7.10: Test vehicle antenna mounting locations.

antennas in the configuration shown in Figure 7.10. The antennas are mounted perpendicular to the longitudinal axis of the vehicle, and any mounting errors are assumed to be negligible. The baseline length was determined to be 1.892 meters. The relative position vectors from a static base station to the two antennas were estimated in separate RTK VPLL navigation processors. The relative position vector from antenna 1 to antenna 2 was then calculated using Equation (7.20)

$$r^e_{12} = r^e_{b2} - r^e_{b1} \tag{7.20}$$

In the equation, the superscript signifies that the relative position vectors are calculated in the ECEF coordinate frame. A standard conversion was used to transform the relative position vector into north, east, down coordinates using antenna 1 as the origin of the coordinate frame. Based on the analysis presented earlier in this chapter, the angle measured from true north to the vector defined by the north and east components of the relative positive

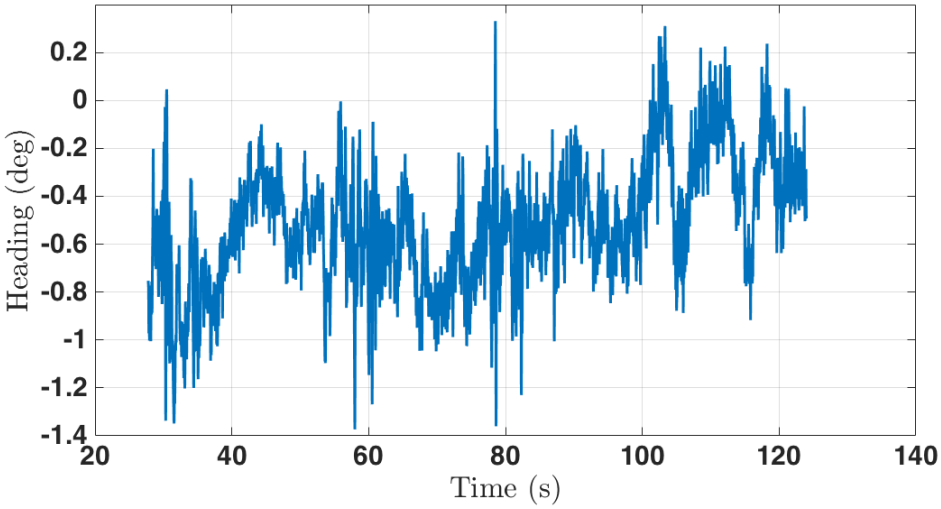

Figure 7.11: The heading estimate standard deviation during static test is consistent with centimeter level baseline errors for the antenna locations on the test vehicle.

vector is found using Equation (7.21)

$$\psi = \tan^{-1}\left(\frac{e_{12}}{n_{12}}\right) \tag{7.21}$$

The vehicle heading is calculated by adding 90 degrees to the direction of the relative position because the two antennas are mounted along the lateral axis of the vehicle.

During the first two minutes of the test, the vehicle was stationary and facing approximately north. The estimated heading of the vehicle during the static portion of the test is shown in Figure 7.11. The heading estimate shows that the longitudinal axis of the vehicle was offset from true north approximately 0.5 degrees to the west. The standard deviation of the heading angle during the static test was 0.299 degrees.

The accuracy of the heading angle is dependent on the accuracy of the relative position estimate and the true baseline length. It was shown in [67] that the standard deviation of the heading angle can be predicted as a function of the standard deviation of the relative

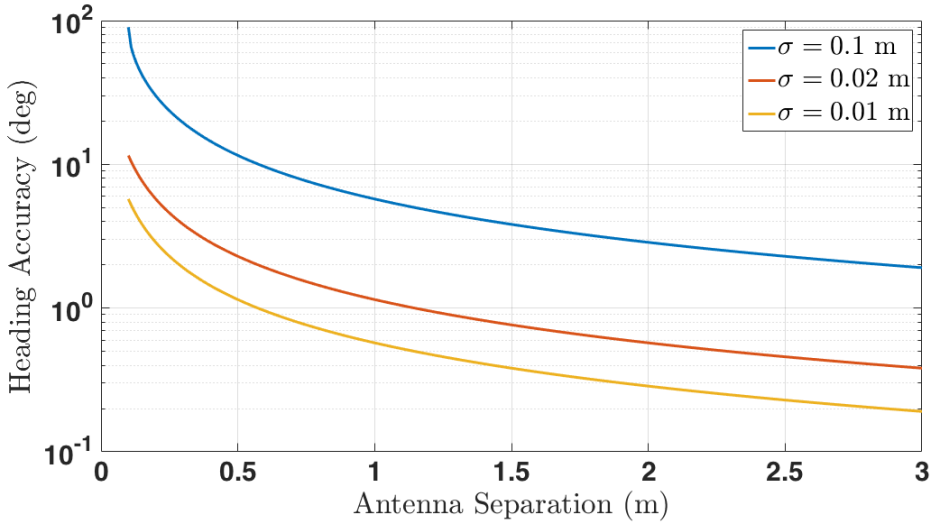

Figure 7.12: The heading accuracy improves with increasing antenna separation distance for a given baseline measurement variance.

position estimate and the baseline length using Equation (7.22)

$$\sigma_\psi = \sin^{-1}\left(\frac{\sigma_{r_{12}}}{b_{12}}\right) \tag{7.22}$$

Figure 7.12 shows the predicted heading standard deviation for three different relative position standard deviations. The largest error shown in the figure is consistent with the expected accuracy of the low precision baseline estimate. For a baseline length of two meters, a decimeter level error in relative position translates to a heading error standard deviation of approximately 3 degrees. The RTK VPLL receiver provides estimates of the relative position vector with an accuracy of approximately one centimeter. Based on the baseline length of the antenna (1.892 m) and the expected accuracy of the navigation solution (0.01 m), the expected heading standard deviation is approximately 0.3 degrees. This is almost exactly the standard deviation of the heading estimates during the static test.

To validate the heading estimator during vehicle motion, the heading is compared to the GPS course measurement from the reference receiver. The course and heading of the vehicle differ by the slip angle, but that difference is minimal during straight driving. A

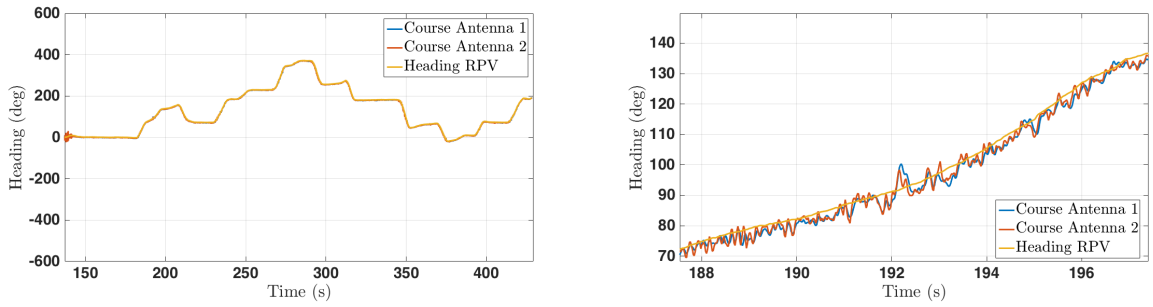

Figure 7.13: The estimated heading is consistent with the GPS course measurement during straight driving.

comparison of the course measurements and the heading estimates is provided in Figure 7.13 The dynamic portion of the test is shown in full on the left. Note that the accuracy of the course measurement improves with increasing velocity. The initial course measurements have higher variance due to the slow movement of the car, however, the heading estimates and the course measurements are similar throughout the test. A closer view of the two solutions is shown in the plot on the right. The improved precision of the heading estimates is clear in the figure.

Finally, Figure 7.14 shows discrete samples on the estimated heading of the vehicle along with the path of the vehicle superimposed on satellite imagery of the test area. Two turns are shown in the figure to highlight the difference between the estimated heading and the direction of travel. The heading estimates were calculated at 50 Hz, but one half Hz samples are shown in the figure for clarity.

7.6 Conclusion

In this chapter, platform attitude determination using three GPS antenna and carrier phase relative positioning was described. Two studies were performed to assess possible improvement to the performance of the software receiver developed in this dissertation. First, an evaluation of a modified fixed baseline carrier phase ambiguity estimation was performed. Use of a baseline measurement in the estimator was shown to improve the accuracy of the

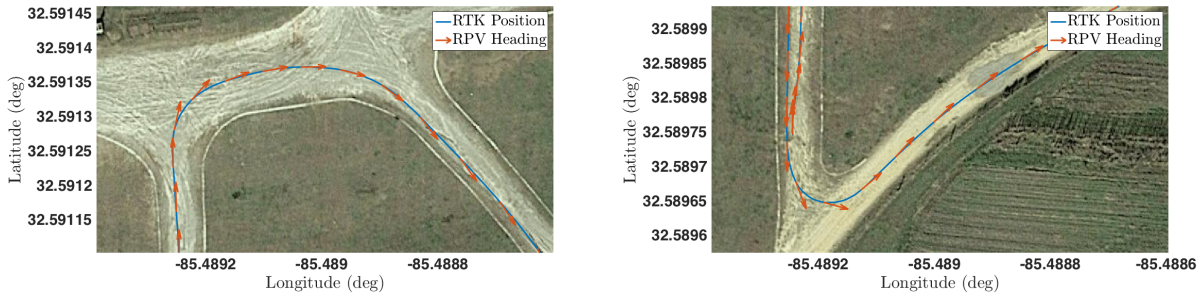

Figure 7.14: The vehicle heading direction is shown with the path of the vehicle for two turns of the test route. Imagery by Google, DigitalGlobe.

low precision baseline accuracy and reduce the time to fix integers. Next, the RTK VPLL receiver architecture was modified to estimate the relative position vectors from a base station to two rover antennas mounted on a rigid frame. The two antennas were assumed to have a common reference clock, and the baseline distance was applied as a measurement to correct the navigation solution. The two antenna RTK VPLL receiver did not perform better than the single antenna receiver, and was shown to potentially degrade performance in some circumstances. Therefore, the RTK VPLL receiver should be implemented independently on each antenna on the rover vehicle.

Chapter 8

Conclusions and Future Work

Real time kinematic GPS receivers provide high precision position estimates using the carrier phase measurement with applications in surveying and unmanned vehicle navigation. The carrier phase tracking loop is the weak link in the GPS receiver due to the required precision of the local replica carrier signal. To maintain phase lock, the carrier replica must remain within one quarter cycle of the true received phase to prevent cycle slips or loss of lock. Previous work has shown that the vector tracking receiver architecture provides improved code phase and carrier frequency tracking in low C/N_0 and high dynamic environments. The non-coherent vector tracking receiver does not maintain carrier phase lock. Therefore, the receiver is not capable of providing high precision RTK position estimates. In past work, improved carrier phase tracking approaches have been proposed which exploit the spatial correlation of the received signals as the vector tracking receiver does. However, the algorithms rely on additional local loop filters to correct slow changing phase errors due to environmental affects such as atmospheric delay.

In this dissertation, two approaches were developed to improve the carrier phase tracking performance of a software defined GPS receiver. The first approach combines a non-coherent vector tracking architecture with a local phase locked loop to improve carrier phase tracking performance of a stand-alone (i.e. not base station) GPS receiver. The performance of the vector frequency locked loop (VFLL) aided phase locked loop (PLL) architecture was studied in comparison to a traditional scalar tracking phase locked loop using a nonlinear simulation tool which generated correlator outputs for algorithm testing. Low signal strengths were simulated to analyze the receiver performance in degraded GPS environments. The VFLL aided PLL receiver was shown to provide more robust carrier phase tracking performance at

low C/N_0 ratios. In particular, the scalar tracking loop quickly lost phase lock completely at low signal strengths. The VFLL aided PLL tracking architecture allowed the receiver to continue to track the phase of the received signal with an increasing number of cycles slips as the signal strength decreased.

A modified version of the VFLL aided PLL was designed for implementation on a stationary receiver at a known location. The receiver was developed to operate as a base station receiver in an environment where the received signal is disrupted by wide area affects like ionospheric scintillation. Rapid changes in the electron content in the ionosphere can have a dramatic effect on the GPS signal received by a user on Earth. Rapid phase changes and amplitude fades cause cycle slips and loss of phase lock in traditional receivers. The performance of the developed static base VFLL aided PLL receiver was evaluated using simulated ionospheric scintillation. The modified receiver architecture was shown to provide significant carrier phase tracking performance over a traditional scalar tracking receiver under moderate scintillation activity. Simulation of strong scintillation resulted in loss of lock when using a traditional scalar tracking receiver. The VFLL aided PLL receiver experienced regular cycle slips under strong scintillation, but the receiver did not loss lock completely during the simulated test.

RTK GPS relies on the precision of the carrier phase measurement and the spatial correlator of atmosphere induced errors to compute high precision position estimates. To use the carrier phase measurement as a range measurement, the carrier ambiguity must be resolved. In Chapter 5, a detailed description of a software receiver architecture used for RTK positioning was provided. Time synchronization and measurement generation are key components to providing RTK quality carrier phase measurements. The software receiver was shown to provide position estimates with accuracy consistent with high-end survey grade GPS receivers.

The RTK vector phase locked loop receiver was derived in Chapter 6. The RTK VPLL receiver is a true carrier phase tracking receiver in that the navigation filter is updated using

correlator outputs, and there is no local loop filter for each tracking channel. The tracking loop is closed by predicting the received carrier phase using the navigation solution. Base station measurements are combined with relative position vector estimates from the navigation filter and fixed carrier ambiguities to close the tracking loops. The performance of the RTK VPLL receiver was studyed using the nonlinear correlator simulator and experimental data. In simulation, the RTK VPLL was shown to maintain phase lock at C/N_0 ratios 4 to 8 dB lower than a traditional scalar tracking receiver. The RTK VPLL receiver was tested using experimental data collected in clear sky, moderate foliage, and heavy foliage environments. The positioning performance of the RTK VPLL receiver was compared to that of a survey grade GPS receiver. During the moderate and heavy foliage test, the reference receiver was not able to report a high precision solution for periods due to the environment. The RTK VPLL receiver maintained the navigation solution and carrier phase tracking throughout each test; however, there were times during the test that the RTK VPLL receiver slipped cycles of the carrier, and the navigation solution was degraded as a result.

In addition to the global position accuracy provided by RTK GPS positioning, the high precision solution may also be used to estimate the attitude of a vehicle that is equipped with multiple antennas. Attitude estimation using three GPS antennas was discussed in Chapter 7. It is assumed that the GPS antennas are mounted along the longitudinal and lateral axes of the body, and the desired attitude relates the body frame to a local north, east, down coordinate frame. The solution for finding the three Euler angles (i.e. roll, pitch, and yaw) of the platform given two relative position vectors was provided. Two studies were performed to identify possible improvements to the software receiver design developed in this dissertation. An improved RTK carrier ambiguity estimation procedure was shown and tested. Also, a modified two antenna RTK VPLL algorithm was developed and tested in simulation. It was shown that the two antenna algorithm did not significantly improve the carrier phase tracking performance as low C/N_0 ratios. Therefore, two independent RTK

VPLL algorithms were used to provide accurate heading estimates using two antennas on a rover vehicle.

8.1 Future Work

There are compelling opportunities to continue to advance the work presented in this dissertation. The need for high precision navigation during ionospheric scintillation was considered in the development of the static base VFLL aided PLL architecture and the RTK VPLL receiver. The performance of each algorithm was studied using simulated scintillation data. However the simulation can not fully capture the variability of the environment, and actual data is needed to evaluate the two systems. In particular, data collected at two locations with a short baseline ($<$ 1km) is needed to determine how the difference in phase scintillation at the two locations will impact the RTK VPLL receiver.

There are several additional avenues to consider in attempting to improve the carrier phase tracking performance of the RTK VPLL receiver in low signal strength environments. In this dissertation, the RTK VPLL receiver design was limited to traditional GPS receiver hardware. The analysis did not consider integrating external sensors or improving the receiver hardware (particularly the clock). Incorporating additional sensors, like an IMU, would provide an opportunity for improved state estimates during brief periods of significant signal attenuation. A high quality IMU would also allow for improved fault detection and exclusion to reduce cycle slips. Additional sources of odometry could have a similar impact. Cameras or Lidars could be used to provide measurements of the platform motion by detecting features in the environment. Many modern receiver implementations consider the inclusion of a chip scale atomic clock (CSAC). Additional research is needed to identify the optimal integration method of the CSAC time measurement (e.g. loose, tight, deep integration), but there is potential for improved navigation when less than four satellites are visible.

As stated previously in Chapter 6, there is a need for a cycle slip correction algorithm to update the carrier ambiguities used in the RTK VPLL receiver when a cycle slip occurs. The cycle slip detection algorithm that is currently implemented uses only the carrier phase measurements. The pseudorange measurement is not considered during the test. The RTK VPLL navigation solution is degraded by a cycle slip on one channel, and that error can cause loss of lock or cycle slips in other channels. The correction may not be available instantly, but when the vehicle moves out of the most difficult environments, an external RTK algorithm should be able to calculate the new integers.

A tighter coupling of the known vehicle dynamics and the vector receiver is possible as well. The process noise matrix used in the RTK VPLL navigation filter currently assumes that an acceleration in any direction is equally likely. For a receiver mounted on a ground vehicle, accelerations are most likely to occur in the horizontal plane. If additional vehicle sensors are available like wheel angle, additional constraints may be added to the process noise matrix. Also, the multi-antenna RTK VPLL navigation filter may be re-parameterized in terms of the attitude of the vehicle and the location of one of the antennas. This formulation may make the process noise matrix constraints more intuitive.

Bibliography

[1] A. Aboot and W. Lillo. Global Positioning Systems and Inertial Measuring unit ultra-tight coupling method, 2003. US Patent 6,516,021.

[2] Santiago Alban, Dennis Akos, Stephen Rock, and Demoz Gebre-Egziabher. Performance analysis and architectures for INS-aided GPS tracking loops. In *Proceedings of ION ITM 2003*, 2003.

[3] D. W. Allan. Statistics of atomic frequency standards. *Proceedings of the IEEE*, 54(2):221–230, Feb 1966.

[4] Nation PNT Advisory Board. Jamming the global positioning system - a national security threat: Recent events and potential cures. `http://www.gla-rrnav.org/pdfs/interference_to_gps_v101_3_.pdf`, 2010. Accessed: 2016-8-1.

[5] Kai Borre, Dennis Akos, Nicolaj Bertelsen, Peter Rinder, and Soren Holdt Jensen. *A Software-Defined GPS and Galileo Receiver: A Single Frequency Approach*. Birkhauser, 2007.

[6] James J. Brewer. *The Differential Vector Phase-Locked Loop For Global Navigation Satellite System Signal Tracking*. PhD Dissertation, Air Force Institute of Technology, June 2014.

[7] R. G. Brown and P. Y. C. Hwang. *Introduction to Random Signals and Applied Kalman Filtering*. John Wiley and Sons, Third edition, 1997.

[8] G. Cai, B. M. Chen, and H. Tong. *Unmanned Rotorcraft Systems, Advances in Industrial Control*. Springer-Verlag London Limited, 1st edition, 2011.

[9] Benjamin Clark. *Fault Detection and Exclusion in Deeply Inetegrated GPS/INS Navigation*. PhD Dissertation, 2012.

[10] S. J. Comstock. Development of a low-latency, high data rate, differential GPS relative positioning system for uav formation flight control. Master's Thesis, Air Force Institute of Technology, 2006.

[11] Robert N. Crane. A simplified method for deep coupling of GPS and inertial data. In *Proceedings of the National Technical Meeting of the Institute of Navigation*, San Diego, California, January 2007. Institute of Navigation.

[12] Lina Deambrogio and Crhristophe Macabiau. Vector tracking aiding for carrier phase estimation in the presence of ionospheric scintillation. In *Proceeding of the Institute of Navigation International Technical Meeting 2013*, 2013.

[13] A. J. Van Dierendonck, J. B. McGraw, and R. Grover Brown. Relations between Allan variances and Kalman filter parameters. In *In Proceedings of the Sixteenth Annual Precise Time and Time Interval (PTTI) Applications and Planning*, 1984.

[14] L. Edwards, B. Clark, and D. M. Bevly. Implementation details of a deeply integrated GPS/INS software receiver. In *Proceedings ION-IEEE PLANS 2010*, 2010.

[15] Jay A. Farrel and Matthew Barth. *The Global Positioning System and Inertial Navigation*. McGraw Hill, 1999.

[16] Demoz Gebre-Egziabher, Alireza Razavi, Per Enge, Jennifer Gautier, Dennis Akos, Sam Pullen, and Boris Pervan. Doppler aided tracking loops for srgps integrity monitoring. In *Proceedings of ION GPS/GNSS 2003*, 2003.

[17] Demoz Gebre-Egziabher, Alireza Razavi, Per Enge, Jennifer Gautier, Sam Pullen, Boris Pervan, and Dennis Akos. Sensitivity and performance analysis of doppler-aided GPS carrier-tracking loops. 52(2), 2005.

[18] K. Giger and C. Gunther. Position domain joint tracking. In *Proceedings of the 5th European Workshop on GNSS Signals and Signal Processing*, 2010.

[19] K. Giger and C. Gunther. Multisatellite tracking GNSS receiver in multipath. In *Proceedings ION GNSS 2011*, 2011.

[20] Joseph C. Grabowski. Personal privacy jammers: Locating jersey ppds jamming gbas safety-of-life signals. `http://gpsworld.com/personal-privacy-jammers-12837/`, 2012.

[21] P. Groves, C Mather, and A. Macaulay. Demonstration of non-coherent deep INS/GPS integration for optimised signal-to-noise performance. In *Proceedings of the Internation Techincal Meeting of the ION 2007*, 2007.

[22] P. D. Groves. *GNSS, Inertial, and Multisensor Integrated Navigation Systems*. Artech House, 2008.

[23] D. Gustafson and J. Dowdle. Deeply integrated code tracking: Comparative performance analysis. In *Proceedings of ION GNSS 2003*, 2003.

[24] D. Gustafson, J. Dowdle, and J. Elwell. Deeply-integrated adaptive INS/GPS navigator with extended range code tracking, 2001. US Patent 6,630,904.

[25] D. Gustafson, J. Dowdle, and K. Flueckiger. A deeply integrated adaptive GPS-based navigator with extended range code tracking. In *Proceedings of the IEEE/ION PLANS 2000*, 2000.

[26] P. G. Henkel, K.Giger, and C. Gunther. Multi-frequency, multi-satellite vector phase-locked loop for robust carrier tracking. *IEEE Journal of Selected Topics in Signal Processing*, 3(4), 2009.

[27] L. Hui and Y JingShu. Analysis and simulation of vector tracking algorithms for weak GPS signals. In *Proceedings of the 2nd International Asia Conference on Informatics in Control, Automation, and Robotics*, 2010.

[28] L. Hui and Y. Jingshu. Frequency tracking for high dynamic GPS signals based on vector frequency lock loop. In *Proceedings of the WASE International Conference on Information Engineering*, 2010.

[29] Todd E. Humphreys, Brent M. Ledvina, Mark L. Psiaki, Brady W. OHanlon, and Paul M. Kintner. Assessing the spoofing threat: Development of a portable GPS civilian spoofer. In *In Proceedings of ION GNSS 2008*, 2008.

[30] Todd E. Humphreys, Mark L. Psiaki, Joanna C. Hinks, Brady OHanlon, and Jr. Paul M. Kintner. Simulating ionosphere-induced scintillation for testest GPS receiver phase tracking loops. 3(4), 2009.

[31] James J. Spilker Jr. *Digitial Communications by Satellites*. Prentice-Hall Inc., 1977.

[32] E.D. Kaplan and C.J. Hegarty. *Understanding GPS: Principles and Applications*. Artech House, 2006.

[33] Brian Keyser. Design and implementation of a soc-based real-time vector tracking GPS receiver. Master's Thesis, 2015.

[34] S. Kiesel, C. Ascher, D. Gramm, and G. Trommer. GNSS receiver with vector based fll-assisted pll carrier tracking loop. In *Proceedings of ION ITM 2008*, 2008.

[35] J. A. Klobuchar. *Global Positioning System: Theory and Applications Volume I*, chapter Ionospheric Effects on GPS, pages 485–515. American Institute of Aeronautics and Astronautics, 1996.

[36] M. Lashley and D. Bevly. Comparison in the performance of the vector delay/frequency lock loop and equivalent scalar tracking loops in dense foliage and urban canyon. In *Proceedings of the 24th International Technical Meeting of the Satellite Division of the Institute of Navigation*, 2011.

[37] M. Lashley, D. Bevly, and J. Hung. A valid comparison of vector and scalar tracking loops. In *Proceedings of PLANS 2010*, 2010.

[38] M. Lashley and D. M. Bevly. Analysis of discriminator based vector tracking algorithms. In *Proceedings of the 2007 National Techincal Meeting of the Institute of Navigation*, 2007.

[39] M. Lashley and D. M. Bevly. Comparison of traditional tracking loops and vector based tracking loops for weak GPS signals. In *Proceedings of the 2008 National Techincal Meeting of the Institute of Navigation*, 2008.

[40] Matthew Lashley. *Modeling and Performance Analysis of GPS Vector Tracking Algorithms*. PhD Dissertation, Auburn University, 2009.

[41] IQD Frequency Products Ltd. `http://www.iqdfrequencyproducts.com`, 2016. Accessed: 2017-02-01.

[42] Gang Lu. *Development of a GPS Multi-Antenna System for Attitude Determination*. PhD Dissertation, University of Calgary, 1995.

[43] Scott Martin. Closely coupled GPS/INS relative positioning for automated vehicle convoys. Master's Thesis, Auburn University, 2011.

[44] Chris Matyszczyk. Truck driver has GPS jammer, accidentally jams newark airport. `https://www.cnet.com/news/truck-driver-has-{GPS}-jammer-accidentally-jams-newark-airport/`, 2013.

[45] G. A. McGraw and M. S. Braasch. Modeling of tracking loop noise and dynamics for efficient simulation of spread spectrum ranging systems. *IEEE Transactions on Aerospace and Electronic Systems*, 34(3):1003–1008, Jul 1998.

[46] P. Mirsa and P. Enge. *Global Positioning System: Signals, Measurements, and Performance*. Ganga-Jamuna Press, 2011.

[47] Ryan H. Mitch, Ryan C. Dougherty, Mark L. Psiaki, Steven P. Powell, Brady W. OHanlon, Jahshan A. Bhatti, and Todd E. Humphreys. Signal characteristics of civil GPS jammers. In *In Proceedings of the ION GNSS 2011*, 2011.

[48] US Department of Defense. *Global Positioning System Standard Positioning Service Signal Specification, 2nd Edition*. 1995.

[49] Navstar GPS Joint Program Office. Interface specification is-GPS-200d, 2004.

[50] T. Pany, R. Kaniuth, and B. Eissfeller. Deep integration of navigation solution and signal processing. In *Proceedings of Institute of Navigation GPS/GNSS Conference*, 2005.

[51] Thomas Pany and Bernd Eissfeller. Use of a vector delay lock loop for GNSS signal power analysis in bad signal conditions. In *Proceedings of the IEEE/ION PLANS 2006*, 2006.

[52] B.W. Parkinson and J.J. Spilker. *The global positioning system: theory and applications volume I*. Aiaa, 1996.

[53] M. G. Petovello and G. Lachapelle. Comparison of vector-based software receiver iimplementation with application to ultra-tight GPS/INS integration. In *Proceedings of the ION GNSS 2006*, 2006.

[54] M. G. Petovello, C. O'Driscoll, and G. Lachapelle. Ultra-tight GPS/INS for carrier phase positioning in weak-signal environments. In *Proceedings of NATO RTO SET-104 Symposium on Military Capabilities Enabled by Advances in Navigation Sensors*, 2007.

[55] M. G. Petovello, C. O'Driscoll, and G. Lachapelle. Carrier phase tracking of weak signals using different receiver architectures. In *Proceedings of the ION NTM 2008*, 2008.

[56] M. G. Petovello, C. O'Driscoll, and G. Lachapelle. Weak signal carrier tracking using extended coherent integration with an ultra-tight GNSS/imu receiver. In *Proceedings of the European Navigation Conference 2008*, 2008.

[57] Mark Petovello and Cillian O'Driscoll. GNSS solutions: Carrier phase and its measurement for GNSS. 5(5), 2010.

[58] B. Remondi. Performing centimeter level surveys in seconds with GPS carrier phase: Initial results. *Navigation, Journal of Institute of Navigation*, 32(4):386–400, 1985.

[59] J. Sennott and D. Senffner. The use of satellite constellation geometry and a-priori motion constraints for prevention of cycle slips in a GPS signal processor. In *Proceedings of ION GPS 1991*, 1991.

[60] J. Sennott and D. Senffner. Navigation receiver with coupled signal-tracking channels, 1992. US Patent 5,343,209.

[61] A. Soloviev, D. Bruckner, F. van Graas, and L. Marti. Assessment of GPS signal quality in urban environments using deeply integrated GPS/imu. In *Proceeding of the ION NTM 2007*, 2007.

[62] A. Soloviev, S. Gunawardena, and F. van Graas. Deeply integrated GPS/low-cost imu for low cnr signal processing: Concept description and in-flight demonstration. 55(1):1–13, 2008.

[63] A. Soloviev, F. van Graas, and S. Gunawardena. Implementation of deeply-integrated GPS/lost-cost imu for reaquisition and tracking of low cnr GPS signals. In *Proceeding of ION ITM 2004*, 2004.

[64] J. J. Spilker. *Global Positioning System: Theory and Applications*. American Institute of Aeronautics and Astronautics, 1996.

[65] P. J. G. Teunissen. The least-squares ambiguity decorrelation adjustment: A method for fast GPS integer ambiguity estimation. *Journal of Geodesy*, 70:65–82, 1995.

[66] P. J. G. Teunissen and S. Verhagen. On the foundation of the popular ratio test for GNSS ambiguity resolution. In *Proceedings of the 17th International Technical Meeting of the Satellite Divison of the Institute of Navigation ION GNSS 2004*, pages 2529–2540, 2004.

[67] William Travis. *Path Duplication Using GPS Carrier Based Relative Position for Automated Ground Vehicle Convoys*. PhD dissertation, Auburn University, May 2010.

[68] J. Wang, X. Yan, B. Cai, and W. Shangguan. Research on deeply integrated GPS/INS for autonomous train positioning. In *Proceedings of the 4th International Symposium on Microwave, Antenna, Propagation, and EMC Technologies for Wireless Communications*, pages 687–690. IEEE, 2011.

[69] Phillip Ward. Performance comparison between fll, pll and a novel fll-assisted-pll carrier tracking loop under rf interference conditions. In *Proceeding of Insititue of Navigation ITM*, 1998.

[70] S. Zhao and D. Akos. An open source GPS/GNSS vector tracking loop - implementation, filter tuning, and results. In *Proceedings of the ION ITM 2011*, 2011.

[71] Z. Zhenzhen, C Zhu, T.Guangfu, L. Shunfeng, and H.Fukan. EKF based vector delay lock loop algorithm for GPS signal tracking. In *Proceedings of the International Conference on Computer Design and Applications*, 2010.

[72] M. Zhodzishsky, S. Yudanov, V. Veitsel, and J. Ashjaee. Co-op tracking for carrier phase. In *Porceedings of the Institute of Navigation GPS 1998*, 1998.

Appendices

Appendix A

Nonlinear Correlator Output Based Receiver Simulator

A GPS receiver simulator was developed to analyze the thermal noise and scintillation performance of the vector tracking receiver architectures derived in this dissertation. The simulator is designed to generate correlator outputs that are representative of actual correlator outputs accounted for the signal to noise power of the simulated signal and the errors in the local replicas generated by the code and carrier NCOs. A block diagram of the process is shown in Figure A.1.

In the figure, the intermediate frequency samples and the correlation step are replaced in the simulator. A trajectory simulator is used to generate true user positions, velocities, and time. Since the simulator represents the received signal after the GPS front end, true receiver clock errors must be generated also. Actual satellite ephemerides are used to generate satellite positions, velocities, and clock errors based on the true time of the simulation. Simulated ionosphere and troposphere induced signal delays can be include using the models defined in Chapter 3. The simulated user and satellite data are combined to generate the signal parameters that are used by the receiver to update the local replica and generate a navigation solution. In particular, the time of transmission of the current received CA code phase, and the received carrier phase are simulated by the signal generation block seen in Figure A.1. Next the error in the current states of the local replicas are calculated, and nonlinear correlator outputs are generated using the error values. From this point, the receiver acts just as it would with experimental data. The discriminator function returns measurements of the code phase, carrier phase, and carrier frequency errors. The tracking loop can be closed with any of the closure methods described in this dissertation. Then

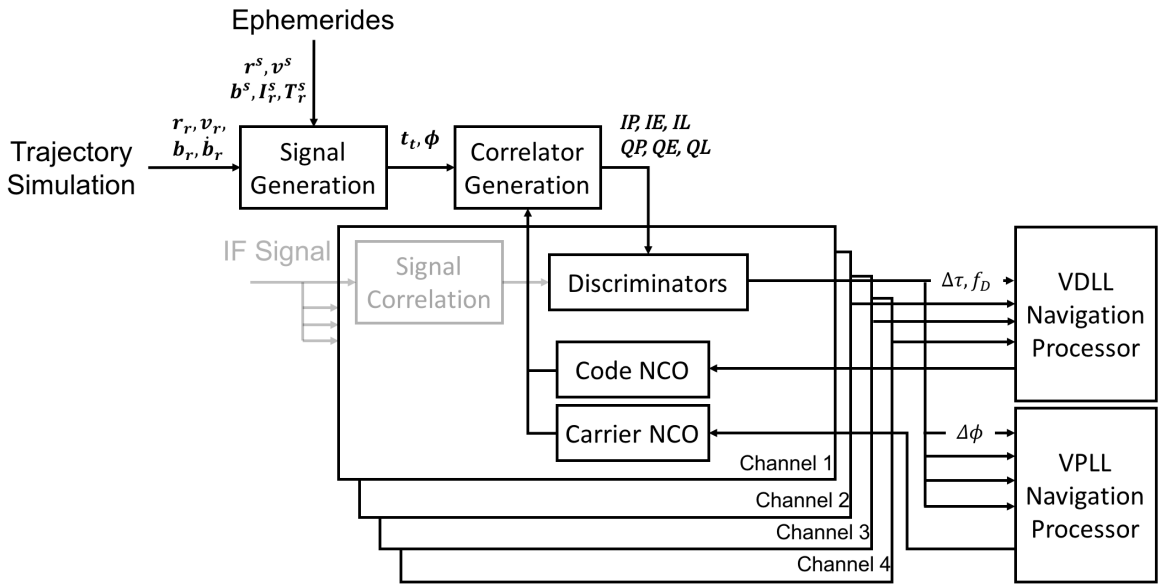

Figure A.1: Block diagram of nonlinear simulation. Intermediate frequency samples are replaced with signal parameters of transmit time and received phase in simulator.

the local replica parameters are used to calculate a position, velocity, and time navigation solution.

The first step is to select a user position, velocity, and time with which to begin the simulation. In the simulation data shown throughout this dissertation, the initial position was selected to be the position of the antenna on the roof of the Woltosz Engineering building. The receiver states can be propagated with any suitable model. The kinematic model described in several places in this dissertation was used to generate the data shown in the dissertation. Gaussian distributed random values were used to drive the true velocity and clock states. The trajectory, signal parameters, and replica errors were simulated at a rate of 5000 Hz to capture the nonlinear signal changes during the integrate and dump periods.

At each epoch of the simulation, the transmission time of the received signal was simulated using Equation (A.1).

$$t_t = t_r - \frac{r + cb_r - cb^s + I^s + T^s}{c} \tag{A.1}$$

In the equation, the received time is treated as a known quantity, and the transmit time, t_t, is calculated as a function of the pseudorange. The true range, r, receiver clock bias, cb_r, satellite clock bias, cb^s, ionosphere delay, I^s, and troposphere delay T^s are calculated using the receiver and satellite trajectory data. The pseudorange is divided by the speed of light to convert to units of seconds.

The equation for calculating the received phase is similar the transmission time calculation. Equation (A.2) is the equation used to calculate the phase of the received signal at each simulated sample.

$$\phi_r = f_{IF}t - \frac{r + cb_r - cb^s - I^s + T^s}{c} \tag{A.2}$$

To account for the mixing and sampling in the GPS front end, a mixer phase is simulated by multiplying the time of the simulation by the simulated intermediate frequency. The phase of the GPS carrier is calculated using the true range to the satellite, the true receiver clock bias, the satellite clock bias and the atmospheric delays. Recall that the ionosphere advances the carrier rather than delaying it like the code. By calculating the received transmission time and received phase at each epoch of the simulation using the user and satellite positions and velocities, the code and carrier frequencies automatically adjust to reflect the true signal dynamics.

At this point, the simulator must interact with the receiver to compute correlator outputs. The receiver code and carrier NCOs generate new code and carrier phase values, and those values are compared to the simulated transmit time and carrier phase. Transmit time and code phase are directly relatable since the transmission time of the code period is synchronized to GPS milliseconds. Code phase, carrier phase and carrier frequency errors are calculated using the receiver and simulated values. The in-phase and quadrature correlator outputs used by the receiver are calculated using Equation (A.3).

$$IP = \sqrt{2\frac{C}{N_0}T}(1 - |e_{chip}|)\text{sinc}(2\pi T e_{freq})\cos(2\pi e_{phase}) + \eta_{IP} \tag{A.3a}$$

$$QP = \sqrt{2\frac{C}{N_0}T}(1 - |e_{chip}|)\text{sinc}(2\pi T e_{freq})\sin(2\pi e_{phase}) + \eta_{QP} \tag{A.3b}$$

In the equations, the e_{chip}, e_{freq}, and e_{phase} represent the code phase, carrier frequency, and carrier phase errors respectively. The amplitude of the correlator output is calculated as a function of the C/N_0 ratio, and is scaled in such a way that the noise term is simulated using a unit variance Gaussian distributed random variable to produce the desired signal strength.

This simulator architecture allows the user to process simulated or experimental data with minimal changes to the software receiver. Only the correlation step must change for the receiver to operate. Using intermediate frequency samples, the software receiver produces correlator outputs through multiplying and accumulating the received samples with samples generated using the NCOs. In simulation, the replica signal errors are calculated first, and the correlator outputs are generated to produce the correct discriminator inputs. This simulator architecture allows the user to transition quickly between simulation or experimental analysis of different receiver designs.

Appendix B

External Velocity Aided PLL Thermal Noise Performance

In Chapter 4, the vector frequency locked loop (VFLL) aided phase locked loop (PLL) carrier phase tracking architecture was investigated. The tracking performance was studied for decreasing C/N_0 ratio and compared to the performance of traditional scalar phase locked loop channels. While the carrier tracking robustness was improved by the feedback from the navigation processor, the performance gains appear to be limited by correlation between the carrier phase discriminator and the error in the feedback from the navigation processor. Velocity measurements derived from an alternative sensor (e.g. IMU, wheel encoders) are not corrupted by the same errors impacting the GPS velocity estimates. Therefore, a carrier frequency error prediction generated using external velocity information will not suffer from the same correlation issues. One benefit of the VFLL aided PLL architecture is that integrating external velocity measurements in the phase tracking routine is straightforward. A block diagram of the VFLL aided PLL receiver with velocity aiding from an external sensor is shown in Figure B.1. As seen in the figure, the predicted carrier frequency error, $\Delta\hat{f}$, is not derived from the velocity measurement of the external sensor. Satellite velocity information and an estimate of the receiver clock drift are provided by the navigation processor.

The frequency error prediction from the navigation processor in the VFLL aided PLL receiver is designed to capture the changes to the received signal that are due to the motion of the receiver. By accounting for the dynamics with the VFLL, the PLL is left to track slow changing errors, and the PLL bandwidth can be decreased to reject more noise. As seen in Figures 4.9 and 4.10, the optimal PLL noise equivalent bandwidth was not significantly reduced when including the VFLL feedback. This result is likely caused by the correlation in the frequency prediction error and the phase discriminator error. Additional simulations were

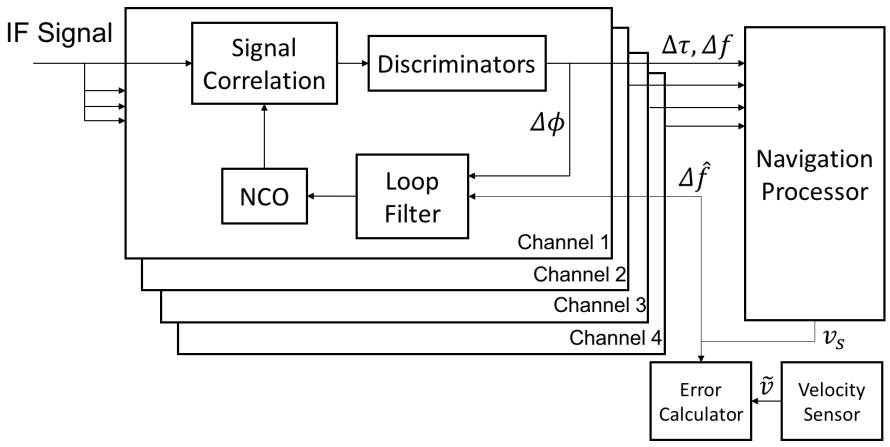

Figure B.1: Block diagram of external velocity based VFLL aided PLL

performed to determine the optimal PLL noise equivalent bandwidth when using frequency error predictions generated from an external velocity source. The velocity measurements of the external sensor were assumed to have errors that are zero mean and Gaussian with a standard deviation of 0.1 m/s. The velocity error is consistent with a navigation grade Inertial Navigation System (INS) [16]. Based on simulations of C/N_0 ratios ranging from 25 to 30 dB-Hz and PLL noise equivalent bandwidth ranging from 4 to 18 Hz, the VFLL aided PLL receiver operated best with a PLL bandwidth of 6 Hz when using the external velocity measurements described above.

Additional simulations were performed with the externally aided PLL with decreasing C/N_0 ratios to analyze the performance. A PLL noise equivalent bandwidth of 6 Hz was used, and the velocity error standard deviation was set to 0.1 m/s as described above. The simulated received signal strength ranged from 25 dB-Hz to 16 dB-Hz C/N_0. In Figure B.2, the results of two tests conducted with C/N_0 ratios of 16 and 17 dB-Hz are shown. There are clear cycle slips for the VFLL aided PLL receiver at 17 dB-Hz C/N_0. On the right, the carrier phase error appears to follow a more random walk rather than settling to half-cycle errors. That would indicate that the phase error is no longer distinguishable in the phase discriminator.

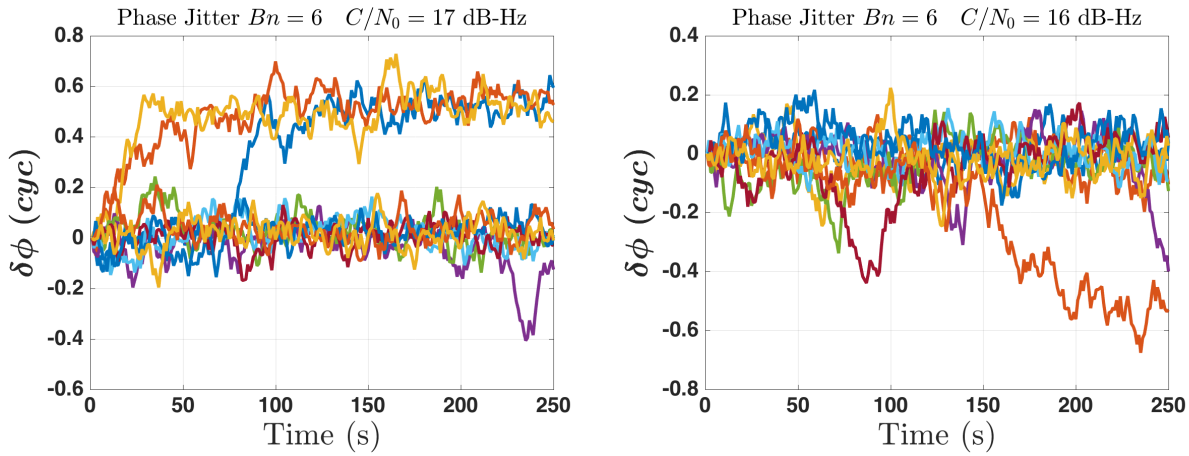

Figure B.2: External velocity based VFLL aided PLL tracking results for C/N_0 ratios of 17 dB-Hz and 16 dB-Hz.

Table B.1: External Velocity Aided PLL Thermal Noise Performance

	σ_ϕ	Num Slips	MTTS	Num Lost
21	13.6	0	NA	0
20	17.6	2	0.55	0
19	16.7	1	0.38	0
18	19.6	6	0.92	0
17	21.8	9	0.75	0
16	23.7	18	0.45	0

The simulation results are compiled as a function of C/N_0 ratio in Figure B.3. The phase jitter increases nearly linearly as the C/N_0 ratio decreases. Based on the simulation study, with accurate external velocity aiding the VFLL aided PLL receiver can maintain phase lock on signals with C/N_0 ratios as low as 20 dB-Hz. This is approximately 5 dB-Hz lower than the VFLL aided PLL using only GPS based velocity estimates. The phase jitter, cycle slip total, and mean time to cycle slip are combined in Table B.1. Again, the robustness of the VFLL aided PLL architecture is reflected in the fact that the receiver never completely lost lock during the simulations.

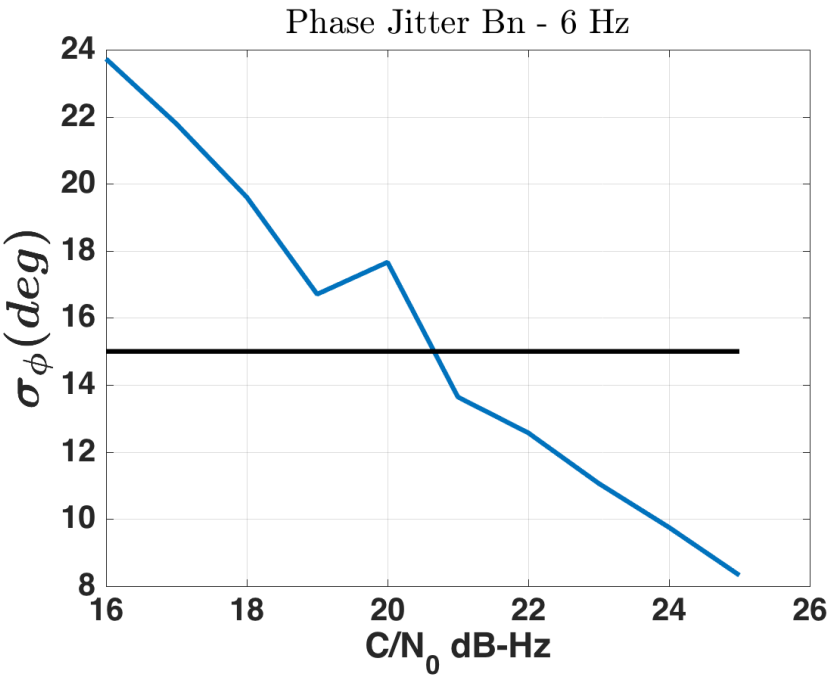

Figure B.3: Standard deviation of carrier phase error for external velocity based VFLL aided PLL as a function of C/N_0 ratio.

Appendix C

Experimental Data Collection

Experimental data was collected in a variety of tests to validate the performance of the algorithms derived in this dissertation. The primary experimental reference sensor used for comparison was a Novatel Propak V3 GPS receiver. When a high precision comparison was needed, data from two Novatel receivers were recorded during data collection. One of the receivers was connected to the same antenna as the rover receiver under test, and the second receiver was connected to the base station antenna. Dual frequency (L1 and L2 frequencies) pseudorange and carrier phase measurements were recorded from the Novatel receivers. A high precision relative position vector was calculated using fixed double difference carrier ambiguities. The RTK algorithm used for the calculation was developed previously at Auburn University, and was validated in [67] and [43] to produce relative position estimates with accuracy on the order of a few centimeters.

The software receiver designed in this dissertation is implemented in C++ programming language, and operates on sampled intermediate frequency GPS data. Multiple Ettus Universal Software Radio Peripheral (USRP) N210 devices were used to collect IF samples for post process using the software GPS receiver. The devices are pictured in Figure C.1. The base N210 contains a FPGA, ADCs, and DACs. A front-end board is required to receive signals in the frequency band of interest. The WBX Rx/Tx daughter board was used in combination with N210 motherboard for data collection. The sample clock was generated with a OCXO with specification similar to those defined in Chapter 3. In-phase and quadrature samples are recorded at a frequency specified by the user. For the experimental results shown in this dissertation the sample frequency was set to 10 MHz.

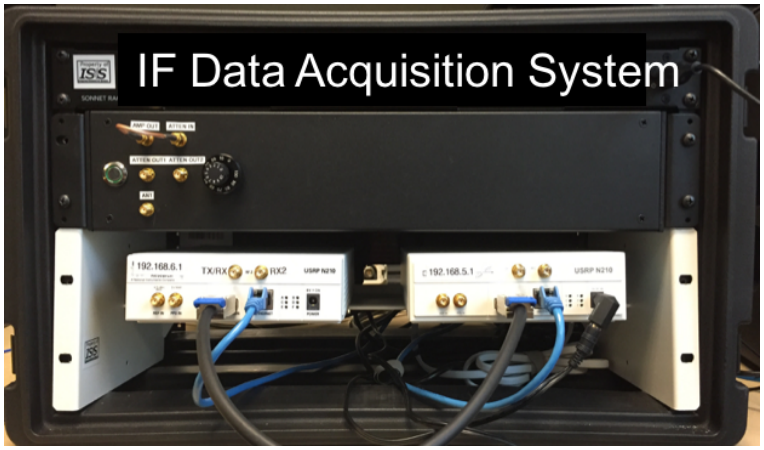

Figure C.1: Two USRP data acquisition systems mounted in mobile carrying case.

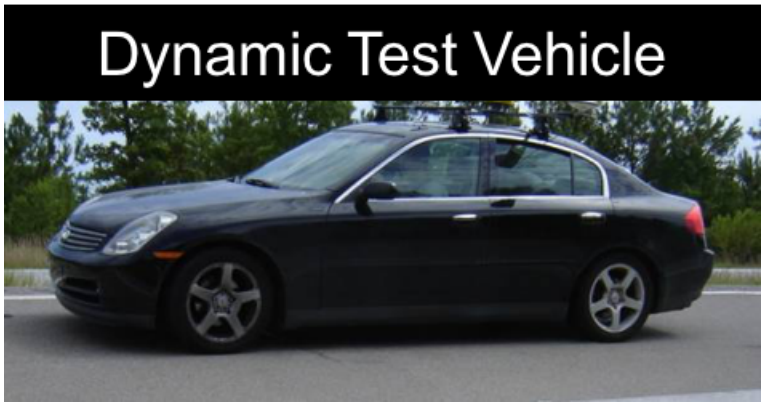

Figure C.2: On road test vehicle with roof mounted GPS antennas.

During dynamic tests, the USRP rack was mounted on the test vehicle. For on road testing the Infiniti G35 shown in Figure C.2 was used as the test platform. Multiple GPS antennas are mounted on the roof, and were connected to signal splitters via coaxial cables. The splitter outputs were connected to the USRP and reference receivers. Data from the USRP and reference receivers were recorded on laptop computers.

Data collection sites included areas with clear sky views, and areas where the sky was partial obstructed by foliage or buildings. Several images are included below showing areas where data was collected to test the performance of the vector tracking software receiver. A description of each area is provided in the image caption.

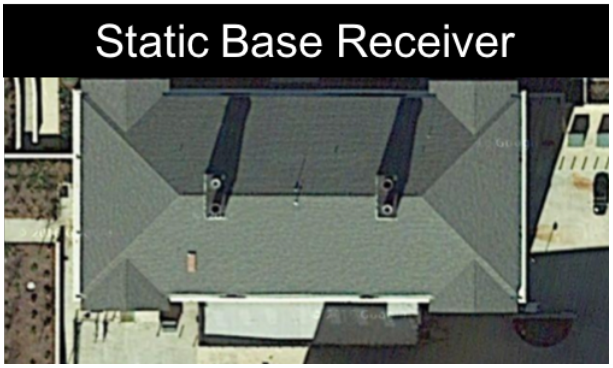

Figure C.3: For initial static testing the antenna mounted on the roof of the Woltosz Engineering building was used. Imagery by Google, DigitalGlobe.

Figure C.4: The precision of the RTK solution was tested over a longer baseline (approximately 600 meters) using data from antenna positioned in a parking lot on the Auburn campus. Imagery by Google, DigitalGlobe.

Figure C.5: Dynamic test area for clear sky data recording using Novatel and USRP receivers. A base station antenna was mounted on a tripod on the southwest corner of the field. Imagery by Google, DigitalGlobe.

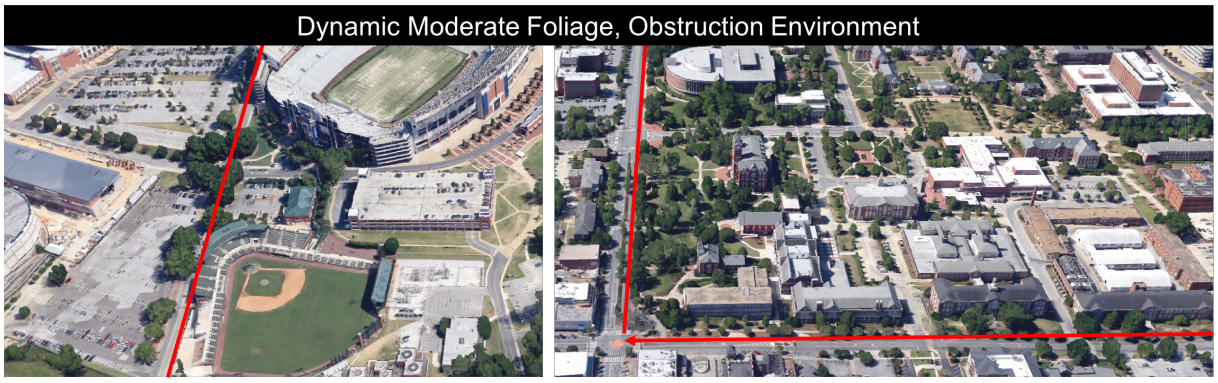

Figure C.6: Dynamic test area with moderate tree cover and intermittent partial sky blockage by multi-story buildings. Imagery by Google, DigitalGlobe.

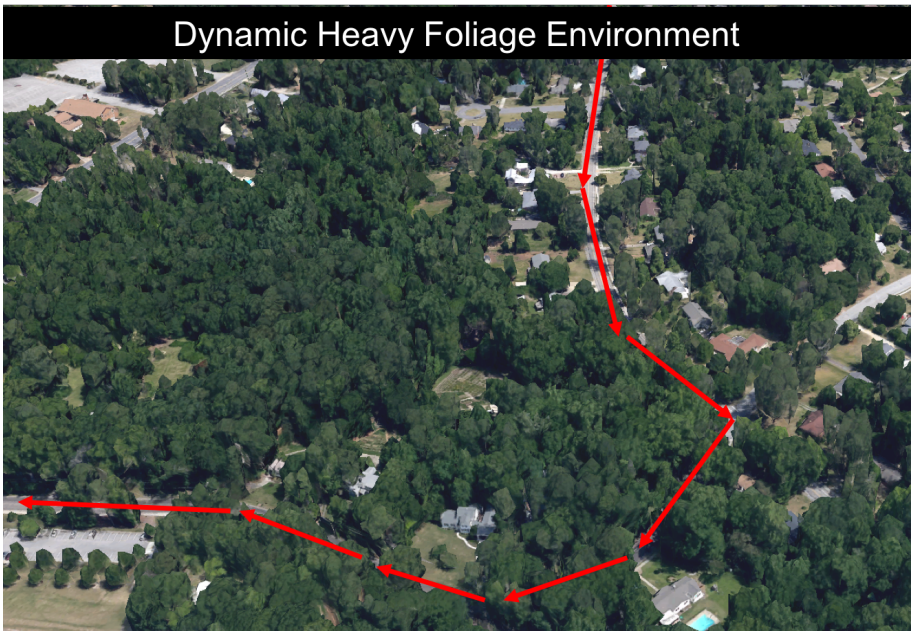

Figure C.7: Dynamic test area with heavy tree cover in local neighborhood. Imagery by Google, DigitalGlobe.